IntechOpen

# Emerging Microwave Technologies in Industrial, Agricultural, Medical and Food Processing

*Edited by Kok Yeow You*

# EMERGING MICROWAVE TECHNOLOGIES IN INDUSTRIAL, AGRICULTURAL, MEDICAL AND FOOD PROCESSING

Edited by **Kok Yeow You**

**Emerging Microwave Technologies in Industrial, Agricultural, Medical and Food Processing**

http://dx.doi.org/10.5772/intechopen.69578
Edited by Kok Yeow You

### Contributors

V.A.Sankar Ponnapalli, V. Y. Jayasree Pappu, Ruhan Aşkın Uzel, Erika Ferrari, Paolo Veronesi, Roberto Rosa, Igor Konstantinovich Kuzmichev, Aleksey Popkov, Ilkyu Kim, Gennadiy Churyumov, Tetyana Frolova, Mohsen Kalantari, José R. Montejo-Garai, Irene Saracho-Pantoja, Jorge A. Ruiz-Cruz, Jesus Rebollar, Lulu Wang, Kok Yeow You

**© The Editor(s) and the Author(s) 2018**
The rights of the editor(s) and the author(s) have been asserted in accordance with the Copyright, Designs and Patents Act 1988. All rights to the book as a whole are reserved by INTECHOPEN LIMITED. The book as a whole (compilation) cannot be reproduced, distributed or used for commercial or non-commercial purposes without INTECHOPEN LIMITED's written permission. Enquiries concerning the use of the book should be directed to INTECHOPEN LIMITED rights and permissions department (permissions@intechopen.com).
Violations are liable to prosecution under the governing Copyright Law.

Individual chapters of this publication are distributed under the terms of the Creative Commons Attribution 3.0 Unported License which permits commercial use, distribution and reproduction of the individual chapters, provided the original author(s) and source publication are appropriately acknowledged. If so indicated, certain images may not be included under the Creative Commons license. In such cases users will need to obtain permission from the license holder to reproduce the material. More details and guidelines concerning content reuse and adaptation can be foundat http://www.intechopen.com/copyright-policy.html.

### Notice

Statements and opinions expressed in the chapters are these of the individual contributors and not necessarily those of the editors or publisher. No responsibility is accepted for the accuracy of information contained in the published chapters. The publisher assumes no responsibility for any damage or injury to persons or property arising out of the use of any materials, instructions, methods or ideas contained in the book.

First published in London, United Kingdom, 2018 by IntechOpen
eBook (PDF) Published by IntechOpen, 2019
IntechOpen is the global imprint of INTECHOPEN LIMITED, registered in England and Wales, registration number: 11086078, The Shard, 25th floor, 32 London Bridge Street
London, SE19SG – United Kingdom
Printed in Croatia

British Library Cataloguing-in-Publication Data
A catalogue record for this book is available from the British Library

Additional hard and PDF copies can be obtained from orders@intechopen.com

Emerging Microwave Technologies in Industrial, Agricultural, Medical and Food Processing
Edited by Kok Yeow You

p. cm.

Print ISBN 978-1-78923-408-4

Online ISBN 978-1-78923-409-1

eBook (PDF) ISBN 978-1-83881-397-0

# Meet the editor

Dr. Kok Yeow You obtained his BSc degree in Physics (Honors) from the Universiti Kebangsaan Malaysia (UKM) in 2001. He pursued his MSc degree in Microwave from the Faculty of Science in 2003 and his PhD degree in Wave Propagation from the Institute for Mathematical Research, Universiti Putra Malaysia (UPM), Serdang, Selangor, Malaysia in 2006. His main personal research interest includes the theory, simulation, and instrumentation of electromagnetic wave propagation at microwave frequencies focusing on the development of microwave passive devices and sensors for medical and agricultural applications. For the past 17 years, he has developed numerous projects concerning microwave waveguide measurement systems for agri-/food, biomedical processing, and microwave devices for biomedical treatments, as well as numerical electromagnetic modeling.

# Contents

# Preface

This book is a self-contained collection of scholarly papers targeting audiences of practicing researchers, academics, postgraduate students, and other scientists whose works are related to microwave technologies. This book intends to provide readers with a comprehensive overview of the current state of the art in microwave technologies. This book is divided into 10 chapters. Chapter 1 is a general introduction that elucidates the principles of microwave and some of the microwave applications. Chapters 2 to 10 are written by several authors. These authors are researchers, scientists, and experts in specific research fields, which are related to microwave engineering. The editor would like to take this opportunity to thank all the authors for their valuable book chapter contribution. In fact, each chapter provides introduction on the specific microwave technology as well as detailed explanation of the methodology on how to solve the raised issues, which include both academic and industry aspects.

Chapters 2, 3, and 4 focus on the analytical models for fractal array antenna design, analytical models of microwave resonance system for high-frequency material characterizations, and simulation modeling for biomedical devices and electromagnetic interference (EMI) measurement setup. Analytical analysis has played a very important role in the academic microwave engineering and industries. Engineers in microwave field will be able to understand the operating background of the microwave systems or devices through analytical analysis easily, as it is the fundamental knowledge in microwave system designs before entering into further application. Based on the analytical models, the time spent on microwave system (antennas, sensors, etc.) designs and measurement setup can be shortened.

Chapters 5, 6 and 7 include emerging microwave instruments and devices. Chapter 5 presents a potential of microwave energy for energy-efficient lighting application using electrodeless sulfur lamp. The electrodeless sulfur lamps with microwave excitation are durable and economical, and they can achieve photosynthetically active radiation (PAR) up to 70% to 80%, which is suitable for larger greenhouse complexes. Chapter 6 presents numerous examples of microwave passive devices made by 3D printing with metal plating. Recently, 3D printing integrated with computer-aided design (CAD) is able to provide relative high precision and rapid and significant cost saving (human resources and material cost) for microwave device fabrication compared to the traditional machining. Chapter 7 presents the microwave imaging system for the concealed metallic forging object detection. The microwave imaging system is made up of Vivaldi antenna array (as sensors) and 3D holographic millimeter-wave algorithm (inverse scattering). In fact, microwave imaging has higher sensitivity with respect to metallic materials, which provides a high contrast of electrical properties between metallic and nonmetallic materials.

Chapters 8, 9, and 10 cover the microwave heating/drying and extraction technologies. Recently, most of the industrial sectors have been using microwave energy in drying or heating process for their products; it is due to the microwave energy, which does not change the structure, color, and nature of the product after the heating/drying process. Furthermore, the cost of the used energy can be saved and easily controlled as well as the heating time.

**Kok Yeow You**
Universiti Teknologi, Malaysia

## Section 1

# Review of Microwave Applications

# Introductory Chapter: RF/Microwave Applications

Kok Yeow You

Additional information is available at the end of the chapter

http://dx.doi.org/10.5772/intechopen.73574

## 1. Introduction

Owing to the rapid development of microwave technology, the microwave components and devices are increasingly common and relative low price compared to 10 years ago. Nowadays, microwave devices are often used and become an indispensable necessity in our daily routines, such as microwave ovens, mobile phones, and Internet. This introductory chapter reviews the microwave applications in this era based on a detailed literature survey and author's experience in microwave researches.

Radio waves and microwaves are a form of electromagnetic radiation with operating frequencies ranging from 30 to 300 MHz and 300 MHz to 300 GHz, respectively [1]. Different microwave applications and technologies will use certain frequency band to avoid frequency interference. These frequencies are grouped into several smaller bands. The most commonly used frequency spectrum classification today is created by the Institute of Electrical and Electronics Engineers (IEEE), which is listed in **Table 1**. Microwave applications for heating and crushing normally use high microwave power which is up to megawatts. In contrast, low microwave power (less than milliwatts) is widely used for domestic wireless communication or high-frequency electronic devices. Microwave applications can be categorized into two groups, namely, communication and noncommunication. Industrial, scientific, and medical (ISM) applications are normally classified as noncommunication group. Several scopes of microwave applications are listed in **Table 2**. The first three industrial, scientific, and medical (ISM) frequency allocations (at 13.66 MHz, 27.32 MHz, and 40.98 MHz) were designated by US Federal Communications Commission (FCC) in 1945 [2]. Recently, there are two microwave frequencies allocated by the FCC for ISM usage, namely, 915 MHz and 2.45 GHz.

Currently, most of the applications are devoted to the 2.45 GHz point, since it provides a suitable compromise between power deposition and penetration depth. The ISM bands defined

| Electromagnetic wave spectrum | Frequency band | Wavelength |
|---|---|---|
| **Radio waves** | **Very high frequency (VHF) (30–300 MHz)** | **10–1 m** |
| **Microwaves** | **Ultrahigh frequency (UHF) (300–3000 MHz)** | **(100–10 cm)** |
| | P band (230 MHz–1 GHz) | 130–30 cm |
| | L band (1–2 GHz) | 30–15 cm |
| | S band (2–4 GHz) | 15–7.5 cm |
| | **Super high frequency (SHF) (3–30 GHz)** | **(10–1 cm)** |
| | S band (2–4 GHz) | 15–7.5 cm |
| | C band (4–8 GHz) | 7.5–3.75 cm |
| | X band (8–12.5 GHz) | 3.75–2.4 cm |
| | Ku band (12.5–18 GHz) | 2.4–1.67 cm |
| | K band (18–26.5 GHz) | 1.67–1.13 cm |
| | Ka band (26.5–40 GHz) | 1.13–0.75 cm |
| **Millimeter waves** | **Extremely high frequency (EHF) (30–300 GHz)** | **(10–1 mm)** |
| | Ka band (26.5–40 GHz) | 1.13–0.75 cm |
| | V band (40–75 GHz) | 7.5–4 mm |
| | W band (75–110 GHz) | 4–2.73 mm |
| | Millimeter band (110–300 GHz) | 2.73–1 mm |

**Table 1.** Institute of Electrical and Electronics Engineers (IEEE) frequency spectrum.

by the International Telecommunication Union (ITU) are listed in **Table 3** [1]. However, during recent years, ISM bands have also been shared with license-free error-tolerant communications applications, such as wireless LANs. In addition, now is the era of the fourth industrial revolution, so-called Industry 4.0, which most operation systems in the industry are in cyber based. Hence, the combination between communication (Internet) and noncommunication (microwave things) technologies is increasingly popular in order to produce smart devices, so-called Internet of Things (IoT), in which the devices are embedded with electronics, software, sensors, actuators, and network connectivity that are capable of covering a variety of protocols, domains, and applications, which include the automotive industry, public safety, emergency services, and medical field [3].

Within the past 40 years, microwave technology using frequency operation exceeding 300 GHz to 3 THz also existed, so-called Terahertz technology. In fact, operating frequency of 300 GHz to 3 THz occupies a middle ground between microwaves and infrared light waves. The corresponding range of the wavelength for the Terahertz frequencies is 0.1–1 mm; thus, it is a denominated submillimeter wave [27]. The Terahertz technology is widely utilized in the field of astronomy, medical, and security, such as space-based remote

| **Communication [3–8]** | **Noncommunication [9–26]** |
|---|---|
| 1 Communication network systems, such as high-speed home and business networking devices (modem and router), device-to-device communication (D2D) system, massive MIMO technology, cloud technologies, and small cell access points | 1 Sensors for industrial, agricultural/food, and medical processing, such as moisture measurement, ripeness/storage period determination, fruit sweetness detection, control of milk of lime, monitoring of nitrogen/phosphorus content in fertilizer, medical diagnostic, moisture soil testing, metal crack detector, and storage tank measurement devices |
| 2 Communication devices and test instruments, such as spectrum analyzer, RF power meter, frequency counter, signal generator, and vector network analyzer | 2 Heating/drying or freeze-drying process (sterilization / pasteurization) in food industry to control pathogenic and spoilage microorganisms in packaged foods |
| 3 Navigation systems such as maritime navigation, Global Positioning System (GPS), air traffic control, airborne radars, and satellite communication | 3 Industrial heating applications, such as casting waxes, sintering ceramics/metal powders, melting of glass/rubber, metal coating, brazing, and paper/wood drying |
| 4 Wireless remote control for security and healthcare systems such as automatic gate/door, automatic barrier systems, burglar alarms, and industrial automation systems (Industry 4.0) | 4 Medical applications, such as hyperthermia treatments, bio-impedance instrumentation, and medical diagnostic imaging (to detect a location or movement of objects within a human body or animal body) |
| 5 Vehicular radar systems to detect the location and movement of objects near a vehicle, enabling features such as near collision avoidance, improved airbag activation, and suspension systems that better respond to road conditions | 5 Material characterization fixtures (materials including graphene, metamaterials, carbon nanotube, conductive polymer, high-temperature superconductor, aerogel, ceramics, semiconductor, polymer insulation, fibers, gases, and chemical liquids) |
| 6 Entertainment and information communication devices/systems such as television broadcast, FM broadcast, radio beacons, maritime radio, walkie-talkie, coast guard communication, satellite communication, and weather radars | 6 Image scan systems to detect the images of buried objects, location of objects contained within a wall, location or movement of persons or objects which are located on the other side of a wall, as well as the intrusion of persons |
| 7 Domestic communication devices, such as 4G/5G smart phone, computer, Bluetooth, Wi-Fi devices, wireless webcam, and wireless microphones | 7 Civil engineering applications (rock crushing, tar road comminuting) |
| | 8 Radiation for agricultural pest control |

**Table 2.** Microwave applications for communication and noncommunication technologies.

sensing and medical diagnostic imaging [28–31], due to the submillimeter waves that are nonionizing, and it can penetrate a wide variety of nonconducting materials. Recently, high operating frequency requirements for microwave test instruments are increasing, such as recent commercial vector network analyzer which is capable of achieving 1.1 THz. Hence, in future, these microwave components and devices are expected to be very small and sensitive.

| **Frequency range (*f*)** | | **Bandwidth (Δ*f*)** | **Center frequency ($f_0$)** |
|---|---|---|---|
| MHz | *6.765–6.795 MHz | *30 kHz | *6.780 MHz |
| | 13.553–13.567 MHz | 14 kHz | 13.560 MHz |
| | 26.957–27.283 MHz | 326 kHz | 27.120 MHz |
| | 40.660–40.700 MHz | 40 kHz | 40.680 MHz |
| | **433.050–434.790 MHz | *1.74 MHz | *433.920 MHz |
| | ***902.000–928.000 MHz | *26 MHz | *915.000 MHz |
| GHz | 2.400–2.500 GHz | 100 MHz | 2.450 GHz |
| | 5.725–5.875 GHz | 150 MHz | 5.800 GHz |
| | 24.000–24.250 GHz | 250 MHz | 24.125 GHz |
| | *26.975–27.283 GHz | *308 MHz | *27.129 GHz |
| | *61.000–61.500 GHz | *500 MHz | *61.250 GHz |
| | *122.000–123.000 GHz | *1 GHz | *122.500 GHz |
| | *244.000–246.000 GHz | *2 GHz | *245.000 GHz |

*Subject to local acceptance

**Only Europe, Africa, the Middle East/Middle West of the Persian Gulf, the former Soviet Union, and Mongolia

***Only Americas, Greenland, and some of the eastern Pacific Islands

**Table 3.** Industrial, scientific, and medical (ISM) operating frequency band defined by the International Telecommunication Union (ITU).

## Author details

Kok Yeow You

Address all correspondence to: kyyou@fke.utm.my

Department of Communication Engineering, Faculty of Electrical Engineering, Universiti Teknologi Malaysia, Johor Bahru, Johor, Malaysia

## References

[1] You KY. RF Coaxial Slot Radiators: Modeling, Measurements, and Applications. USA: Artech House; 2015. ISBN: 978-1-60807-822-6

[2] Osepchuk JM. A history of microwave heating applications. IEEE Transactions on Microwave Theory and Techniques. 1984;**32**(9):1200-1224. DOI: 10.1109/TMTT.1984.1132831

[3] Riazul Islam SM, Kwak D, Humaun Kabir MD, Hossain M, Kwak KS. The Internet of Things for health care: A comprehensive survey. IEEE Access. 2015;**3**:678-708. DOI: 10.1109/ACCESS.2015.2437951

[4] Sobol H. Microwave communications—An historical perspective. IEEE Transactions on Microwave Theory and Techniques. 1984;**32**(9):1170-1181. DOI: 10.1109/TMTT.1984.1132829

[5] Gresham I, Jenkins A, Egri R, Eswarappa C, Kinayman N, Jain N, Anderson R, Kolak F, Wohlert R, Bawell SP, Bennett J, Lanteri J-P. Ultra-wideband radar sensors for short-range vehicular applications. IEEE Transactions on Microwave Theory and Techniques. 2004;**52**(9):2105-2122. DOI: 10.1109/TMTT.2004.834185

[6] Draganov S, Harlacher M, Haas L, Wenske M, Schneider C. Synthetic aperture navigation in multipath environments. IEEE Wireless Communications. 2011;**18**(2):52-58. DOI: 10.1109/MWC.2011.5751296

[7] Wang W-Q, Jiang D. Integrated wireless sensor systems via near-space and satellite platforms: A review. IEEE Sensors Journal. 2014;**14**(11):3903-3914. DOI: 10.1109/JSEN.2014.2356580

[8] Gupta A, Rakesh Kumar JHA. A survey of 5G network: Architecture and emerging technologies. IEEE Access. 2015;**3**:1206-1232. DOI: 10.1109/ACCESS.2015.2437951

[9] Zhang H, Yang R, Foudazi A, Cheng L, Tian G. A review of microwave thermography nondestructive testing and evaluation. Sensors. 2017;**17**(1123):1-33. DOI: 10.3390/s17051123

[10] Berthold Technologies. Concentration Measurements for Milk of Lime: Microwave Measurement. Food-Sugar Production Manual. Retrieved on June 6, 2017. Available from: https://www.berthold.com/en/system/asset/application_milk_of_lime_measurment.pdf

[11] Berthold Technologies. Moisture Measurement on Bales of Lucerne, Tobacco and Others. Microwave Application Manual. Retrieved on June 6, 2017. Available from: https://www.berthold.com/en/pc/downloads

[12] Hydronix. New moisture management technology by Hydronix. Industry Manual. April 2010. Retrieved on August 31, 2017. Available from: https://www.hydronix.com/downloads/articles/product_range/new_moisture_management_technology_for_grain.pdf

[13] George M. Microwave moisture measurement. Grain & Feed Milling Technology. 2008;**119**:14-16

[14] Rezaei M, Ebrahimi E, Naseh S, Mohajerpour M. A new 1.4 GHz soil moisture sensor. Measurement. 2012;**45**(2012):1723-1728. DOI: 10.1016/j.measurement.2012.04.014

[15] Singh S, Gupta D, Jain V, Apurbba K. Sharma: Microwave processing of materials and applications in manufacturing industries: A review. Materials and Manufacturing Processes. 2015;**30**:1-29. DOI: 10.1080/10426914.2014.952028

[16] Okamura S, Zhang Y, Tsukamoto N. A new microstrip line-type moisture sensor for heavily wet tea leaves. Measurement Science and Technology. 2007;**18**:1022-1028. DOI: 10.1080/10426914.2014.952028

[17] Nelson S. Dielectric Properties of Agricultural Materials and their Applications; USA: Academic Press. 2015. ISBN: 9780128023051

[18] You KY, You LL, Yue CS, Mun HK, Lee CY. Chapter 6. Physical and chemical characterization of rice using laboratory and microwave methods. In: Rice—Technology and Production, Edit by Amanullah and Shah Fahad. USA: InTech; 2017. pp. 81-99. ISBN: 978-953-51-5200-2

[19] You KY. Chapter 14 Materials Characterization Using Microwave Waveguide Systems. In: Goudos SK, editor. Microwave Systems and Applications. USA: InTech; 2017. pp. 341-358. ISBN: 978-953-51-2867-0

[20] You KY, Then YL. Simple calibration and dielectric measurement technique for thin material using coaxial probe. IEEE Sensors Journal. 2015;**15**(10):5393-5397. DOI: 10.1109/JSEN.2015.2427873

[21] You KY, Lee YS, Zahid L, MFA M, Lee KY, Cheng EM. Dielectric measurements for low-loss materials using transmission phase-shift method. Jurnal Teknologi. 2015;**77**(10):69-77. DOI: 10.11113/jt.v77.6286

[22] Mason A, Korostynska O, Louis J, Cordova-Lopez LE, Abdullah B, Greene J, Connell R, Hopkins J. Non-invasive in-situ measurement of blood lactate using microwave sensors. IEEE Transactions on Biomedical Engineering. 2017. DOI: 10.1109/TBME.2017.2715071

[23] Choi H, Naylon J, Luzio S, Beutler J, Birchall J, Martin C, Porch A. Design and in vitro interference test of microwave noninvasive blood glucose monitoring sensor. IEEE Transactions on Microwave Theory and Techniques. 2015;**63**(10):3016-3025. DOI: 10.1109/TMTT.2015.2472019

[24] Nguyen PT, Abbosh A, Crozier S. Three-dimensional focused microwave hyperthermia for breast cancer treatment with experimental validation. IEEE Transactions on Antennas and Propagation. 2017;**65**(7):3489-3500. DOI: 10.1109/TAP.2017.2700164

[25] Shultz K, Stang P, Kerr A, Pauly J, Scott G. RF field visualization of RF ablation at the Larmor frequency. IEEE Transactions on Medical Imaging. 2012;**31**(4):938-947. DOI: 10.1109/TMI.2011.2162248

[26] Zhang X, Liu J, He B. Magnetic-resonance-based electrical properties tomography: A review. IEEE Reviews in Biomedical Engineering. 2014;**7**:87-96. DOI: 10.1109/RBME.2013.2297206

[27] Wiltse JC. History of millimeter and submillimeter waves. IEEE Transactions on Microwave Theory and Techniques. 1984;**32**(9):1118-1127. DOI: 10.1109/TMTT.1984.1132823

[28] Siegel PH. Terahertz technology. IEEE Transactions on Microwave Theory and Techniques. 2002;**50**(3):910-928. DOI: 10.1109/22.989974

[29] Chattopadhyay G. Technology, capabilities, and performance of low power Terahertz sources. IEEE Transactions on Terahertz Science and Technology. 2011;**1**(1):33-53. DOI: 10.1109/TTHZ.2011.2159561

[30] Ke W, Jian Cheng Y, Djerafi T, Hong W. Substrate-integrated millimeter-wave and terahertz antenna technology. Proceedings of the IEEE. 2012;**100**(7):2219-2232. DOI: 10.1109/JPROC.2012.2190252

[31] Tabata H. Application of terahertz wave technology in the biomedical field. IEEE Transactions on Terahertz Science and Technology. 2015;**5**(6):1146-1153

## Section 2

# Microwave System Design Models

# Fractal Array Antennas and Applications

V. A. Sankar Ponnapalli and P. V. Y. Jayasree

Additional information is available at the end of the chapter

http://dx.doi.org/10.5772/intechopen.74729

### Abstract

Modern celestial and other advanced wireless communication systems require feasible array antennas with reconfigurable multibeams, broadband, high end of coverage, high gain, less side-lobe level with wider side-lobe level angles, better signal-to-noise ratio and small in size than conventionally achievable. This has initiated array antenna research in different tracks, one of which is by using fractal array antennas. The investigation on fractal-shaped antennas is basically focused on two fundamental areas such as the analysis and design of fractal antenna elements and the application of fractal geometric technology to the design of array antennas. These recursively generated antennas provide new insights into the antenna properties due to their self-similar behaviour. Owing to the feasible geometric construction and advanced properties, fractal antennas find applications in advanced wireless communications, MIMO radars, satellite communications and space observations. This work concentrated here is primarily aimed on the design of fractal array antennas using concentric elliptical ring sub-array fractal geometric design methodology and the reduction of total number of antenna elements at higher expansion factors of both conventional and proposed fractal array antennas.

**Keywords:** fractal, array antennas, array factor properties, concentric elliptical ring sub-array design methodology

## 1. Introduction

A fractal structure is a never-finishing pattern. These structures are infinitely complex patterns that are self-similar across diverse scales [1]. Due to this self-similar performance, fractals find diverse applications in both science and engineering. The word fractal has its origin in the Latin word fractus, meaning an irregular surface. Coastal line of sea, mountains, sea shells, snowflakes, leaves and eye strain of a peacock are some of the naturally existed fractals [2].

**Figure 1** shows some of the naturally existed fractals in the nature. By their geometrical constructions, fractal patterns come in two main variations:

1. Random fractals
2. Deterministic or geometric fractals

All natural fractals come under random fractals because they do not have a particular deterministic way of generation and they are non-integral surfaces. These are also known as stochastic fractals. The generation of these fractals is analysed by different statistical techniques. The randomness of these fractals varies with structure to structure and way of generation. The Brownian motion of microscopic particles in fluid is also the best example for random fractal behaviour as shown in **Figure 2**. Deterministic fractals are geometry-based structures having scaled repetitive nature. These fractals have exact dimensions for the expansion unlike random fractals. Generally, all deterministic fractals are generated using iterated function system (IFS), recurrent iterated function systems (RIFS) and complex number methods. In these methods of

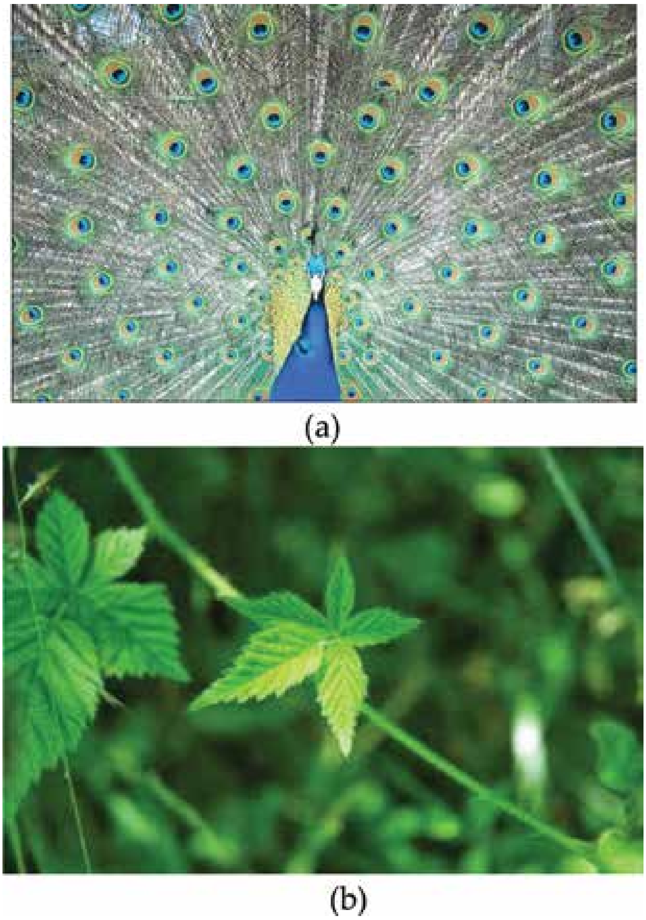

**Figure 1.** (a) Eye strain of a peacock. (b) Fractal-shaped leaf.

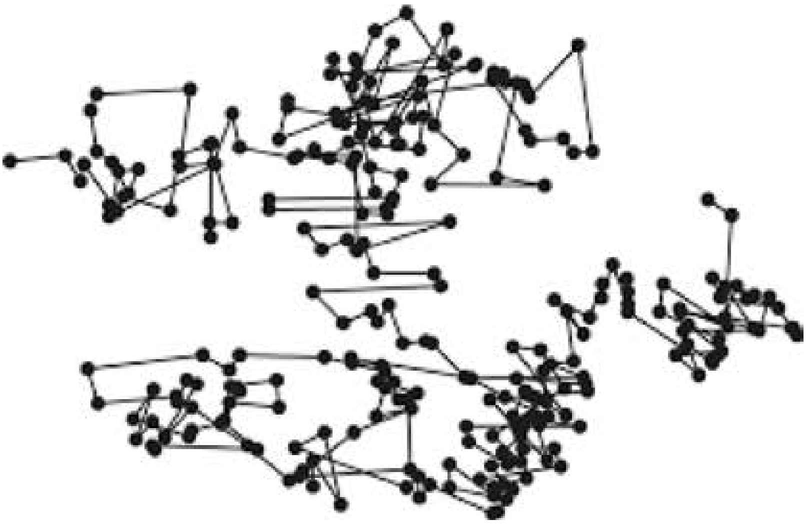

**Figure 2.** The Brownian motion of microscopic particles.

generation, fractal structures are created on the source of scaling, plan axis rotation and dislocation. The most popular IFS and complex number fractals are the Koch curve, the Sierpinski triangle, Julia sets and the Sierpinski square which are shown in **Figure 3**. In these deterministic fractal structures, the basic generator or seed is copied itself up to infinite iterations (p) [3–5]. The design methodology proposed in this chapter for the generation of various fractal array antennas is also having a deterministic way of generation.

## 2. Applications of fractals

Fractal geometric technology has permeated numerous areas of science and engineering, such as astrophysics, image processing, biological sciences, bioinformatics, antenna engineering, computer graphics and medical applications:

- Image compression using fractal image coding has led to a major fall in memory requirements and processing time than conventional techniques [6]. **Figure 4** exemplifies the process of fractal image compression. The output images of shape 'A' unite to the Sierpinski triangle. This last image is called 'attractor' for this photocopying mechanism. Any original image will be transformed to the attractor if the mechanism runs repetitively. This characteristic is the advantage to the fractal image compression.
- The fractal structures inspired from the human blood vessels of fractal nature offer an easy low-pressure network to achieve a silicon chip to allow a cooling fluid to uniformly flow across the surface of the chip, and this keeps the computer cool.
- The human body is also having fractal nature. The DNA, retina, blood vessels and lobes of the lungs are self-similar structures. Euclidean geometry is powerless to study and

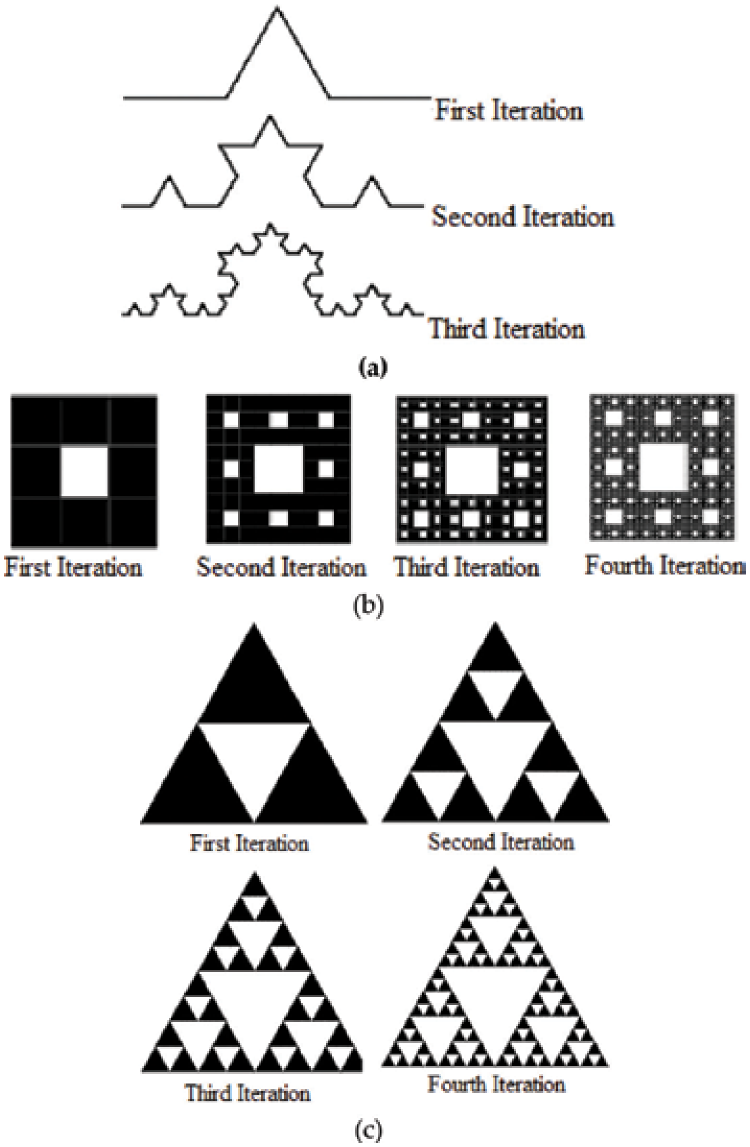

**Figure 3.** (a) Koch curve up to three iterations. (b) Sierpinski square or carpet up to four iterations. (c) Sierpinski triangle up to four iterations.

analyse abnormalities in these structures. Fractal geometric technology and fractal analysis tools are more useful to diagnose irregularities in the human body [7], and **Figure 5** shows the retina network of fractal nature.

- Fractal mesh invention has divulged to diminish memory requisites and CPU time for finite element analysis of quivering problems [8].

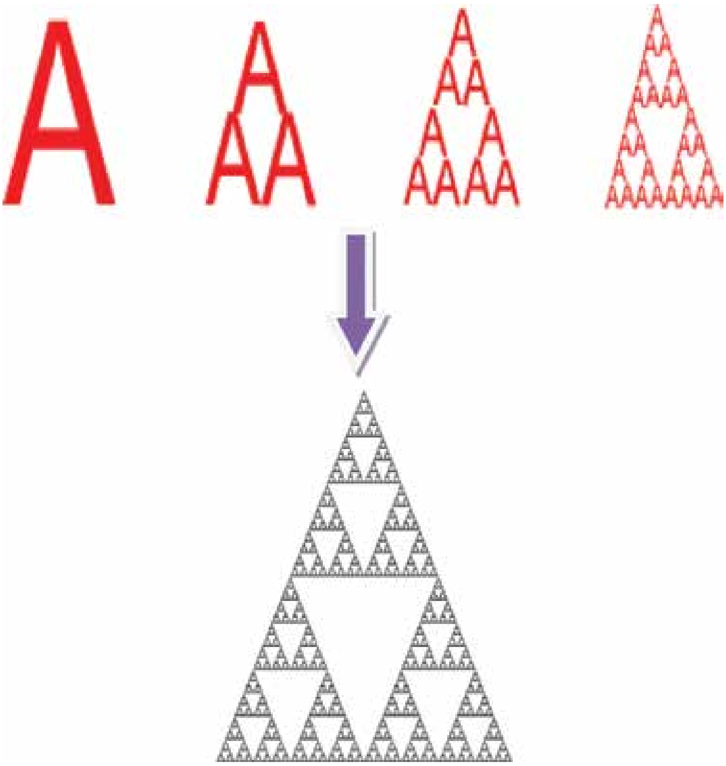

Figure 4. Fractal image compression using Sierpinski triangle.

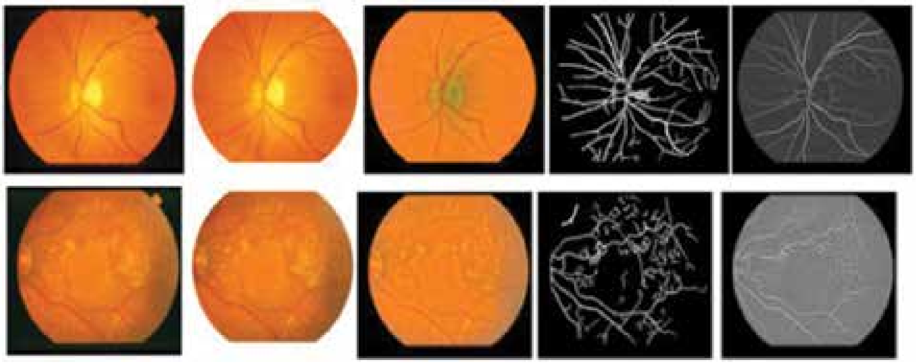

Figure 5. The retina network of fractal nature.

- Bridges, cables and different zones in cities such as industrial, commercial and residential places are designed using this repetitive fractal geometric technology as shown in **Figure 6** [9].
- The largest use of fractals exists in computer graphics. Many image processing schemes use fractal algorithms to create natural and artificial fractal structures digitally [10].

**Figure 6.** Triangular and circular landscape of a city zone.

## 3. Fractal geometric technology in antenna engineering

The concept of fractal geometric technology to the antenna engineering was pioneered by Kim and D. L. Jaggard [11]. They introduced random fractal array antennas for less side-lobe levels. Conventional methods to the design and analysis of antennas have their base in Euclidean geometric methodology. There has been a substantial amount of current interest, however, in the option of developing antennas and array antennas that utilize fractal geometric technology in their design methodologies. Actually, designing of antennas using Euclidean geometry is based on a certain formula and analytical equations, but in this fractal geometry, designing of antennas depends on iterative functions and their recursive algorithms.

Fractal antenna engineering is having two main branches of antenna design methods to fulfil the requirements of wireless-based communication systems. **Figure 7** shows the two main branches of 'fractal antenna engineering'. Depending on their properties and designing parameters, both fractal-shaped radiators and fractal array antennas are again classified into various types. Both types are playing a significant role in the advanced communication systems owing to their magnificent radiation characteristics and miniaturized design techniques.

## 4. Fractal-shaped radiators

The multiband behaviour of fractal-shaped antennas was introduced by C. P. Baliarda. In that study, Sierpinski and Koch monopole antennas were initiated, and these fractal antennas have multiband performance over different frequency bands as shown in **Figure 8**. Such performance

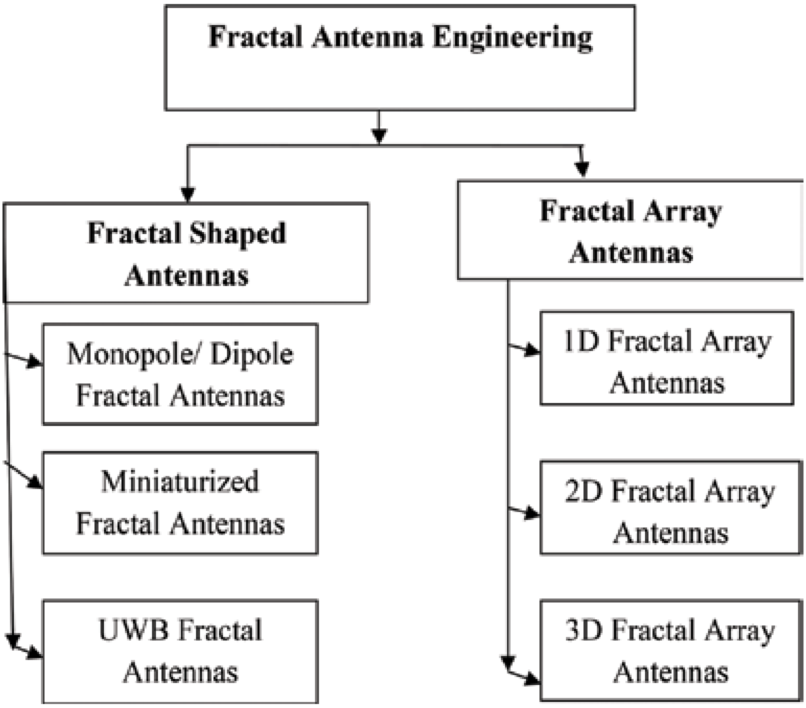

**Figure 7.** Basic classifications of fractal antennas.

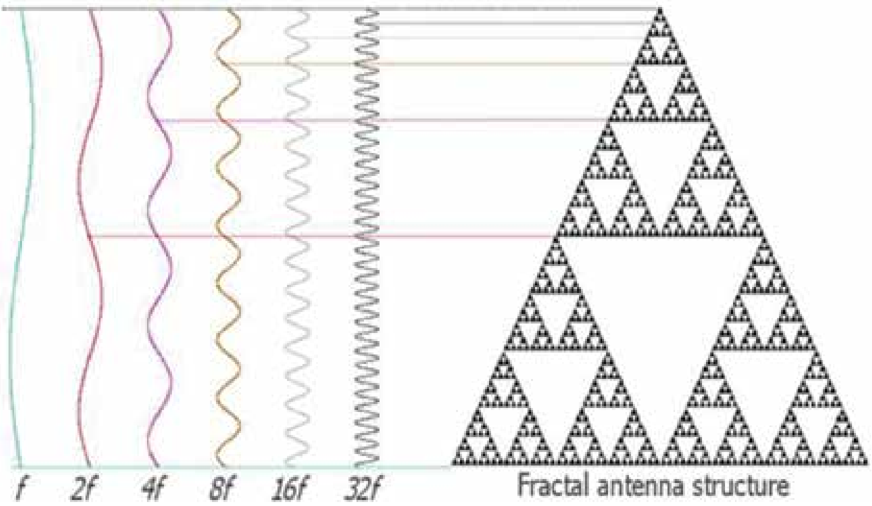

**Figure 8.** Logarithmic frequency response of from Sierpinski fractal structure.

is based on the repetitive nature of the fractal structures, bends and corners [12–15], and some more fractal antennas such as modified Sierpinski monopole, modified half-Sierpinski gasket and Mod-P Sierpinski fractal antennas were introduced for multiband applications in [16–18].

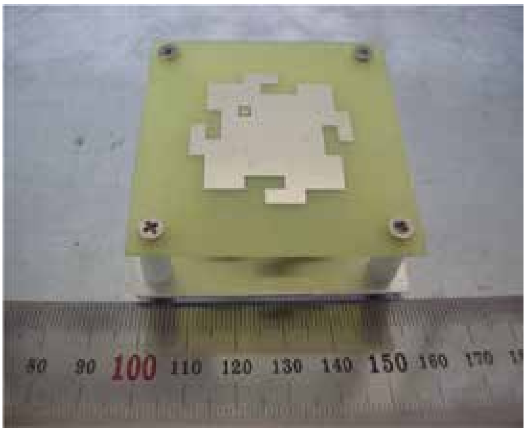

**Figure 9.** Miniaturized Giuseppe Peano microstrip patch antenna [32].

Like Sierpinski fractal gasket antennas, Sierpinski fractal carpet structures have also been used in the designing of antenna elements [19]. One of the serious setbacks with a small loop antenna is that the input resistance is very small, building it hard to couple power to the antenna. By using a fractal loop, the input impedance of the antenna increases. Koch Island, Minkowski and hexagonal geometry with triangular loop are the best examples for the fractal loop antennas [20–24].

Fractal geometric technology was also introduced in microstrip patch antennas instead of conventional rectangular, circular and square geometries, and this leads to improved gain of those antennas with multiband and ultrawideband behaviour [25]. The analogous insight of raising the electrical length of a radiator can be applied to a patch antenna [26]. The patch antenna can be analysed as a 'microstrip transmission line'. So, if the current will be forced to pass through the convoluted path of a fractal structure rather than a conventional Euclidean pathway, the area needed to engage the resonant transmission line will be reduced. This method has been applied to patch antennas in a range of forms [27–29]. Recently, novel patterns of fractal antennas are projected for miniaturization applications, and miniaturized Giuseppe Peano microstrip patch is shown **Figure 9** [30–32].

## 5. Fractal array antennas

An array antenna is one of the best solutions for the long-range communication systems rather than aperture antennas. The multiplicity of antenna elements allows more particular control of the radiation pattern, thus resulting in lower side lobe level and high directive scanned beams. Due to these fundamental properties, array antennas play a vital role in military, defence and other space applications. Owing to novel insights into array antenna parameters like low side lobe level with narrow beams and wider side lobe level angles, ultrawideband, multibeams, feasible and simple design methodologies and algorithms of fractal array antennas, usage of these arrays increases quite commonly in the antenna literature from the past two to three decades. Due to these properties, fractal array antennas find applications in celestial and other advanced communication systems.

Random and deterministic fractal array antennas are the two basic types of fractal arrays based on their geometric construction. Again, deterministic fractal array antennas are also divided into three types based on their geometric patterns [33–36]:

1. Linear (1D) fractal array antennas
2. Planar (2D) fractal array antennas
3. Conformal (3D) fractal array antennas

This chapter focused on the design methodology of linear and planar deterministic fractal array antennas using concentric elliptical ring sub-array design methodology. In this process of design, the behaviour of fractal nature should apply to the regular concentric elliptical antenna array. This recursive process will produce self-similar concentric elliptical geometry as depicted in **Figure 10**. It is clear from the definition of fractal that the same shape repeats again and again; in this manner geometric structure considered here also repeats again and again. The array antennas proposed in this work can be defined as arrays of arrays, which means that the original counterpart of the array antennas repeats again and again. The general array factor of fractal nature is defined in Eq. (1), which is based on the definition of self-similar nature. The equation for the fractal array factor is the product of generating sub-array factor [37–38]:

$$A.F_p(A.F(\theta,\varphi)) = \prod_{p=1}^{P} GSA\left(S^{p-1}(A.F(\theta,\varphi)\right) \tag{1}$$

where GSA and A.F stand for generating sub-array and array factors, respectively. The array factor of concentric elliptical ring sub-array geometric generator for the design of linear and planar deterministic fractal array antennas is given in Eq. (2):

$$A.F_P(\theta,\varphi) = \prod_{p=1}^{P}\left[\sum_{m=1}^{M}\sum_{n=1}^{N} I_{mn} e^{jkS^{p-1}\Psi_{mn}}\right] \tag{2}$$

$$\begin{aligned}\psi_{mn} = {} & \left(a\cos\varphi_{mn}\cos\varphi + b\sin\varphi_{mn}\sin\varphi\right)\sin\theta \\ & -\left(a\cos\varphi_{mn}\cos\varphi_0 + b\sin\varphi_{mn}\sin\varphi_0\right)\sin\theta_0\end{aligned} \tag{3}$$

$$\varphi_{mn} = \frac{2\pi}{N}(mn-1) \tag{4}$$

where S is the scaling factor and two is the scaling factor of the considered sub-array; P is the iterations and four successive iterations have considered in this work, and it can be extended up to infinite iterations; M is the number of concentric rings and here only one concentric has been considered; N is the number of antenna elements and a number of antenna elements are depending on the iterations; k is the wave equation, $I_{mn}$, uniform current amplitudes; $\varphi_{mn}$ is the position of the antenna element in x-y region; and $\theta_0$ and $\varphi_0$ are steering angles. This geometric technique replicates the concentric circular ring sub-array design methodology, but in this case, the circular generator is replaced with the elliptical generator as depicted in **Figure 10**. The proposed methodology permits choice in broadening the shape of a radiation beam or for designing multiple beams for any deterministic 1D and 2D fractal array antennas without entailing any amplitude variation and with less power constrain. The triangular fractal array antenna of expansion factor of 2 and four successive iterations have been designed by concentric elliptical ring sub-array design methodology which is observed in **Figure 11**, and

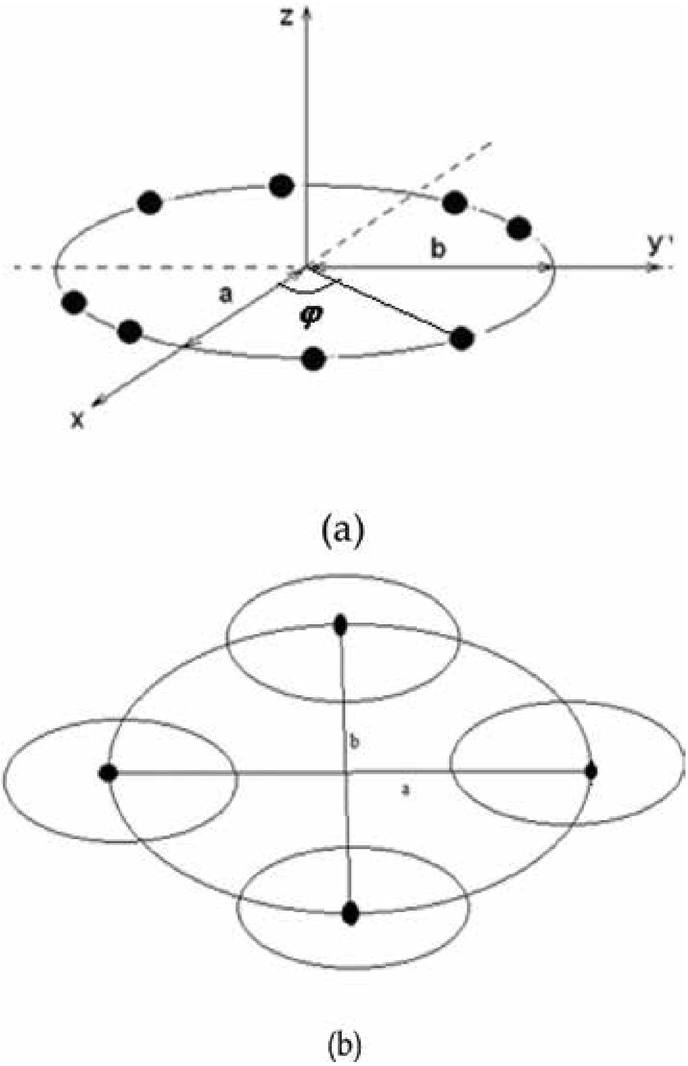

**Figure 10.** Concentric elliptical sub-array geometric generators for (a) stage 1 and (b) stage 2 [38].

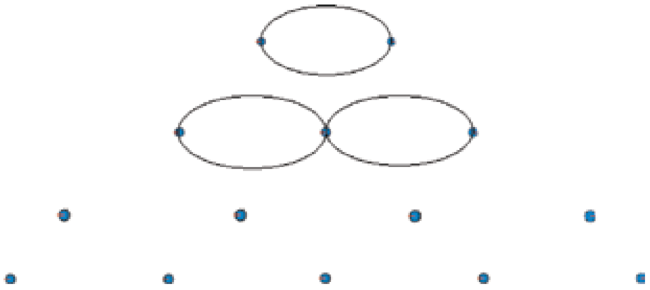

**Figure 11.** The first four iterations of linear fractal array antenna for an expansion factor of 1 [37].

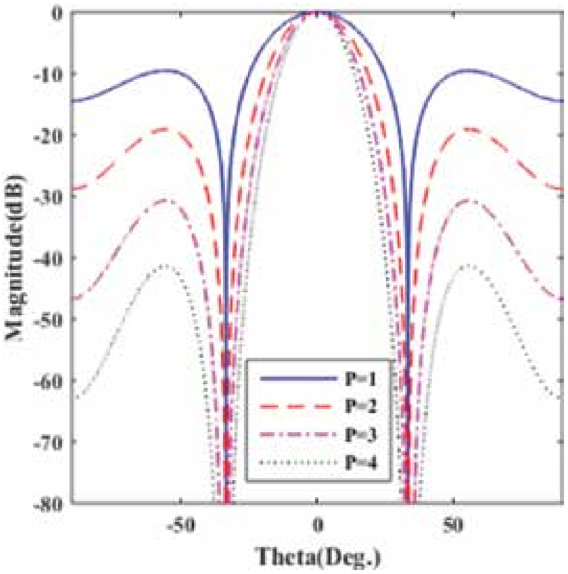

**Figure 12.** Array factors of triangular fractal planar array antennas generated by concentric elliptical sub-array methodology for S = 1 and up to four iterations [37].

the corresponding design equation is described in Eq. (4). The basic triangular array starts with three elements and expands up to four iterations in this chapter. Same distance (d = λ/2) between the antenna elements maintained for both expansion factors (S) of 1 and 2. Nearly one third of the antenna elements can be thinned in the first iterations due to recursive nature of the proposed methodology. **Figure 12** depicts array factor of proposed triangular fractal array antenna. Wide side lobe level angles of 53.1°, 55.4°, 54.1° and 55.8° are observed in four successive iterations with a proper balance between the remaining array factor properties:

$$A.F_P(\theta,\varphi) = \prod_{p=1}^{4}\left[\sum_{m=1}^{1}\sum_{n=1}^{3} I_{mn} e^{jkS^{P-1}\Psi_{mn}}\right] \tag{5}$$

## 6. Conclusions

Fractals are self-similar structures. Various fields of science and technology have inspired by these self-similar structures to develop easy and reliable systems. Application of fractal concepts to the antenna engineering leads to new insights into the antenna parameters. Any polygon-shaped fractal array can be constructed using concentric elliptical ring sub-array design methodology. This design methodology and fractal array antennas generated by this methodology can be helpful for the generation of multiple beams with different array factor properties using a single fractal array antenna without any hardware complexity.

## Author details

V. A. Sankar Ponnapalli[1]* and P. V. Y. Jayasree[2]

*Address all correspondence to: vadityasankar3@gmail.com

1 Department of Electronics and Communication Engineering, Sreyas Institute of Engineering and Technology, Hyderabad, India

2 Department of Electronics and Communication Engineering, GITAM (Deemed to be University), Visakhapatnam, India

## References

[1] Mandelbrot BB. The Fractal Geometry of Nature. New York: W.H. Freeman; 1983

[2] Peitgen HO, Jurgens H, Saupe D. Chaos and Fractals: New Frontiers of Science. New York: Springer-Verlag; 1992

[3] Kaye BH. A Random Walk through Fractal Dimensions. New York: VCH; 1994

[4] Mora P. Random and deterministic fractals, PhD Thesis. Budapest University of Technology and Economics; 2013

[5] Falconer KJ. Fractal Geometry: Mathematical Foundations and Applications. New York: Wiley; 1990

[6] Jacquin AE. Fractal image coding: A review. Proceedings of the IEEE. 1993;**81**:1451-1465

[7] LamriniUahabi K, Atounti M. Applications of fractals in medicine. Annals of the University of Craiova: Mathematics and Computer Science Series. 2015;**42**(1):167-174

[8] Jeng JH, Varadan VV, Varadan VK. Fractal finite element mesh generation for vibration problems. The Journal of the Acoustical Society of America. 1987;**82**:1829-1833

[9] Available from: http://www.fractal.org/Bewustzijns-Besturings-Model/Fractals-Useful-Beauty.htm

[10] Available from: http://fractalfoundation.org/OFC/OFC-index.htm

[11] Kim Y, Jaggard DL. The fractal random array. Proceedings of the IEEE. 1986;**74**(9):1278-1280

[12] Puente C, Romeu J, Pous R, Garcia X, Benitez F. Fractal multiband antenna based on the Sierpinski gasket. Electronics Letters. 1996;**32**(1):1-2

[13] Puente-Baliarda C, Romeu J, Pous R, Cardama A. On the behavior of the Sierpinski multiband fractal antenna. IEEE Transactions on Antennas and Propagation. 1998;**46**(4): 517-524

[14] Puente-Baliarda C, Pous R. Fractal design of multiband and low side-lobe arrays. IEEE Transactions on Antennas and Propagation. 1996;**44**(5):730-739

[15] Puente C, Romeu J, Pous R, Ramis J, Hijazo A. Small but long Koch fractal monopole. Electronics Letters. 1998;**34**(1):9-10

[16] Krzysztofik W. Modified Sierpinski fractal monopole for ISM-bands handset applications. IEEE Transactions on Antennas and Propagation. 2009;**57**(3):606-615

[17] Hwang K. Dual-wideband monopole antenna using a modified half-sierpinski fractal gasket. Electronics Letters. 2009;**45**(10):487-489

[18] Castany JS, Robert JR, Puente C. Mod-P Sierpinski Fractal Multi-Band Antenna. In: Proc. Millennium Conference on Antennas and Propagation; 2000

[19] Song CTP, Hall PS, Ghafouri-Shiraz H, Wake D. Fractal stacked monopole with very wide bandwidth. Electronics Letters. 1999;**35**:945-946

[20] Vinoy K. Fractal shaped antenna elements for wideband and multi band wireless applications. Ph.d. dissertation. The Pennsylvania State University; 2002

[21] Best S. On the performance properties of the Koch fractal and other bent wire monopoles. IEEE Transactions on Antennas and Propagation. 2003;**51**:1292-1300

[22] Borja C, Romeu J. On the behavior of Koch Island fractal boundary microstrip patch antenna. IEEE Transactions on Antennas and Propagation. 2003;**51**:1281-1291

[23] Behera S, Vinoy KJ. Multi-port network approach for the analysis of dual band fractal microstrip antennas. IEEE Transactions on Antennas and Propagation. 2012;**60**:5100-5106

[24] Oloumi D, Ebadi S, Kordzadeh A, Semnani A, Mousavi P, Gong X. Miniaturized reflectarray unit cell using fractal-shaped patch-slot configuration. IEEE Antennas and Wireless Propagation Letters. 2012;**11**:10-13

[25] Hara Prasad RV, Purushottam Y, Misra VC, Ashok N. Microstrip fractal patch antenna for multi-band communication. Electronics Letters. 2000;**36**:1179-1180

[26] Gianvittorio J, Rahmat-Samii Y. Fractal antennas: A novel antenna miniaturization technique, and applications. IEEE Antennas and Propagation Magazine. 2002;**44**:20-36

[27] Sinha S, Jain M. A self-affine fractal multiband antenna. IEEE Antennas and Wireless Propagation Letters. 2007;**6**:110-112

[28] Chen WL, Wang GM, xin Zhang C. Small-size microstrip patch antennas combining Koch and Sierpinski fractal-shapes. IEEE Antennas and Wireless Propagation Letters. 2008;**7**: 738-741

[29] Lui W, Cheng C, Zhu H. Compact frequency notched UWB fractal printed slot antenna. IEEE Microwave and Wireless Components Letters. 2006;**16**(4):224-226

[30] Shaker GSA, and Safavi-Naeini S. Highly miniaturized fractal antennas. IEEE- Radio and Wireless Symposium; 2007

[31] Bayatmaku N, Lotfi P, Azarmanesh M, Soltani S. Design of simple multiband patch antenna for mobile communication applications using new E-shape fractal. IEEE Antennas and Wireless Propagation Letters. 2011;**10**:873-875

[32] Oraizi H, Hedayati S. Miniaturization of microstrip antennas by the novel application of the Giuseppe Peano fractal geometries. IEEE Transactions on Antennas and Propagation. 2012;**60**:3559-3567

[33] Jaggard DL, Jaggar AL. Cantor ring arrays. IEEE Antennas and Propagation Society International Symposium; 1998

[34] Werner DH, Haupt RL, Werner PL. Small and fractal antennas in modern antenna handbook the theory and design of antenna arrays. IEEE Xplore: IEEE Antennas and Propagation Magazine. 1999;**41**(5):37-59

[35] Kuhirun W. A new design methodology for modular broadband arrays based on fractal tilings. Ph.D. Thesis, USA: Department of Electrical Engineering, Pennsylvania State University; 2003

[36] Werner DH, Ganguly S. An overview of fractal antenna engineering research. IEEE Xplore: IEEE Antennas and Propagation Magazine. 2003;**45**(1):38-57

[37] Sankar Ponnapalli VA, Jayasree PVY. Design and analysis of novel fractal linear and planar array antennas for satellite applications. Advanced Electromagnetics. 2016;**5**(3): 56-62

[38] Sankar Ponnapalli VA, Jayasree PVY. Design of multi-beam rhombus fractal array antenna using new geometric design methodology. Progress in Electromagnetics Research C. 2016; **64**:151-158

# Resonant Systems for Measurement of Electromagnetic Properties of Substances at V-Band Frequencies

Kuzmichev Igor K. and Popkov Aleksey Yu.

Additional information is available at the end of the chapter

http://dx.doi.org/10.5772/intechopen.73643

## Abstract

Hemispherical open resonator (OR) with the segment of the oversized circular waveguide is considered. The cavity is formed by cylindrical, conical and spherical surfaces, and only axial-symmetric modes are excited. The power and spectral characteristics of such cavity with a dielectric bead and a rod have been studied. The quasi-periodic behavior of those dependencies was found out. Their qualitative agreement with similar dependencies for a cylindrical cavity is shown. It was found that physical processes in the cavity and in the hemispherical OR with the segment of the oversized circular waveguide are identical. Dielectric permittivity and loss-angle tangent measurements have been carried out in millimeter wavelength range for the Teflon and Plexiglas samples having the shape of the bead as well as for the fused quartz and glass samples of the rod shape. It was found out that such a resonant system allows measuring samples with high losses, that is, especially important for quality control of food stuffs and analysis of biological liquids. Energy analysis of the OR with the segment of the oversized rectangular waveguide has been performed. Basic possibility to apply such a resonant system for measurement of the dielectric permittivity of cylindrical samples with high losses has been shown as well.

**Keywords:** permittivity, cavity, open resonator, circular waveguide, rectangular waveguide, oversized waveguide

## 1. Introduction

Measurement of electromagnetic properties of existing and novel materials in new frequency ranges is an important issue of the day. Recently emerged new class of artificial materials—composite materials (composites) are characterized by the negative refraction coefficient. Investigations showed that devices based on such materials can possess entirely unique properties and characteristics [1]. Caused by technology progress, advance of composite materials into millimeter and especially sub-millimeter ranges requires knowing of information about their electromagnetic characteristics. On the other hand, the real part of dielectric permittivity $\varepsilon'$ and dielectric loss-angle tangent tan $\delta$ of water, which is the main component of the whole series of food stuff and biological liquids, decrease with the wavelength shortening. Therefore, for effective control of their quality, we also should move to the specified ranges of the wavelengths. For measurement of electromagnetic characteristics of such substances, the application of the resonant techniques is needed due to their higher accuracy. The main point of such methods consists of observation of resonant curves of the oscillatory circuit, in which the sample of the studied substance is placed.

Comparing the resonance curves corresponding to the cases of resonator with and without sample allows determining both $\varepsilon'$ and tg $\delta$ using the $Q$-factor and frequency shift. Open resonators (OR) are used as circuits in millimeter and sub-millimeter ranges for such measurements. The peculiarity of such resonant systems consists of the fact that, apart from high $Q$-factor, their geometrical dimensions account a few tens of wavelengths, and coupling with free space provides an additional mode selection and free access to the resonant volume. However, such resonant systems are applicable to use just for investigations of substances with low losses. In the case of high losses, sample thickness should not exceed the size of the skin layer since it can result in oscillation suppression in such resonant systems. This circumstance imposes limitations to the application of the OR in the research of electromagnetic characteristics of composite materials and biological liquids, quality control of food stuffs since they are characterized by high losses. Therefore, the most promising resonant system to use for investigations of such substances is the OR proposed in [2, 3]. It represents symbiosis of the OR and the segment of the oversized waveguide, which could be both circular and rectangular. A distinctive feature of such resonant systems is that they are characterized by the single frequency response in the wide range of frequencies [3]. It is an advantage at investigations of electromagnetic characteristics of substances. At placement of the sample in the waveguide part of the OR, the measurement accuracy increases due to keeping high $Q$-factor, and therefore, the range of the analyzed values $\varepsilon'$ and tan$\delta$ extends.

The studied sample having the shape of a bead is located in the bottom of the circular waveguide segment, in which there is a plane wave front of the propagating $TE_{01}$ mode. It allows measuring samples, the thickness of which exceeds the wavelength of the excited oscillation. At the research of substances with the application of the OR having a cylindrical shape, difficulties related to their positioning in resonant volume may arise. At each measurement, the samples should be placed in the area with the same electric field intensity. The proposed resonator allows solving of this problem. The sample should be located along the OR axis, where the electric field intensity of the excited oscillation is minimal. It provides analyzing of substances with high losses. In the case of the OR having the segment of the oversized rectangular waveguide with the $TE_{10}$ mode, it is expedient to use the samples of a cylindrical shape. They should be located in the waveguide part parallel to the vector of the electric field intensity of the mode.

On the basis of the all above-stated, we can summarize that the goal of investigations, performed in this chapter, is theoretical and experimental research of the considered OR, which will allow to measure, in millimeter and in sub-millimeter ranges, the electromagnetic characteristics of composite materials and biological liquids, as well as to control the quality of food stuff.

## 2. Open resonator with a dielectric bead

### 2.1. Resonator model

In the OR, axial-symmetric modes are confined by caustics and hence they are with low diffraction losses. Placing of perfectly conducting boundary (**Figure 1**, dotted lines) in the area of exponentially vanishing intensity, almost does not affect the field pattern in OR. Our method is based on such physical principles.

Therefore, the task transforms to the study of the cavity resonator and approximate solution for the OR is achieved by selecting only modes with near axis distributed intensity (exponentially vanishing near conical boundary) from the cavity spectrum. We noticed that such approach for the electrodynamic model of the OR was proposed in [4].

Let us consider the cavity as a body of revolution with perfectly conducting boundary and dielectric bead located in the bottom of the cylindrical part (**Figure 1**). We assume that the resonator is filled with a homogeneous isotropic medium having specific dielectric and magnetic conductivities $\varepsilon_1$, $\mu_1$ in the area (1) and $\varepsilon_2$, $\mu_2$ in the area (2). We consider only axial-symmetric TE modes with $E_\varphi$, $H_r$ and $E_z$ are components of the electromagnetic field in the cylindrical coordinate system with the axis $z$, coinciding with the axis of symmetry.

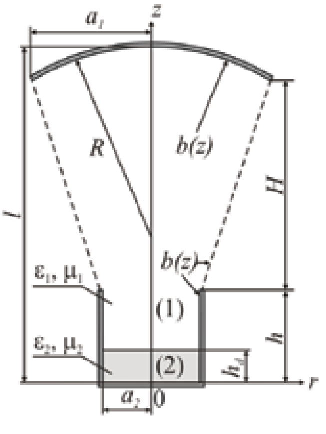

**Figure 1.** Geometric model of the OR with the dielectric bead.

Here, the initial problem for Maxwell equations reduces to the problem of finding the wave numbers $k = \omega/c$ (where $c$ is the speed of the light in vacuum and $\omega$ is a circular frequency), for which exist non-zero solutions $U_1$ and $U_2$ of the two-dimensional Helmholtz's equations.

$$\Delta_{rz}U_1 + \left(k^2\varepsilon_1\mu_1 - \left(1/r^2\right)\right)U_1 = 0,\ \ h_d < z < l,\ \ 0 < r < b(z), \tag{1}$$

$$\Delta_{rz}U_2 + \left(k^2\varepsilon_2\mu_2 - \left(1/r^2\right)\right)U_2 = 0,\ \ 0 < z < h_d,\ \ 0 < r < b(z), \tag{2}$$

which meet boundary conditions.

$$\begin{cases} U_1(r,l) = 0, \ \ U_2(r,0) = 0, \\ U_{1,2}(b(z),z) = 0, \qquad U_{1,2}(0,z) = 0, \end{cases} \tag{3}$$

and conditions of the fields matching at the medium interface $z = h_d$.

$$U_1(r,h_d) = U_2(r,h_d), \quad \frac{1}{\mu_1}\frac{\partial U_1(r,h_d)}{\partial z} = \frac{1}{\mu_2}\frac{\partial U_2(r,h_d)}{\partial z}. \tag{4}$$

Here, $U_{1,2}(r,z)$ is azimuthal component of electric field of a mode; function $b(z)$ is boundary surface, which is supposed to be piecewise-differentiable in the interval $0 < z < l$, where $l$ is the length of the cavity; $h_d$ is the thickness of the dielectric bead; $\Delta_{rz} = \partial^2/\partial r^2 + \partial/r\partial r + \partial^2/\partial z^2$ is the two-dimensional Laplace's operator; $(r, \varphi, z)$ are cylindrical coordinate system with axis $z$, coinciding with the axis of the cavity symmetry.

Equations (1)-(4) with application of Bubnov-Galerkin's method reduced to the system of the linear algebraic equations.

$$\mathbf{AC} + k^2\mathbf{BC} = 0, \tag{5}$$

where $\mathbf{C} = (c_n)_{n=1}^{N}$ is the vector-column of unknown factors, $\mathbf{A} = \|a_{mn}\|_{m,n=1}^{N}$ and $\mathbf{B} = \|b_{mn}\|_{m,n=1}^{N}$ are matrixes with matrix elements, which are prescribed by the formulas presented in [5, 6].

An approximate solution of the initial task [Equations (1)-(4)] could be represented as follows:

$$E(r,z) = \begin{cases} \sum\limits_{i=1}^{I} J_1\left(\frac{\mu_i r}{b}\right)\sum\limits_{p=1}^{P} c_p^i \frac{\mu_1\varepsilon_2}{\mu_2\varepsilon_1}\frac{\cos\lambda_p\sqrt{\varepsilon_1\mu_1}h_d}{\cos\lambda_p\sqrt{\varepsilon_1\mu_1}(l-h_d)}\sin\lambda_p\sqrt{\varepsilon_1\mu_1}(l-z),\ \ h_d < z < l, \\ \sum\limits_{i=1}^{I} J_1\left(\frac{\mu_i r}{b}\right)\sum\limits_{p=1}^{P} c_p^i \sin\lambda_p\sqrt{\varepsilon_1\mu_1}z,\ \ 0 < z < h_d, \end{cases} \tag{6}$$

$$\omega = kc,$$

where $k$ and $\mathbf{C}^N$ are solutions of the [Eq. (5)]; $\omega = \omega' + i\omega''$ is complex frequency of the natural oscillation and $N = P \cdot I$ is the dimension of the algebraic task.

For measurement of the loss-angle tangent when a sample is placed in a cavity, both the resonator frequency shift and energy characteristic of the resonator are necessary to calculate [7]. For such calculations, it is required to find the following: the resonator $Q$-factor $Q_\varepsilon$ caused by losses in the sample; energy factor $K_E$ of the resonator filling by electric field [7] and an ohmic $Q$-factor $Q_{R\varepsilon}$ of the resonator with the sample [8]. At the same time,

$$Q_\varepsilon = -2\omega'/\omega'', \tag{7}$$

$$K_E(\varepsilon) = -2\frac{\varepsilon_2'}{\omega'}\frac{\partial\omega'}{\partial\varepsilon_2'}, \tag{8}$$

$$Q_{R\varepsilon} = (2/\Delta_R)\left(\int_V |\mathbf{H}|^2 dV \Big/ \int_S |\mathbf{H}_\tau|^2 dS\right), \tag{9}$$

where $\Delta_R$ is depth of the electromagnetic field penetration into metal; $V, S$ are volume and area of the resonator surface; $\mathbf{H}$ is the distribution of the magnetic components of the electromagnetic field in the volume of the resonator; $\mathbf{H}_\tau$ is the tangent component of the magnetic. Distributions of magnetic components $\mathbf{H}$ and $\mathbf{H}_\tau$ of the electromagnetic field are calculated with the application of the developed theoretical model.

### 2.2. Numerical results

Dimensions of the considered cavity at numerical simulations have been chosen equal to sizes of the hemispherical OR used in the experiment. The curvature radius of the spherical mirror is $R = 39$ mm, aperture of this mirror is $2a_1 = 38$ mm, the diameter of the circular waveguide segment and dielectric samples is $2a_2 = 18$ mm, the length of the resonator cylindrical part is $h = 12.434$ mm, the resonator length is $l = 35.295$ mm (**Figure 1**).

The developed algorithm was validated using rigorous formulas for the spectrum of empty spherical volume resonator [9]. Evaluation of the algorithm convergence, related to the increase of the algebraic equation dimension, was carried out as well (Eq. (5)). As a result of such evaluation matrixes' dimensions, **A** and **B** from (Eq. (5)) have been chosen to be equal to $N = P \cdot I$ at $P = 60,\ \ I = 6$ (Eq. (6)). Further increase of $P$ and $I$ does not provide considerable changes at calculation results of the eigenvalues and the eigenvectors of the task (Eq. (5)). The examples of distribution for an electric field component of the $\mathrm{TE}_{0116}$ mode in the cavity with the bead made of Plexiglas having thickness $h_d = 2.75$ mm and permittivity $\varepsilon_2' = 2.61$ are presented in **Figure 2a** [10]. At the same time, frequency of resonant oscillation decreases down to the value $f = 68.052$ GHz as compared to $f = 71.382$ GHz for an empty resonator with the same dimensions. For the bead made of Plexiglas having the same diameter, but thickness $h_d = 3.6$ mm, resonance frequency decreases down to the value $f = 66.999$ GHz (**Figure 2b**). As can be seen in **Figure 2a** and **b**, depending on the dielectric bead thickness, its top boundary can coincide both with the node and the antinode of the electric field component of the standing wave in the cavity. Therefore, it should be expected that in such a resonant system, dependence of the oscillation frequency $TE_{0116}$ on the thickness of the dielectric bead will have a quasi-periodic behavior [11].

Dependencies of the frequency shift in the cavity on the thickness of the sample located at the bottom of cylindrical part are presented in **Figure 2c**. Curve 1 in **Figure 2c** corresponds to the bead made of Teflon ($\varepsilon_2' = 2.07$ [10]), and curve 2 is for the bead made of Plexiglas. Marks (a) and (b) at the curve 2 show the beads' thicknesses, corresponding to the field distributions presented in **Figure 2a** and **b**. Apparently, the weak dependence of the frequency and the bead thickness takes place in the case, when the node of the electric field component of the standing wave in the cavity is located near to the top of the sample (**Figure 2a**, point (a) in **Figure 2c**). In the case of electric components antinode location near to the top of the sample (**Figure 2b**,

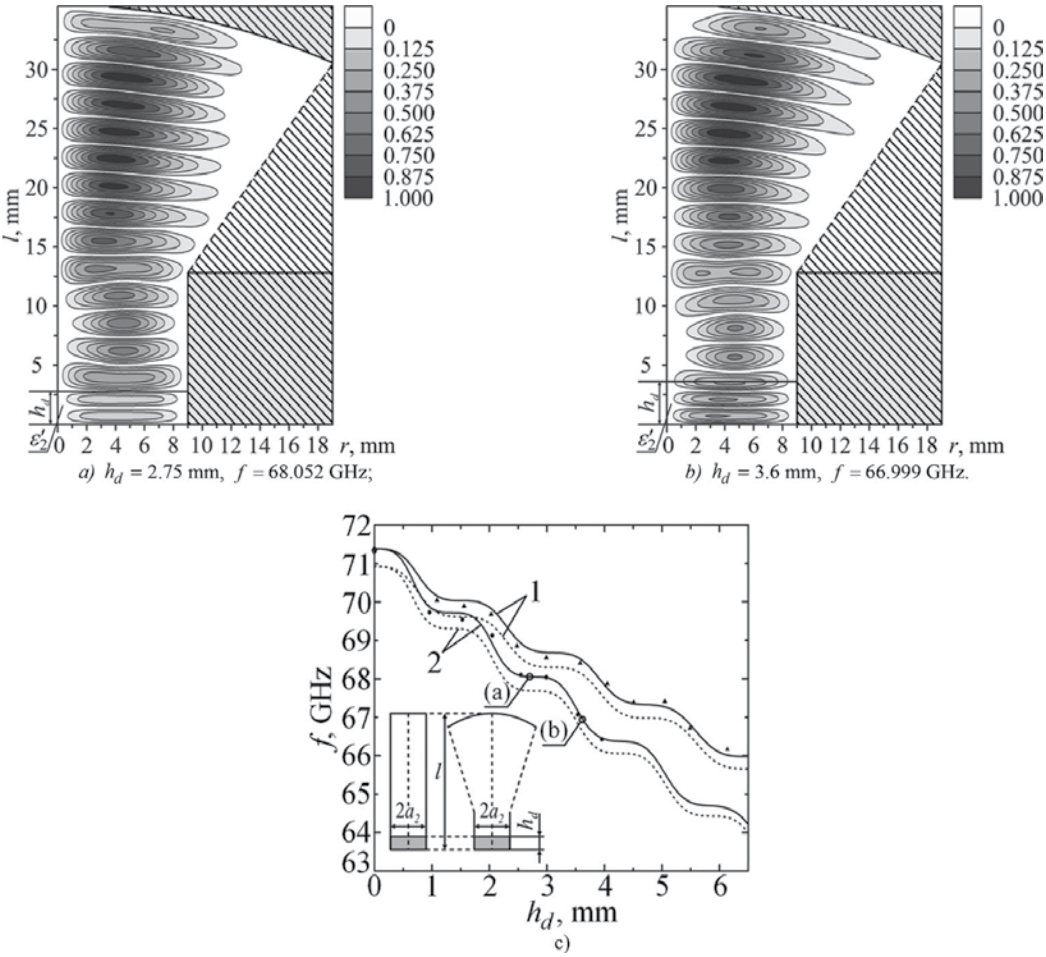

a) $h_d = 2.75$ mm, $f = 68.052$ GHz;

b) $h_d = 3.6$ mm, $f = 66.999$ GHz.

**Figure 2.** The examples of distribution of the electric field component of the $TE_{0116}$ mode in the cavity with beads from Plexiglas (a, b) and dependencies of the resonance frequency on the thickness of beads made of different material for two types of cavities (c).

point (b) in **Figure 2c**), the dispersive dependence of the resonator frequency on the sample thickness has a large steepness.

Dependencies of the resonance frequency on the thickness of the dielectric beads made of Teflon (curve 1) and Plexiglas (curve 2) for cylindrical cavity are shown in **Figure 2c** by dotted curves. The diameter of this cavity is equal to the diameter of the cylindrical part of the studied cavity, and lengths of both the cavities coincide (**Figure 2c**). At the same time, a rigorous solution for a cylindrical cavity was obtained by application of the method based on the separation of variables. As it follows from **Figure 2c**, curves corresponding to both resonant systems qualitatively agree and have a quasi-periodic character. At the same time, a difference of eigen-frequencies of these cavities with beads having the same thickness and permittivity does not exceed 500 MHz.

Experimentally measured values of resonance frequency are shown in **Figure 2c** at the placement of beads made of Teflon (triangular marks) and Plexiglas (round marks) on the bottom of cylindrical part of the hemispherical OR [12]. The difference of experimentally obtained values of resonance frequency from calculated by using developed electrodynamic model of the OR does not exceed 50 MHz, and an error of the frequency measurement by using a resonant wavemeter in the considered frequency bandwidth is about 37 MHz [13]. With regard to the above, we can state validity of the proposed electrodynamic model of the cavity (**Figure 1**) to measure the electromagnetic parameters of substances using the OR [3].

As shown earlier (**Figure 2c**), dependencies of the resonance frequency on the bead thickness at the constant value of its permittivity have a quasi-periodic character. Dependencies of the resonance frequency on permittivity of the bead having constant thickness should look similar. It can be explained by the fact that with a change of $\varepsilon_2'$ the nodes and antinodes of electric component of the standing wave appear periodically on the top of the bead, and condition of equality of the bead thickness to integer number of half wavelength does not hold for any $\varepsilon_2'$.

Dependencies of $TE_{0116}$ mode resonant frequency $f$ of the considered cavity (**Figure 1**) on the permittivity of the beads having various thicknesses $h_d$ are presented in **Figure 3a**. Curve 1 is for the bead, with thickness of 2.99 mm, and curve 2 is for the bead having thickness 3.58 mm.

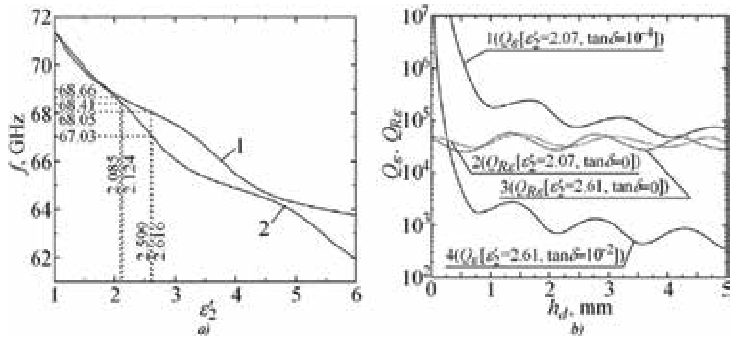

**Figure 3.** Dependencies of the resonant frequency on the permittivity of the beads having a various thickness (a) and of the Q-factor of the cavity on the thickness of the sample (b).

Dependencies in **Figure 3a** corresponding to the sample thickness provide defining a real part of the samples permittivity $\varepsilon_2'$ by resonant frequency shift.

As an important characteristic, needed for valuation of the loss-angle tangent for dielectric samples, is $Q$-factor $Q_\varepsilon$, caused by losses in a dielectric (Eq. (7)), and an ohmic $Q$-factor $Q_{R\varepsilon}$ of the resonator with (Eq. (9)). Dependencies of $Q_\varepsilon$ (solid curves) and $Q_{R\varepsilon}$ (dotted curves) on the beads' thickness $h_d$ calculated using the developed theoretical model are presented in **Figure 3b**. The $Q$-factor $Q_\varepsilon$ of the cavity with the sample of the shape of a bead, permittivity of which $\varepsilon_2' = 2.07$ and loss-angle tangent $\tan\delta = 10^{-4}$, is designated by the curve 1. The curves 2 and 3 correspond to the ohmic $Q$-factor of the resonator $Q_{R\varepsilon}$ with the samples having $\varepsilon_2' = 2.07$ and $\varepsilon_2' = 2.61$ in the absence of losses ($\tan\delta = 0$). The $Q$-factor $Q_\varepsilon$, caused by losses in the dielectric is designated by the curve 4, for the sample having parameters: $\varepsilon_2' = 2.61$ and $\tan\delta = 10^{-2}$.

From the presented diagram one can see that behavior of the $Q$-factors $Q_\varepsilon$ and $Q_{R\varepsilon}$ is quasi-periodic with the increase of the thickness $h_d$ of the samples. Such behavior, as shown earlier, is related to distribution of the electric component of the standing wave in the resonator in the plane of the top of the samples located on the bottom of the cylindrical part. The ohmic $Q$-factor $Q_{R0}$ of the "empty" resonator ($h_d = 0$) is equal to 48,005. As one can see in **Figure 3b**, the $Q$-factor $Q_{R\varepsilon}$ can essentially differ from the $Q$-factor $Q_{R0}$. For example, for the sample with $\varepsilon_2' = 2.07$ and $\tan\delta = 10^{-4}$ at $h_d = 2.48$ mm, $Q_{R\varepsilon} = 33{,}493$, that is, the ratio $Q_{R0}/Q_{R\varepsilon} = 1.43$. Therefore, in order to understand how it can affect the calculation of $\tan\delta$, we write down an expression, determining its natural $Q$-factor $Q_{0\varepsilon}$ of the cavity with the sample, which expresses as $1/Q_{0\varepsilon} = (1/Q_\varepsilon) + (1/Q_{R\varepsilon})$. For samples with low losses, the $Q$-factor $Q_{0\varepsilon}$ is entirely determined by the resonator ohmic $Q$-factor $Q_{R\varepsilon}$, since at the same time, $Q_\varepsilon >> Q_{R\varepsilon}$ (**Figure 3b**, curves 1 and 2). Hence, in the calculation of the resonator $Q$-factor, it is inadmissible to replace the ohmic $Q$-factor of the resonator with the sample by the ohmic $Q$-factor of the "empty" resonator, as it can result in significant errors in the valuation of $\tan\delta$ for the samples having low losses ($< 10^{-4}$). Obtained conclusion is well in agreement with the results in [7].

In the investigation of the samples with high losses, a $Q$-factor of the resonator $Q_{0\varepsilon}$ will already be determined by the $Q$-factor $Q_\varepsilon$, since here $Q_\varepsilon << Q_{R\varepsilon}$ (**Figure 3b**, curves 3 and 4). If the sample thickness $h_d < 0.25$ mm, then, its placement on the bottom of the resonator cylindrical part can also lead to an incorrect result in measurement of dielectric samples losses, since in this case $Q_\varepsilon >> Q_{R\varepsilon}$. Just noted means that the natural $Q$-factor of the resonator should be defined by the $Q$-factor $Q_{R\varepsilon}$, instead of $Q_\varepsilon$ (**Figure 3b**, curves 3 and 4). Hence, at the measurement of losses in thin samples ($h_d << \lambda$), they should be located not on the bottom of the cylindrical part, but at the antinode of the standing wave electric field in the resonator [7].

Here, it should be noted that in the $Q$-factor calculations, the conductivity of the cylindrical part surface of the considered cavity was as for aluminum, and of the spherical mirror was as for brass (**Figure 1**). Choice of the metals depends upon the necessity to carry out an evaluation of the losses in the samples of the known dielectrics using the hemispherical OR with the segment of the oversized circular waveguide, the mirrors of which are made of the specified metals. Conical cavity surface is considered as a perfectly conducting one.

http://dx.doi.org/10.5772/intechopen.73643

Thus, analysis of the energy and spectral characteristics of the cavity with dielectric inclusions, formed by the cylindrical, conical and spherical surfaces was carried out in this subsection. As a result of the performed study, it was found out that physical processes in the considered cavity and in the hemispherical OR with the segment of the oversized circular waveguide having dielectric beads are identical. It allows to conclude that the proposed model is valid for the resonator to measure electromagnetic parameters of substances in the millimeter range of the wavelengths.

### 2.3. Measurement of the permittivity and losses in the samples

The hemispherical OR, formed by the spherical 13 and flat 14 mirrors having diameter 38 mm (**Figure 4**) [6, 14], is used for measurements. Short-segment of the oversized circular waveguide 15 of diameter 18 mm is located in the center of the flat mirror. The studied sample 17 having the shape of a bead is placed at the waveguide plunge 16. Distance from the flat mirror to the plunge is equal to $3\lambda_w$ ($\lambda_w$-waveguide wavelength). On the surface of the spherical mirror of curvature radius $R = 39$ mm, two coupling slots are located, through one of which the signal with 1 kHz amplitude modulation from the high-frequency generator G4–142 inputs into the resonant volume, and through the second one, signal outputs to the load. The slots are tapering from the main section of the rectangular waveguide 3.6 × 1.8 mm into the narrow one 3.6 × 0.14 mm. Both coupling elements are oriented in such a manner that the vector of $TE_{10}$ mode electric field in the rectangular waveguides is orthogonal to the plane of **Figure 4**.

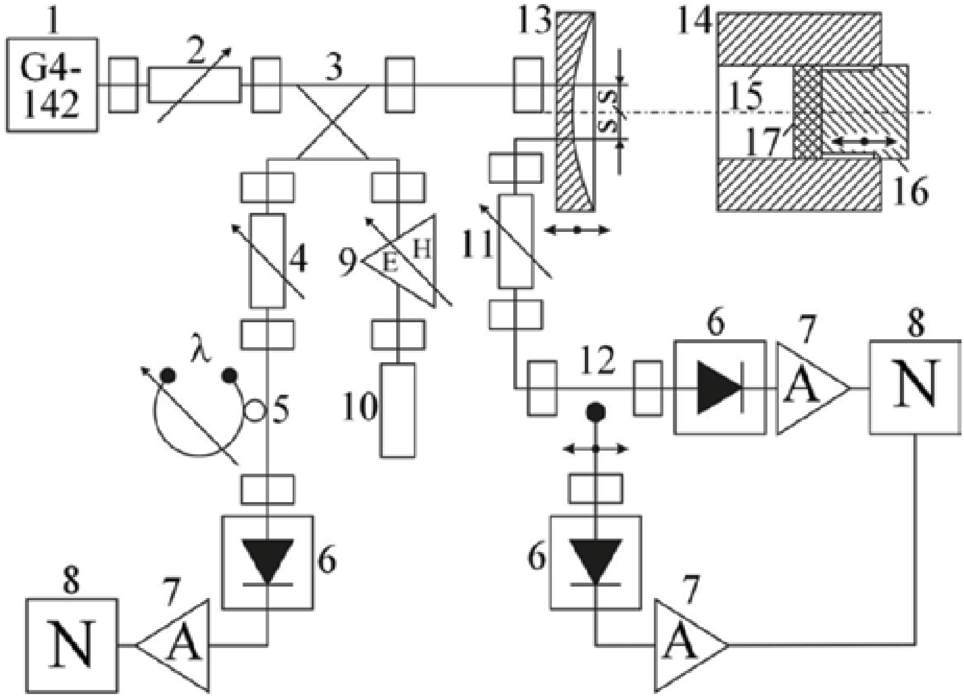

**Figure 4.** Block diagram of the experimental setup.

The distance $s$ from the resonator axis, on which coupling elements are located, is defined by the peak value of the electric field of $\text{TEM}_{01q}$ mode in the plane of the spherical mirror and is equal to 5.5 mm (**Figure 4**). In this case $\text{TE}_{01\text{q}}$ mode is excited with maximal efficiency. For the isolation of the generator G4–142 and the resonator, additional setting attenuator 2 is included in the circuit. The tuning to the resonance is implemented by moving the spherical mirror 13 along the resonator axis. The distance between the reflectors is evaluated by using a measuring projective device having accuracy of ±0.001 mm. The signal extraction from the OR is performed by using the second slot coupling element, which, as stated earlier, is on the spherical mirror and has the same dimensions as the first one, and is located at the distance 11 mm from it.

In the circuit, an additional receiving transmission line is included for the measurement of the reflection coefficient from the resonator. This transmission line comprises a directional coupler 3, a measuring polarizing attenuator 4, a crystal detector 6, a resonant amplifier 7, tuned to the frequency of modulating voltage and an oscillograph 8. Reflectivity is measured in the plane, in which input impedance of the resonator with a certain part of the waveguide is purely active [15].

The reflectivity factor on voltage is defined by the formula $|\Gamma| = 10^{-A/20}$ [16]. Here, $A$ is the difference in dB between data from the measuring polarizing attenuator 4 at the arrangement of the shorting plug in the coupling element plane and at the point of resonance. A resonant wavemeter 5 is included in the transmission line for more accurate measurement of the generator G4–142 frequency. A double-stub matcher 9 is placed into the branch of the directed coupler 3, containing a matched load 10, enabling compensation of the possible reflected from the waveguide junction signals, which can affect the accuracy of the resonance tuning. The signal, which passed through the OR, inputs into the receiving transmission line, consisting of a measuring polarizing attenuator 11, a measuring line 12, a detector 6, a resonant amplifier 7 and an oscillograph 8. The signal, proportional to the amplitude of the standing wave voltage in the waveguide, is registered by the measuring line 12 and enters into the receiving transmission line, consisting of a crystal detector 6, a resonant amplifier 7 and oscillograph 8. $VSWR$ of the studied OR is calculated using the formula $VSWR = 10^{B/20}$. Here, $B$ is the difference in dB between the maximum and minimum attenuation values of the polarizing attenuator 11 during the probe movement along the waveguide. The photo of the experimental unit and the OR is given in **Figure 5**.

The validation of the proposed method of permittivity measurement using the considered OR (**Figure 4**) was performed with the samples having the shape of dielectric beads made of Teflon and Plexiglas. The diameter of the beads was equal to $2a_2 = 18$ mm, and it was equal to the diameter of the resonator cylindrical part. Values $\varepsilon_2'$ of the samples have been measured using the described experimental setup and curves presented in **Figure 3a**.

We measured $\varepsilon_2'$ for two beads having the diameter equal to 18 mm and the thickness 2.99 and 3.58 mm both made of Teflon, and two beads with the same dimensions but made of Plexiglas. Originally, the plunge is installed flush with the flat mirror, and in the hemispherical OR, the axial-asymmetric mode $\text{TEM}_{0110}$ is excited. At the same time, the distance between the mirrors is equal to 22.139 mm ($f = 71.372$ GHz). The modes have been identified by application of the

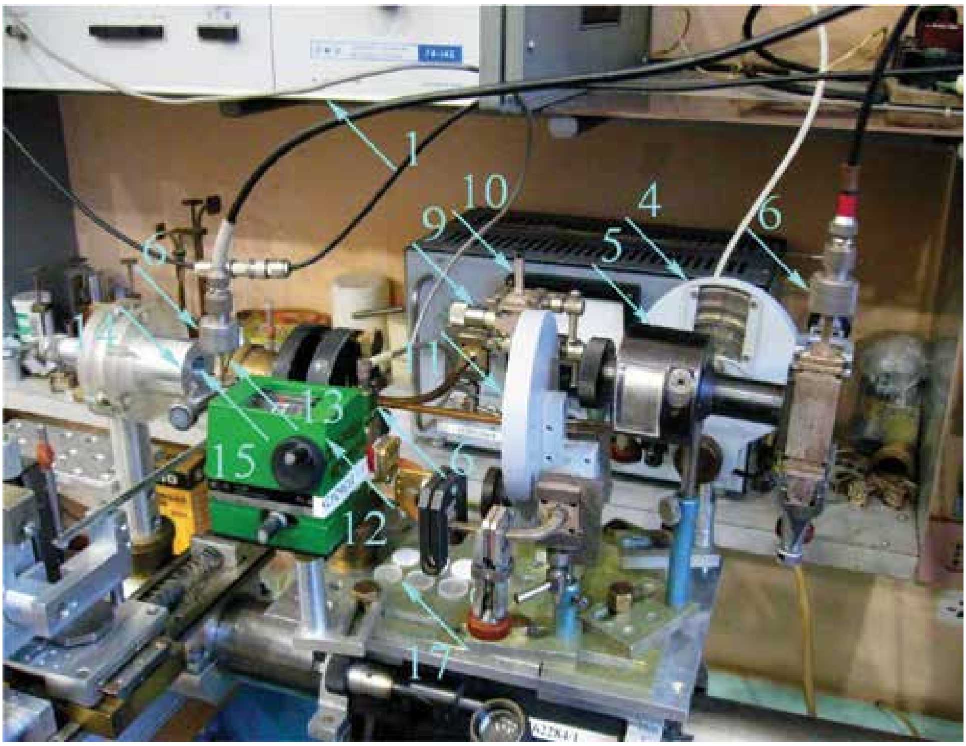

**Figure 5.** The photo of the OR with the segment of circular waveguide and the experimental unit.

perturbation technique [13]. In the next step, the plunge 16 is moved inside the oversized circular waveguide 15 on the distance $h = 3\lambda_w = 13.172$ mm (calculated value of $h = 3\lambda_w = 13.155$ mm). Availability of the oversized circular waveguide segment results in the fact that the $\mathrm{TEM}_{0110}$ mode of the hemispherical OR is being transformed into the axial-symmetric mode $\mathrm{TE}_{0116}$ [3]. In that case, the resonant distance is being measured already between the spherical OR mirror and the plunge.

Now the bead 17 having the thickness 2.99 mm and the diameter 18 mm, made of Teflon is placed on the plunge 16. Frequency of the generator G4–142 is tuned to achieve the resonant response. In the resonator at the frequency $f = 68.667$ GHz, which is measured by the wavemeter 5, again $\mathrm{TE}_{0116}$ mode is excited, that is identified by using the perturbation technique. Getting the value of the resonance frequency, we can evaluate permittivity of the studied sample with thickness 2.99 mm. For that purpose, we use the curve 1 (**Figure 3a**). In a similar way, we evaluate permittivity of the sample made of Teflon and having thickness 3.58 mm. In this situation, placing the sample on the plunge located in the cylindrical part of the OR, we got the value of the resonance frequency 68.410 GHz for the $\mathrm{TE}_{0116}$ mode. In order to value $\varepsilon_2'$ in that case, we use the curve 2 (**Figure 3a**). Measurement of two samples with the same dimensions and made of Plexiglas are carried out similarly. The mode $\mathrm{TE}_{0116}$ is excited but now only at the frequencies 68.051 GHz and ($h_d = 2.99$ mm) and $f = 67.030$ GHz ($h_d = 3.58$ mm). Using the curves 1 and 2 (**Figure 3a**), we evaluate permittivity of the samples having

| Material | Thickness of the sample $h_d$ (mm) | The measured value $\varepsilon_2'$ | Literary value $\varepsilon_2'$ | The difference | $\Delta f$, GHz |
|---|---|---|---|---|---|
| Teflon | 2.99 | 2.085 ± 0.020 | 2.07 ± 0.04 [10] | 0.7% | 2.705 |
| Teflon | 3.58 | 2.124 ± 0.020 | 2.07 ± 0.04 [10] | 2.5% | 2.962 |
| Plexiglas | 2.99 | 2.599 ± 0.026 | 2.557 ± 0.026 [10] | 1.6% | 3.321 |
| Plexiglas | 3.58 | 2.616 ± 0.026 | 2.557 ± 0.026 [10] | 2.2% | 4.342 |

**Table 1.** Measured values of $\varepsilon_2'$ for beads made of Teflon and Plexiglas.

various thickness and made of Plexiglas. Frequency measurement error in the millimeter range using a resonant wavemeter is ±0.05% [13]. Taking into account the frequency valuation by using the calibration curves of the resonant wavemeter, the total error of the samples permittivity measurement by application of the considered resonant cell is about ≈1%. The measurements results of the permittivity real part for considered samples are shown in **Table 1**.

In **Table 1**, $\Delta f$ designates the frequency shift of $TE_{0116}$ mode when putting the sample into "empty" OR.

In the next step, the dielectric losses in the samples made of Teflon and Plexiglas and having thickness 2.99 mm are evaluated. For their finding, one should calculate the energy filling factor of the resonator with the sample on the electric field $K_E$ [7]. For its calculation, we use (Eq. (8)). The advantage of that expression is in the possibility to find the energy factor $K_E$ not by the calculations of stored energies $W_{1E}$ and $W_{2E}$ in the volumes $V^{(2)}$ and $V^{(1)}$ (**Figure 1**), but by differentiation of the resonant circular frequency $\omega'(\varepsilon_2')$ dependence, presented in **Figure 3a**.

The behavior $K_E = \psi(\varepsilon_2')$ for the samples having the shape of beads and diameter 18 mm made of Teflon ($\varepsilon_2' = 2.07$) located on the bottom of the cylindrical part of the electrodynamic model of the OR and having various thickness $h_d$ is shown in **Figure 6** as an example.

In calculations, we assume that there is nondegenerate mode $TE_{0116}$ exists in the considered resonator. In **Figure 6**, also by dotted shows the factor $K_E$ for a cylindrical resonator, in which

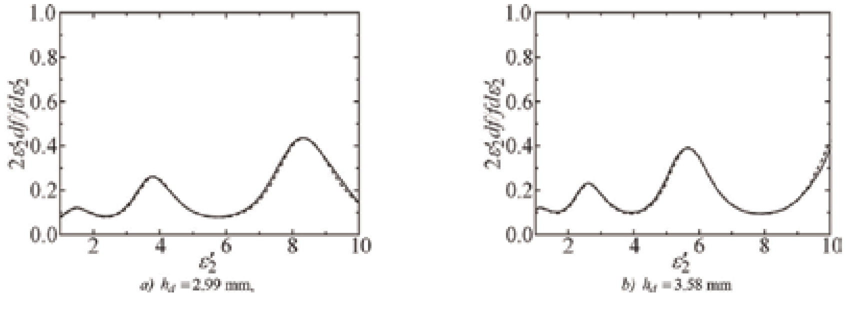

a) $h_d$ = 2.99 mm,

b) $h_d$ = 3.58 mm

**Figure 6.** Dependencies of the energy filling factor of the resonator $K_E$ on permittivity of the samples having various thicknesses.

the same axial-symmetric mode $TE_{0116}$ is excited. The diameter of the resonator is equal to the diameter of the cylindrical part of the considered OR model, and lengths of the both resonators coincide (**Figure 2c**). The studied samples of various thicknesses are placed on the end cover of the cylindrical cavity. From the presented dependencies one can see that for the samples of various thickness in whole range of the $\varepsilon_2'$ change, the behavior of the resonators energy filling factor on the electric field, both in cavity formed by cylindrical, conical and spherical surfaces, and in cylindrical, one almost coincide. In turn, it confirms the conclusion, noted earlier, that the patterns of the electromagnetic field both in the OR with the segment of the oversized circular waveguide and in the cylindrical cavity of same length $l$ and diameter $2a_2$ (**Figure 1**) are identical.

Now let us evaluate losses in the bead having diameter 18 mm and $h_d = 2.99$ mm thickness made of Teflon ($\varepsilon_2' = 2.07$). The sample is placed on the plunge located in the waveguide part of the OR, the length of which $h$ = 13.172 mm. Measurements are carried out using the experimental setup, a block diagram of which is presented in **Figure 4**, and its photo is shown in **Figure 5**. Eigen $Q$-factor of the resonant system with the measured sample $Q_{0\varepsilon}$ is defined by the relation [7, 17]

$$\frac{1}{Q_{0\varepsilon}} = \frac{1}{Q_{R\varepsilon}} + \frac{1}{Q_{rad\varepsilon}} + K_E \tan\delta, \tag{10}$$

where $Q_{R\varepsilon}$ is an ohmic $Q$-factor of the resonator with the sample; $Q_{rad\varepsilon}$ is a diffraction $Q$-factor of the OR with the sample caused by the coupling of the mode with free space.

In the absence of the measured sample in the resonant volume, unloaded $Q_{00}$ of the OR with the same mode can be presented as follows:

$$\frac{1}{Q_{00}} = \frac{1}{Q_{R0}} + \frac{1}{Q_{rad0}}, \tag{11}$$

where $Q_{R0}$ is an ohmic $Q$-factor of the resonator without the sample; $Q_{rad0}$ is a diffraction $Q$-factor of the OR without the sample.

If we deduct (Eq. (11)) from (Eq. (10)), then, we will get the relation determining the dielectric losses tangent in the sample.

$$\tan\delta = \frac{1}{K_E}\left[\left(\frac{1}{Q_{0\varepsilon}} - \frac{1}{Q_{00}}\right) - \left(\frac{1}{Q_{R\varepsilon}} - \frac{1}{Q_{R0}}\right) - \left(\frac{1}{Q_{rad\varepsilon}} - \frac{1}{Q_{rad0}}\right)\right]. \tag{12}$$

Diffraction $Q$-factors, which are rather difficult to measure, enter into (Eq. (12)). The resonant system under consideration (**Figures 4** and **5**) allows to do the assumptions, which provide definition of $\mathrm{tg}\,\delta$ without measuring $Q_{rad\varepsilon}$ and $Q_{rad0}$. Since the sample is placed into the resonator cylindrical part, then it should not disturb strongly the electromagnetic field in the open part of the OR (**Figure 5a** and **b**). Therefore, we can assume that the diffraction $Q$-factor of the resonator with the sample is equal to the diffraction $Q$-factor of the "empty" resonator, that is, $Q_{rad\varepsilon} \approx Q_{rad0}$. Taking this into account, we write down in the final form an expression determining the tangent of dielectric losses in the sample as follows:

$$\tan\delta = \frac{1}{K_E}\left[\left(\frac{1}{Q_{0\varepsilon}} - \frac{1}{Q_{00}}\right) - \left(\frac{1}{Q_{R\varepsilon}} - \frac{1}{Q_{R0}}\right)\right]. \tag{13}$$

For the samples under studies having the shape of the bead ($2a_2 = 18$ mm, $h_d = 2.99$ mm) made of Teflon and Plexiglas, $Q$-factors $Q_{0\varepsilon}$ and $Q_{00}$ are evaluated from the experiment, energy filling factor of the OR on the electric field $K_E$ is calculated (**Figure 6a**), $Q_{R\varepsilon}$ and $Q_{R0}$ are also calculated theoretically (**Figure 3b**, curve 2, 3).

In order to find tan$\delta$ of the samples, loaded $Q$-factors $Q_{L\varepsilon}$ and $Q_{L0}$ of the resonator with the sample and without were measured in the case of $TE_{0116}$ mode excitation. At the same time, loaded and unloaded $Q$-factors of the OR are related as follows [9]:

$$\begin{cases} Q_{L\varepsilon} = \eta Q_{0\varepsilon}/(1 + \beta_{1\varepsilon} + \beta_{2\varepsilon}), \\ Q_{L0} = \eta Q_{00}/(1 + \beta_1 + \beta_2), \end{cases} \tag{14}$$

where $\beta_{1\varepsilon}$ and $\beta_1$ are coupling coefficients of the resonator with the receiving waveguide line with the sample on the bottom of the cylindrical part and without it; $\beta_{2\varepsilon}$ and $\beta_2$ are coupling coefficients of the resonator with a load with the measured sample and without it, $\eta$ is efficiency of excitation of the $TE_{0116}$ mode in the considered resonator.

Based on the research carried out with a metal screen covering the OR [18], it was determined that excitation efficiency of the considered $TE_{0116}$ mode can be accepted to be equal to 0.96. Since two slot coupling elements having identical dimensions (3.6 × 0.14 mm) and located symmetrically to the resonator axis are used for excitation of the resonator and the signal output into the load, the input and output coupling should be the same, that is, $\beta_{1\varepsilon} = \beta_{2\varepsilon} = \beta_\varepsilon$ and $\beta_1 = \beta_2 = \beta$. In the paper [19], it was shown that the transmission type resonator having equal input and output coupling cannot be recoupled. It indicates that $\beta_\varepsilon$ and $\beta$ in this case are less than 1 and therefore are equal to $1/VSWR$ and the reflection coefficient $\Gamma > 0$. Measurements of $\Gamma$ performed using the directional coupler ($VSWR = (1 + \Gamma)/(1 - \Gamma)$) and of $VSWR$ using the measuring line (**Figures 4** and **5**) confirmed the conclusion made of an equality of the input and output coupling. In such a way, from (Eq. (14)) we can find out the natural $Q$-factors of the resonant cell with the sample $Q_{0\varepsilon}$ and without it $Q_{00}$ in (Eq. (13)).

$$\begin{cases} Q_{0\varepsilon} = Q_{L\varepsilon}(1 + 2\beta_\varepsilon)/0.96, \\ Q_{00} = Q_{L0}(1 + 2\beta)/0.96. \end{cases} \tag{15}$$

For calculation of the loss-angle tangent in the samples made of Teflon and Plexiglas, we calculate the ohmic $Q$-factor of the "empty" resonator using (Eq. (13)). As seen from **Figure 3b** (curves 2, 3, $h_d = 0$), $Q_{R0} = 48{,}005$. Experimentally measured loaded $Q$-factor $Q_{L0}$ of the "empty" resonator, in which the mode $TE_{0116}$ exists, turned out to be equal to 1660. At the same time, the coupling coefficient $\beta = 0.310$ ($\Gamma = 0.527$). Now from (Eq. (15)), we can calculate that the natural $Q$-factor of the "empty" resonator equals to $Q_{00} = 2801$.

| Material | $K_E$ | $Q_{R\varepsilon}$ | $Q_{L\varepsilon}$ | $\beta_\varepsilon$ | $Q_{0\varepsilon}$ | tg $\delta$ |
|---|---|---|---|---|---|---|
| Teflon | 0.0886 | 49,339 | 1588 | 0.287 | 2604 | $(3.117 \pm 0.034) \times 10^{-4}$ |
| Plexiglas | 0.0878 | 48,005 | 502 | 0.181 | 712 | $(1.192 \pm 0.035) \times 10^{-2}$ |

**Table 2.** Measurement results of tan$\delta$ for the studied samples.

Taking into account the obtained values $Q_{R0}$ and $Q_{00}$, the results of tan$\delta$ measurements for the samples having the shape of the beads made of Teflon and Plexiglas of thickness equal to 2.99 mm are shown in **Table 2**. Measuring error of the losses in dielectric sample amounts (1÷3)% and is defined, mainly, by the errors of the frequency measurement using a wavemeter and loaded $Q$-factors $Q_{L\varepsilon}$ and $Q_{L0}$ of the resonator with the sample and without it.

As may be seen in **Table 2**, measured values of tan$\delta$ for the samples made of Teflon and Plexiglas coincide with the results obtained by other authors. For material with low losses (Teflon), we got tan$\delta$ = $(2.8 \pm 0.2) \times 10^{-4}$ [20], which differs by 11% from the result obtained using the proposed resonator cell. In the case of the material with high losses (Plexiglas), obtained value of tan$\delta$ differs by 1.7% from the results of other authors (tan$\delta$ = $(1.1 \pm 0.06) \times 10^{-2}$) [20].

The authors did not aim to get high accuracy $\varepsilon_2'$ and tan$\delta$ measurements. We showed only the basic possibility to measure electromagnetic parameters of materials with high losses in millimeter and sub-millimeter ranges by means of the resonant system consisting of the hemispherical OR with the segment of the oversized circular waveguide. In order to increase the accuracy of $\varepsilon_2'$ and tan$\delta$ measurements for dielectric materials with low losses, it is necessary to increase the $Q$-factor of the resonant system. To achieve it, the resonator with the mirrors of large aperture and the spherical reflector of the larger curvature radius should be used.

## 3. Open resonator with a dielectric rod

### 3.1. Resonator model

The method of the solution is based on the same physical principles as in the case of the resonator with the dielectric bead. Thus, we consider a resonance cavity with the boundary made of a spherical, a conical and a cylindrical perfectly conducting surface. There is a cylindrical rod extended all along the resonator axis (area 2 in **Figure 7**), which is assumed to be a homogeneous and isotropic medium, having the material parameters $\varepsilon_2$, $\mu_2$. The rest part of the resonator is assumed to be empty $\varepsilon_1 = \mu_1 = 1$ (area 1).

We confine ourselves to the analysis of axially-symmetric oscillations of TE-mode, which in cylindrical coordinates, where axis $z$ coincides with the resonator symmetry axis, have $E_\varphi$-, $H_r$- and $H_z$- components of the electromagnetic field. For this oscillation mode, the initial problem for the Maxwell equations can be reduced to finding wave numbers $k$, for which there exist the nontrivial solutions $U_1$ and $U_2$ of the two-dimensional Helmholtz equations.

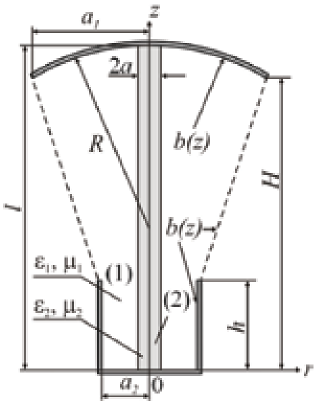

**Figure 7.** Geometric model of OR with the dielectric rod.

$$\Delta_{rz}U_1 + \left(k^2\varepsilon_1\mu_1 - \left(1/r^2\right)\right)U_1 = 0, \ \ 0 < z < l, \ \ a < r < b(z), \tag{16}$$

$$\Delta_{rz}U_2 + \left(k^2\varepsilon_2\mu_2 - \left(1/r^2\right)\right)U_2 = 0, \ \ 0 < z < l, \ \ 0 < r < a, \tag{17}$$

that satisfy the boundary conditions:

$$U_{1,2}(r,0) = 0, \ \ U_{1,2}(r,l) = 0, \ \ U_1(b(z),z) = 0, \ \ U_2(0,z) = 0, \tag{18}$$

and the field matching conditions at $r = a$:

$$U_1(a,z) = U_2(a,z), \ \ \frac{1}{\mu_1}\frac{\partial U_1(a,z)}{\partial z} = \frac{1}{\mu_2}\frac{\partial U_2(a,z)}{\partial z}. \tag{19}$$

Here, $a$ is the rod radius.

The numerical algorithm for the problem (Eq. (16))÷(Eq. (19)) utilizes the method of Bubnov-Galerkin, as described earlier, and the problem is reduced to the system of linear algebraic equalizations (Eq. (5)) [6, 21].

The developed algorithm, as in the case with the dielectric bead, was tested by the passing to the limit from the geometry of the considered resonator to the cavities of spherical and cylindrical shape. The correctness of the described approach is validated by the papers [9, 12, 22]. Moreover, the algorithm convergence rate was estimated numerically for the growing dimensional representation of the algebraic problem (Eq. (5)).

### 3.2. Numerical and experimental results

The computations have been carried out for a resonator having the same dimensions, as in the case of the resonator with the bead. In **Figure 8**, the lines of equal amplitudes $E_\varphi$ - components of the electromagnetic field of the mode $TE_{0115}$ in the resonator with rods, made of Teflon and having permittivity $\varepsilon_2'$ = 2.07, are presented. Apparently, the rod with relatively low

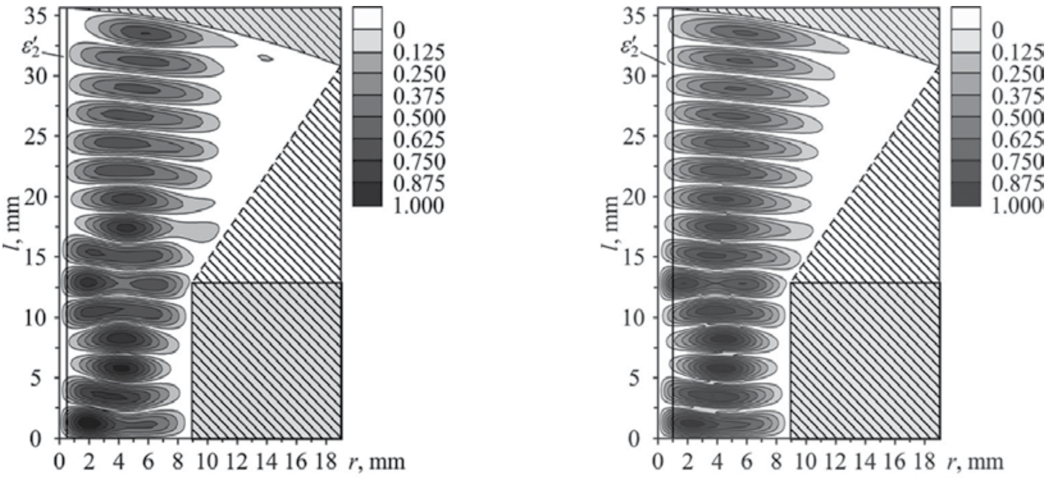

a) $2a = 1$ mm, $\varepsilon_2' = 2.07$, $f = 67.07$ GHz, b) $2a = 2$ mm, $\varepsilon_2' = 2.07$, $f = 66.97$ GHz,

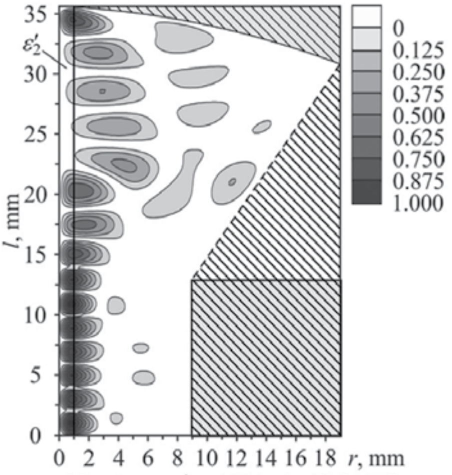

c) $2a = 2$ mm, $\varepsilon_2' = 3.824$, $f = 57.36$ GHz.

**Figure 8.** Field distribution in a cavity with a dielectric rod.

permittivity placed in the resonator weakly influences the distribution of the standing wave electric field components. The structure of the field at the placing of the rod, having diameter $2a = 1$ mm, into the resonator is shown in **Figure 8a**. Actually, it is identical to the structure of the field in the resonator at the rod diameter $2a = 2$ mm (**Figure 8b**). The difference of the $TE_{0115}$ mode resonance frequencies at the increase of the rod diameter from 1 to 2 mm is insignificant. It decreases from $f = 67.07$ to $f = 66.97$ GHz. That says about the low correlation of the resonant oscillation with the dielectric rod and could be explained by the fact that the sample is located in the area with low electric field intensity. An increase of the sample permittivity can change the situation. In **Figure 8c**, the lines of equal amplitudes of $E_\varphi$ - electromagnetic field component for the same mode $TE_{0115}$ in the resonator with the same dimensions for the rod, made of fused quartz ($\varepsilon_2'$ = 3.824) at the diameter $2a = 2$ mm, are presented. It could be seen that, in this case, the field is located in the rod, and resonance frequency decreases down to $f = 57.36$ GHz. Particularly, it concerns the cylindrical part of the considered resonator. For the resonator without a rod, as shown earlier, frequency $f = 71.382$ GHz.

The carried out research (**Figure 8c**) demonstrated the strong relation of the sample with the electromagnetic field and high filling coefficient of the resonator on the electromagnetic field [7]. In such a manner, for qualitative control of liquid samples, the composition of which includes water, it is necessary to use pipes, made of the material having low permittivity, as compared with the substance under studies.

On the basis of the analysis carried out, one can say that sensitivity of the resonant cell is defined by the diameter of the cylindrical sample and by the value of its permittivity. From **Figure 8**, one can see that electric field intensity near the conical metal surface (dotted lines) is low. It indicates that the considered cavity is equivalent to the OR, in which high- $Q$ oscillations, having low diffraction losses, are excited.

The experimental measurements of the permittivity of materials can be performed with the aid of calibration curves, that is, the dependencies of the resonator frequency shift on the permittivity of the cylindrical samples of various diameters, introduced into the resonance cavity. These characteristics are shown in **Figure 9**.

The upper part of the figure presents the series of curves plotted for the $TE_{0116}$ mode by the rod diameter of 2 mm (curve 1) and 1.5 mm (curve 2). The bottom part presents the $TE_{0115}$ mode by the same diameters of the samples, that is, 2 mm (curve 3) and 1.5 mm (curve 4). The dotted lines in the same figure, being almost parallel to those described earlier, illustrate similar dependencies for $TE_{0116}$ and $TE_{0115}$ modes in a cylindrical resonance cavity, with the cylindrical test pieces of the said size arranged along the resonator axis.

The length and the diameter of the cylindrical resonator were chosen to be equal to the length of the considered resonator and to the diameter of its cylindrical part (**Figure 7**). The problem

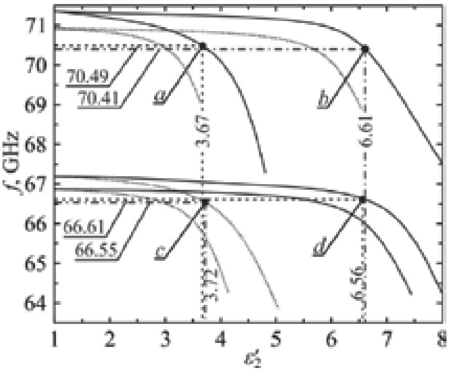

**Figure 9.** Dependencies of the resonance frequency on the permittivity of cylindrical bodies of various diameter for $TE_{0116}$ and $TE_{0115}$ modes.

considering the cylindrical resonator with a rod was solved using the method of variable separation, that is, its resonance frequency was described by rigorous formulas.

The figure demonstrates an obvious similarity of the curves for the both resonator types. It proves the fact that the nature of the physical processes occurring in the resonators is similar, both in the resonator under consideration and in the cylindrical cavity. It is an indirect evidence of the adequacy of our theoretical considerations. One more point to emphasize is that small changes of samples' permittivity, which are critical for oil quality control and food stuff, should be measured at the areas with a stronger disperse dependence, which is solely up to the diameter of the cylindrical sample (**Figure 9**).

The block diagram of the experimental unit used in the research is given in **Figure 4**. Only, in this case, the cylindrical sample was used. A sample was inserted into the cavity through a hole in the middle of the waveguide plunger, with a guide for the precise alignment of the sample along the resonator axis.

The measured shift of the resonance frequencies and the calibration curves in **Figure 9** were used to determine the dielectric permittivities of two cylindrical samples made of fused quartz and silicate glass. The value of resonance frequencies obtained in the experimental measurements for $TE_{0116}$- and $TE_{0115}$-modes for the case when the cylindrical samples of 2 mm and 1.5 mm in diameter were located along the resonator axis are marked with squares at the calculated curve. The results of measuring the dielectric permittivity of cylindrical samples of various diameters are listed in **Table 3**.

| Material | Sample diameter (mm) | Mode | Measured value of $\varepsilon_2'$ | Reference value of $\varepsilon_2'$ | Difference (%) |
|---|---|---|---|---|---|
| Fused quartz | 2 | $TE_{0116}$ | 3.67 (a) | 3.8 [7] | 3.4 |
| Fused quartz | 2 | $TE_{0115}$ | 3.72 (c) | 3.8 [7] | 2.1 |
| Soda-lime glass | 1.5 | $TE_{0116}$ | 6.61 (b) | 6.7 [23] | 1.3 |
| Soda-lime glass | 1.5 | $TE_{0115}$ | 6.56 (d) | 6.7 [23] | 2.0 |

**Table 3.** The measured values of the $\varepsilon_2'$ of the dielectric rods from Teflon and Plexiglas.

## 4. Open resonator with a segment of rectangular waveguide

A new electrodynamic system appears when inserting the segment of the short-circuited rectangular waveguide in the center of one of the OR mirrors [24]. Cross-section sizes of the waveguide $a \times b$ are chosen by the condition of the peak efficiency of the $TE_{10}$ mode excitation by the fundamental mode $TEM_{00q}$. One can consider such OR as a resonant cell for measurement of composite materials and biological liquids electromagnetic specifications as well as to control the quality of food stuff in millimeter and in sub-millimeter ranges.

We consider the hemispherical OR with a rectangular waveguide located in the center of the flat mirror. Reflection from the waveguide horn is neglected. We consider the resonator mirrors apertures as an infinite one. Omitting intermediate computations, we write down in the final form the expression, determining efficiency of the $\mathrm{TE}_{10}$ mode excitation in the waveguide of the OR, using the $\mathrm{TEM}_{00q}$ mode [25].

$$\eta = \frac{16\pi}{\tilde{a}\tilde{b}} \Phi^2\left(\frac{\tilde{b}}{2}\right)\left\{ e^{-(\pi/2\tilde{a})^2} + \frac{e^{-(\tilde{a}/2)^2}}{2}\left[W^*\left(\frac{\pi}{2\tilde{a}} + i\frac{\tilde{a}}{2}\right) - W\left(\frac{\pi}{2\tilde{a}} + i\frac{\tilde{a}}{2}\right)\right]\right\} \tag{20}$$

Here, $w_0$ is the radius of the beam waist of the fundamental mode on the flat mirror, $\tilde{a} = a/w_0$; $\tilde{b} = b/w_0$; $\Phi\left(\tilde{b}/2\right)$ is the probability integral and $W[(\pi/2\tilde{a}) + i(\tilde{a}/2)]$ is the integral of the complex argument probability.

Dependence $\eta\left(\tilde{a}, \tilde{b}\right)$, computed using (Eq. (20)), is presented in **Figure 10**. As evident from the figure, at $\tilde{a} = 2.844$ and $\tilde{b} = 1.98$, the efficiency of the $\mathrm{TE}_{10}$ mode excitation in the rectangular waveguide, located in the center of the OR flat mirror, using $\mathrm{TEM}_{00q}$ fundamental mode of the resonator is maximal and equal to 0.881.

As a result of the theoretical analysis, it was demonstrated that the efficiency of the $\mathrm{TE}_{10}$ mode excitation in the segment of the rectangular waveguide, using the OR fundamental oscillation, can amount the value about 90%. Therefore, such resonant system should have good selective properties, that is, an advantage for the analysis of dielectric samples with high losses. Besides, since the cross-section sizes $a \times b$ of the rectangular waveguide segment several times exceed radius of the beam waist $w_0$ of the fundamental OR mode, then it should be considered as the oversized.

In such OR, losses should increase, since ohmic losses in the walls of the rectangular waveguide segment are added. It would result in a decrease of the loaded $Q$-factor $Q_L$ and, as a consequence, in decrease of the resonant system sensitivity. Therefore, in order to understand how the rectangular waveguide segment will influence the spectral and energy specifications of the considered resonant system, experimental researches have been carried out [25].

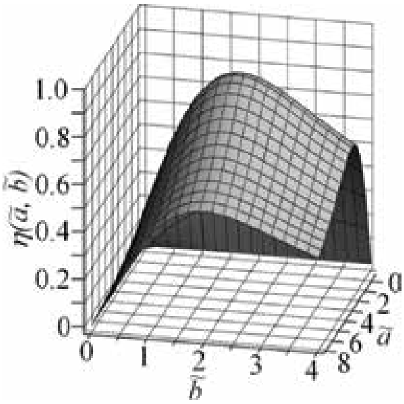

**Figure 10.** Efficiency of $\mathrm{TE}_{10}$ mode excitation in the rectangular waveguide versus its cross-section sizes.

Block diagram of the experimental setup, which was used for carrying out research of the hemispherical OR with the segment of the oversized rectangular waveguide, is shown in **Figure 11**.

The OR is formed by the flat mirror 5, having aperture 60 mm, and by the spherical focusing mirror 4, having a curvature radius $R$ = 113 mm and aperture 60 mm. In the center of the flat mirror, the segment of the oversized short-circuited rectangular waveguide 6 is located, cross-section sizes of which have been chosen in such a way to meet the peak efficiency condition of the $TE_{10}$ mode excitation by the fundamental mode of the OR. As it turned out, for presented dimensions of the resonator at $\lambda = 4.203$ mm and $L/R = 0.7$ (in [26] it was shown that approximately at such normalized distance between mirrors of the hemispherical OR, the $Q$-factor of the fundamental mode is maximal) such condition corresponds to $a = 23.7$ mm and $b = 16.5$ mm. The plunge 7 provides changing the waveguide length. Taking into account the dimensions of the waveguide, such OR will be the most promising in the short-wave part of millimeter and sub-millimeter ranges.

The resonator is excited by the slot coupling element, having sizes 3.6 × 0.16 mm, located in the center of the spherical mirror. The adjusting attenuator 2 is included into the setup for decoupling of the frequency generator and the resonator. Alignment to resonance is implemented by moving the spherical mirror 4 with the elements of the waveguide along the resonator axis. The input waveguide is oriented in such a manner that the vector **E** of the fundamental mode $TE_{10}$ is orthogonal to the plane of the drawing (**Figure 11**).

Receiving transmission line consists of the auxiliary line of the directional coupler 3, measuring polarizing attenuator 8, detector 10, resonant amplifier 11 and oscillograph 12. The resonant wavemeter 9 is included into the setup for monitoring frequency of the high-frequency generator 1. A double-stub matcher 13 is installed in the branch of the matched load 14 of the directional couplers 3. The photo of the OR and the experimental unit is represented in **Figure 12**.

The above-described procedure is used for computing of the resonant reflection factor of the resonator. Results of measurement of the resonant reflection factor on the distance between mirrors $L/R$ of the hemispherical OR, are shown in **Figure 13** (curve 1). In the resonator, $TEM_{00q}$ mode is excited. Identification of the oscillations modes was performed using the

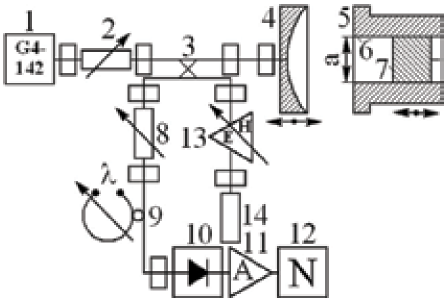

**Figure 11.** Block diagram of the experimental unit.

**Figure 12.** The photo of the OR with the segment of rectangular waveguide and the experimental unit.

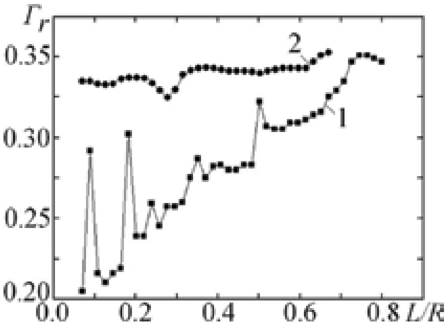

**Figure 13.** Dependencies of the reflection factor $\Gamma_r$ on the distance between mirrors $L/R$ for $\mathrm{TEM}_{00q}$ mode in the hemispherical OR (1) and resonator with the segment of the oversized waveguide (2).

perturbation technique [13]. The technique described in [27] was applied for the definition of the $\Gamma_r$ character.

As can be seen from **Figure 13**, with decrease of the distance between mirrors, the reflection factor from the resonator diminishes. It is related to the reduction of the diffraction and ohmic losses in the resonant system. Exceptions include the cases of the interaction of the considered oscillation with other oscillations excited in the OR ($L/R = 0.351$, $L/R = 0.259$, $L/R = 0.183$, $L/R = 0.089$), that it is displayed in the stepwise change of the $\Gamma_r$. The distance between mirrors $L/R = 0.501$ corresponds to the semi-confocal geometry of the resonator. The increase of the number of modes interacting with $\mathrm{TEM}_{00q}$ mode at $L/R < 0.3$ is related with reduction of the losses in the resonant system for specified distances between reflectors.

Dependence $\Gamma_r = \psi(L/R)$ for the same mode when segment of the oversized rectangular waveguide is located in the center of the flat resonator mirror (curve 2) is shown in that diagram. The segment length is $S = 19.082$ mm, which accounts nine-and-half waveguide wavelengths. At the same time, calculated value $S = 9\lambda_w/2 = 18.988$ mm $\left(\lambda_w = \lambda/\sqrt{1-(\lambda/2a)^2}\right)$. Apparently, the difference does not exceed 0.5%. The length of the waveguide is chosen in such a way to remove reflection of the Gaussian beam from the plunge, like from the second resonator mirror. Presence of the rectangular waveguide segment results in an increase of the OR ohmic losses in the whole tuning range. It is seen from a comparison of the reflection factors of the considered resonator (curve 2) and the empty hemispherical OR (curve 1). In whole range of the resonator tuning, only the fundamental mode is excited, which confirms the above-stated conclusion about selective properties of the OR with the segment of the oversized rectangular waveguide. That conclusion follows from the absence of the $\Gamma_r$ abrupt changes, which, as stated earlier, are caused by interaction of the considered mode with other modes of the resonant system. From the presented diagram one can see, that at the distance between resonator mirrors $L/R = 0.276$, the reflection factor has the minimum value equal to 0.329. When defining cross-section sizes of the rectangular waveguide, we supposed $L/R = 0.7$. The radius of the fundamental mode beam waist on the flat mirror of the hemispherical OR is defined by the expression $w_0 = \sqrt{\frac{\lambda}{\pi} R \sqrt{\frac{L}{R}\left(1-\frac{L}{R}\right)}}$ [28]. From this relation, it follows that $w_0$ will be the same at $L/R = 0.7$ and $L/R = 0.3$. Since in such resonator only the fundamental mode exists, then such behavior of $\Gamma_r$ is related to efficiency of the waveguide mode $TE_{10}$ excitation by means of the OR mode $TEM_{0015}$. The difference between experimentally obtained value $L/R = 0.276$ and the computed one (in this case $L/R = 0.3$), at which $\eta$ should have its peak value, and accounts for 8%. Such difference shows good agreement between computational and experimental results.

The dependence of reflection from resonator on the length of the oversized rectangular waveguide segment for certain mode is of the practical interest as well. We assume that in the hemispherical OR (**Figure 13**, curve 1), a no degenerate mode should exist. Moreover, the distance between resonator mirrors should correspond to low diffraction losses. Therefore, in terms of the diagram presented in **Figure 13**, we choose the mode $TEM_{0016}$ ($L/R$ = 0.295, $\Gamma_r = 0.257$). Results of the measurements are presented in **Figure 14**.

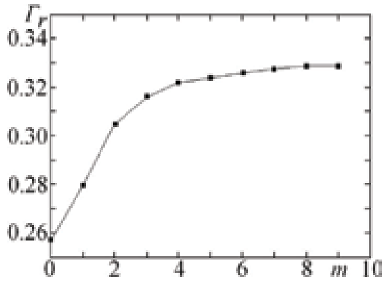

**Figure 14.** Dependence of reflectivity factor $\Gamma_r$ on the waveguide half waves number $m$, keeping along rectangular waveguide for $TEM_{0016}$ mode of the OR oscillations.

From the figure, one can see that moving the plunge from the surface of the flat mirror ($m = 0$) along the waveguide up to four waveguide half waves ($m = 4$), increase of the losses is observed ($\Gamma_r$ growth from 0.257 till 0.322). This apparently could be explained by transformation of the Gaussian beam into the waveguide wave. At further increasing of the waveguide segment length up to $m = 8$, there is insignificant growth of loss is caused by ohmic losses in the waveguide segment. If $m$ is increased further, then, $\Gamma_r$ is almost without any change.

Considered here resonant system will be the most promising at the analysis of biological liquids and food stuffs, the basic element of which is water (wines, juices, drinks). For carrying out measurements, a pipe made of the material of lower permittivity than that of a sample is placed into the oversized rectangular waveguide parallel to the vector of electric field intensity of the $TE_{10}$ mode. For reduction of losses inserted to the resonant system, it can be displaced to one of the side walls of the waveguide.

## 5. Conclusions

The cavity with the dielectric layer, being an electrodynamic model of the hemispherical OR with the segment of the oversized circular waveguide and dielectric bead, is considered in this chapter. As a result of the carried out theoretical analysis, it is shown that dependence of the frequency upon the thickness of the dielectric bead, located on the bottom of the cavity cylindrical part, has a quasi-periodic behavior. Such behavior is related to the amplitude distribution of $E_\varphi$ - component of the axial-symmetric mode at the top of the sample. The weak dependence of frequency on the bead thickness takes place when near to the sample top the node of the electric field component of the standing wave in the resonator is located. If in the area of the sample top, there is an antinode of the electric field component of the standing wave in the resonator, and the frequency dependence on the sample thickness is strong. Measurement of the permittivity and the tangent losses of beads, made of Teflon and Plexiglas at the various thickness, using the OR with the segment of the oversized circular waveguide, have been carried out. Obtained values $\varepsilon_2'$ and $\tan\delta$ are in agreement with the data of the other authors. In such a way, the proposed resonant system can be applied for measurement of electromagnetic parameters of substances in the short wave part of the millimeter and submillimeter ranges, both with high and with low losses.

The hemispherical OR, with the segment of the rectangular oversized waveguide located in the center of the flat mirror, has been considered in this chapter as well. As a result of the carried out theoretical analysis, it was demonstrated that efficiency of the $TE_{10}$ mode excitation in such waveguide by means of the resonator fundamental mode $TEM_{00q}$ can reach the value ~90% at cross-section sizes $\tilde{a} = 2.844$ and $\tilde{b} = 1.98$. The experimental researches carried out by the authors made it possible to establish that the resonator with the segment of the rectangular oversized waveguide possesses selective properties in the wide band of frequencies. Presence of the rectangular waveguide segment does not result in an abrupt increase of the ohmic losses. These circumstances are advantageous for application of such resonator for research of dielectric substances. Considered resonant system will be the most promising for the analysis of liquid dielectrics. For performing measurements, the pipe with the sample is placed into the oversized rectangular waveguide parallel to the vector of electric intensity of the $TE_{10}$ mode. For reduction of the losses inserted into the resonant system, it can be displaced to one of the side walls of the waveguide.

## Author details

Kuzmichev Igor K.* and Popkov Aleksey Yu.

*Address all correspondence to: kuzmichev.igr@i.ua

The A.Ya. Usikov's Institute for Radio Physics and Electronics of the NAS of Ukraine, Kharkiv, Ukraine

## References

[1] Vendik IB, Vendik OG. Metamaterials and their application in the technology of superhigh frequencies (survey). ZhTF. 2013;**83**:3-28 (in Russian)

[2] Kuzmichev IK, Glybytskiy GM, Melezhik PN. Open cavity for measuring the dielectric permittivity of materials. Patent 67978 A Ukraine, МПК$^7$ G 01 R 27/26; 2004 (in Russian)

[3] Kuzmichev IK, Melezhik PN, Poedinchuk AY. An open resonator for physical studies. International Journal of Infrared and Millimeter Waves. 2006;**27**:857-869. DOI: 10.1007/s10762-006-9122-7

[4] Il'inckiy AS, Slepyan GY. Oscillations and Waves in the Electrodynamic Systems with the Losses. Moskow: Izd-vo MGU; 1983. p. 232 (in Russian)

[5] Kuzmichev IK, Popkov AY. An open resonator for measuring electrical physical parameters of substances. Part I. Resonator model. Fizicheskie Osnovy Priborostroeniy. 2013;**2**:94-103 (in Russian)

[6] Kuzmichev IK, Popkov AY. Quasi-Optical Resonance Systems in the Millimeter Range Technology. Germany: LAP LAMBERT Academic Publishing; 2014. p. 173 (in Russian)

[7] Yegorov VN. Resonance methods in dielectric research in microwave range. Pribory and Tekhnika Eksperimenta. 2007;**2**:5-38 (in Russian)

[8] Wainshtein LA. Electromagnetic Waves. Moskow: Radio i Svyaz; 1988. p. 440 (in Russian)

[9] Popkov AY, Poyedinchuk AY, Kuzmichev IK. Resonant cavities in the form of bodies of revolution of complex geometry: A numerical algorithm for calculating the spectrum. Telecommunications and Radio Engineering. 2010;**69**:341-354. DOI: 10.1615/TelecomRadEng.v69.i4.40

[10] Afsar MN, Button K. Millimeter – Wave dielectric measurement of materials. Proceedings of the IEEE. 1985;**73**:131-153. DOI: 10.1109/PROC.1985.13114

[11] Vlasov SN, Koposova YV, Myasnikova SY, Parshin VV. Open resonators with thin dielectric plates. Izvestiya Vuzov. Radiofizika. 2006;**49**:219-226 (in Russian)

[12] Popkov AY. Electrodynamic model of the open resonator with a dielectric layer. Telecommunications and Radio Engineering. 2011;**70**:1323-1331. DOI: 10.1615/TelecomRadEng.v70.i15.20

[13] Valitov RA, editor. Submillimeter Wave Engineering. Moscow: Sov. Radio; 1969. p. 480 (in Russian)

[14] Kuzmichev IK, Popkov AY. An open resonator for measuring electrical physical parameters of substances. Part II. Experiment. Fizicheskie Osnovy Priborostroeniy. 2013;**2**:107-114 (in Russian)

[15] Altman JL. Microwave Circuits. Princeton/New Jersey/Toronto/New York/London: D. Van Nostrand Company; 1964. p. 462

[16] Frait Z, Patton CE. Simple analytic method for microwave cavity Q determination. Review of Scientific Instruments. 1980;**51**:1092-1094. DOI: 10.1063/1.1136368

[17] Miroshnichenko VS, Melezhyk PN, Senkevich EB. An open resonance cell for millimeter wave dielectrometer applications. Progress in Electromagnetics Research. 2008;**4**:47-65. DOI: 10.2528/PIERM08062406

[18] Kuzmichev IK. Equivalent schemes of representation of the open resonator. Radio Physics and Radio Astronomy. 2005;**10**:303-313 (in Russian)

[19] Feher G. Sensitivity considerations in microwave paramagnetic resonance absorption techniques. The Bell System Technical Journal. 1957;**36**:449-484. DOI: 10.1002/j.1538-7305.1957.tb02406.x

[20] Dryagin YA, Chuhovtsev AN. Measuring of the parameters of solid dielectrics in the short-wave part of the millimeter range by the resonance method. Izvestiya Vuzov. Radiofizika. 1969;**12**:1245-1248 (in Russian)

[21] Kuzmichev IK, Popkov AY. Resonance system for analyzing cylindrical samples in millimeter wave band. Telecommunications and Radio Engineering. 2012;**71**:1247-1257

[22] Popkov AY, Kuzmichev IK. Open resonator with a circular waveguide segment: Calculation and experiments. Radio Physics and Radio Astronomy. 2009;**14**:425-432 (in Russian)

[23] Shestopalov VP, Yatsuk KP. Methods of measuring the dielectric permeability of materials at microwave frequency range. Uspekhi Fizicheskikh Nauk. 1961;**74**:721-754 (in Russian)

[24] Kuzmichev IK, Khlopov GI. Matched Excitation of Quasi-Optical Open Resonators. Quasi-Optical Technology of Mm and Submm Wave Ranges. Kharkov: Izd-vo IRE; 1989. pp. 149-156 (in Russian)

[25] Kuzmichev IK. Open resonator with the length of the rectangular waveguide. Radio Physics and Radio Astronomy. 2014;**19**:249-257 (in Russian)

[26] Soohoo RF. Nonconfocal multimode resonators for masers. Proceedings of the IEEE. 1963; **51**:70-75. DOI: 10.1109/PROC.1963.1661

[27] Androsov VP, Kuzmichev IK. Influence of the Internal Heterogeneities of the Open Resonator on the Connection of its Oscillation with the Waveguide Lines. Kharkov: Izd-vo IRE; 1987. p. 14 (in Russian)

[28] Tarasov LV. Physics of Processes in the Generators of Coherent Optical Radiation. Moskow: Radio i Svyaz; 1981. p. 440 (in Russian)

# Electromagnetic Computation of the Short-range Wireless Linkbuget for Biomedical Communication

Ilkyu Kim

Additional information is available at the end of the chapter

http://dx.doi.org/10.5772/intechopen.76141

**Abstract**

The biomedical monitoring and imaging system requires data and power transmission through short-range communication, and the interference between large antennas placed within near-field region becomes the important consideration in designing an entire system. For the short-range communication, the electromagnetic computation becomes more complex, which requires huge computational resources. The efficient numerical methods that can be used in short-range communication are (1) Friis formula with correction term and (2) integral coupling formula. Both formulas are similar in an aspect that far-field gain pattern is used to calculate the link budget in a short range. The range of the communication link between two antennas can be defined as reactive near-field, radiating near-field including Fresnel region, a far-field region in the order of nearest distance. Friis formula with correction term can be useful for the simple on-axis antenna displacement in Fresnel region. The integral coupling formula is flexible to compute the mutual coupling of diverse antenna geometries within an entire radiating near-field and a far-field region. Those two methods are evaluated using several examples of short-range communication and interference, and indoor measurement evaluates the validity of the calculated results.

**Keywords:** mutual coupling, near-field region, Fresnel-field region, far-field region, Friis formula, integral form of coupling formula, biomedical devices, electromagnetic interference (EMI)

## 1. Introduction

The appearance of body-centric sensing system can realize real-time health care for patients who suffer from several internal diseases. There has been a recent advancement in the biomedical devices for body-centric sensing system. Several researches have been focused on a new frontier area, such as implanted antenna and wearable antenna for body-centric communication [1–3]. As well as an advancement of biomedical devices, it is also important to maintain a stable communication link between biomedical devices for body-centric sensing system. An accurate operational range of the biomedical devices for power and data telemetry should be determined in an early design process. Recently, low-powered sensor using radio frequency identification (RFID) back-scattering technology has attracted attention due to the concern about the safety issue of patients. The several studies on wireless communication link have been reported in order to realize bio-telemetry. The range of power transmission under the conditions such as in-body, on-body, and off-body has been studied through electromagnetic numerical methods [4]. In addition, it is crucial to predicting the radiative electromagnetic interference (EMI) and adherent strict requirements to avoid the possible interference with other communication links [5–8]. However, most of the evaluation on power transmission has been focused on simple scenarios such as boresight power transmission, and huge computing resources and storage has been involved. An accurate estimation including near-field region was difficult because the interpretation of power transmission in the near-field region is more complicated than one in the far-field region. Therefore, at this moment, the accurate and efficient computation method to estimate the power transmission is more desirable.

## 2. Wireless communication link

The range of the communication link between two antennas can be defined as reactive near-field, radiating near-field, and a far-field region in the order of nearest distance as shown in **Figure 1**. In the far-field region, it is well-known that the radiation pattern of the antenna is identical regardless of the distance from the antenna. However, in the near-field region, the radiation pattern changes as the distance from the phase center of the antenna changes. Within the near-field region, radiation pattern becomes broadened, and the gain of the antenna is reduced.

It is worth noting that the on-axis power density of the antenna within the Fresnel region decreases monotonically. The approximated on-axis power densities of a radiating aperture varies as [15].

$$|E|^2(R) \propto \left[1 - cos\left(\frac{2D^2/\lambda}{8R}\pi\right)\right]/2 \tag{1}$$

**Figure 1** shows the on-axis power densities of the circular aperture with $10\lambda$ diameter. The on-axis power transmission using far-field approximation deviates from both Fresnel and near-field curves. The Fresnel approximation also deviates from near-field curve while it shows its effectiveness beyond the last peak of on-axis power transmission. The Fresnel field region can be approximately defined as the area from the point of the last peak to the far-field edge defined by $2D^2/\lambda$.

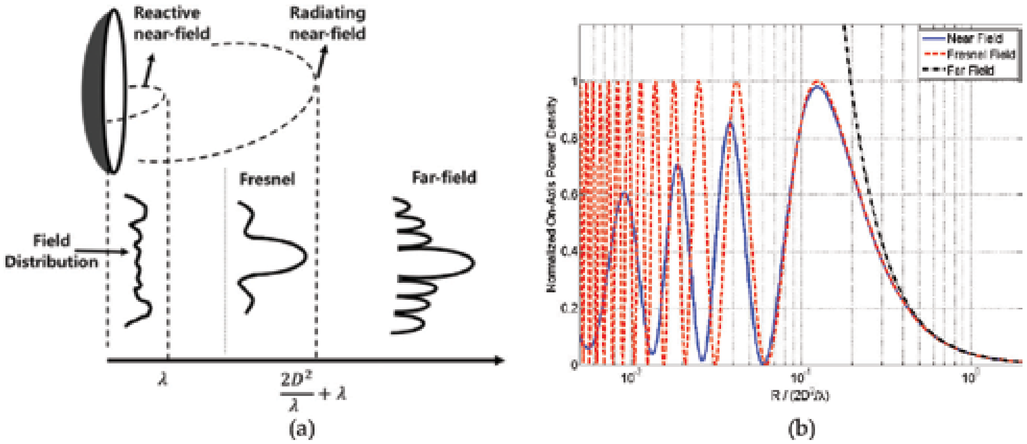

**Figure 1.** (a) Field distribution for different field ranges and (b) normalized on-axis power density of a uniform circular aperture with 10$\lambda$ diameter.

Therefore, the distance $R$ of the last peak value can be calculated by.

$$R = \frac{1}{8}\frac{2D^2}{\lambda} = \frac{A}{\lambda\pi} \tag{2}$$

where $A$ is the physical area of the aperture. The definition of Fresnel region would be more accurate including the effects of tapering efficiency and phase errors. Using the definition of the antenna effective area, (2) can be redefined as.

$$R = \frac{A^e}{\lambda\pi} = \frac{\lambda G}{4\pi^2} \tag{3}$$

where the effective area $A^e$ can be defined as $\lambda^2\, G/(4\pi)$.

The definition in (3) can be another approach to determine the Fresnel region. The on-axis power densities for several analytical aperture fields were reported in [15], which all confirm the effectiveness of (3).

## 3. Methods of evaluation on power transmission

The accuracy of the formula can be determined by how well the gain reduction is estimated, compared to the Friis formula. The nearest distance for estimation, flexibility in antenna geometry and computational resources needs to be considered. **Figure 2** presents the flowchart for evaluating the power transmission in near-field and a far-field region. Estimating a power transmission is presented in this chapter using following methods:

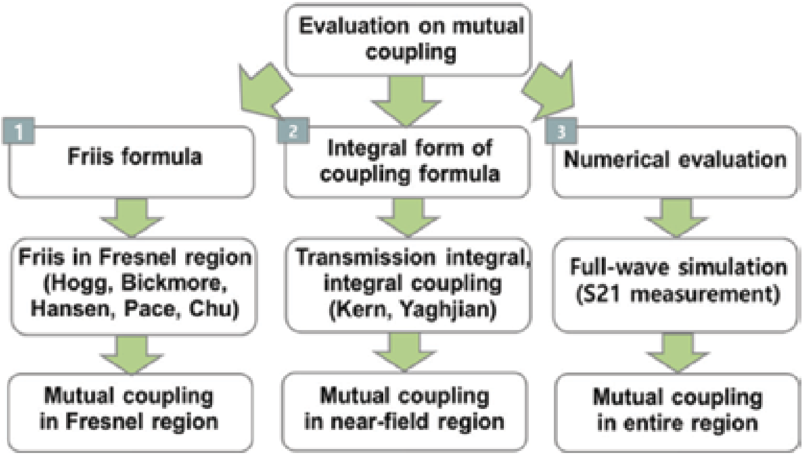

**Figure 2.** Flowchart of the mutual coupling evaluation in radiating near-field and a far-field region.

1. Friis formula with a correction term
2. The integral form of coupling formula
3. Evaluation using full-wave simulations and indoor measurement.

Those methods are different with respect to (a) possible antenna geometries, (b) required information, and (c) computational resources. The Friis formula can be expressed with a correction term of [11–18]. The formula can accommodate the instant computation with the basic information, such as gain at bore-sight and operational frequency while its effectiveness is confined within the Fresnel region. The integral form of coupling formula [20–24] is expressed with the integral of the scalar products between two far-field patterns. This formula can accommodate an accurate computation within an entire radiating near-field region with reasonable complication. The various antenna scenarios such as rotation and off-axis can be calculated using the formula. Final research method is the use of full-wave simulation and measurement. Recent advancement in computing resources makes it possible to use numerical evaluation such as full-wave simulation. The range of numerical evaluation includes radiative and reactive near-field region while its computation is most complex among three research methods.

## 4. Friis formula with correction term

### 4.1. Introduction

The standard Friis formula [9] has been successful in calculating the link budget in wireless communications between two distant antennas. The Friis formula is simple to use and practical to quickly determine the power transmission. Four different methods were used in order to derive the Friis formula, and all results in same conclusion [10]. It is assumed in the derivations that accuracy of the formula is limited to the far-field region. The attempt to predict power transmission in a Fresnel region has been made through using the concept of gain reduction factor. The gain reduction factor can be defined as the ratio of gain in a near-field region to the gain in the far-field region. Several efforts have been made to present an appropriate model to estimate an accurate gain reduction factor. The defocusing effect in a Fresnel region was derived in the gain reduction factor of uniform and tapered apertures [11]. An asymptotic series with Friis formula and correction term computed on-axis power transmission in a Fresnel region [12]. Gaussian approximation composed of effective aperture area shows its effectiveness for practical use in a Fresnel region [13]. The on-axis Fresnel gain is evaluated [14, 15]. The higher order interaction between two closely spaced horn antennas was investigated, and the power transmission was evaluated [16]. However, there has been limitation with respect to the applications of those proposed formulas, due to the lacking of numerical capabilities at that time. Most of scenarios were focused on simple boresight power transmission. Recent research activities related to the Friis formula were very handful, and its effectiveness was only valid in the far-field region [17, 18].

In this chapter, the power transmission is evaluated using an asymptotic form of the Friis formula [19], which is advantageous with respect to computational complexity, compared to the previous work. The formula is effective in both near-field (Fresnel) and far-field regions. The computation of gain reduction factor depends on the way how to normalize the distance between two antennas. Most of the previous researches have focused on normalization of separation distance in terms of antenna directivity and wavelength. However, using this normalization, gain reduction factor depends on shape and size of antenna aperture. However, by taking a normalization with respect to antenna gain (or effective area) and wavelength, a single gain reduction factor is achieved for any type of antennas. This method may be more useful in the case where the quick and simple calculation is required.

### 4.2. Standard Friis formula in the far-field region

**Figure 3** depicts the antenna geometry where a receiving antenna is placed in the far-field or in the Fresnel region of transmitting antennas. The ratio of receiving power to the transmitting power ($P_r/P_t$) between two antennas in the far-field region can be obtained using the Friis formula.

$$\frac{P_r}{P_t} = \frac{\lambda^2}{16\pi^2 R^2} G_t(\theta_t, \phi_t) G_r(\theta_r, \phi_r) \left(1 - |\Gamma_t|^2\right) \left(1 - |\Gamma_r|^2\right) |\widehat{\rho}_t \cdot \widehat{\rho}_r|^2 \tag{4}$$

where $G_t(\theta, \phi)$: the far-field gain pattern of transmitting antenna,

$G_r(\theta, \phi)$: the far-field gain pattern of receiving antenna,

$1 - |\Gamma|^2$: input impedance mismatch,

$|\widehat{\rho}_t \cdot \widehat{\rho}_r|^2$: the polarization mismatch.

$R$ is the separation distance measured between the phase centers of the Tx and Rx antennas, and the far-field gain pattern differs depending on the angular direction. The relationship between the mutual coupling $|S_{21}|$ and the ratio of $P_r/P_t$ can be defined as.

$$|S_{21}| = \sqrt{\frac{P_r}{P_t}} \tag{5}$$

The radiation patterns of two antennas are important to determine the power transmission between two antennas. A receiving antenna is placed at the distance of near-field or far-field of the other antenna. The on-axis power transmission between two antennas is evaluated with full-wave simulation and Friis formula. The standard Friis formula shows its effectiveness in the far-field region while degradation of the accuracy is observed in the near-field region. The difference between two results grows as one antenna is located closer to the other antenna. **Figure 3** shows a comparison of power transmission of horn antennas and simulated result exhibits a huge deviation from the Friis formula which is equivalent to 5 dB at $R = 2\lambda$. The main reason resulting in the deviation is that the Friis formula only uses the far-field gain. However, the actual gain pattern in the Fresnel region depends on different distances from the antenna phase center.

### 4.3. Friis formula in the Fresnel region

As previously mentioned, the accuracy of the standard Friis formula deteriorates at close distances. Its accuracy can be improved by incorporating the distance-dependent antenna gain variations in the Fresnel region. By replacing the far-field antenna gains used in (4) with the gain variations in the Fresnel region $G_F(R)$, a Friis formula in the Fresnel region is obtained as,

$$\frac{P_r}{P_t} = \frac{\lambda^2}{16\pi^2 R^2} G_{F,t}(R)\, G_{F,r}(R) \tag{6}$$

It is worth noting that the gain variations in Fresnel region are now a function of $R$. A gain reduction factor $\gamma$ usually represents the gain decrease effect in the Fresnel region, which is the ratio between the antenna gains in the Fresnel and one in the far-field regions. It can be defined as.

$$\gamma(R) = \frac{G_F(R)}{G} \tag{7}$$

Using (7), the formula can be rewritten as.

$$\frac{P_r}{P_t} = \frac{\lambda^2}{16\pi^2 R^2} \gamma_t(R)\, G_t\, \gamma_r(R)\, G_r \tag{8}$$

Eqs. (7) and (8) assumes that it is possible to separate the gain reduction factor for each individual antenna, and they can be obtained through analytical derivation, full-wave simulations or measurements of the antenna gain pattern. [12] suggested that an antenna gain in the Fresnel region can be approximated with a quadratic form of variation in terms of its far-field gain:

$$\gamma(\Delta) = \frac{G_F(\Delta)}{G} = 1 - \alpha\Delta^{-2} + O(\Delta^{-4}) \tag{9}$$

where $\Delta$: the normalized form of the distance $R$ between two antennas, $\alpha$: a coefficient that determines the reduction rate of the antenna gain.

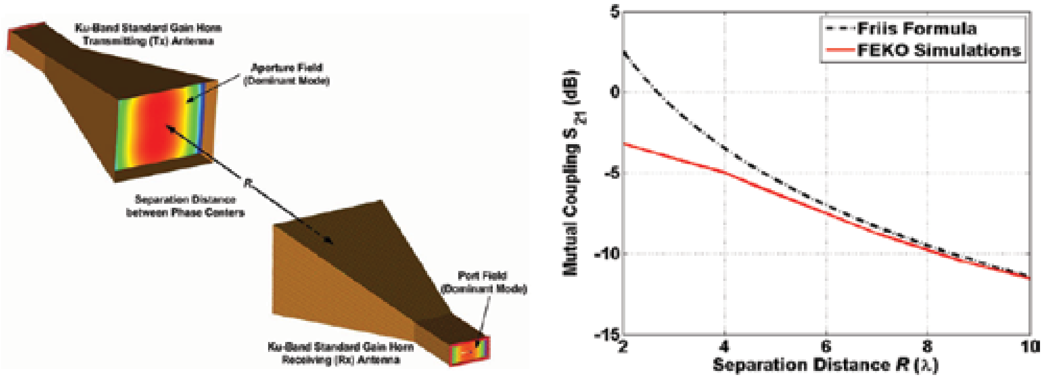

(a) (b)

**Figure 3.** (a) On-axis mutual coupling between two Ku-band horn antennas and (b) failure of standard Friis formula in near-field region.

In general, the gain reduction factor $\alpha$ may be different for different types of antennas with a conventional definition of normalized distance $R$. The conventional derivation utilized far-field edge distance, $(2D^2/\lambda)$ to normalize separation $R$. However, with a new derivation of the normalized separation $R$. distance $\Delta$, a single coefficient $\alpha$ for various types of antennas can be obtained. The assumption used in the derivation is that physical area of the aperture $A$ in (11) can be replaced by its effective area $A_e$. This method would be more realistic so that the effects of operating frequency, antenna size, and tapering efficiency can all be included in $\Delta$. This may be able to result in a more single $\alpha$. It is supposed that input impedances are matched and the two antennas are aligned in boresight direction with matched polarization.

$$\Delta = \frac{R}{2\lambda G/\pi^2} \ \left(\text{Proposed normalization}\right) \tag{10}$$

$$\Delta' = \frac{R}{2D^2/\lambda} \ (\text{Conventional normalization}) \tag{11}$$

where $G$: the antenna gain in the far-field region, $R$: the separation distance between two antennas.

The proposed method utilizes the separation distance $\Delta$, normalized with respect to the antenna gain (or the effective area) and wavelength. Using the definition of normalization, we follow the quadratic asymptotic form of the gain reduction factor used in literature an propose a novel normalization form of separation distance $R$.

### 4.4. Gain reduction factor in the Fresnel region

Using proposed normalization in (10), more converged curves are observed for aperture antennas such as horns and reflectors. The effectiveness of $2\lambda G/\pi^2$ proposed normalization is validated through these examples. However, except for the aperture antennas, it does not provide enough convergence for relatively low-gain antennas such as small dipoles and open-ended waveguides. This is because the far-field gain $G$ used in (10) is defined as one of

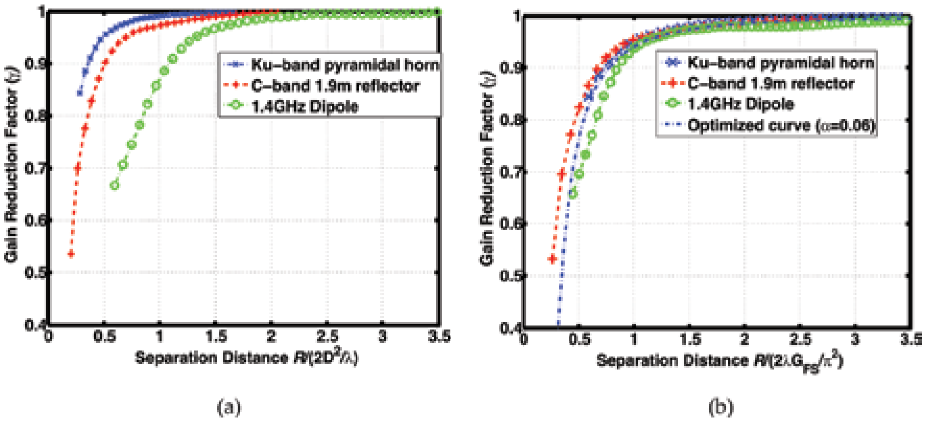

**Figure 4.** The gain reduction factor (a) using normalized distance $R$ with respect to $2D^2/\lambda$ and (b) using normalized distance $R$ with respect to $2\lambda G_{FS}/\pi^2$ (right).

the aperture antenna, which is well-known to radiate toward the direction of front-side of the aperture. Thus, in order to include the low-gain antennas, the modified antenna gain can be defined using total radiated power over a half sphere. The modified gain, namely the front-side gains $G_{FS}$, can be used instead of the far-field gain $G$ presented in (10). The front-side gain and associated gain reduction factor can be expressed as:

$$G_{FS} = \frac{4\pi U_m}{P_F}, \qquad \gamma_{FS}(\Delta) = 1 - \alpha_U \left(\frac{R}{2\lambda G_{FS}/\pi^2}\right)^{-2} \tag{12}$$

where $U_m$: the maximum radiation intensity, $P_F$: the total radiated power over a half sphere where maximum occurs.

**Figure 4** shows the gain reduction factors using the front-side gain, which can achieve sufficient convergence of all curves. The trend of all the curves suggests that an empirical coefficient $\alpha$ can be $\alpha$ = 0.06. The major weakness of this method is that we need to calculate the front-side gain, based on complex 3D radiation pattern.

Instead of using front-side gain, the simpler adjusted gain would be more desirable with respect to the instant calculation of the mutual coupling. The proposed antenna gain can be obtained depending on its classification: low-gain or high-gain antennas defined as below:

$$G_A = G\ (G \geq 10\text{ dB} : \text{high } G) = G + 3\text{ dB}\ (G < 10\text{ dB} : \text{low } G), \gamma_A(\Delta) = 1 - \alpha_U \left(\frac{R}{2\lambda G_A/\pi^2}\right)^{-2} \tag{13}$$

where $G_A$ is the proposed adjusted gain.

Otherwise, more sophisticated switching model can be used such as:

$$\gamma_A(\Delta) = 1 - \alpha_U F(G) \left(\frac{R}{2\lambda G_A/\pi^2}\right)^{-2}, \quad F(G) = 2.5 - \frac{a}{\pi} \cdot arctan[c \cdot (G - b)] \tag{14}$$

where the constant is found to be $a$ = 3, $b$ = 10, and $c$ = 1.

Note that the adjusted gain $G_A$ is recommended after an empirical case studies. It is also verified that the proposed method in (13) also exhibits similar convergence to the result of (12). It implies that the empirical coefficient $\alpha$ for (13) can be obtained as $\alpha = 0.06$ for the class of the various antennas. The numerous case studies suggest that maximum deviation of gain reduction factor can be converted into 0.5 dB error in power level. The effectiveness of the gain reduction factor will be discussed evaluating the power transmission in following sections.

## 5. Integral form of coupling formula

### 5.1. Introduction

Another method to evaluate mutual coupling is the use of integral form of coupling formula, which is advantageous in its flexibility. The power transmission for various antenna geometries such as rotation and offset in a closer distance maybe required for a comprehensive coupling evaluation. The formula is advantageous since it estimates the coupling in the very close distance, which covers an entire radiating near-field region. The integral form of coupling formula takes a form of a scalar integral of two vector far-field patterns. Transmission integral was studied, which is based on plane-wave scattering matrix (PWSM) theory, and its validity is evaluated through the power transmission between two identical apertures [20]. Two different computer programs were developed to calculate the coupling between two antennas located in a longitudinal and transverse displacement [21]. The coupling in both near-field and far-field is evaluated. The measured far-fields of array and reflector antennas are used for the calculation of near-field pattern [22]. An advancement in computer program increases freedom of possible antenna orientation and displacement [23, 24].

### 5.2. Integral form of coupling formula

The integral form of coupling formula is practical and flexible, which enables to calculate power transmission in diverse scenarios such as rotation and off-axis cases. The complexity of required information slightly increases, compared to the Friis formula with a correction term. While simple bore-sight gain and antenna geometry are employed in Friis formula, the integral form of coupling formula utilizes 3D vector far-field patterns of two antennas and antenna displacement. Several cases are studied using the integral form of coupling formula and validity of the result is evaluated comparing with the full-wave simulation FEldberechnung für Körper mit beliebiger Oberfläche (FEKO).

The ratio between input wave and output wave presented in [21, 22] can be expressed as normalized vector far-field pattern of transmit antenna $\bar{f}_{TX}(\bar{k})$ and receive antenna $\bar{f}_{RX}(-\bar{k})$.

$$\frac{b_0'}{a_0}(R) = -\frac{C}{4\pi k}\iint_{\sqrt{{k_x}^2+{k_y}^2}<k} \frac{\bar{f}_{Tx}(\bar{k})\cdot\bar{f}_{RX}(-\bar{k})}{k_z} e^{-j\bar{k}\cdot\bar{r}}\ dk_x dk_y \tag{15}$$

$a_0$ is the amplitude of input wave of transmitting antenna, $b_0$ is the amplitude of output wave of receiving antenna, and $\bar{k}$ is the wave vector. The Eq. (15) has $e^{jwt}$ time dependence in free space, and the constant $C$ can defined as:

$$C = -\frac{Z_{wg,Rx}}{Z_0}\frac{1}{1 - \Gamma_{L,Rx}\Gamma_{0,Rx}} \tag{16}$$

$Z_{wg,\ Rx}$, $Z_0$ are the impedance of feed waveguide in receive antenna and free space impedance. $\Gamma_{L,Rx}$, $\Gamma_{0,Rx}$ are reflection coefficient of the load impedance and the receive antenna impedance, respectively. The discretization of the sampling space $k_x$-$k_y$ and discrete Fourier transform is required in order to obtain the coupling quotient, and the sampling frequency is defined as

$$f_s = 2\kappa \times (D_{Tx} + D_{Rx}) \tag{17}$$

$D_{Tx}$ and $D_{Rx}$ are the diameters of a sphere, which encloses the geometry of transmit and receive antenna, respectively. The constant $\kappa$ is the oversampling ratio, which limits the movement of antennas in the transverse direction. The separation distance between two antennas can also be defined as:

$$\frac{D_{Tx} + D_{Rx}}{2} \leq R \leq \frac{(D_{Tx} + D_{Rx})^2}{2} \tag{18}$$

At the minimum separation distance, the accuracy deteriorates due to the growing reactive field component. When $R$ approaches the maximum separation distance, the only near-axis plane wave is taken into consideration, which leads to the inaccurate result of calculation [22].

## 6. Evaluation using numerical methods

### 6.1. Evaluation using Friis formula with a correction term

The on-axis power transmission between two identical antennas is evaluated at various separation distances. Both far-field antenna gain of the antenna and separation distance is required information. In addition, the point of phase center is important to measure the accurate separation distance. The first example is selected as two half-wavelength dipole antennas, which operate at 1.4GHz with the far-field gain of 2.14 dB. The next example uses two standard gain horns at 12.7GHz with the far-field gain of 15.2 dB, and the phase center of the horn antenna is located at 5 mm below the antenna aperture.

$$\begin{aligned}\frac{P_r}{P_t} = &\frac{\lambda^2 G_t G_r}{16\pi^2 R^2}\left(1 - \alpha_E\left(\frac{R}{2\lambda G/\pi^2}\right)^{-2}\right)\left(1 - \alpha_E\left(\frac{R}{2\lambda G/\pi^2}\right)^{-2}\right)\\ &\times\left(1 - |\Gamma_t|^2\right)\left(1 - |\Gamma_r|^2\right)|\widehat{\rho}_t \cdot \widehat{\rho}_r|\end{aligned} \tag{19}$$

The coupling level is obtained using the Friis formula with correction term, and the validity of the formula is evaluated by comparing it with the full-wave simulation FEKO. The comparison among standard Friis formula, Friis formula with correction term (asymptotic Friis formula),

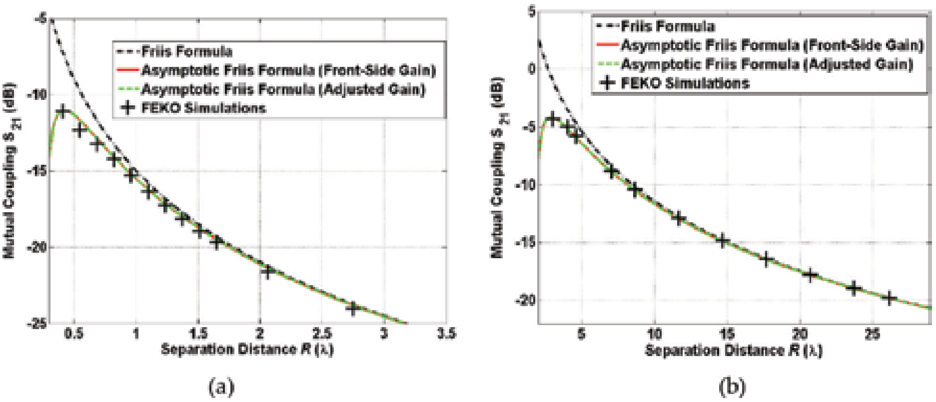

**Figure 5.** (a) Mutual coupling between two dipole antennas operated at 1.4GHz and (b) mutual coupling between two Ku-band horn antennas operated at 12.7GHz.

and simulated results is made as shown in **Figure 5**. The Friis formula with correction term agrees well with the simulated coupling level. In addition, it does provide a significant enhancement after the nearest distance of Fresnel region while the standard Friis formula results in huge deviation. However, it is also shown that the calculated result drops drastically before the nearest distance of Fresnel region, which indicates that its effectiveness is limited to the Fresnel region and far-field region. The formula is made up of quadratic form of the gain reduction factor, which turns out to be negative at a very close distance. In order to predict the coupling at a closer distance, higher order term of interaction should be considered in the quadratic form of gain reduction factor. The nearest prediction ranges for the high-gain antenna is around $1.44\times(D^2/2\lambda)$. The nearest range for dipole antenna is approximately $0.35\lambda$.

### 6.2. Evaluation using integral form of coupling formula

The first step is to obtain the 3D vector far-field pattern with phase and amplitude using FEKO. Next step is to take the integral of scalar product between two far-field patterns so that the coupling with respect to the antenna geometries can be calculated. For the purpose of evaluation, 2 m and 1.9 m prime-focus reflector operated at 5.5GHz are used as an example. The far-field pattern is simulated using FEKO, and the maximum directivity of 42.5 dB and 42.1 dB is obtained for each reflector antenna, respectively. Integral coupling formula is calculated for the bore-sight scenario using the far-field patterns of both antennas. The calculated result is compared to the Friis formula and FEKO simulation as shown in **Figure 7**. The integral coupling agrees well with the FEKO simulation within 0.5 dB deviation. It is worthy noting that the formula is effective within the radiating near-field region, and no sudden decrease of the coupling level in the nearest distance is observed. The second example is selected as the ground station antennas pointing to the multiple satellites. The interference between two antennas is investigated using the integral form of a formula. In order to communicate with satellites, antennas are both tilted at $\theta = 45°$ toward the sky, and the separation of two antennas is around 3 m. The configuration of both antennas is also shown in **Figure 6**. In a similar way, coupling integral is calculated, and the comparison of the results is shown in **Table 1**. Considering that the cross-pol component becomes significant in off-axis radiation pattern, the comparison shows reasonable agreement within 3 dB difference.

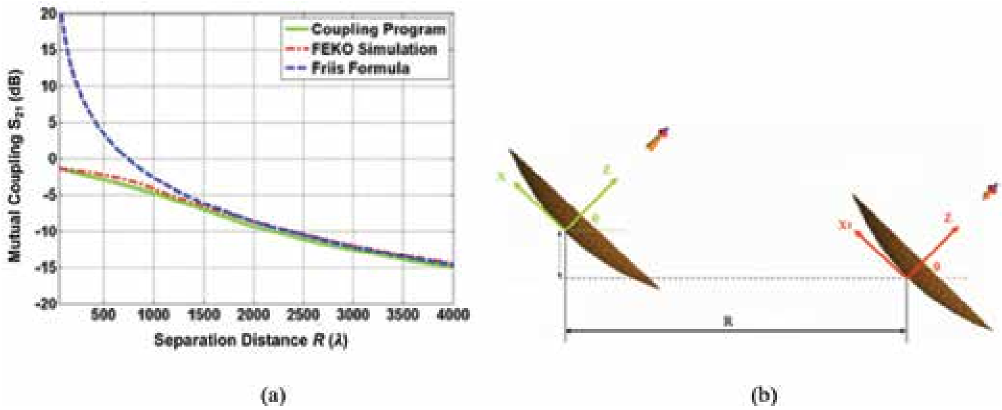

(a) (b)

**Figure 6.** (a) On-axis mutual coupling between C-band 2 m and 1.9 m reflector antennas and (b) off-axis mutual coupling between the two reflector antennas.

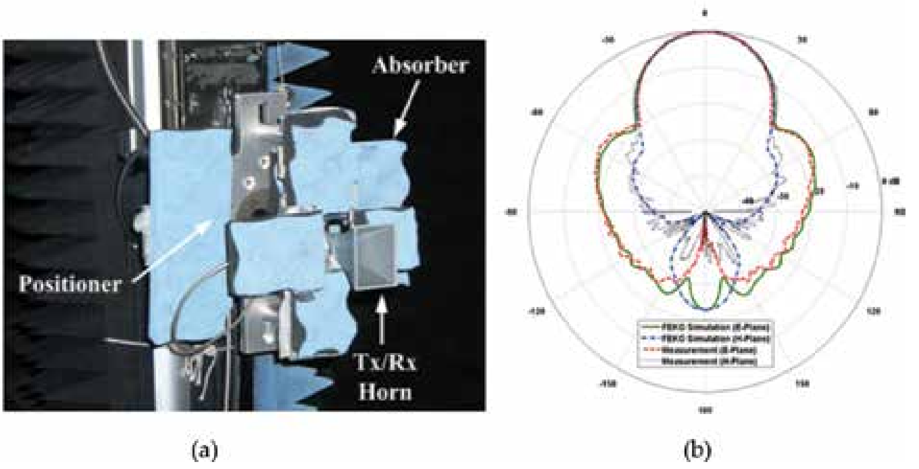

(a) (b)

**Figure 7.** (a) Setup of horn antenna inside near-field anechoic chamber and (b) far-field radiation pattern from the measurement.

| | FEKO | Integral coupling |
|---|---|---|
| Coupling level | −77.14 dB | −80.81 dB |

**Table 1.** Off-axis mutual coupling between the two reflector antennas.

## 7. Evaluation using the two numerical methods

### 7.1. Evaluation using mutual coupling measurement

The coupling level between two identical Ku-band standard gain horns is measured in order to evaluate the proposed formula. The standard gain horn operates at 12.7GHz, the center frequency of Ku-band, and the radius of the sphere, which encloses the horn antenna, is around 2.15$\lambda$. The radiation pattern of the Ku-band standard gain horn is measured inside the UCLA spherical near-field range as shown in **Figure 7**. The amplitude and phase of the radiated near-field are acquired by rotating the horn mounted on the positioner. The near-field information can be converted into far-field radiation pattern. The comparison between measured far-field and the simulated far-field pattern using FEKO is depicted in **Figure 8**. The max simulated and measured gain patterns are 15.28 dB and 15.47 dB, respectively.

As shown in **Figure 8**, the two horn antennas are mounted on an optical table and the mutual coupling $S_{21}$ is measured using a vector network analyzer. To properly measure $S_{21}$, we need to carefully setup the measurement as below:

1. The polarization of both horn antennas must be perfectly matched in order to avoid any loss due to the mismatch of polarization.
2. The insertion loss proportional to the length of cable should be carefully measured and counted in calculating the coupling level.
3. Separation distance *R* needs to be measured from one phase center to the other phase center. Prior to measuring the distance, it is critical to determine the phase center where the phase response of far-field pattern is uniform. In general, the simulated model can be used to find the location of the phase center.

The separation distance *R* varies from 4 to 31$\lambda$ in the on-axis direction. The mutual coupling levels using different methods are compared as shown in **Figure 8**. The simulated results show

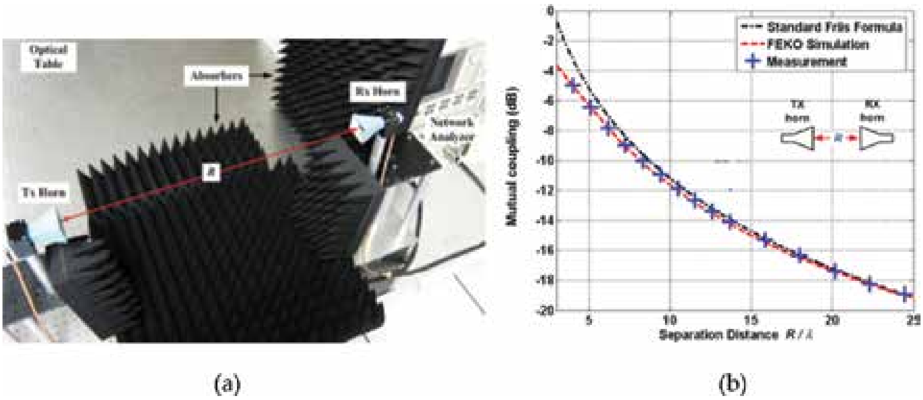

(a)

(b)

**Figure 8.** (a) Indoor measurement of mutual coupling and (b) measured mutual coupling level in order to evaluate the simulated coupling level.

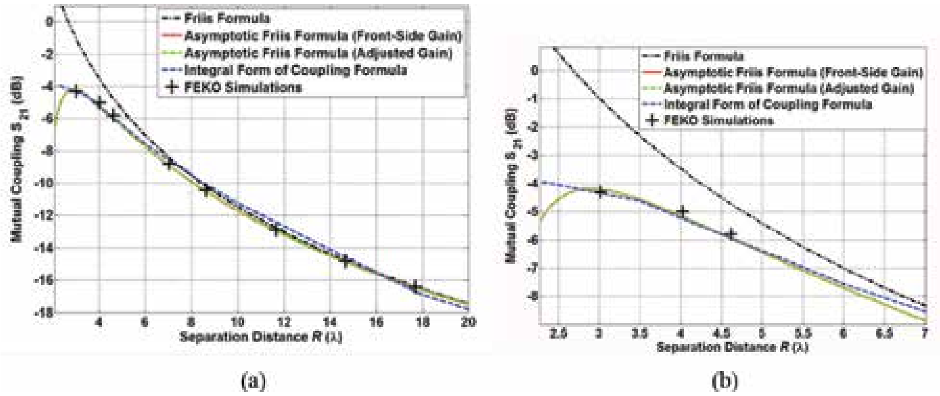

**Figure 9.** (a) Evaluation using Friis formula, asymptotic Friis formula, integral form of coupling formula, and FEKO simulation and (b) close up in the radiating near-field region.

a good agreement with the measurements. It can be concluded that the validity of the simulation is successfully evaluated with the measurement.

### 7.2. Error analysis of the two numerical methods

An error of the proposed numerical methods is evaluated with respect to the full-wave simulation. The mutual coupling between identical Ku-band horn antennas is computed using the two methods: (1) Friis formula with gain reduction factor and (2) Integral form of coupling formula. The graphs of the proposed methods and measurement are shown in **Figure 9**. It is worthy noting that the proposed two methods are all effective within Fresnel region while the integral coupling formula extends its effectiveness to the radiating near-field region. The mutual coupling of the asymptotic Friis formula and integral form of coupling formula deviates from the simulated one at the distance of less than $R = 3\lambda$ and $R = 2.3\lambda$, respectively. Beyond the each nearest separation distance, it is observed that maximum error with respect to the simulated result is less than 0.5 dB, which corresponds to around 11% deviation in power level. It verifies that the two numerical methods can provide the reasonable agreement with respect to the full-wave simulation.

## 8. Conclusion

The mutual coupling between one antennas placed in radiating near-field and far-field ranges of the other antenna is calculated using proposed formulas and evaluated through full-wave simulation and measurement. It is shown that those formulas enable to provide enhancement in the radiating near-field region in comparison to the standard Friis formula. The optimal formula can be selected depending on the availability of input information, the proximity of range, and the flexibility of antenna geometry. The important features of those two formulas are summarized in **Table 2**. The validity of simulated mutual coupling level is evaluated through the measurement. The setup of indoor measurement is discussed, and the key factors to affect the accuracy of the measurement are addressed. Those methods can be also expanded to the antenna measurement and near-field applications.

| | Friis formula with correction term | Integral form of coupling formula | Full-wave simulation |
|---|---|---|---|
| Required information | Low | High | — |
| Proximity of range | Fresnel region | Radiating near-field | Entire near-field |
| Flexibility of geometry | Low | High | High |

**Table 2.** Comparison of the proposed numerical methods.

## Author details

Ilkyu Kim

Address all correspondence to: ilkyukim@gmail.com

Defense Agency for Technology and Quality, South Korea

## References

[1] Izdebski P, Rajagopalan H, Rahmat-Samii Y. Conformal ingestible capsule antenna: A novel chandelier meandered design. IEEE Transactions on Antennas and Propagation. April 2009;**57**(4):900-909

[2] Esko S, Jouni K, Juha P, Arto Y, Ilkka K. Application of near field communication for health monitoring in daily life. IEEE Proceeding 28th Annual International Conference Engineering in Medicine and Biology Society. August 2006:3246-3249

[3] Rao S, Llombart N, Moradi E, Koski K, Bjorninen T, Sydanheimo L, Rabaey J, Carmena J, Rahmat-Samii Y, Ukkonen L. Miniature implantable and wearable on-body antennas: Toward the new era of wireless body-centric. IEEE Antennas and Propagation Magazine. February 2014;**56**(1):271-291

[4] Wilson PF, Hill DA, Holloway CL. On determining the maximum emissions from electrically large sources. IEEE Transactions on Antennas and Propagation, August. 2002;**44**(1):79-86

[5] Hernando MM, Fernandez A, Arias M, Rodriguez M, Alvarez Y, Las-Heras F. EMI radiated noise measurement system using the source reconstruction technique. IEEE Transactions on Industrial Electronics. August, 2008;**55**(9):3258-3265

[6] Tarusawa Y, Ohshita K, Suzuki Y, Nojima T, Toyoshima T. Experimental estimation of EMI from cellular base-station antennas on implantable cardiac pacemakers. IEEE Transactions on Electromagnetic Compatibility. November, 2005;**47**(4):938-950

[7] Lee SG, Hoang H, Choi YH, Bien F. Efficiency Improvement for Magnetic Resonance Based Wireless Power Transfer with Axial-misalignment. Electronics Letters. 6, March 2012;**48**:339-340

[8] Kim J, Rahmat-Samii Y. "Implanted antennas inside a human body: simulations, designs and characterizations," IEEE Transactions on Microwave Theory and Techniques, August 2004;**52**(8):1934-1943

[9] Friis GHT. A note on a simple transmission formula. Proceedings of the IRE. May 1946;**34**: 254-256

[10] Hogg DC. Fun with the Friis free-space transmission formula. IEEE Antennas and Propagation Magazine. August 1993;**35**(4):33-35

[11] Soejima T. Fresnel gain of aperture aerials. Proceedings of the IEE. June 1963;**110**(6):1021-1027

[12] Pace JR. Asymptotic formulas for coupling between two antennas in the fresnel region. IEEE Transactions on Antennas and Propagation. May 1969;**AP-17**(3):285-291

[13] Chu TS. An Approximate generalization of the Friis transmission formula. Proceedings of the IEEE. March 1965:296-297

[14] Polk C. Optical Fresnel-region gain of a rectangular aperture. IRE Transactions on Antennas and Propagation. January 1956;**AP-4**:65-69

[15] Bickmore RW, Hansen RC. Antenna power densities in the Fresnel region. Proceedings of the IRE (Correspondence). December 1959;**47**:2119-2120

[16] Iskander M, Hamid M. Numerical solution for the near-field transmission between two H-plane sectoral electromagnetic horns. IEEE Transactions on Antennas and Propagation. January 1976;**AP-24**(1):87-89

[17] Pozar DM. Closed-form approximations for link loss in a UWB radio system using small antennas. IEEE Transactions on Antennas and Propagation. January 2003;**51**(9):2346-2354

[18] Promwong S, Hachitani W, Ching GS, Takada J. Characterization of ultra-wideband antenna with human body. IEEE International Symposium on Communications and Information Technology, ISCIT. July 2004;**2004**

[19] Kim I, Xu S, Rahmat-Samii Y. Generalized correction to the Friis formula: Quick determination of the coupling in the Fresnel region. IET Microwave Antennas And Propagation. Oct. 2013, 7, 1101;**13**:1092

[20] Kerns DM. Plane-wave scattering matrix theory for antenna-antenna interactions. National Bureau of Standards Monograph. 1981;**162**:5-51

[21] Stubenrauch C, Francis M. Comparison of measured and calculated mutual coupling in the near field between microwave antennas. IEEE Transactions on Antennas and Propagation. July 1986;**34**(7):952-955

[22] Yaghjian AD. Efficient computation of antenna coupling and fields within the near-field region. IEEE Transactions on Antennas and Propagation. January 1982;**AP-30**(1):113-128

[23] Akgiray A, Rahmat-Samii Y. Mutual coupling between two arbitrarily oriented and positioned antennas in near- and far-field regions. 2010 URSI International Symposium on Electromagnetic Theory (EMTS); August 2010

[24] Kim I, Rahmat-Samii Y. Calculation of Mutual Coupling between Two Antennas for Satellite Communication. 2016 AP-RASC; August 2016

## Section 3

# Emerging Microwave Devices

Chapter 5

# Microwave Energy and Light Energy Transformation: Methods, Schemes and Designs

Gennadiy Churyumov and Tetyana Frolova

Additional information is available at the end of the chapter

http://dx.doi.org/10.5772/intechopen.73755

## Abstract

Nowadays, electrodeless sulfur lamps with microwave excitation (ESLME) are finding ever-widening application in energy-efficiency lighting systems. A reason of increased interest to these lamps is due to high values of their parameters including a high light flux (120-145 klm), a light intensity (~ 9000 cd), a high value of light output (80-110 lm/W), color rendition coefficient (Ra ~ 90), as well as an application of environmentally friendly materials (argon and sulfur). This chapter presents a novel approach of creating an energy-efficiency lighting source on the basis of the ESLME. For an electrodynamic structure of the lighting system, one can propose to use an optically transparent (mesh) waveguide instead of a microwave cavity. It is shown that the use of proximity of the spectra of optical radiation generated by the sulfur lamp and solar radiation allows more efficiently (in comparison with other light sources) their application as the simulators of sunlight for testing photoelectric converters and solar cells. For extending application of the lighting systems on the basis of the sulfur lamp and further increasing an energy efficiency of these systems, their integration with other electron devices (for example, solar cells) is proposed.

**Keywords:** lighting system, electrodeless sulfur lamp, magnetron, electromagnetic field, microwave excitation

## 1. Introduction

According to the estimates of the International Energy Agency (IEA), almost a fifth of all consumed electricity in the world is spent on lighting. One way to reduce the proportion of consumed electricity and its economical expenditure is the development of new energy-efficient light sources and lighting devices based on them. Requirements for such light sources are dictated by market demands, as well as the development and capabilities of modern technologies. Modern light sources must satisfy a number of parameters, combining high light output and efficiency with the comfort of perceiving generated radiation by the eye (a wide spectrum of radiation and color rendering), durability and environmental friendliness with low cost and a wide range of applications.

It is known that the problem of lighting is being solved by converting electrical energy into optical energy (visible light) with the help of various media and the processes occurring in them: metals and thermal processes (incandescent lamps (IL)), gaseous media and discharge (including plasma) phenomena (fluorescent (FL) and metal halide (MHL) lamps, etc.), as well as semiconductor materials and processes of spontaneous recombination of injected minority carriers (light-emitting diodes (LEDs)). Comparative efficiency of existing light sources is shown in **Figure 1**. It can be seen that the heat sources of light (incandescent lamps) in view of their low efficiency (only 3% of the supplied electric energy is converted into the energy of light waves) are much inferior to discharge lamps and LEDs.

Among the existing promising sources of light, special attention is paid to the development of plasma lighting devices based on the use of an electrodeless sulfur lamp with microwave excitation (ESLME). For the first time, such kind of lamp was presented in 1992 at the VI International Symposium on the Science and Technology of Light Sources in Budapest [1]. Later, based on it, Fusion Lighting Co. company created the lighting system Solar 1000 (1994), as well as its modification Light-drive 1000 (1997). Significant efforts to expand the use of these lamps were made by the Korean company LG Electronics, which, in 2005, held a presentation of the plasma lamp Plasma Lighting System (PLS), and also organized a series production of a number of designs of such light sources in the form of a ceiling lamp and spotlight lamp. In parallel, studies of electrodeless sulfur lamp with microwave excitation

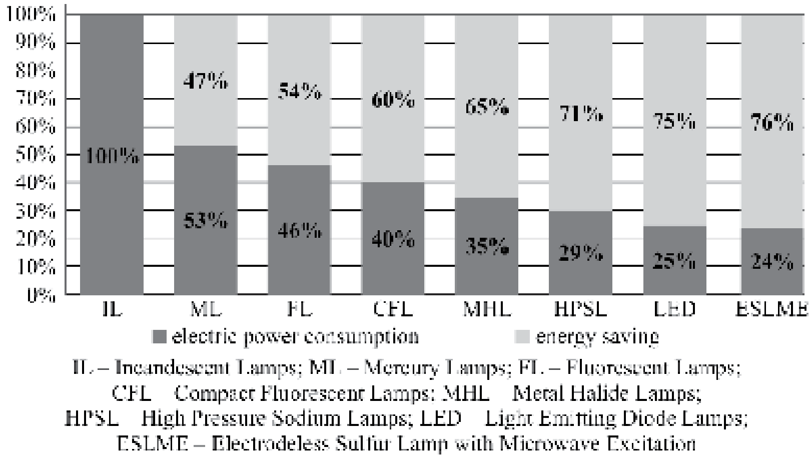

**Figure 1.** Evaluation of the effectiveness of light sources.

were conducted in Europe by Plasma International Group [2]. In 2010, the lighting system AS1300 was presented, consisting of a power supply, a microwave generator (magnetron) and the light module. However, their production was complicated by the complexity of the design and the high cost of the lighting device.

Recently, there have been designs of relatively low-power plasma lighting devices based on light emitting plasma (LEP) lamps with power from ~160 W to 300–400 W, in which solid-state microwave generators are used as an electromagnetic field source [3]. Now, the scope of such lamps is growing: from architectural lighting and street lighting to their application in the automobile industry.

The peculiarity of the topic of plasma light sources with microwave excitation is the long and constant interest to them (more than 25 years), which is expressed in a great number of scientific publications, including monographs, articles, patents obtained in different countries of the world. What is the heightened interest to the lighting systems based on plasma lamps with microwave excitation in? The answer to this question lies in the unique combination of their technical and lighting characteristics and parameters that most fully meet the requirements for light sources formulated above. For example, light generated by these lamps is characterized by high light flux (120–145 klm), light intensity (~9000 cd) and brightness, as well as good light output (80–110 Lm/W). Technical parameters of lighting devices based on plasma light sources with microwave excitation are characterized by relatively low power consumption, a continuous spectrum close to natural (solar) illumination with a color coefficient $R_a > 90$ (with a maximum value of 100) and the ability to control the intensity of light. An important advantage is also their environmental friendliness, which is due to the lack of mercury and the use of environmentally friendly materials—argon and sulfur.

Among the problems that need to be addressed, we should note the insufficiently long service life of magnetrons and the uneven heating of the surface of the lamp bulb, which requires to provide its rotation in the cavity space as well as studies aimed at selecting new materials. This will increase the durability of the lamp, which today does not exceed ~50 thousand hours.

This chapter is organized in five main sections. Section 1 describes the construction of a lighting device based on an electrodeless sulfur lamp with microwave excitation, gives a brief characteristic of its main components and analyzes their operation parameters. Section 2 considers an application of the electrodeless sulfur lamps with microwave excitation as the simulators of solar radiation, gives the comparative characteristics of such lamps with other lighting sources. Section 3 concerns promising directions for practical application of a lighting installation based on an electrodeless sulfur lamp with microwave excitation, in particular, for using in greenhouses. Section 4 presents the construction of the lighting system with the possibility of regenerating the energy of optical radiation into direct current energy for increasing its full efficiency. The main conclusions are formulated in Section 5.

## 2. Principle of operation and designs

A general scheme for the generation of optical radiation in the visible wavelength range (visible light) using plasma illuminating devices based on an electrodeless sulfur lamp with microwave excitation is shown in **Figure 2**. It is necessary to note that these devices use the transformation of electrical energy into the energy of light waves by stages. In the first stage, the secondary power source 1 converts the alternating voltage of 220 V and the frequency of 50 Hz into a constant voltage of 3.8–4.2 kV, which is fed to the anode of the magnetron.

In the second stage, the magnetron generator 2 converts the DC energy into the energy of electromagnetic oscillations. As a result, at the output of the magnetron in the waveguide 4, there are oscillations having the frequency of 2.45 GHz and the output power of about ~900 W. These oscillations excite the electromagnetic field in the electrodynamic structure 5, at the maximum of the electric field of which the sulfur lamp is placed.

At the third stage, physicochemical processes proceed in the inner space of the sulfur lamp under the influence of an electromagnetic field, as a result of which is the generation of optical radiation in the visible wavelength range (380–780 nm). This radiation is focused and output into the free space.

In order to determine the energy efficiency of the lighting system, the power consumed by the magnetron generator from the external (primary) network was investigated. The results of these studies are shown in **Figure 3**. It can be seen that the power consumed from the network by the lighting system is constantly increasing until the appearance of the primary glow of the lamp, which corresponds to 1700–1750 W of power consumption. Thereafter the power consumption from the network is stopped; the energy of the electromagnetic field is absorbed at once by the argon-sulfur mixture. As result, the generation of optical radiation takes place. The lighting system consumes ~2000 W in a stationary mode providing stable light emission.

The main elements of the lighting device and values of its main parameters are shown in **Figure 4**.

An important element of the lighting device on the basis of the sulfur lamp is the construction of an electrodynamic structure, the main purpose of which is to form a special structure of the electromagnetic field required to excite (pump) an electrodeless sulfur lamp. A bulb of the sulfur lamp is placed at the maximum of the electrical component of the electromagnetic field excited in the electrodynamic structure.

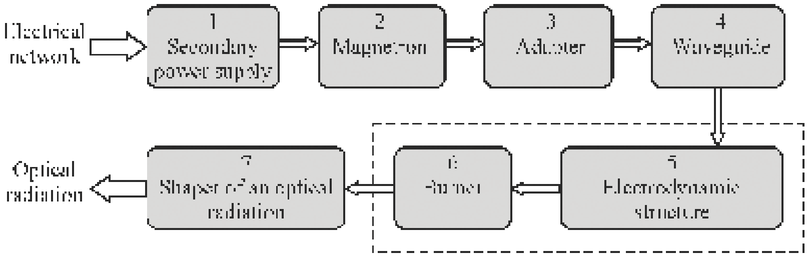

**Figure 2.** General scheme of converting energy in the plasma lighting device.

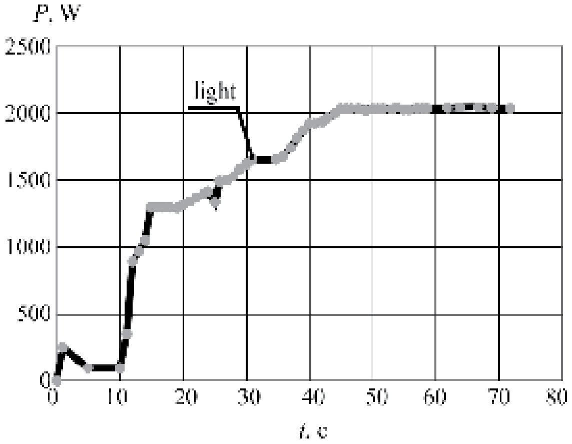

**Figure 3.** Dynamics of the power consumed by the magnetron generator.

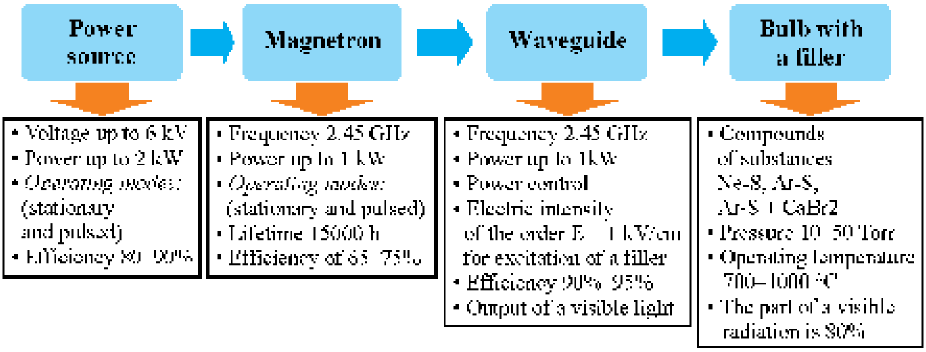

**Figure 4.** List of basic parameters of the elements of the lighting device based on an electrodeless sulfur lamp with microwave excitation.

As an electrodynamic structure, one is usually used optically transparent (mesh) cylindrical microwave cavity, inside of which a quartz bulb of the sulfur lamp is placed [4]. The outside surface of the cavity is done from thin wire and has mesh surface for free passage of optical radiation. A general view of the cavity with a bulb of the sulfur lamp is shown in **Figure 5**.

The main requirement for a resonant method of excitation of the electrodeless sulfur lamp is to maintain a mode of stable oscillations of the electromagnetic field in the cavity (resonance) (for example, for cylindrical cavity, one can use the following modes of oscillations: $TE_{111}$, $TE_{112}$, $TE_{011}$, $TM_{010}$ and $TM_{111}$). The use of a cylindrical cavity allows reasonably simply to hold the sulfur lamp along its longitudinal axis, to ensure its stable rotation for uniform cooling of its surface and thus to select an optimum temperature regime for its operation.

In addition to the resonant method of exciting the sulfur lamp, of great interest is the method enabling to form an electromagnetic field in a waveguide by adding two counter-propagating coherent monochromatic waves $\vec{E}_1$ and $\vec{E}_2$ possessing the identical linear polarization [5]. The general view of the lighting device in which used this excitation method of the sulfur lamp is shown in **Figure 6**.

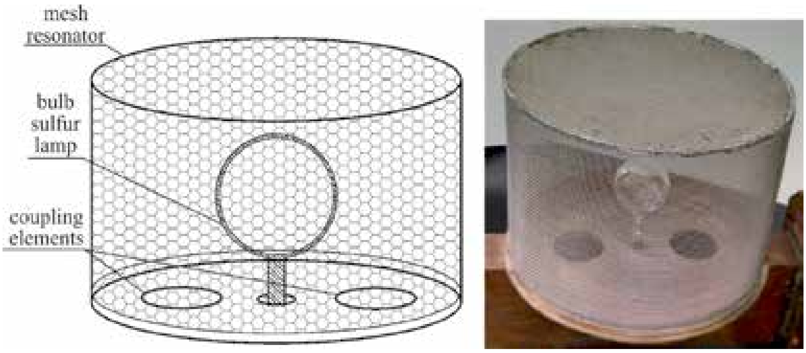

**Figure 5.** General view of the cavity with a sulfur lamp bulb.

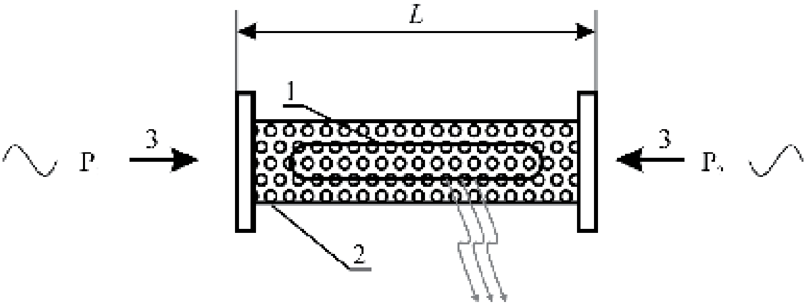

**Figure 6.** Schematic of the sulfur lamp in a waveguide. 1—a bulb of the sulfur lamp; 2—a waveguide; 3—optical radiation (light).

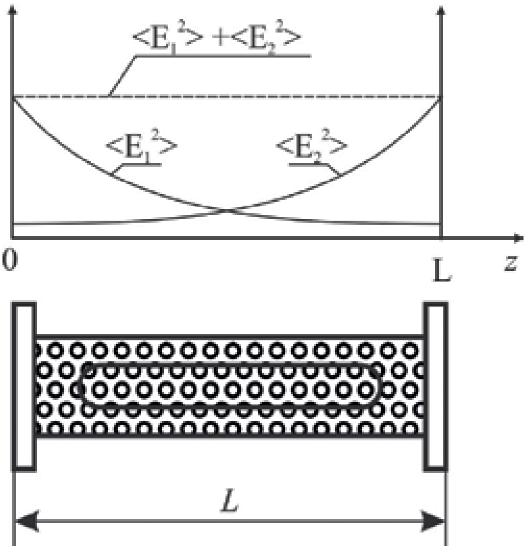

**Figure 7.** The distribution of energies of the electromagnetic waves in a waveguide.

In this case, there is a condition satisfied for the frequencies of these waves to be the same ($\omega_1 = \omega_2 = \omega$) and their propagation constant to be complex and equal to $\gamma = \alpha + j\beta$, where $\alpha$ is the attenuation constant determined by plasma parameters and $\beta$ is the phase constant of the traveling electromagnetic wave. According to the principle of superposition, the intensity of the resultant electromagnetic field is

$$\vec{E} = \vec{E}_1 + \vec{E}_2 \tag{1}$$

Herein consider the energy description of the wave processes and put the first expression (1) in the square. After averaging over time, we finally obtain

$$< E^2 > =< \left(\vec{E}_1 + \vec{E}_2\right)^2 > =< E_1^2 > +< E_1^2 > +2 \cdot < \vec{E}_1 \cdot \vec{E}_2 > \tag{2}$$

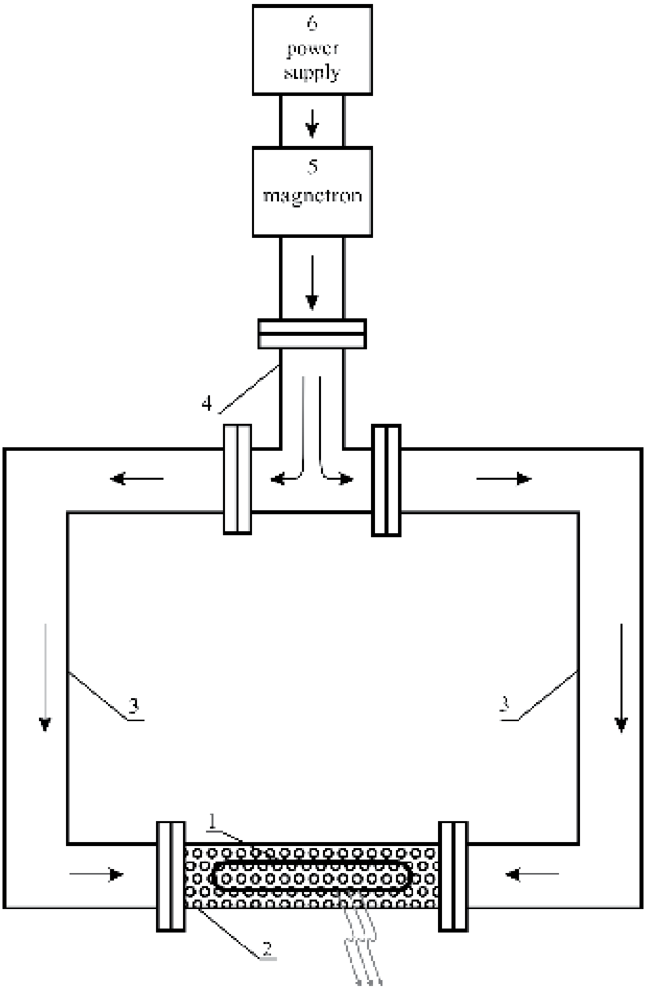

**Figure 8.** Schematic diagram of lighting device based on an electrodeless sulfur lamp with microwave excitation.

In the second expression (2), the total average total energy $< E^2 >$ depends on the value of the interference term $< \vec{E}_1 \cdot \vec{E}_2 >$. In the case when $< \vec{E}_1 \cdot \vec{E}_2 > = 0$ (there is no interference), the total energy in the waveguide is equal to the sum of the energies of the main and counter electromagnetic waves. When the condition is fulfilled, when $< \vec{E}_1 \cdot \vec{E}_2 > \neq 0$, the total energy is not equal to the sum of the energies of the waves running toward each other, but in the waveguide, there is interference of the waves.

Of practical interest for exciting a sulfur lamp in a waveguide causes is the case when the condition $< \vec{E}_1 \cdot \vec{E}_2 > = 0$ is fulfilled. As a result, it is possible to ensure a uniform distribution of the total electromagnetic field in the region of the electrodeless lamp location and a stable gas discharge in the lamp by creating a standing wave in a waveguide of arbitrary length $L$ with optically transparent outside surface (mesh surface).

**Figure 7** shows the distributions of full energy of the electromagnetic waves $< E_1^2 > + < E_2^2 >$, which is introduced from different ends of the waveguide as fundamental $< E_1^2 >$ and counter-propagating $< E_2^2 >$ electromagnetic waves. **Figure 8** schematically presents diagram of lighting devices on the basis of the electrodeless sulfur lamp with microwave excitation.

**Figure 8** demonstrates a schematic diagram of lighting device based on an electrodeless sulfur lamp in the case excitation by adding two counter-propagating coherent monochromatic waves. For this excitation method, an electromagnetic wave is generated by a magnetron 5 and through a waveguide tee 4 through waveguide 3 enters a mesh waveguide 2 within which an electrodeless sulfur lamp 1 is located.

## 3. Simulators of solar radiation

Simulators of solar radiation (SSR) are radiation sources that form and direct a light stream into a fixed area. Such devices can be used for investigating the light characteristics of the photoelectric converter and solar batteries for space and ground applications as well as for carrying out high-temperature studies and tests on the resistance to light effects of various dyes and paint coatings, paper and labels, optical components, etc., [6–8]. The SSRs create a stream of pulsed or continuous optical radiation whose spectral characteristics are close to those of solar radiation. Ideally, the simulators should, with the best approximation, reproduce all the parameters of solar radiation including its spectral composition, flux density, parallelism of rays, stability in time and uniformity of illumination. However, such devices are extremely complex and expensive, demand qualified maintenance, and therefore, as the specific purpose requires, the specialized simulators are created (for example, large SSR for testing space vehicles [7]).

The solar simulators include powerful gas discharge, halogen or other lamps, correcting filters and also serving subsystems. There are quite a lot of familiar artificial light sources used to simulate solar radiation beginning with the carbon arc lamp; with sodium lamps, argon arc lamps, quartz-tungsten halogen lamps, mercury xenon lamps, arc xenon lamps, xenon flash lamps, metal halide lamps, light-emitting diodes and super sources of continuous laser radiation also being applied, but only incandescent and gas-discharge lamps were used in PC studies.

**Figure 9** presents a comparison of the spectral characteristics of extra-atmospheric solar radiation and the simulators of solar radiation on the basis of lamps of the artificial lighting.

For testing the photoelectric converters and solar batteries, as a rule, the incandescent and gas-discharger lamps are applied in the SSRs as the light sources. This is due to the requirements to get the values of parameters such as the identity of the SSRs emission spectrum and spectrum of solar radiation, the color temperature (the color temperature of the extra-atmospheric solar radiation is ~5900 K), the high stability of the radiation flux and the small nonuniformity of energy illumination that determines the adequacy of measuring the parameters of the photoelectric converters and solar cells [8]. At the same time, for example, a necessity of temporal stability of the radiation flux is a significant limiting factor for using a number of arc sources in photovoltaic investigations, although their spectral composition is most consistent with the solar emission under conditions of zero atmospheric mass (AM0). The use of pulse gas-discharge lamps having a satisfactory spectral composition, in addition to the indicated temporary instability associated with the characteristics of their launch systems, requires to use high-speed measuring equipment, which significantly increases the expenses for creating the entire installation. According to the above parameters, the greatest interest can be found in such sources as:

1. The mirror incandescent and quartz halogen lamps that provide a satisfactory spectral composition of the radiation located in the range of 0.4–1.1 μm. These lamps are used in simple SSRs in order to simulate solar radiation for research and technological purposes in the tests of photovoltaic cells.
2. The arc-shaped gas-discharge xenon lamps (including with combined gas filling) for high-quality SSRs, used in precise measurements of the photovoltaic convertors parameters.
3. The most widely used are arc xenon spherical lamps, which have a spectrum very close to the solar one (see **Figure 9**); however, owing to an energy release in the infrared region of its spectrum, it is necessary to use corrective optical filters in the SSRs that use the lamps of this type.

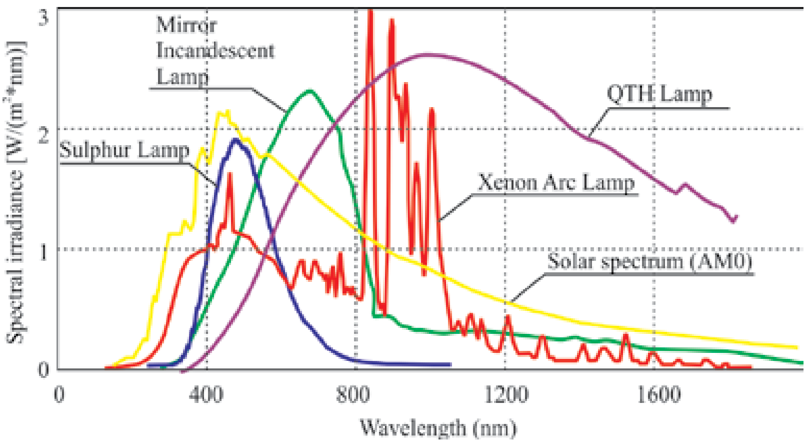

**Figure 9.** Spectral emission curves of the extra-atmospheric solar emission and sources of radiation for SSRs.

| Characteristic | Halogen lamp KG-220-10000 | Gas discharge xenon lamp OSRAM XBO 10000 | Sulfur lamp Plasma-i AS1300 |
|---|---|---|---|
| Power consumption (kW) | 10 | 10 | 1.3 |
| Light output (lm/W) | 26 | 50 | 140 |
| Luminous flux (lm) | 260,000 | 500,000 | 163,000 |
| Color temperature (K) | 3200 | 6000 | 6000 |
| Operating time (h) | 2000 | 500 | 50,000 |

**Table 1.** Characteristics of lamps.

As shown in **Figure 9**, the spectral characteristic of the electrodeless sulfur lamp has a continuous quasisolar spectrum of optical radiation and is very close to the solar spectrum in its visible region. The second advantage of this lamp worth noting is its durability, which is important for its application in the SSRs [9].

**Table 1** demonstrates the comparison of the lamps' characteristics that are most widely used in SSRs, as well as the parameters of the electrodeless sulfur lamp with microwave excitation.

Analyzing the characteristics of the electrodeless sulfur lamp with microwave excitation and comparing them with other light sources that applied in the SSRs, we can say that this lamp can also be successfully used in SSRs enabling to produce not only high-precise measurements of the characteristics of the photovoltaic convertors and solar cells of space application, but also to provide correct modeling of various modes of their operation under laboratory conditions.

## 4. The features of application of the lighting systems in greenhouses

The advent of the energy-efficient light sources on the basis of the electrodeless sulfur lamps with microwave excitation having a wide spectrum of radiation in visible region of electromagnetic spectrum (from 0.38 to 0.78 μm) allows to extend practical application of artificial light sources. In particular, the greatest interest is an application of such lighting sources in modern greenhouse and cattle-breeding farms for raising the level of crop yield and cost saving. On the one hand, the portion of the sectorial electricity consumption in the technological processes of the greenhouse farms using optical radiation is 10–15%, and the losses in them reach to ~40%. To reduce electricity consumption, it is necessary to modernize lighting systems with energy-intensive light sources to modern energy-efficient and economical ones. On the other hand, choosing artificial light sources that must have a certain spectral characteristic, the influence of optical radiation on the efficiency of the main photochemical processes of the plant is first of all taken into account. This is because each pigment has its own individual absorption spectrum and, thereafter, its own spectral characteristic of the light activity of the exciting radiation.

The most important and energy-intensive process is the process of photosynthesis. As shown, an investigation of the spectrum efficiency of the photosynthesis, that was carried out in [10, 11], the leaves of different systematic groups had approximately the same spectra of photosynthesis activity. An average curve of the spectrum of photosynthesis activity of the green leaf is shown in **Figure 10**.

All parts of the solar spectrum are important for the normal outgrowth of plants. More detailed information about results of an impact of the optical radiation having spectrum close to the solar spectrum is shown in **Table 2**.

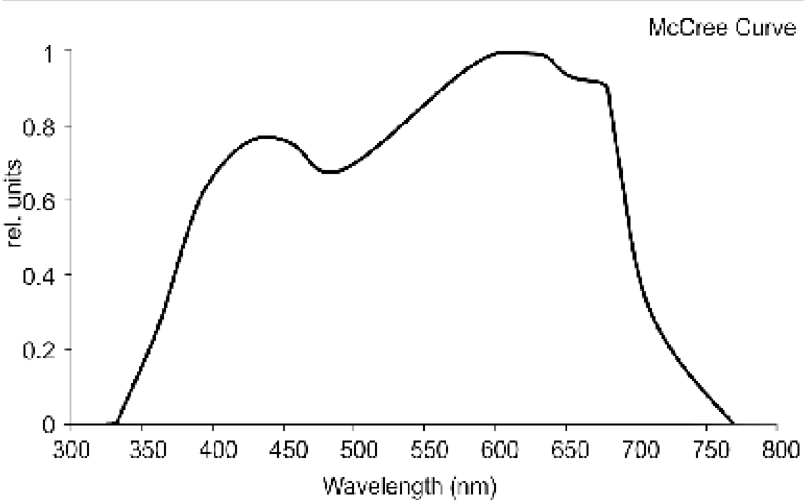

**Figure 10.** Averaged curve of the spectrum of photosynthesis activity of green leaf.

| Wavelength | Effects on plants |
|---|---|
| 280–320 nm | Harmful to plant growth and development. Some plants require a low effect of this spectrum for normal development. |
| 320–400 nm | It influences the regulatory processes in the development of plants. The presence of this range should be a few percent of the radiant flux. |
| 400–500 nm ("blue") | Absorbed by yellow pigments, is the second peak of absorption by chlorophyll, the second peak of photosynthesis. Included to ensure photosynthesis and regulation. However, its excess leads to the formation of stunted plants with thickened stems. |
| 500–600 nm ("green") | It has a high penetrating power, is useful for photosynthesis of optically dense leaves, leaves of lower layers, thick plantings, the smallest physiological reaction. Its surplus leads to the formation of plants with elongated axial organs and thin leaves. |
| 600–700 nm ("red") | The zone of the maximum photosynthetic effect of chlorophyll synthesis, the most important site for the development and regulation of processes. Required in a radiant stream. However, its excess can lead to abnormal development or to the death of the plant. |
| 700–750 nm ("far red") | In general, the effect of stretching the stem, a pronounced regulatory action; a few percent in the radiant flux is sufficient. |

**Table 2.** Effect of the spectrum of optical radiation on plants.

The part of the solar radiation reaching the plants and used for the process of photosynthesis is called photosynthetically active radiation (PAR). PAR is the density of the photosynthetic photon flux, that is, the total number of photons emitted per second in the wavelength range from 400 to 700 nm (μmol $m^{-2}$ $s^{-1}$·). Different plant species, as well as the identical species at different age stages, may have different requirements for the PAR spectrum. To obtain full-fledged plants when growing under artificial light conditions, a certain ratio of energy over the spectrum in used lamps is required: 20–25%—in the blue area (380–490 nm); 20–25%—in the green one (490–600 nm) and 60–50%—in the red one (600–700 nm).

The use of the sources of artificial light in crop production is diverse, but not all of them are effective and safe. The characteristics of widely used lamps in the lighting systems of greenhouses are presented in **Table 3**.

As can be seen, the most perspective lamps for practical application as a modern source of visible radiation are light-emitting diode (LED) lamps and electrodeless sulfur lamps with microwave excitation [12–14]. The LED and sulfur lamps are durable, economical, have a high PAR efficiency (LED: 30–45%, sulfur lamp: 70–80%), are environmentally friendly (do not

| Lamp type | Source of radiation | P, kW | $\tau$, thousand hours | Efficiency PAR, % |
|---|---|---|---|---|
| Fluorescent lamps | FL-40 | 0.04 | 12 | 22 |
| | Osram Fluora | 0.018 | 10 | 20–22 |
| High-pressure mercury lamps | DRLF-400 | 0.4 | 1 | 11 |
| | DRF-1000-04 | 1.0 | 2 | — |
| High-pressure sodium lamps | MASTER SON-T PIA Agro-400 | 0.4 | 17 | 28 |
| | DNaZ-400 | 0.4 | 12 | 26 |
| | DNaZ-600 | 0.6 | 18 | 30 |
| | Sylvania Grolux SHP-TS | 0.25 | 24 | 26–28 |
| | Sylvania Grolux SHP-TS | 0.4 | 24 | 26–28 |
| | MASTER GreenPower | 0.6 | 10 | 26–28 |
| | PLANTASTAR | 0.6 | 12 | 35 |
| Metal halide lamps | Growmaster HIT | 0.25 | 10 | 25 |
| | DRI 2000–6 | 2.0 | 2 | 26 |
| Xenon lamps | DKSTL 10000 | 10.0 | <1 | 12–16 |
| | DKSTV 6000 | 6.0 | <1 | — |
| LED lamps | LED GLOW-E27 | 0.135 | 50 | 20–35 |
| | AGRO-24 | 0.024 | 50 | 30–35 |
| Sulfur lamp | PLS-PSH07 | 0.73 | 60 | 70–80 |

**Table 3.** Characteristics of radiation sources.

contain mercury and do not require disposal). However, there are a number of differences between these lamps that allow them to occupy different fields of application.

The LED lamps are low power and effective when the light flux is about ~100 lm, so they can be used for small rooms. Besides, the LED lamps have a narrow band of optical radiation. In order to obtain the entire range of the visible spectrum, it is necessary to use LEDs with different spectral characteristics, the overall spectrum of which can cover the entire region (380–700 nm). This complicates the technology of manufacturing the LED lamp, since the corresponding currents have to be selected for each LED.

The electrodeless sulfur lamp with microwave excitation, on the contrary, is a powerful light source having a quasisolar emission spectrum with reduced intensity in the region of ultraviolet and infrared radiation (**Figure 11**), and providing light fluxes of ~140 klm, which is three orders of magnitude higher than that of the LEDs as well as color temperature of ~6400 K. Also, the electrodeless sulfur lamp with microwave excitation has the ability to control the radiation power, which allows imitating the modes of sunrise and sunset.

Thus, the modern lighting system under conditions of protected soil (greenhouses) has to economically reduce electricity costs, as well as raise the quantity and quality of the crop yields. The promising sources of artificial lighting are LED and electrodeless sulfur lamps with microwave excitation. The LED lamps are most successfully used in small greenhouses, while the sulfur lamps are suitable for larger greenhouse complexes.

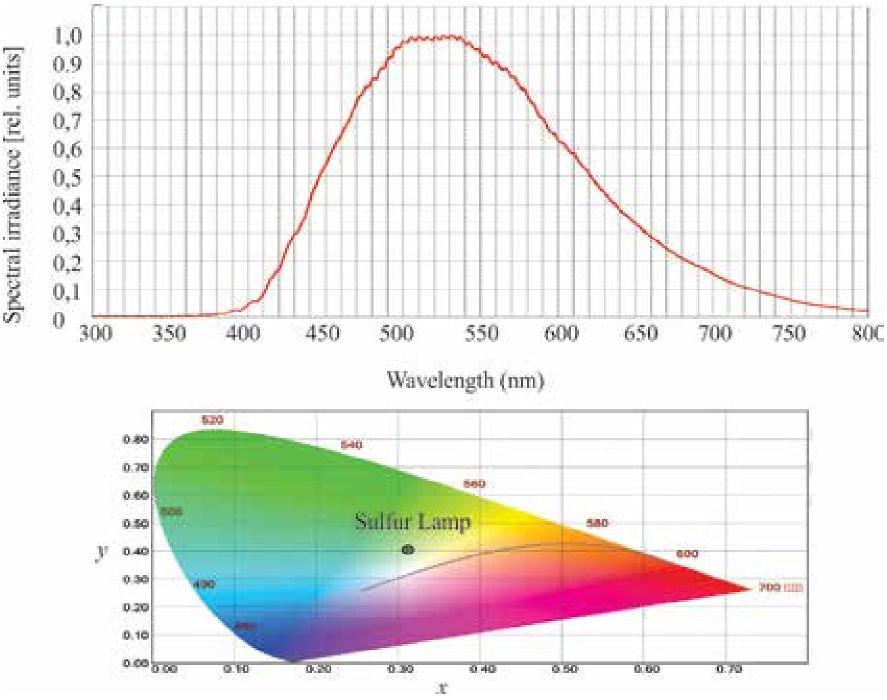

**Figure 11.** Spectral and color characteristics of electrodeless sulfur lamp with microwave excitation.

## 5. The prospects of evolution and application of the lighting systems

Despite the fact that electrodeless sulfur lamps with microwave excitation are still very young, powerful lighting devices based on them have opened a new direction in lighting and found a new application of microwave technologies, which can become even more massive than the use of microwave ovens.

Due to the positive qualities of the lighting characteristics, an area of application of optical radiation sources on the basis of the electrodeless sulfur lamps with microwave excitation is considerably extended [15, 16]. From problems of a lighting technology associated with lighting by a narrow, intense beam of light (spotlamp) or lighting of streets, large areas, tunnels, decorative lighting of interiors, lighting fountains, architectural monuments and other municipal facilities and services, to the integration of lighting systems in various technological processes. The implementation of new technical solutions for the design of lighting systems on the basis of the electrodeless sulfur lamp with microwave excitation has become possible due to the use of its positive qualities and advantages as, for example, the availability of a quasisolar spectrum of radiation with reduced level of radiation in the ultraviolet and infrared regions of an electromagnetic spectrum. This allows apart from the creation of therapeutic and preventive effects on humans and other wildlife to provide also safe working conditions, excluding the destructive, dangerous or other harmful effects of ultraviolet and infrared radiations on illuminated objects and the environment, especially at high illumination levels.

Further progress of the electrodeless sulfur lamps with microwave excitation can be their integration with other electron devices for creating the power energy-efficient lighting systems. As an example of such system, one can be considered a lighting device developed on the basis of linking the electrodeless sulfur lamp with microwave excitation and solar batteries [17]. A general view of block diagram of proposed lighting device is schematically shown in **Figure 12**.

The solar batteries allow to achieve partial regeneration of the electric power, which are connected to the control unit by an illumination system, a store of electric energy and an external power network. The principle of operation of the lighting device on the basis of the electrodeless sulfur lamp with microwave excitation is in employing solar batteries 2 for converting the optical radiation generated by the lighting system 1 directly to the direct current. A control unit of the lighting device controls a process of charge-discharge of the storage batteries 4, and in the case of their low voltage, it switches to an external power network 5.

Taking into account the spectrum of radiation of the sulfur lamp close to a spectrum of natural (solar) radiation as the solar batteries, one can use their standard construction, which usually applies for transformation of natural (solar) light flux in direct current.

The solar batteries are located inside the structure of premises (for example, greenhouses), allowing several advantages: firstly, it facilitates the maintenance of the solar batteries (avoiding snow, rain, hail and other natural phenomena); secondly, with reducing sunny days, the necessity to use artificial light increases (for example, when the plants get supplementary

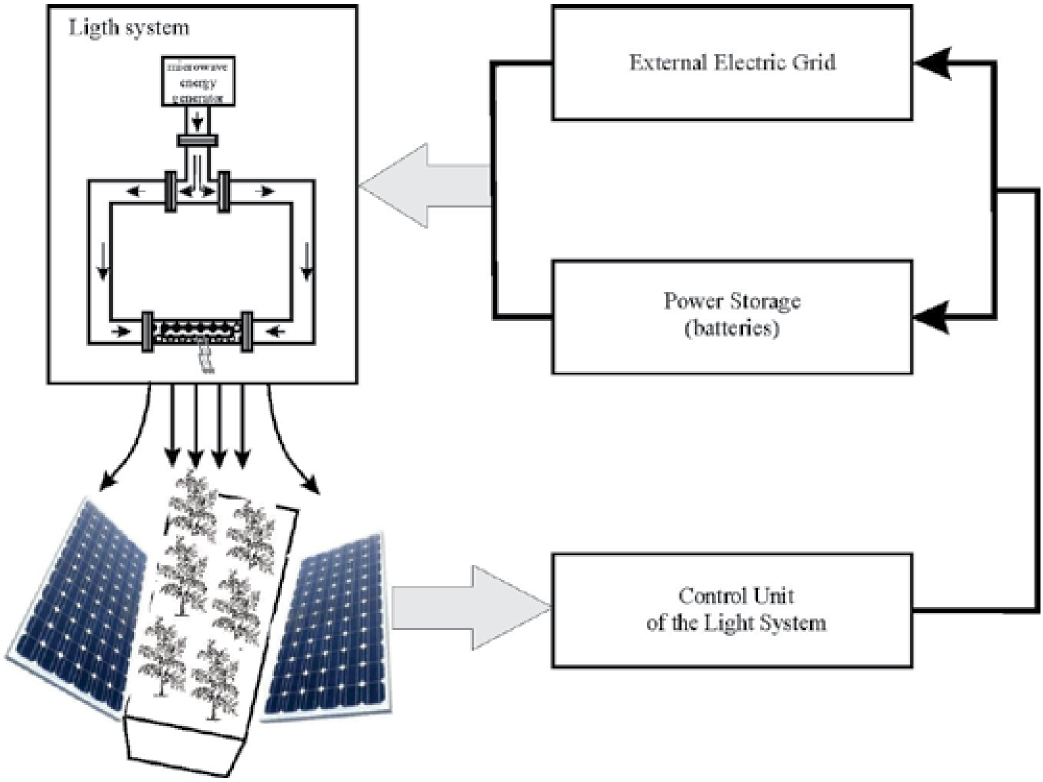

**Figure 12.** General block diagram of a lighting device on the basis of linking an electrodeless sulfur lamp with microwave excitation and solar battery. 1—electrodeless sulfur lamp with microwave excitation; 2—solar batteries; 3—control unit for lighting system; 4—electric power accumulator (storage batteries); 5—external power network.

lighting in greenhouses), but if the lighting devices have a spectrum close to that of the sun, solar batteries can more effectively produce electricity and reduce the prime cost of production as a whole (for example, in a greenhouse farm when growing agricultural products).

Thus, when using a light-emitting device on the basis of an electrodeless sulfur lamp with microwave excitation in combination with solar batteries, one has an additional regeneration of electricity for its further use in the work of both the lighting device itself and other electrical equipment or to feed it into the power network.

## Author details

Gennadiy Churyumov* and Tetyana Frolova

*Address all correspondence to: g.churyumov@ukr.net

Kharkiv National University of Radio Electronics, Ukraine

## References

[1] Doland JT, Ury MG, Wood CH. A novel high efficacy microwave powered light source. In: Proceedings of the Sixth International Symposium on the Science and Technology of Light Sources (Lighting Sciences 6); Budapest. Technical University of Budapest; 1992. pp. 301-302

[2] Plasma International. Plasma-i AS1300 Light Engine [Internet]. 2009. Available from: http://www.plasma-i.com/plasma-i-products.htm [Accessed: 28 September 2017]

[3] LUXIM. Light Emitting Plasma [Internet]. 2015. Available from: http://luxim.resilient.lighting/ [Accessed: 28 September 2017]

[4] Dolan JT, Ury MG, Wood CH. Lamp Including Sulfur. Patent No. 5404076 USA, H01J 17/20, H01J 61/12, H01J 61/18: April 4, 1995. p. 9

[5] Frolova TI, Churyumov GI. Sposib zbudzhennya bezelektrodnoyi NVCH lampy. Patent No. 94842 Ukraine: 2014. p. 4

[6] Mann AE, Michael Dubey. Solar Simulators. Space/Aeronautics; 1962. pp. 67-70

[7] Krat S, Khristich V, Sharov A. Large solar radiation simulators for thermal vacuum tests of the non-container spacecraft. Photonics. 2014;**2**(44):12-19

[8] Esen V, Sağlam Ş, Oral B. Light sources of solar simulators for photovoltaic devices: A review. Renewable and Sustainable Energy Reviews. 2017;**77**:1240-1250. DOI: 10.1016/j.rser.2017.03.062

[9] Frolova TI, Frolov VV, Tereshchenko VV. Immitatory solnechnogo izlucheniya na osnove sernoy lampy. In: Funktsional'naya baza nanoelektroniki: IV mezhdunar. nauchn. konf.; 30 sent. Okt 3, 2011; Katsiveli. Kharkiv: KhNURE; 2011. pp. 92-94

[10] McCree KJ. The action spectrum, absorptance and quantum yield of photosynthesis in crop plants. Agricultural Meteorology. 1972;**9**:191-216. DOI: 10.1016/0002-1571(71)90022-7

[11] Inada K. Spectral dependence of photosynthesis in crop plants. Acta Horticulturae. 1978; **87**:177-184

[12] Hogewoning SW, Douwstra P, Trouwborst G, Ieperen W v, Harbinson J. An artificial solar spectrum substantially alters plant development compared with usual climate room irradiance spectra. Journal of Experimental Botany. 2010;**61**(5):1267-1276. DOI: 10.1093/jxb/erq005

[13] Frolova TI, Churyumov GI. Perspektivy razvitiya vysokoeffektivnykh istochnikov sveta: ot teorii k real'nym osvetitel'nym sistemam. Prikladnaya radioelektronika. 2014;**13**(2): 42-53. DOI: http://nbuv.gov.ua/UJRN/Prre_2014_13_2_7

[14] Bula RJ, Morrow RC, Tibbitts TW, Barta DJ. Light-emitting diodes as a radiation source for plants. Hortscience. 1991;**26**(2):203-205

[15] Gutzeit EM. Electrodeless light sources employing high-frequency and microwave electromagnetic energy. Journal of Communications Technology and Electronics. 2003; **48**(1):1-30

[16] Shlifer ED. Bezelektrodnyye SVCH-razryadnyye istochniki sveta. Perspektivy prosmatrivayutsya. Elektronika: Nauka, Tekhnologiya Biznes. 2002;**3**:52-55

[17] Frolova TI, Churyumov GI. Osvitlyuval'nyy prystriy na osnovi bezelektrodnoyi sirchanoyi lampy z NVCH zbudzhennyam. Patent No. u 2017 08829 Ukraine; Sep 4, 2017. p. 4

# Additive Manufacturing of 3D Printed Microwave Passive Components

Irene O. Saracho-Pantoja, José R. Montejo-Garai,
Jorge A. Ruiz-Cruz and Jesús M. Rebollar

Additional information is available at the end of the chapter

http://dx.doi.org/10.5772/intechopen.74275

## Abstract

This chapter presents a comprehensive analysis of the applications of a low-cost version of additive manufacturing (AM). The technique called Fused Filament Fabrication (FFF), which makes use of plastic as raw material, is explained in the context of its applications to the microwave waveguide engineering field. The main advantages of this technology include the promptness to print models, the variety of feasible geometries, and specially the reduced cost. The main limitations are also explained. Two important applications are considered: (1) rapid prototyping of complex devices and (2) manufacturing of fully functional devices. The former is relevant to get a more realistic perspective of the actual geometry in computer-aided designs, as shown in several examples. It also helps to forecast possible issues in the fabrication process that the computer sometimes fails to detect at the design stage. In the latter case (2), the subsequent and necessary metallization of plastic devices is also addressed. Several examples of state-of-the-art passive waveguide devices are presented, including waveguide filters, a diplexer, a branch-line coupler, a load or horn antennas, which have been printed, metallized, and measured. The results show the potential of three-dimensional (3D) printing and provide a different insight into this innovative technology.

**Keywords:** additive manufacturing, 3D printing, waveguide, prototyping, filter, diplexer, coupler, horn antennas

## 1. Introduction

The idea of Additive Manufacturing (AM) has turned out to be a great disruption in the recent years. In this new technological paradigm where speed, adaptability, or sustainability plays a very important role, the use of new materials and manufacturing techniques is gaining momentum. Consequently, the idea of three-dimensional (3D) printing has affected many different fields in ways previously unconceivable, and microwave engineering is not an exception.

Some of the main advantages of 3D printing include the promptness to manufacture a model, the ability to produce personalized items, the great variety of available geometries, or the fast and clearer communication of new ideas. These statements may sound quite unspecific, but they are indeed true for both an engineering company and a jewelry designer. The goal of this chapter is to narrow down those general ideas of how useful 3D printing may be in the context of the microwave engineering field.

Moreover, there is one important issue that has not been mentioned yet: the cost. One of the causes of the versatility of 3D printing is that it can be applied to almost any material, with the correspondent cost variation. However, in this work, the technology is addressed from an extreme low-cost perspective, aiming to reach a large audience.

In brief, the application of low-cost AM to the microwave engineering field is explained in detail through several real-world examples—designed, manufactured, and measured devices—which have been previously reported in the literature. Consequently, the down-to-earth advantages of this technology are not only highlighted but the drawbacks are also analyzed. The aim is to help students and radio frequency (RF) and microwave engineers to discover the full potential of the AM directly applied to their area of expertise.

### 1.1. What is low-cost additive manufacturing? Historical background

It is not possible to address AM as neither single nor simple concept. As a general description, it may be explained as the addition of materials in layers in order to build an object from a digital model [1]. This object can be made from many different raw materials—from wood or metal to food or human tissues—and therefore a great range of physical processes or technologies are involved. For example, the materials or techniques used to 3D print jewelry may not be the same as the ones used in the architectural field or for biological research. This intuitive idea has been recently standardized [2] leading to seven categories of AM processes [3]:

- Binder jetting: A liquid bending agent is deposited to join powder particles.
- Powder bed fusion: Material powder is melted and fused together by using a laser or electron beam.
- Directed energy deposition: The material—in wire or powder form—is extruded from a nozzle and melted with a laser or electron beam upon deposition.
- Material extrusion: Melted material is extruded from a nozzle and fused together upon deposition.
- Material jetting: Droplets of viscous material (polymers, waxes) are deposited, solidified, and then cured with ultra-violet (UV) light.
- Vat photopolymerization: A vat of resin is selectively hardened with UV light.
- Sheet lamination: Sheets of metal are bound together by using adhesive or welding.

Roughly, there are four main technologies: to extrude, to compact powder, to selectively solidify the material, or to use lamination techniques. The detailed differences and applications of each of them are beyond the scope of this chapter. However, as in any engineering process, cost is a key factor in order to decide which AM process is more relevant in each case.

Low-cost 3D printing is usually related to thermoplastic for obtaining objects through "material extrusion." A common name for this technique is Fused Filament Fabrication (FFF), and it is the most popular technology chosen by private end users.

The 3D printing industry has been in the stage of development for several decades. It started in the late 1980s, yet the technology was only available to professional levels because of the high cost of the equipment [4]. However, the real trigger in the development of low-cost 3D printing is caused by the expiration of FFF patents in 2009 and the rise of the open-source movement, involving both hardware and software. The do-it-yourself philosophy has become very popular and has created the "maker" culture in this technological field. As a final consequence, 3D printing is now available and affordable to masses: having your own 3D printer is worth a few hundred dollars.

Apart from the 3D printer itself, other components are needed likewise low cost. The machine works by extruding a heated thermoplastic filament from a nozzle. The plastic is usually acrylonitrile-butadiene-styrene (ABS) or polylactic acid (PLA), both provided in spools [1]. As a reference, the latter may cost approximately 25 $/kg. Finally, the software needed to process the digital models is open source [5].

Regarding the plastic choice, both ABS and PLA present different characteristics. The latter is the one used to manufacture the devices presented in this work, and it is also the preferred option for low-cost 3D printers because of its bioorganic origin. PLA does not usually require a heated bed print and presents less warping than ABS, apart from being more environmentally friendly.

### 1.2. Advantages and applications of low-cost AM in microwave engineering

As it has been previously mentioned, 3D printing and its low-cost version are used in a great variety of fields. In addition, it is interesting to analyze the main uses of this technology for the microwave engineer to get the maximum throughput.

In this work, when microwave or RF engineering is considered, it is mainly referred to passive waveguide devices. In this way, two main applications can be distinguished: prototyping and manufacturing. Since the material used to build the device is plastic, a subsequent metallization process may be conducted. In the former case, the device would remain as a model; whereas in the latter it can be used for real applications.

When 3D printing for prototyping is considered, the main goal is to reach a clearer communication in the discussion between the microwave designer and the professionals of the manufacturing workshop. There is a saying that an image is worth a thousand words, with the AM taking this a step further by considering that a 3D physical model is worth a thousand 2D representation. The microwave engineer may sometimes design some difficult geometries and then another party may take care of the manufacturing. If an initial prototype is available for discussion, it may be easier for the mechanical engineer to identify the main structural challenges as well as having a global vision of the whole device itself. The engineer may also realize that some parts of the design could be improved or modified. Of course, computational 3D models are normally used, but with low-cost 3D printing, a full-scale model is available almost instantly. AM becomes a tool to gain a deeper understanding throughout the design process.

Besides, the availability of real models may be useful for another application full of potential: education [6, 7]. Models provide outstanding intuition without replacing theoretical results. Students have started to use computational tools to complement their academic training, and AM brings that to a whole new level. After studying the theory, the students are capable of handling state-of-the-art filters, antennas, orthogonal mode transducers (OMTs), or power combiners in the laboratory.

For these prototyping applications, the designed devices are not intended to work, that is, the model can remain a dummy with no further utility. However, in order to obtain a device with proper electrical response, it is mandatory to include metal in the process. When metal is the raw material used to 3D print the model, many advantages of AM appear more evident. For instance, unfeasible geometries by traditional means such as computer numerical control (CNC) milling may be achieved. Besides, there is a saving in consumed material, making the whole process more sustainable. Yet to combine those advantages with plastic 3D printing represents a bigger challenge, that is, low-cost.

Metallization of the plastic device may be done by different means, but the specific approach followed in this work is metallic paint. For some devices, the results show that it is acceptable to use the final devices in real communication systems, whereas others eventually require some modifications. In spite of that, they both open up another possibility within the educational field. If prototyping offers the possibility of *touching* microwave devices, manufacturing allows performing a full design process at a bachelor or master's level.

In RF courses, the first step is usually to acquire a theoretical background. In the best-case scenario, students are later asked to design a device that must fulfill certain specifications and obtain a simulated response through software tools. However, experimental validation is sometimes avoided or limited due to the lack of resources. Consequently, students may measure or test specific devices intended for that use but very rarely do they test what they have done themselves. Low-cost 3D printing changes this paradigm and allows students to conduct a full design process: from the initial design stage to the measurement of their own models [6]. The physical structure may be printed in few hours once the design is completed. Therefore, it is possible to verify whether the real-measured response matches the expected one, causing a deeper engagement in the courses. Another advantage is that each student may design their own model with different specifications, as well as facing the real challenges of real-life manufacturing. Fabrication entails restrictions that must be borne in mind: students must design a physically achievable device, something that may be forgotten when the design process ends with a simulated response in the computer.

Finally, the common denominator in both cases is that the low-cost approach makes the technology accessible to all kinds of engineering environments: from individuals to small research groups instead of just large companies or high-level laboratories. The prototypes or functional devices are promptly manufactured within hours after being designed for less than 25 $ each.

## 2. Prototyping

Prototyping is one of the applications of additive manufacturing in many diverse fields, including also microwave engineering. In recent years, there has been a notorious increase in the amount and quality of computer-aided design (CAD) tools for design and visualization purposes. These developments are of great help for designers and engineers, but, at the end, physical realization gives an irreplaceable insight: this is the context where AM plays a key role. Moreover, when the design process moves to the manufacturing stage, it is mandatory to pay special attention to mechanical and structural issues.

Since the printed prototypes are only relevant from a mechanical perspective, plastic is a suitable material with no further metallization needed. The manufactured geometries are feasible for real devices thanks to complex and expensive fabrication techniques such as CNC milling. However, FFF allows obtaining a model in few hours.

**Figures 1** and **2** represent two examples of prototypes of state-of-the-art waveguide devices. They are Ku-band power combiners with 8 and 16 ports, respectively. The top part in **Figure 2** is a circular $TE_{01}$ mode converter which has already been presented in [8] together with its printed model to forecast any problems in the ongoing CNC milling fabrication process.

**Figure 3** shows a model of a diplexer intended to work in Ka-band made out of two band-pass filters with elliptic response. This kind of design is suitable for satellite applications due to its outstanding electric performance and robust and compact structure [9].

Finally, other manufacturing techniques may also benefit from low-cost additive manufacturing. One example appears in **Figure 4**, where the different pieces of an ortho-mode transducer (OMT) based on the turnstile junction, working in W-band are presented, allowing to anticipate and to discuss any issue in the final manufacturing. In this case, the final fabrication technology was layered SU-8 photoresist, and the plastic pieces allow seeing the different layers in which the structure is divided.

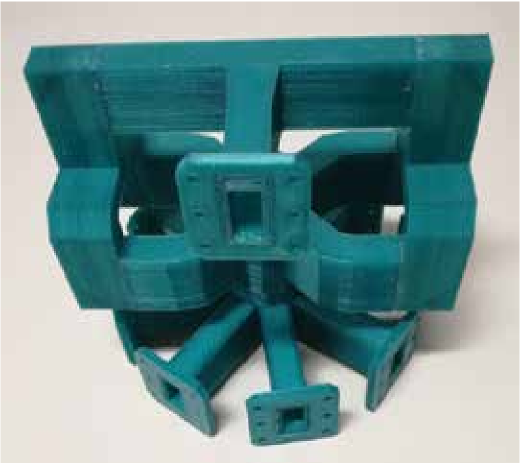

**Figure 1.** 3D–printed prototype of a Ku-band 8-port power combiner.

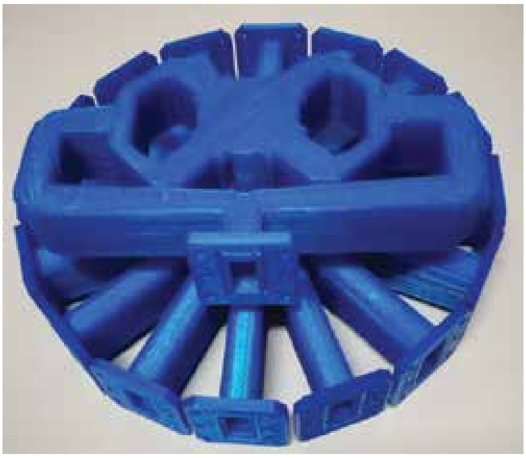

**Figure 2.** 3D–printed prototype of a Ku-band 16-port power combiner.

**Figure 3.** Printed model of a Ka-band diplexer with two band-pass filters with elliptical response.

**Figure 4.** Printed layers of an ortho-mode transducer (OMT) based on turnstile junction, working in W-band.

In all these cases, very complex designs with reduced price are rapidly available. Some geometries involve many difficult details, even with the available visualization tools nowadays. These cases are therefore good examples of how 3D printing can help to reach a clearer communication between the different teams involved in an engineering product.

## 3. Manufacturing of waveguide devices

After addressing the first application of low-cost 3D printing in the microwave field, another step is introduced. Now, the printed devices are meant to be measured, and therefore, they have to be metallized first. These two requirements set a frame of limitations, which confine the usability of this technology—at least the low-cost version—and are crucial to understand the electrical responses of the devices presented later in this chapter.

First, the three main restrictions are thoroughly explained. Then, a full set of waveguide devices and two horn antennas are presented. They cover from relatively simple straight sections to fully operational devices such as a waveguide diplexer with challenging specifications. They try to push low-cost 3D printing to its limits, also in terms of frequency and bandwidth.

### 3.1. Limitations of low-cost 3D printing process

The main drawbacks of low-cost 3D printing when manufacturing fully functional devices may be summarized as follows: the working frequency, the metallization process, and the structural issues.

#### *3.1.1. Dimensions*

The first one is intrinsically related to the dimensions of the design and the printing accuracy, that is, the layer height. In a normal low-cost machine, the minimum value is ±0.1 mm. It marks the minimum variation of dimensions that can be built, and, therefore, it establishes an upper limit for the working frequency. It is unrealistic to print devices with working band above 15 GHz. Besides this limit, this issue becomes even more evident when dealing with sensitive devices, where a tiny variation of dimensions leads to a very different electrical behavior.

Printing accuracy is also related to the achievable matching losses in a waveguide device. In an experiment performed with printed 50-mm-long WR75 waveguide sections such as the one in **Figure 5**, the matching level is similar for the waveguides regardless of the paint they are covered with: around 20–25 dB in Ku band, as it appears in **Figure 6**.

All things considered, this limitation is probably the easiest to deal with. There is a quite clear limit regarding frequency, and computational design tools are of great help to account for precision. That means that before obtaining the final model of the device, all geometrical dimensions should have the number of decimal digits in agreement with the printing accuracy.

#### *3.1.2. Metallization*

The second drawback includes all the aspects related to the metallization process. As it has been mentioned, it is imperative to cover the inner surface of the printed waveguide devices with metal paint, in order to confine the electromagnetic energy within the structures. Consequently, the devices cannot be printed as a single piece, as it would be desirable, but they have to be printed in separate parts instead. Their inner part must be accessible for painting and that may limit the feasible geometries in some cases. This may be seen as damaging one of the biggest advantages of 3D printing, yet it is a trade-off and from this perspective the total cost is very low.

**Figure 5.** 3D printed WR75 waveguide section ready to be measured.

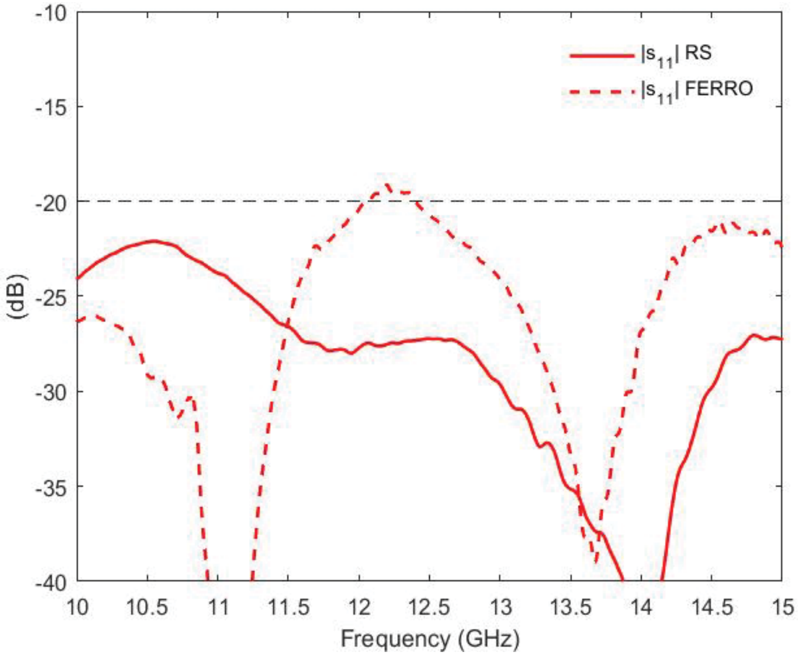

**Figure 6.** Measured matching level of 3D printed 50-mm-long WR75 waveguide sections covered with RS and Ferro paint.

Besides this trade-off, it is crucial to find a metal-loaded paint with good quality and a reasonable price. It is a hard task, since the obtained conductivity is not very high and depends on frequency. It causes relevant insertion losses which may clearly deteriorate and even *hide* narrow-band responses. For this work, several commercial paints were tested before manufacturing complex devices. The first one was a repair kit for rear windscreen defoggers [10]. The conductivity value was claimed to be high due to the silver content, yet no specific value was provided. Conducted tests showed high insertion losses, and thus the paint was left out.

Two other metal paints with silver content, supplied by Ferro [11] and RS [12], were considered. In both cases, the conductivity was provided, although the value given was for DC. In the same experiment with the waveguide sections, insertion losses were also analyzed. Their provided nominal conductivity was $\sigma = 10^5$ S/m (RS) and $\sigma = 1.6–5\cdot10^6$ S/m (Ferro), which is one or two orders of magnitude below silver conductivity itself ($\sigma = 6.3\cdot10^7$ S/m). However, the effective conductivity is better for RS paint in Ku band, as shown in **Figure 7**. Such results are critical and RS paint is the natural choice to metallize 3D–printed devices. Its price was approximately 60 $/20 g at the time of the experiment. The effective conductivity used in subsequent simulations was $\sigma = 5\cdot10^4$ S/m.

Metallization was performed by hand and each section was painted twice to ensure a homogeneous layer with no air gaps or drops of paint remaining. In fact, conductivity is not the only issue affecting the response. That may explain why the effective conductivity of RS paint is higher than Ferro, although for nominal values it is the other way around. The density of the paint may play an important role as well. For instance, the Ferro paint is not very thick and therefore it may not be well absorbed by the plastic, resulting in a defective metallization process.

The problems derived from the metallization process are not only related to the paint itself. Since the waveguide structures need to be split, the eventual alignment turns out to be critical. The different parts must be joined back together and glued, since any misalignment would cause a significant variation in the electrical response. Extra parts such as fastening pieces may also been used, as mentioned later in the chapter.

Finally, the influence of the plastic spools may be worth mentioning, since the quality of the plastic affects how well the paint is slicked to the plastic. Plastic characteristics may vary from one supplier

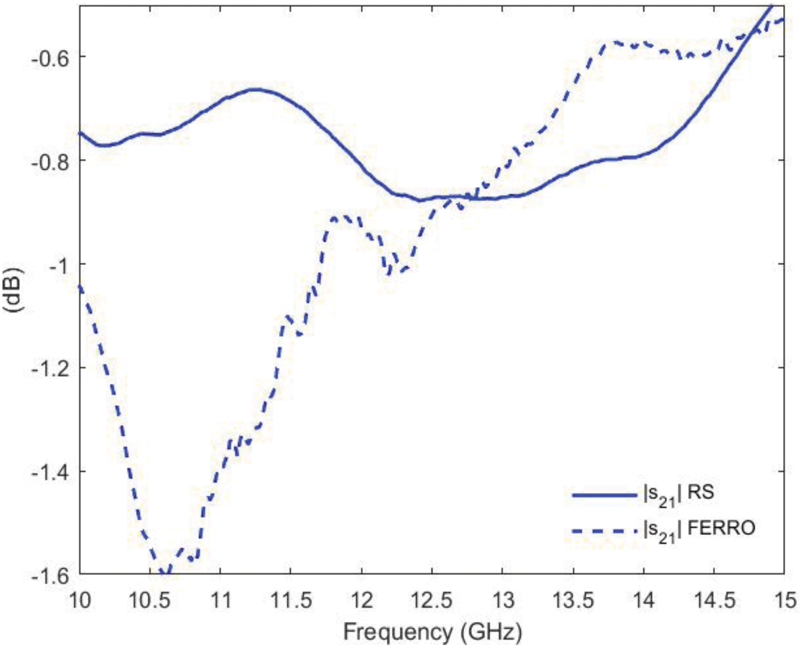

**Figure 7.** Measured insertion losses of 3D printed 50-mm-long WR75 waveguides painted with RS and Ferro paint.

to another, and even between spools or colors. Consequently, the plastic may absorb the paint differently. The behavior with humidity or temperature variations may vary as well. As a reasonable practice, it is recommended to maintain the material supplier in order to try to reduce such variations.

### *3.1.3. Structure*

This last limitation is more specific for passive waveguide devices such as filters, diplexers, or couplers. Its effect in the horn antennas presented later is much less important.

Since the structures must be split into pieces to metallize them, two main possible divisions are considered: E-plane or H-plane (**Figure 8**) [13]. The former consists in splitting the structure into two identical halves, following the so-called E-plane approach (cutting in the plane where the E-field is maximum), whereas the latter separates the structure in body and cover. Trying to determine the best approach, some experiments were conducted.

**Figure 9** shows the insertion-loss level of 40-mm-long WR75 waveguide sections covered with the same paint. The H-plane structure presents higher losses. That may be explained by considering problems assembling the structure or misalignments. H-plane structures are more sensitive

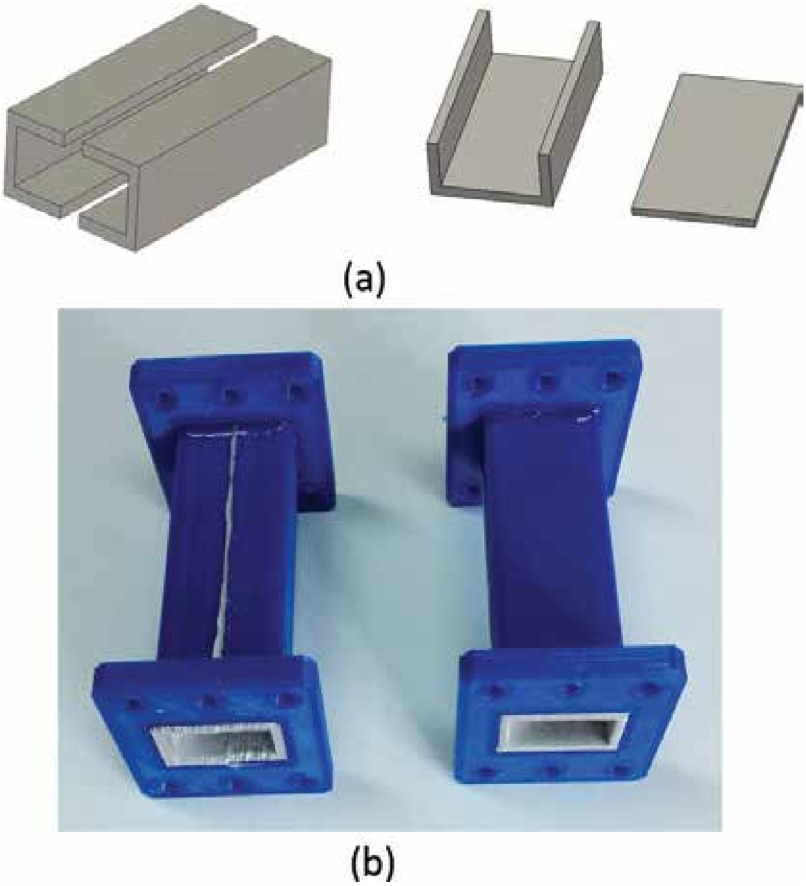

**Figure 8.** (a) CAD model and (b) 3D printed E-plane and H-plane structures at left and right, respectively.

to this kind of issues, since a perfect contact between the body and the cover must be reached. In traditional mechanizing, screws are used to tackle this problem, but a tiny air gap in 3D–printed designs is almost unavoidable. Besides this, there might be a bending of the top layer.

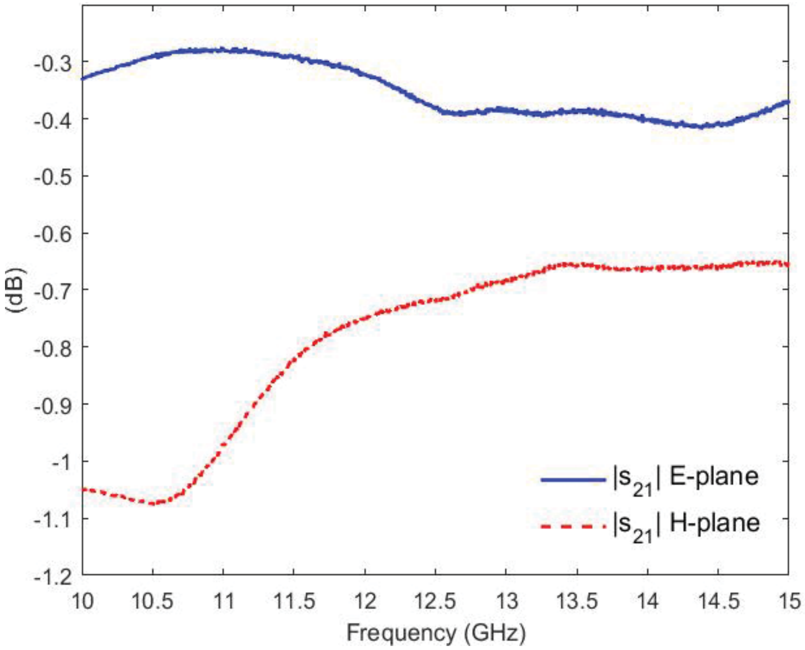

**Figure 9.** Insertion losses for WR75 waveguide sections (E-plane and H-plane).

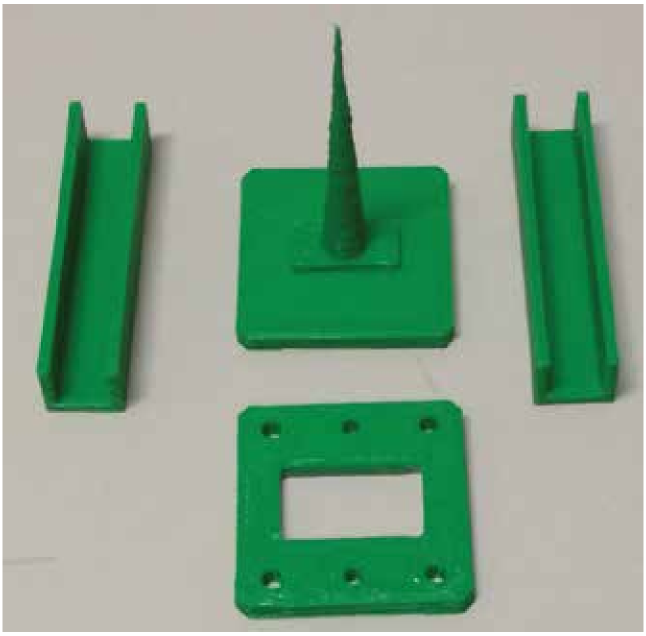

**Figure 10.** PLA-printed pieces of the waveguide load before being covered with the graphite powder.

On the other hand, E-plane structures show lower losses since they do not depend that much on the assembling. This is due to the absence of currents along the cutting plane. Consequently, dividing the structure into two halves is the best way to proceed and that is how it has been done in this work.

### 3.2. 3D printed devices: experimental results

#### *3.2.1. Waveguide load*

The first waveguide structure to be characterized is a load for Ku-band. It is split in several pieces, printed in plastic, and subsequently covered in Graphite 33 [14], a graphite lacquer for conductive coatings which shows a good electrical conductivity due to the high level of pure and fine graphite powder. Both inner and outer surfaces are coated. The two stages of the manufacturing process appear in **Figure 10** and **Figure 11**. The former shows the different parts of the load before coating them with the graphite powder, whereas the measurement setup with the assembled load appears in the latter.

The matching response is shown in **Figure 12**, with a matching level better than 21 dB in the whole band. Such result is equivalent to some commercial short waveguide loads working in the same band [15].

#### *3.2.2. Waveguide section*

After the loads, a simple two-port device is tested: a straight waveguide section. Although some of them were tested to decide between the different paints or the most suitable way to cut the structure, the S-parameters of a 3D–printed 50-mm-long WR75 waveguide section are presented in **Figure 13**. Perhaps a remarkable fact is the lack of symmetry between S11 and S22, which is due to the inherent asymmetries associated to the 3D–printing process. However, the matching level agrees with previously obtained values, as well as the insertion losses in Ku band.

**Figure 11.** Measurement setup of the waveguide load.

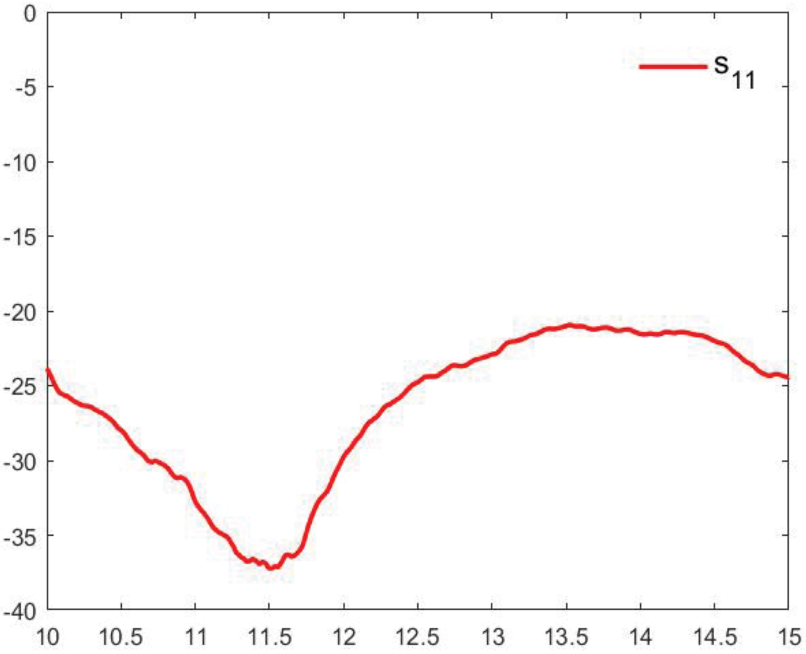

**Figure 12.** Matching response of the 3D printed load.

### *3.2.3. Filter: low-pass, high-pass, band-pass*

After having analyzed simple waveguide elements such as the load or the straight section, a very challenging passive device is addressed. Filters are key components in the microwave field and their main purpose is to allow a good transmission of desired signals while rejecting the unwanted ones. Depending on their response, they are classified in low-pass, high-pass, band-pass or band-stop filters. In this work, examples of the first three groups are implemented using 3D–printed rectangular waveguides. The results were first presented in [6, 7, 16, 17]. For these and all the other passive devices, the mode-matching technique [18] has been the design tool, whereas Microwave Studio CST [19] has allowed performing the simulations including manufacturing effects.

### *3.2.3.1. Low-pass filter*

Low-pass filters implemented in waveguide technology are based on corrugated structures. The different impedances caused by the varying height of the sections lead to rejection at higher frequencies. In this case, an eight-order low-pass filter with four corrugations has been designed and presented in detail in [6, 17]. It is an E-plane structure. The working bandwidth is from 11.9 GHz to 12.2 GHz. Specifications include 28-dB matching level and rejection higher than 50 dB from 13.75 GHz to 14 GHz. These requirement levels and the frequency bands are typical of satellite telecommunication systems in Ku band and therefore very demanding for low-cost 3D printing technology.

The printed parts of the filter and the assembled structure are presented in **Figure 14**. The most important part of this device is the corrugation width. In this case, it is set to 2.5 mm considering

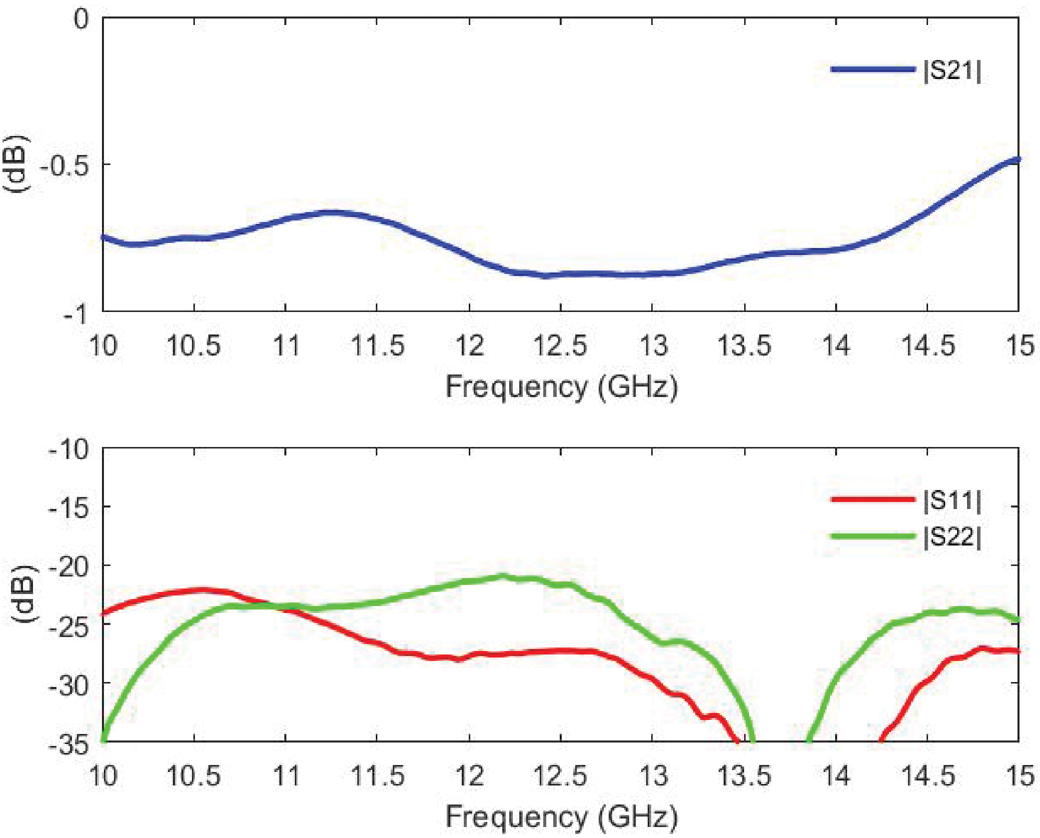

**Figure 13.** (a) Reflection and (b) transmission S-parameters for a printed WR75 waveguide section.

the printer accuracy. Besides this, it has been possible to avoid input/output transformers, that is, the filter height corresponds to the standard WR75. Consequently, insertion losses have been reduced as much as possible. Finally, it is very important to reach a perfect alignment.

The measurement setup is presented in **Figure 15** and the results are shown in **Figure 16**. The main characteristic of the measured response is that it is wider than the simulated one. In addition, the matching level does not reach the intended level, yet it agrees with the aforementioned limits of the technology and proves how unrealistic it is to try to get more than 22–25 dB return loss in Ku band with low-cost additive manufacturing.

The rejection response differs from the expected one as well. Since the corrugations are the parts causing the reflection, it may be inferred that some modifications should be introduced in future designs. For instance, wider corrugations would allow a better metallization process and therefore a potentially better response. However, it would cause a larger structure with more sections and more insertion losses, which are now around 1.8 dB.

### 3.2.3.2. *High-pass filter*

The next design was also included in [6, 17]. It is a high-pass filter based on a waveguide section under cutoff with stepped taper for matching at both input and output ports. The requirements

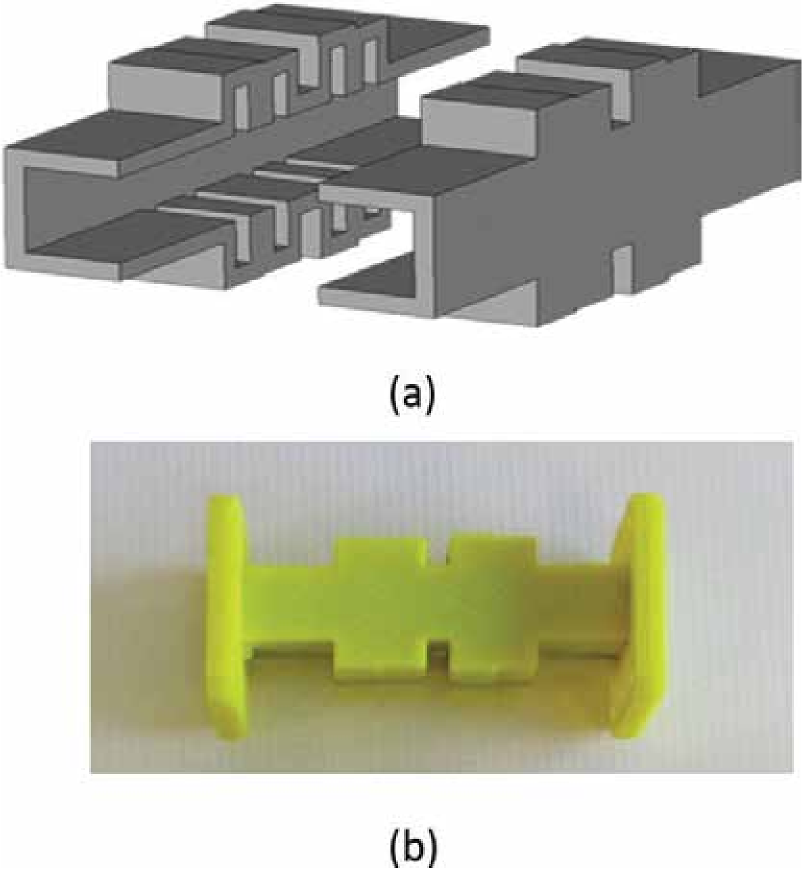

**Figure 14.** (a) CAD pieces and (b) assembled low-pass filter.

in terms of return-loss and rejection level are the same as in the low-pass filter but for opposite bands, that is, return loss of 28 dB between 13.75 GHz and 14 GHz and rejection greater than 50 dB between 11.9 GHz and 12.2 GHz. From a full-wave design perspective, the filter is an H-plane structure, yet an E-plane implementation has been followed, as shown in **Figure 17**.

**Figure 18** shows the measured results. In this case, the filter itself is less sensitive than the previous one; therefore, a quite good agreement is expected and achieved. The matching level is even better than the usual one.

### *3.2.3.3. Band-pass filter*

The last filter was introduced in [7, 16]. It is a band-pass one, where selective frequency response is directly related to the resonance phenomenon [20]. The process involves high standing waves and electromagnetic field intensities, and, therefore, insertion losses are expected higher than in high-pass or low-pass filters.

The band-pass filter in **Figure 19** is a third-order Chebychev filter. The figure shows both the CAD layout and the fully assembled structure. Inductive irises are used to couple between cavities. It is centered in 12 GHz and the bandwidth is 600 MHz. Return losses were specified to be 23 dB.

**Figure 15.** Measurement setup for the low-pass filter connected to the VNA.

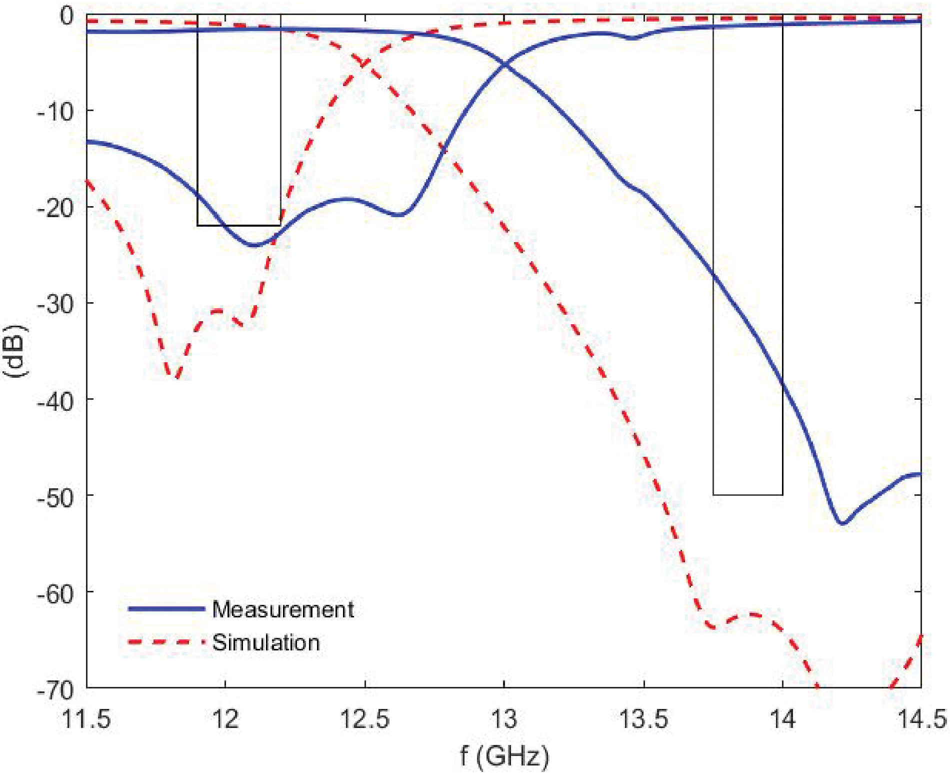

**Figure 16.** Measurement and simulation results for the low-pass filter.

**Figure 20** shows the measured response together with the simulation. The effective conductivity has been considered in the simulations. The matching value is reduced in the 3D–printed model, yet both responses are very close. It shows good agreement with the mean value for 3D–printed waveguides in Ku band. Besides, insertion losses are 1.3 dB at the central frequency.

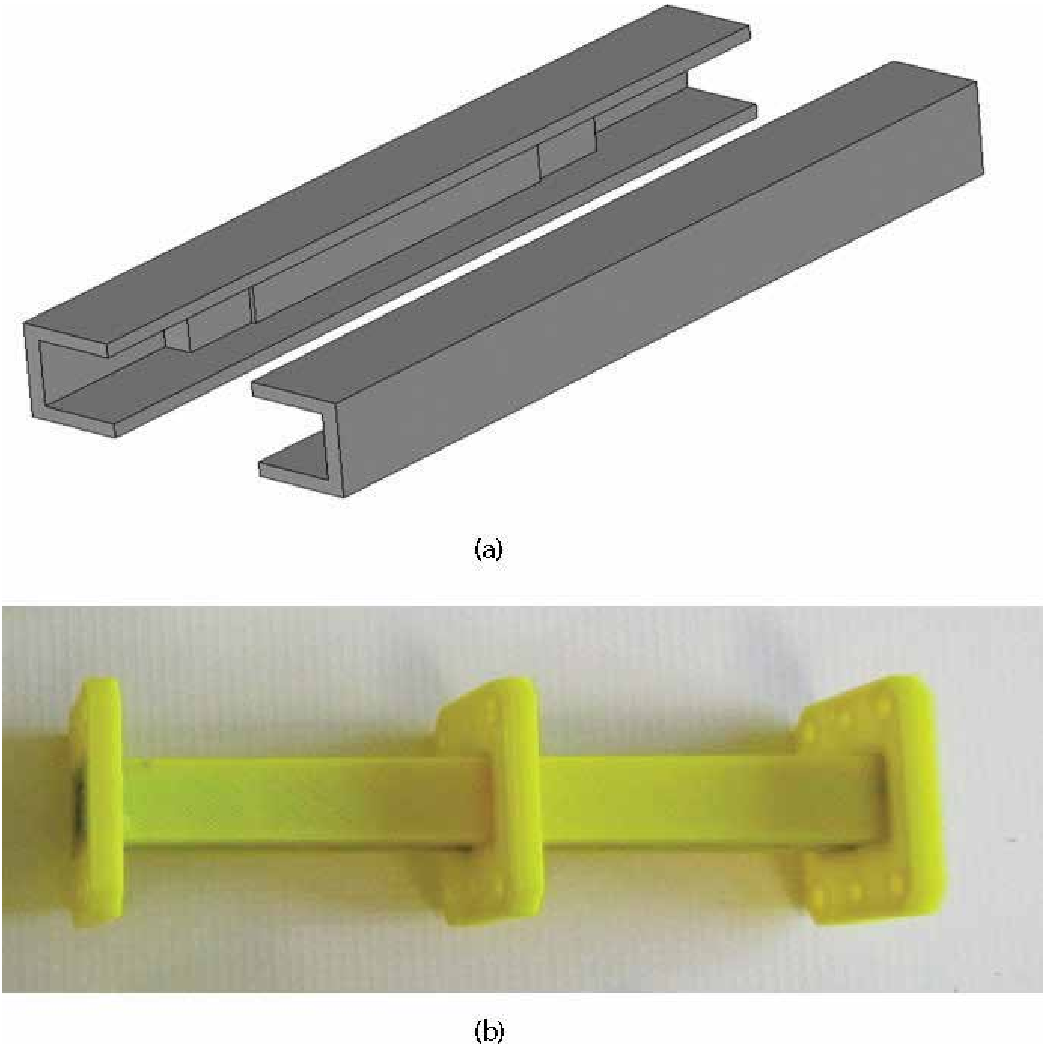

(a)

(b)

**Figure 17.** (a) CAD pieces and (b) assembled high-pass filter.

### *3.2.4. Diplexer*

A more complex device is now presented: a diplexer, which is also included in [7]. It is a passive microwave device formed by two filtering structures joined by a three-port junction. Its main application is the use of a single antenna for both transmission and reception in communication systems.

For this design, real satellite communications specifications are used. The passbands are 11.9–12.2 GHz for reception and 13.75–14 GHz for transmission. Return losses and out-of-band rejection are included in the specifications. The former is around 22 dB, whereas the latter is required to be more than 50 dB in complementary bands. For such requirements, different implementations may be used: two band-pass filters or a low-pass combined with a high-pass filter. In this case, the second approach is used since it is the implementation with less insertion losses.

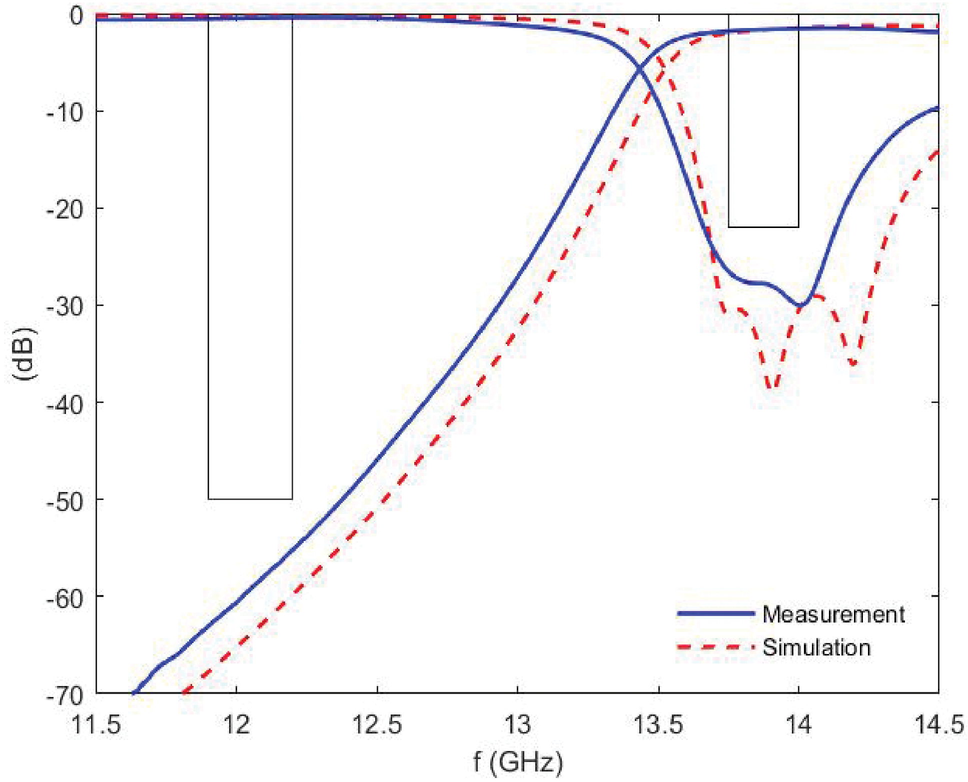

**Figure 18.** Measurement and simulation results for the high-pass filter.

However, the low-pass filter presents some challenges, as mentioned earlier. Again, the corrugations are the most sensitive part. Consequently, they have been made wider than in traditionally manufactured filters, also to have them painted more easily. Corrugations are 4.5-mm wide, which implies more sections to achieve the same electrical response.

**Figure 21** shows the development of the diplexer: (a) the layout, (b) the CAD model, (c) one printed half, and (d) the device prepared to be measured. To join the filters, a three-port junction is designed. Moreover, a double bend is included to allow the waveguide flanges to be attached. Finally, a fastening piece has been printed to keep the two pieces close and avoid any possible air gaps.

The diplexer response is presented in **Figure 22** compared to a simulation with losses. Insertion losses are up to 3.5 dB in the passband. The matching level in both channels agrees with the achievable levels with low-cost 3D printing: approximately 20 dB. It is important to highlight that both responses have moved to lower frequencies as a result of possible printing inaccuracies.

### *3.2.5. Branch-line coupler*

Directional couplers are four-port devices in which the power available at the input port is distributed between two output ports [20]. Perhaps the most common ones are the 3-dB couplers, widely used as input/output in balanced amplifier circuits, in beam-forming networks, as power dividers, and so on. In particular, branch-line couplers consist in two shunt

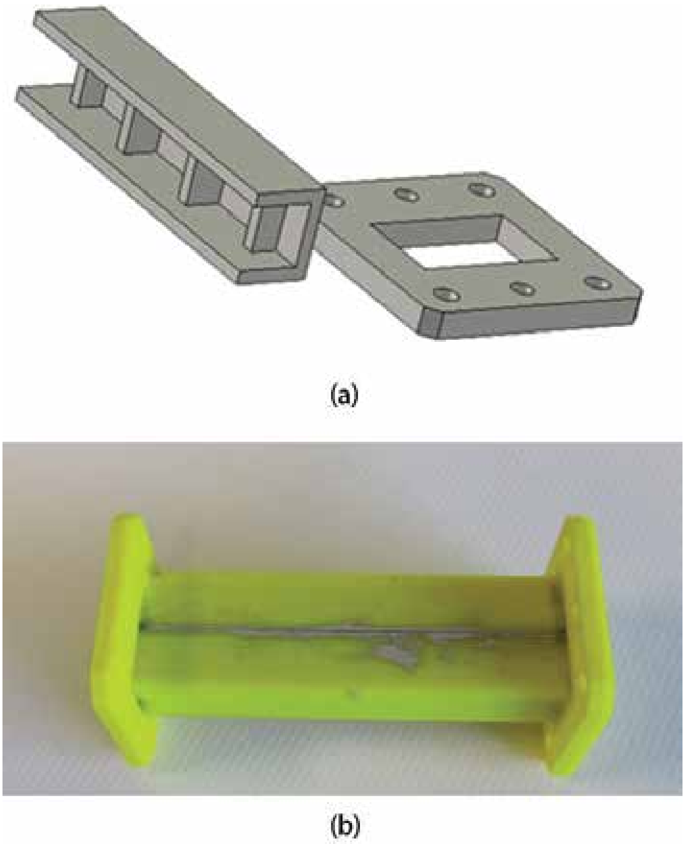
(a)
(b)

**Figure 19.** (a) CAD model and (b) assembled band-pass filter.

transmission lines connected by two secondary (branch) lines. They present a narrow bandwidth, although it can be improved by cascading several sections.

A 3-dB branch-line coupler working in Ku band has been designed and the results presented in [7]. Aiming to achieve a broad bandwidth, five branches have been designed. Isolation and matching levels are intended to be 25 dB in the working band. **Figure 23** shows the designed device from the simulation model to the measurement setup. Two double bends have been added to the coupler in order to attach the standard WR75 flanges.

The experimental response is shown in **Figure 24**. In terms of matching and isolation, the results are very satisfactory. The former is greater than 20 dB between 11 GHz and 14 GHz, although if the bandwidth from 11.5 GHz to 14 GHz is considered the matching value results to be greater than 25 dB. The isolation reached is very high as well, considering the limitations of 3D printing. From 11 GHz to 14 GHz, it is better than 24 dB.

The response of the printed branch-line coupler in terms of power coupled to each output port is evaluated on the enhanced part of **Figure 24**. The measurements are compared to a full-wave simulation including losses. They are lower in the transmitted port (P2) than in

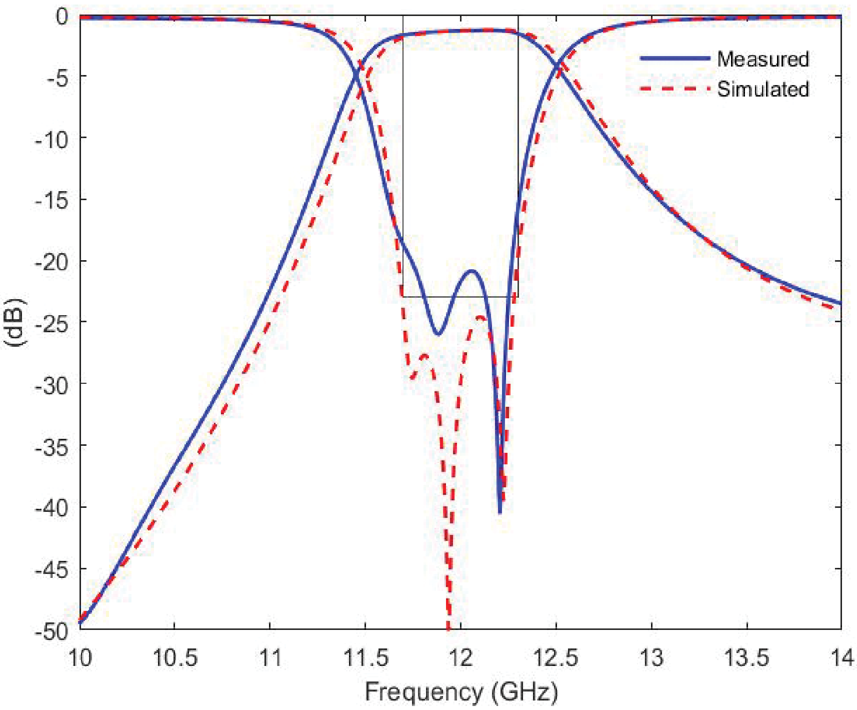

**Figure 20.** Measurement and simulation results for the band-pass filter.

the coupled one (P3), although the former has a double bend attached. It may be explained by considering that the coupled signal passes through the branches on its way to the output port. Moreover, misalignments are likely to happen, particularly in the small posts among the branches. They are the smallest part of the design, as well as the most sensitive one, as it happened with the corrugations in the low-pass filter.

### *3.2.6. Horn antennas*

The two horn antennas [21] presented in this work fulfill standard horn specifications, according to available commercial models working in the same band, like the Flann horn in [22]. Their gain reaches 15 dBi at the center of the Ku band. The first one is a classical pyramidal horn, whereas the second one has a rectangular aperture and a conformed profile. Their input corresponds to the WR75 rectangular waveguide. The return-loss level for both antennas has been optimized to remain below 20 dB between 10 GHz and 15 GHz. Measurements show a remarkably good agreement with theoretical values, which makes the horns perfectly useful for real communication applications, for instance, indoor systems.

The process is presented in **Figure 25**, together with the CAD design of one horn. The antennas are monolayer structures, that is, only one layer of plastic has been used. Due to this fact, the antennas are extraordinary light—less than 15 gr.—contrary to the weight of traditional

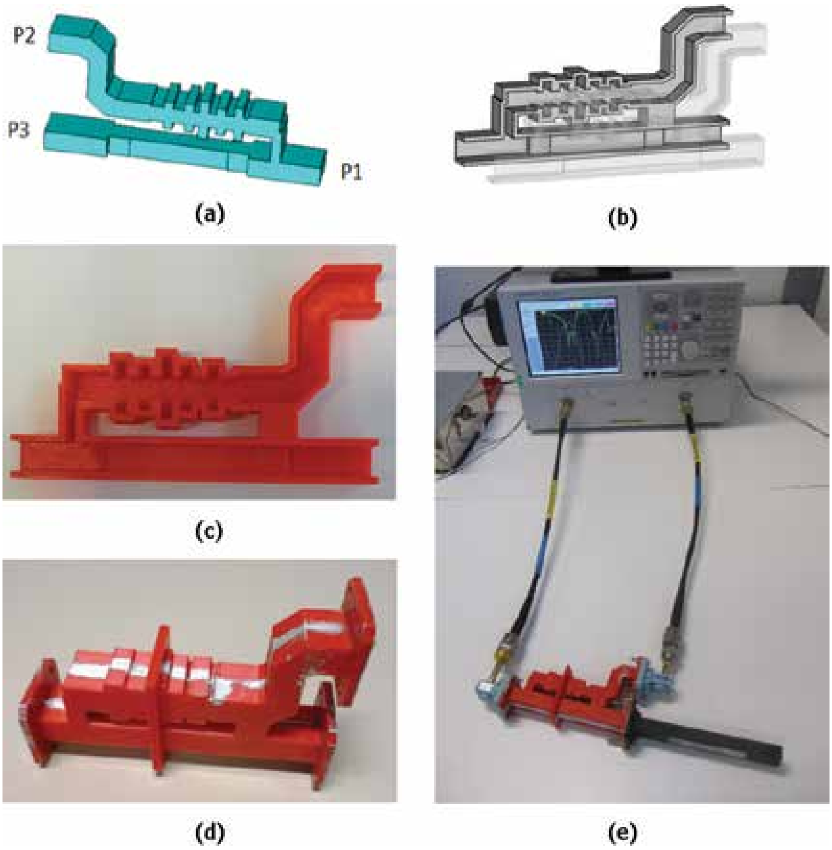

**Figure 21.** (a) Diplexer layout, (b) half CAD model, (c) one printed half, (d) the device metallized and assembled, and (e) measurement setup.

and mass-produced metal horns. At the same time, they are robust enough and their smooth surface makes it feasible to print them as single structures, instead of splitting them into two parts as it occurred with the previous waveguide devices. It must be highlighted that the printed structures also include the waveguide input (the standard WR75 flange).

The time required to print each horn antenna is approximately 2 hours, notably less than a traditional manufacturing process. Finally, the conformed profile of the second horn would have been very difficult to achieve by traditional means, and it would have required the use of molds. At the end, the total cost of each antenna is approximately 15 $.

Both horn antennas have been characterized in terms of matching level, gain, and radiation patterns. **Figure 26** shows the experimental setup for the pyramidal horn in the network analyzer and the anechoic chamber. The theoretical responses have been obtained with CST. Moreover, the measured gain of the antennas has been compared not only to the simulated response but also to the commercial model supplied by Flann working in the same band.

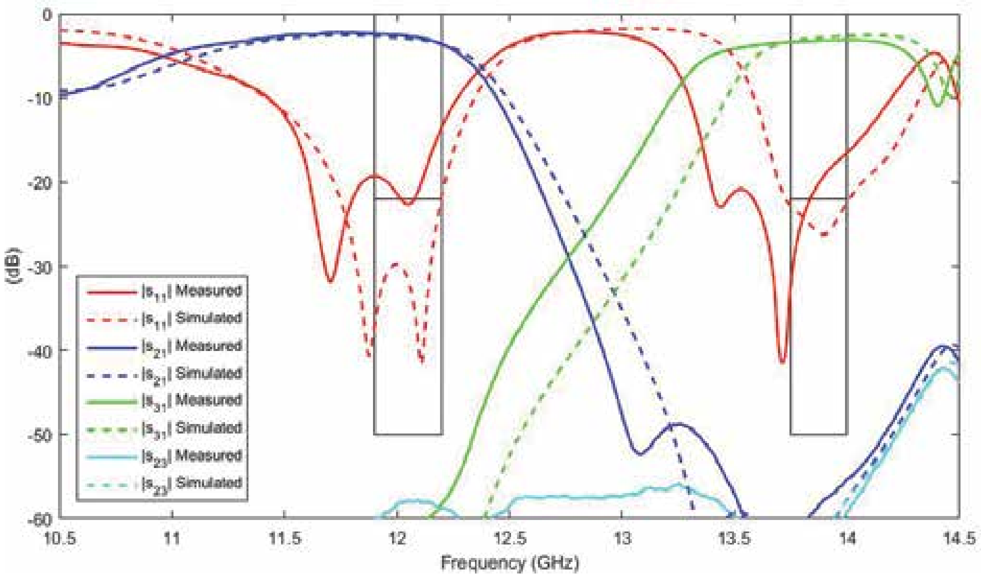

**Figure 22.** Measurement and simulation results for the diplexer.

### *3.2.6.1. Matching level*

The horn antennas were designed with a return-loss level better than 20 dB between 10 GHz and 15 GHz. The measured responses and the simulated ones ($\sigma = 5 \cdot 10^4$ S/m) are shown in **Figures 27** and **28**. Despite a return-loss level slightly worse than 20 dB between 10 GHz and 10.5 GHz for the conformed horn, the response of the reflection coefficient follows the expected one. However, a small ripple can be observed in both antennas. It is explained by considering multiple reflections due to the inherent roughness and small discontinuities on the walls.

### *3.2.6.2. Radiation pattern*

The normalized radiation patterns in the E and H-plane—elevation and azimuth, respectively—have been obtained at 12.5 GHz for both antennas. The pattern corresponding to the classical pyramidal horn is shown in **Figure 29** along with the simulated co-polar response. The measured response follows the theoretical one very accurately, with a difference in the 3-dB beamwidth of only 1° (**Table 1**). With respect to the cross-polarization level, its measurement is limited by the anechoic chamber used in the horn characterization. In this case, its level is always 30 dB under the main lobe in both planes.

The conformed-profile horn shows a very good response as well, as presented in **Figure 30**. The radiation pattern matches the simulated one accurately and the 3-dB beamwidth barely differs 5° in the worst-case scenario (**Table 1**). Finally, the cross-polarization level remains more than 30 dB under the main lobe in both planes.

### *3.2.6.3. Antenna gain*

The gain over broadband has also been measured for both antennas. The pyramidal horn gain is presented in **Figure 31** compared with the simulated one and the commercial pyramidal horn provided by Flann [22]. It can be seen that the gain of the 3D–printed horn is not as high

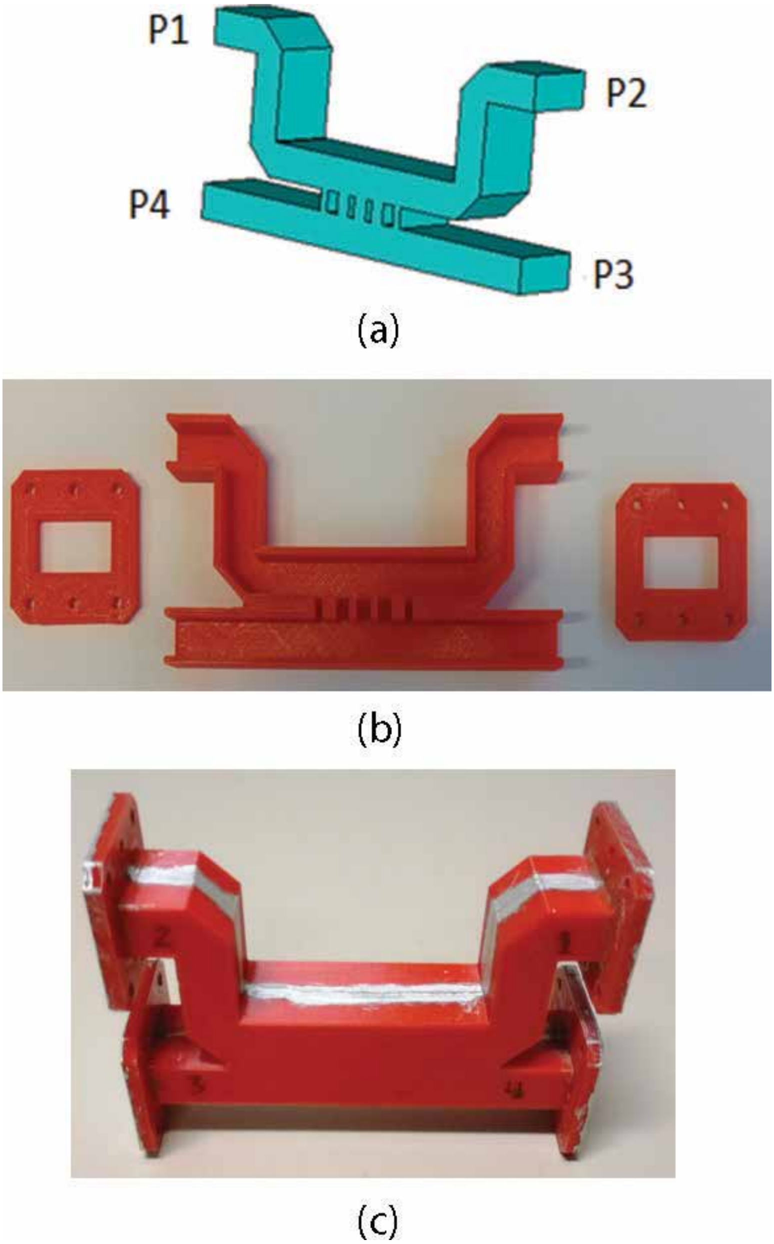

**Figure 23.** (a) Layout, (b) printed half, and (c) assembled and metallized branch-line coupler.

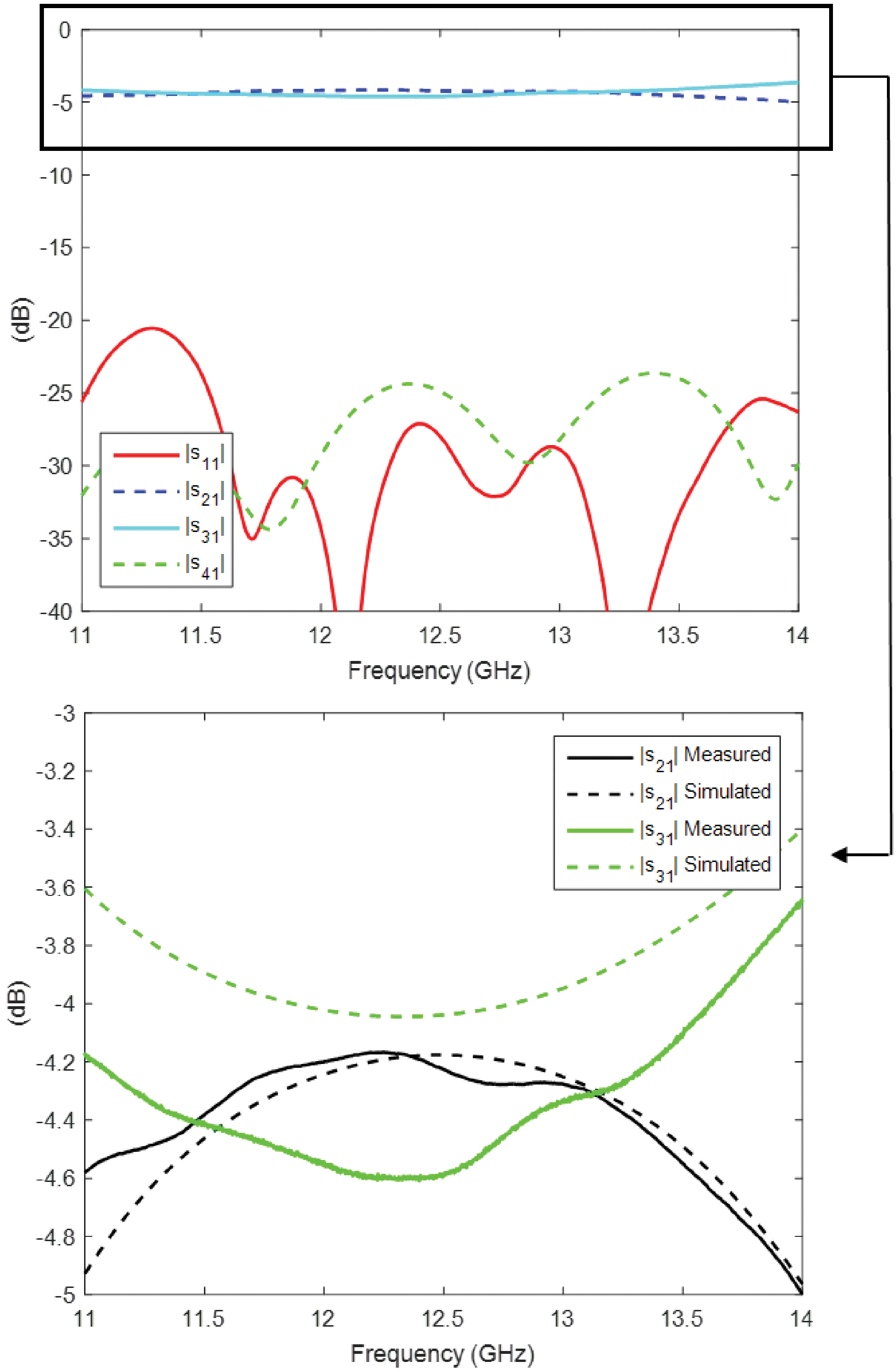

**Figure 24.** Measurement and simulation results for the branch-line coupler. To the right, enhanced view of the transmission parameters.

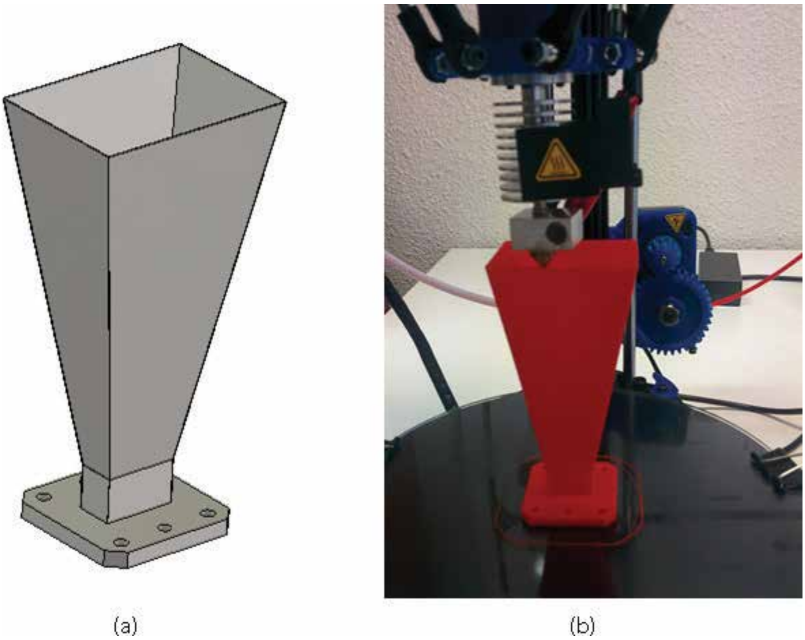

**Figure 25.** (a) CAD model of the pyramidal horn. (b) Horn antenna being printed with the low-cost PLA 3D printer.

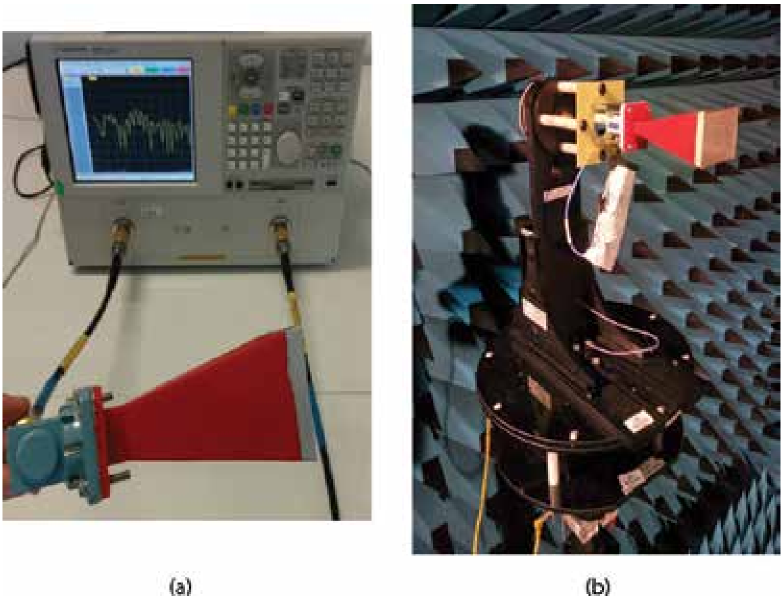

**Figure 26.** Measurement arrangement for the pyramidal horn in (a) the network analyzer and (b) the anechoic chamber.

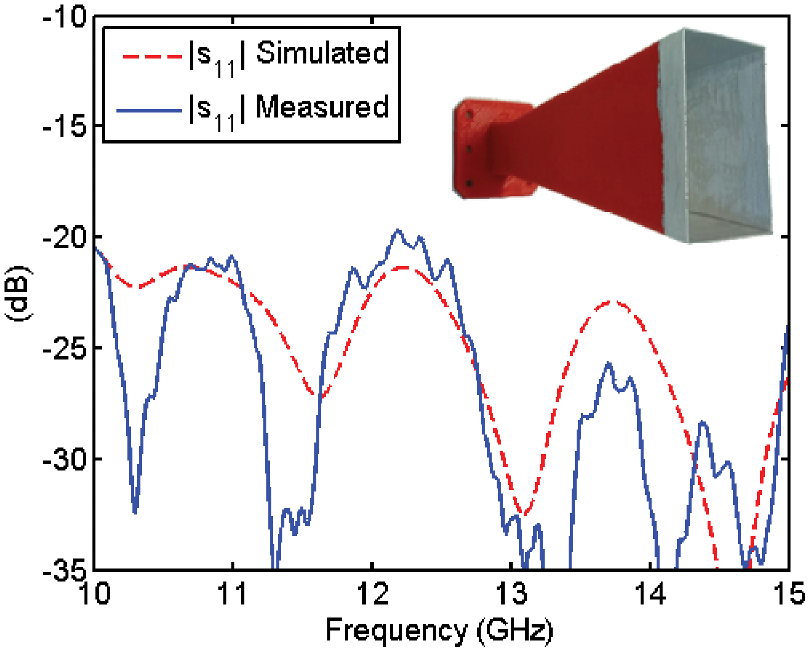

**Figure 27.** Return-loss level over Ku-band for the classical pyramidal horn. Top right inset: Printed and metallized structure.

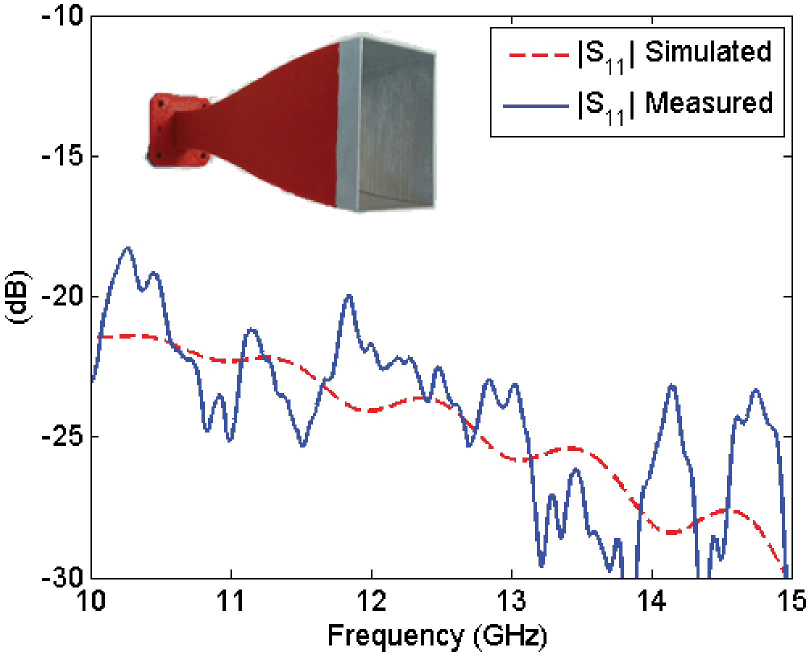

**Figure 28.** Return-loss level over Ku-band for the conformed-profile horn. Top left inset: Printed and metallized structure.

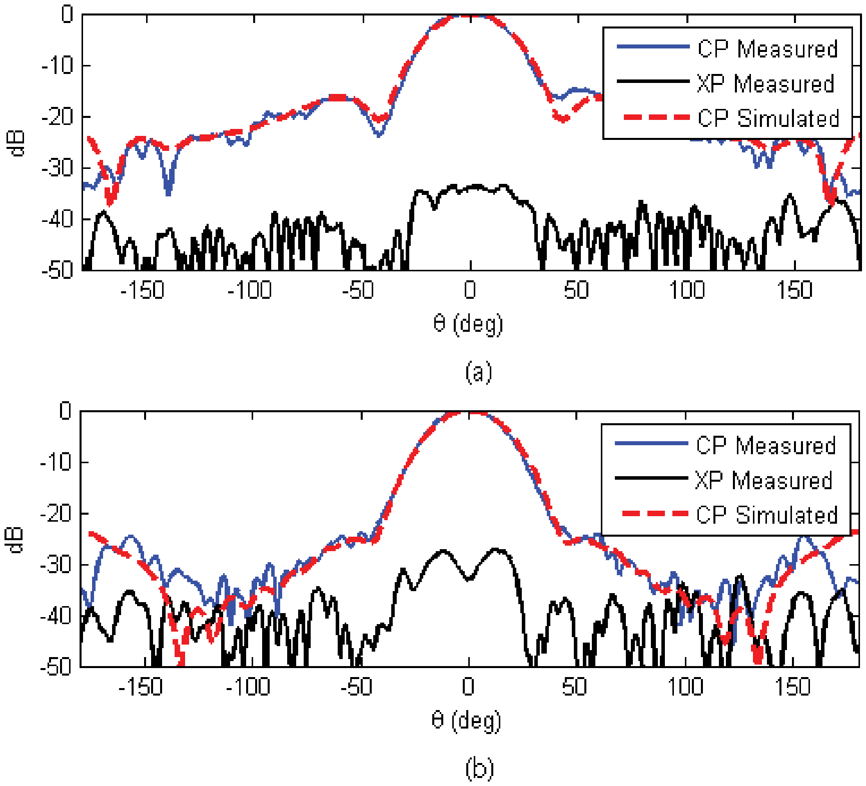

**Figure 29.** Normalized radiation pattern of the pyramidal horn at frequency 12.5 GHz in (a) E-plane and (b) H-plane.

as the one of the commercial model, with differences up to 1.5 dB, especially in the lower band. There are discrepancies with the simulation too, caused by the limitations of the manufacturing process. However, the results are satisfactory, considering the intrinsic variability of the metallization and the substantial difference in terms of cost between the Flann horn and the printed one.

For the conformed-profile horn, the measured gain matches the simulated response with a remarkable accuracy, as shown in **Figure 32**. It presents a good behavior when compared with the Flann model as well, although some variations caused by manufacturing issues exist. However, they do not exceed 1.35 dB.

| | **E-plane** | | **H-plane** | |
|---|---|---|---|---|
| | **Measured** | **Simulated** | **Measured** | **Simulated** |
| Pyramidal horn | 34° | 33° | 31.4° | 30.7° |
| Conformed horn | 24.8° | 30.2° | 28.6° | 31.1° |

**Table 1.** Simulated and measured 3-dB beamwidth.

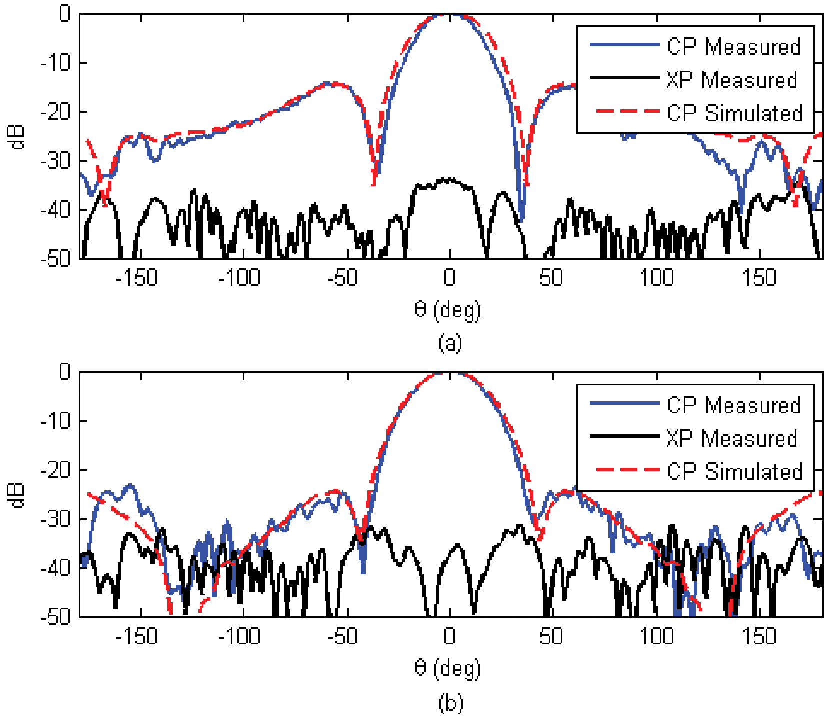

**Figure 30.** Normalized radiation pattern of the conformed-profile horn at frequency 12.5 GHz in (a) E-plane and (b) H-plane.

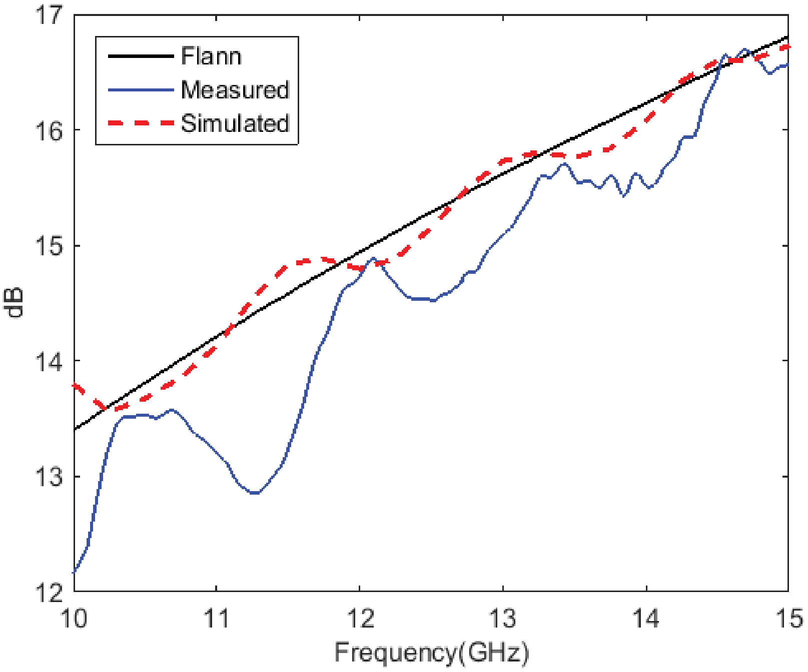

**Figure 31.** Pyramidal horn gain over broadband compared with simulation and commercial horn antenna from Flann.

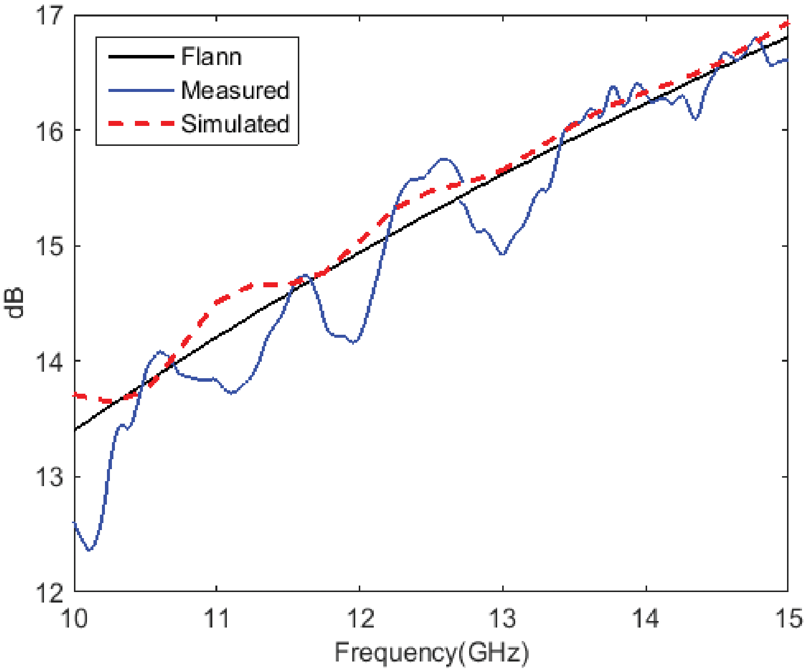

**Figure 32.** Conformed-profile horn gain over broadband compared with simulation and commercial horn antenna from Flann.

## 4. Conclusions

Although benefits of additive manufacturing are well known to the engineer community, its real application to a particular field needs a detailed analysis, even more when considering a low-cost perspective. With the work presented throughout this chapter, it can be concluded that low-cost 3D printing presents great advantages for the microwave engineer. The promptness to print models of great quality or to implement traditionally unfeasible geometries may be used for two main applications: prototyping and manufacturing of functional devices. Both applications may also increase the quality of microwave engineering education, especially for institutions without extraordinary resources.

In order to successfully address a low-cost 3D printing process in the microwave field, it is necessary to first take into account several key aspects: to set the maximum achievable working frequency, the best way to perform a metallization process, and the most suitable structure segmentation. This work has described all of them, emphasizing the best solutions as per authors' knowledge.

In addition, several prototypes of state-of-the art designs have been presented, together with real passive waveguide devices—individual filters, a diplexer, and a branch-line coupler—and two horn antennas. Experimental results have been discussed to evaluate their use in real-world applications. In general terms, the results agree quite well with the expected response, yet the discrepancies have also been explained.

In summary, additive manufacturing, and, in particular, its low-cost version, has a very promising future in the engineering field. Although further research is required—for instance, to enhance conductivity—it is a powerful tool worth to be discovered.

## Acknowledgements

This work was supported in part by the Spanish government under grant TEC2016-76070-C3-1/2-R (ADDMATE, (AEI/FEDER, UE)) and the Comunidad de Madrid program S2013/ICE-3000 (SPADERADARCM).

The authors would like to thank Pablo Sanchez-Olivares for the gain and radiation pattern measurements at Escuela Politécnica Superior (Universidad Autónoma de Madrid).

## Author details

Irene O. Saracho-Pantoja[1]*, José R. Montejo-Garai[1], Jorge A. Ruiz-Cruz[2] and Jesús M. Rebollar[1]

*Address all correspondence to: i.ortizdesaracho@alumnos.upm.es

1 Grupo de Electromagnetismo Aplicado, Information Processing and Telecommunications Center, Universidad Politécnica de Madrid, Madrid, Spain

2 Escuela Politécnica Superior, Universidad Autónoma de Madrid, Madrid, Spain

## References

[1] Barnatt C. 3D Printing. 2nd ed; 2014

[2] Additive manufacturing—General principles—Terminology, ISO/ASTM 52900:2015 (ASTM F2792), 2015

[3] About Additive Manufacturing: The 7 Categories of Additive Manufacturing [Online], Loughborough University. Available: http://www.lboro.ac.uk/research/amrg/about/the7categoriesofadditivemanufacturing/

[4] Canessa E. Low-Cost 3D Printing for Science. International Centre for Theoretical Physics: Education & Sustainable Development; 2013

[5] RepRap, [Online]. Available: http://reprap.org

[6] Saracho-Pantoja IO. Ku band waveguide diplexer design for satellite communication. Implementation by additive manufacturing and experimental characterization; 2015. [Online]. Available: http://oa.upm.es/37345/

[7] Saracho-Pantoja IO, Montejo-Garai JR, Ruiz-Cruz JA, Rebollar JM. Low-cost additive manufacturing: A new approach to microwave waveguide engineering education through 3D printing. International Journal of Engineering Education. 2017;**33**(2(A)):741-750

[8] Montejo-Garai JR, Saracho-Pantoja IO, Ruiz-Cruz JA, Rebollar JM. Broadband and High-Purity Ku-Band Circular TE01-Mode Converter. New Delhi, India: Microwave Conference (APMC); 2016

[9] Montejo-Garai JR, Ruiz-Cruz JA, Leal-Sevillano CA, Rebollar JM, Roglá L, Sobrino S. Compact Low-Cost Diplexer with Elliptic Filter Response for Ka-Band Satellite Applications, 6th CNES/ESA International Workshop on Microwave Filters. France: Toulouse; 2015

[10] Loctite R3863 Circuit+. Available: http://www.loctite.es/

[11] Ferro-Silver Conductive Lacquer 6290 0341 (L204N), [Online]. Available: http://www.ferro.com

[12] RS Pro Conductive Adhesive [Online]. Available: http://uk.rs-online.com

[13] Matthaei GL, Young L, Jones EMT. Microwave Filters. Impedance-Matching Networks and Coupling Structures: McGraw-Hill Book Co.; 1964

[14] Graphit 33, Kontakt Chemie. Available: http://www.kontaktchemie.com/koc/KOCproductdetail.csp?division=&product=GRAPHIT%2033

[15] WR-62 Waveguide Load, Pasternack. Available: https://www.pasternack.com/waveguide-termination-frequency-range-1240-1800-ghz-pe6804-p.aspx

[16] Montejo-Garai J, Leal-Sevillano C, Ruiz-Cruz J, Rebollar J. Low-Cost Manufacturing by Fused Filament Fabrication of Microwave Waveguide Passive Devices for Space Applications, Workshop on Additive Manufacturing for Space Application. The Netherlands: Noordwijk; 2014

[17] Montejo-Garai J, Saracho-Pantoja I, Ruiz-Cruz J, Rebollar J. Design of Microwave Waveguide Devices for Space and Ground Applications Implemented by Additive Manufacturing, International Conference on Electromagnetics in Advanced Applications, Torino, Italy; 2015

[18] Ruiz-Cruz J, Montejo-Garai J, Rebollar J. Computer Aided Design of Waveguide Devices by Mode-Matching Methods. InTech: Passive Microwave Components and Antennas; 2010

[19] CST Microwave Studio, [Online]. Available: http://www.cst.com

[20] Pozar D. Microwave Engineering. Wiley; 2012

[21] Balannis C. Antenna Theory: Analysis and Design. Wiley; 2005

[22] Standard Gain Horn, Model 17240. Flann. Available: http://www.flann.com/products/antennas/

Chapter 7

# 3D Holographic Millimeter-Wave Imaging for Concealed Metallic Forging Objects Detection

Lulu Wang

Additional information is available at the end of the chapter

http://dx.doi.org/10.5772/intechopen.73655

## Abstract

This chapter investigates the feasibility of using 3D holographic millimeter-wave (HMMW) imaging for diagnosis of concealed metallic forging objects (MFOs) in inhomogeneous medium. A 3D numerical system, including radio frequency (RF) transmitters and detectors, various realistic MFOs models and signal and imaging processing, is developed to analyze the measured data and reconstruct images of target MFOs. Simulation and experimental validations are performed to evaluate the HMMW approach for diagnosis of concealed MFOs. Results show that various concealed objects can be clearly represented in the reconstructed images with accurate sizes, locations and shapes. The proposed system has the potential for further investigation of concealed MFOs under clothing in the future, which has the potential applications in on body concealed weapon detection at security sites or MFOs detection in children.

**Keywords:** holographic millimeter-wave imaging, concealed metallic object, dielectric properties, millimeter-wave, microwave imaging

## 1. Introduction

Imaging approaches for diagnosis of concealed metallic objects [1], such as on body weapon detection [2, 3] and metallic foreign objects (MFOs) detection in children [4], have received many attentions worldwide in recent years. Concealed weapon detection underneath human subjects' clothing is an active research topic due to rapid screening of human subjects is urgent needed at some security sites, such as airports [1]. In 1995, the United States started the concealed weapon detection program [2] to detect concealed weapons from a standoff distance, especially when it is impossible to arrange the flow of people through a controlled procedure [3].

Various imaging techniques include infrared imaging [5, 6], passive millimeter-wave (MMW) imaging [7–9], active MMW imaging [10, 11], X-ray imaging [12, 13] and holographic imaging [14–17] have been investigated for concealed metallic object detection. Recent studies have demonstrated that passive MMW imaging has the most potential to become a useful tool to identify concealed MFOs under clothing [18, 19], which has been investigated for various applications include security, military, surveillance and biomedical [20].

Passive MMW imaging sensor techniques offer the best near-term potential for providing a non-invasive method of observing metallic and plastic objects concealed underneath common clothing. However, MMW cameras alone cannot provide useful information about the detail and location of the individual being monitored. The passive MMW system can produce indoor and outdoor images in bad weather, such as smoke and fog [21]. It has been applied to scan human subjects moving in an unconstrained flow, however, the MMW image has poor quality due to low-level signals and system noise [5]. In order to improve the accuracy and specificity of MMW for diagnosing concealed MFOs, many researchers aimed to develop a new MMW approach such as imaging algorithm and implement system.

Holographic technique was first applied in microwave imaging in 1948 [22]. An interference pattern between reference wave and diffracted wave (created by an object) is recorded to produce a hologram that can be digitally stored. The holograms are reconstructed by numerically synthesizing the reference wave, which is well-known wave front reconstruction processing. The target object can be reconstructed from the measured reflections and holograms. Holographic approaches are very different from the conventional synthetic aperture radar imaging method particularly in imaging geometry and no field approximations are required for holographic, which have recently been applied in MMW for MFOs detection [14, 15]. Farhat and Guard [14] applied the holographic approach for concealed weapon detection, and this technique was dramatically improved by Collins et al. [15]. The concealed MFOs detection system aims at extracting features of MFOs and reconstructing the MFOs using the measured data. The image quality is often limited by low signal-to-noise ratio and long scan time. Existing MMW methods are multi-frequency approach, which reconstruct a 3D image from a sequence of 2D images that obtained at different frequencies. However, the multi-frequency MMW methods have difficulty in practical implementations and the broadband measurements also cause large noises.

This chapter demonstrates the feasibility of using a single frequency 3D holographic millimeter-wave (HMMW) imaging system and method to detect various small MFOs in inhomogeneous medium. A computer model is developed under MATLAB environment to validate the proposed theory and measurement system setups. The system contains a HMMW measurement model and various realistic models. Simulation and experimental validations are performed to evaluate the accuracy, effectiveness and performance of the proposed theory. The remainder of this chapter is organized as follows. Section 2 introduces the 3D HMMW measure system and imaging processing. Sections 3 and 4 present simulation and experimental performances. Section 5 gives discussion and conclusion of this study.

## 2. Methodology

### 2.1. Imaging measurement system

**Figure 1** shows the proposed HMMW system for concealed metallic object detection. The system contains a RF generator (vector network analyzer, VNA) to illuminate microwave signals, a data acquisition unit consists of a single transmitter to transmit microwave signals into a target object and an array of receivers to measure scattered electric fields from the target object, a signal and imaging processor to analyze the measured signals which contains phase and amplitude information as well as reconstruct image of the target object using an imaging algorithm, and an image display unit to display the reconstructed image.

During data collection, port one of the VNA generates millimeter waves to the object of interest and the backscattered electromagnetic fields from the object are recorded at each receiver in the detector array plane that is connected to the second port of VNA. The distance between the target object and the data acquisition unit is in far-field region. The recorded signals include phase and amplitude information, which are used to compute the complex visibility data for each possible pair of receivers. An image of the object can be reconstructed from recorded data using the HMMW algorithm.

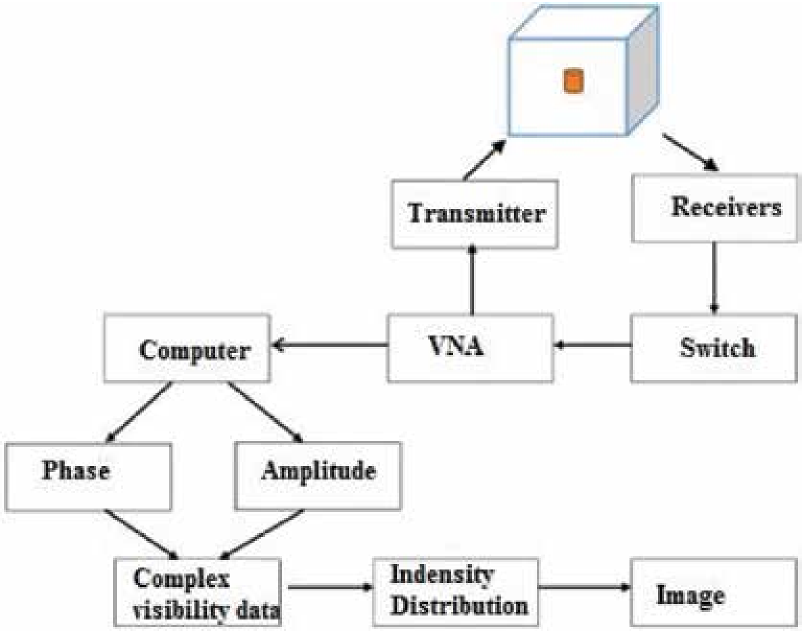

**Figure 1.** Experimental procedure.

## 2.2. Antenna part

In order to investigate the feasibility of using the 3D HMMW to detect concealed MFOs, 16 four-band patch antennas or waveguide antennas were simulated as both transmitters and detectors. **Figure 2** shows the designed four-band patch antenna with length of 10.7 mm, width of 6.3 mm, and height of 0.254 mm. As shown in **Figure 2(b)** and **(c)**, top layer and bottom layer of the proposed antenna contain 12 holes (0.15 mm in diameter) that aims to work in four broadband. The subtract material between the two layers of the antenna is RT/duriod6002 with dielectric property close to 1.

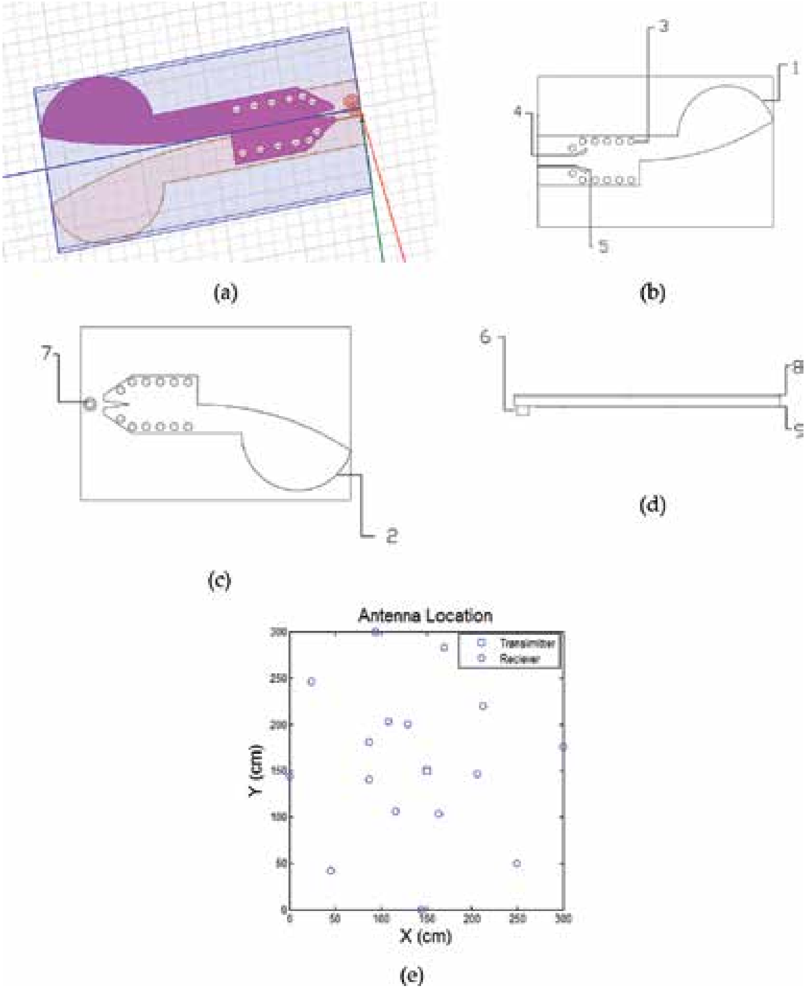

**Figure 2.** (a) Multiband patch antenna; (b) top layer of the designed antenna: (1) top antenna, (3) holes, (4 and 5) trumpet holes; (c) bottom layer of the antenna: (2) bottom antenna, (7) feed probe hole; (d) sideview of the antenna: (6) feed probe, (8) dielectric layer, (9) ground plate; (e) sensor array configuration.

The incident electric field from each transmitter is [23]:

$$\vec{E}_{inc}(R, \theta, \varnothing) = \left(-\frac{j\,k_0}{2\,\pi^2}\right) \vec{E}_0\left(\frac{e^{-jk_0R_0}}{R_0}\right) ABh(\theta, \varnothing)\vec{P}(\theta, \varnothing) \qquad (1)$$

Where $k_0$ is prorogation constant of free-space, $R$ and $R_0$ are the distance from the object to the detector and transmitter, respectively. $\vec{E}_0$ is wave amplitude of TE10 mode at within waveguide aperture, $A$ and $B$ are narrow and wide aperture dimensions of antenna, respectively, $h$ is radiation pattern, $\vec{P}$ is polarization vector.

In far-field condition, the scattered electric field from the object can be computed as [24]:

$$\vec{E}_{scat}(\vec{r}) = \left(\frac{k_0^2}{4\pi}\right) \int_V \left(\varepsilon(\vec{s}) - \varepsilon_0\right) \vec{E}_{inc}(\vec{s}) \frac{e^{-jk_0R}}{R} dV \qquad (2)$$

Where $\varepsilon(\vec{s})$ and $\varepsilon_0$ are the complex relative permittivity of object and free-space, respectively. $R$ means the distance between the object and the detector.

### 2.3. Signal and imaging processing

As shown in **Figure 3**, a point Q is located within a 3D object, the visibility for any two detectors located at $\vec{r}_i$ and $\vec{r}_j$ can be computed [25]:

$$\vec{V}_{ij} = < \vec{E}_{scat}\left(\vec{r}_i\right) \cdot \vec{E}^{*}_{scat}\left(\vec{r}_j\right) > \qquad (3)$$

Where * is the complex conjugate and < > denotes time average.

The total visibility data can be computed as:

$$\vec{V} = \sum_{i}^{N} \vec{V}_{ij}, N \geq 3, i \neq j \qquad (4)$$

Define the object intensity distribution at position $\vec{s}$ as [26]:

$$I(\vec{s}) = \left(\frac{k_0^2}{4\pi}\right)^2 \left|\varepsilon(\vec{s}) - \varepsilon_0\right|^2 \vec{E}_T(\vec{s}) \cdot \overrightarrow{E_T^*}(\vec{s}') \qquad (5)$$

All detectors are located on the same plane, thus, define the line integral as:

$$\tilde{I}(l, m) = \int_s \frac{I(s, l, m)}{\sqrt{1 - l^2 - m^2}} ds \qquad (6)$$

Where $l = sin\theta cos\phi$ and $m = sin\theta sin\phi$. $u = \left(\left(\vec{x}_j\right) - \left(\vec{x}_i\right)\right)/\lambda_0$, $v = \left(\left(\vec{y}_j\right) - \left(\vec{y}_i\right)\right)/\lambda_0$, $\lambda_0$ means the wavelength of free-space.

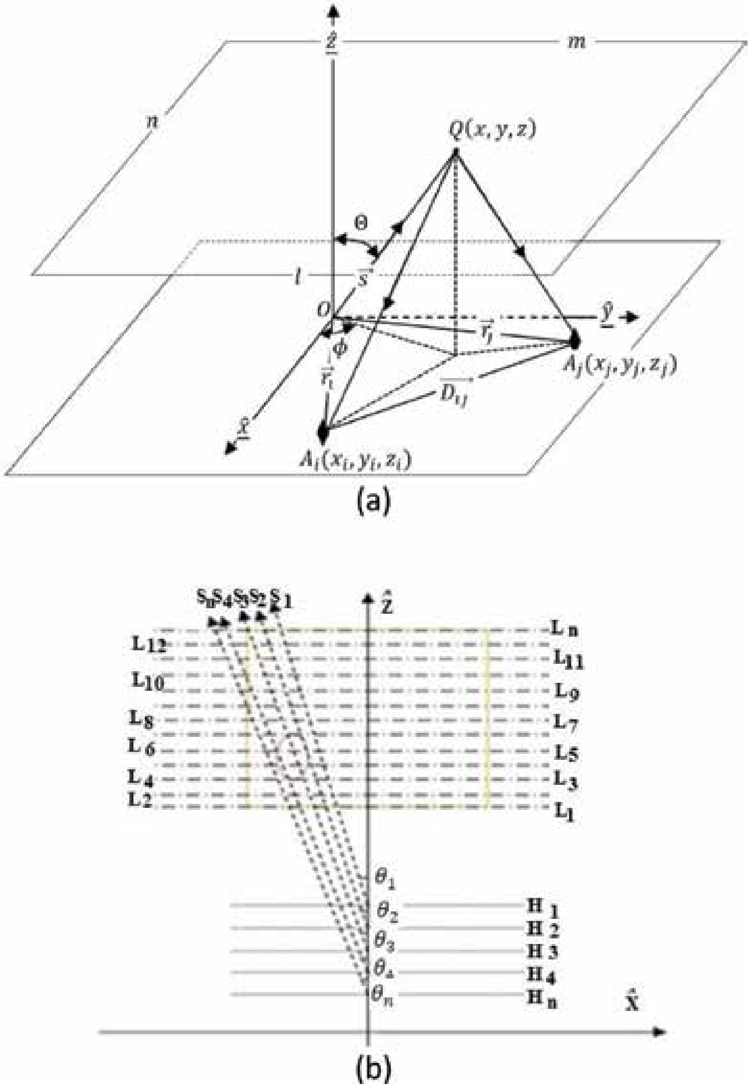

**Figure 3.** (a) Geometry of two detectors, (b) scattering characterization scheme from different receiving height *H* [24].

A 2D image is obtained by using inversion Fast Fourier Transformation:

$$\tilde{I}(l, m) = \iint V(u, v)\, e^{j2\pi(ul+vm)}\, dldm \quad (7)$$

The 2D image difference between each two 2D images is computed by differentiating 2D images when the sensor array plane is placed at different heights (H):

$$I(H = z_n, l, m) = d\tilde{I}(l, m) \cdot (1 - l^2 - m^2)/dz \quad (8)$$

$$d\tilde{I}/dz = \left(\tilde{I}_{Z_n} - \tilde{I}_{Z_{n-1}}\right)/(Z_n - Z_{n-1}) \quad (9)$$

Where $z_n = s_n(\cos\theta_n)$, $\theta_n$ is the receiving angle of the position $s_n$ with the sensor plane placed at the selected height $H_n$ (**Figure 3(b)**).

A 3D image can be reconstructed by acquiring the measured 2D intensity distributions when the sensor array plane is placed at different vertical locations, and computing a sequence of 2D images, $\tilde{I}_{z_n}$.

## 3. Simulation

A numerical system was developed under MATLAB environment to investigate the proposed theory and system for diagnosing concealed MFOs. An array of 16 open-ended waveguide antennas with one element for transmitter and others for receivers. The target object was located at $z = 0$ mm and it was assumed to be fully contained in a rectangle imaging domain with length of 300 mm. The sensor array plane was placed at $z = -200$ m. Five models (see **Figure 4**) were developed using the published dielectric properties to evaluate the 3D HMMW [27].

Model I was made of two metallic spheres (10 mm in diameter, $x_1 = 0, y_1 = 0, z_1 = 35$, $x_2 = 50, y_2 = 0, z_2 = 35$) embedded in a cylindrical tank (240 mm in diameter and 70 mm in height) filled of clothing material; Model II was made of two wood spheres (5 mm in diameter, $x_1 = 0, y_1 = 0, z_1 = 35$) embedded in a cylindrical tank; Model III was made of two wood

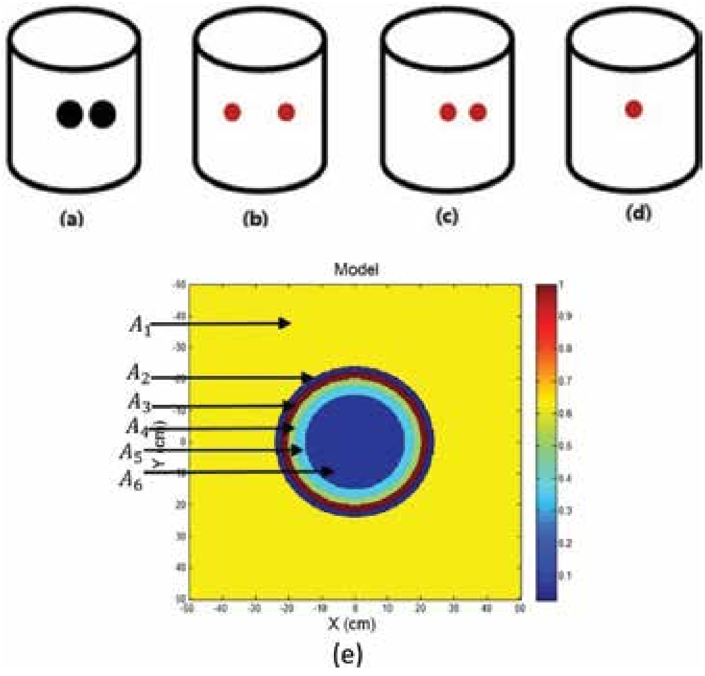

**Figure 4.** (a) Model I, (b) Model II, (c) Model III, (d) Model IV, (e) Model V (*A* 1: matching medium, *A* 2: cloth, *A* 3: metallic object, *A* 4: skin, *A* 5: skull, *A* 6: fat).

spheres (10 mm in diameter, $x_1 = 0, y_1 = 0, z_1 = 35$, $x_1 = 20, y_1 = 0, z_1 = 35$) embedded in a cylindrical tank; Model IV was made of one metallic sphere (10 mm in diameter, $x_1 = 0$, $y_1 = 0, z_1 = 35$) embedded in a cylindrical tank.

To investigate the feasibility of on body conceded weapon detection using the proposed imaging method, a Model V includes human phantom was developed using published dielectric properties of various tissues, and a series of simulations were carried out on a personal computer by the developed computer model. **Figure 4(e)** shows the Model V, where the multimedia dielectric object (cylinder) was located at z = 0 mm and it was assumed to be fully contained in a rectangle imaging domain with length 100 cm. This multimedia object simulates human body (contains skin, skull and fat), clothing and metallic object. The scale values of the published dielectric properties of real tissues were applied (see **Table 1**).

**Figure 5** shows the reconstructed images of Model I at different frequencies in water. Both cylindrical box and two metallic objects are clearly identified in the frequency range of 20–25 GHz, but only metallic object is identified when frequency out of this range.

**Figure 6** shows the reconstructed images of Model II when the two objects located at different distance with frequency of 23 GHz in free-space. Results show that two small wood spheres are successfully identified when the distance between the two items great than 3 mm.

**Figure 7** shows the 3D reconstructed images of Model III and Model IV when the sensor array plane moved from $z = -650$ mm to $z = -600$ mm in 50 equal steps at frequency of 23 GHz.

To simulate on body weapon detection using the HMMW approach, the image measuring system was set-up in free-space with operating of frequency at 96 GHz, a 16-element antenna array plane was placed at the bottom of the model with a distance of 65 cm. A small four-band patch RF antenna was designed as transmitter and receiver and it was simulated using HFSS software with operating frequency of 50–120 GHz. **Figure 8** shows the return loss of the four-band patch antenna, which has the ability to receive good result at 96–116 GHz.

**Figure 9** shows the 2D reconstructed images of Model V at operating frequency of 96 GHz. The rectangle imaging region contains the dielectric object (human model with clothing) and the steel stainless object. Simulation result demonstrates that the metallic object underneath

| No | Region | Dielectric properties | | Scale value of dielectric properties | |
|---|---|---|---|---|---|
| | | $\varepsilon_r$ | $\sigma$ (S/m) | $\varepsilon_r$ | $\sigma$ (S/m) |
| A4 | Skin | 41 | 4 | 0.5125 | 0.4 |
| A5 | Skull | 25 | 2 | 0.31 | 0.2 |
| A6 | Fat | 5 | 0.4 | 0.06 | 0.04 |

**Table 1.** Dielectric properties of human body [26].

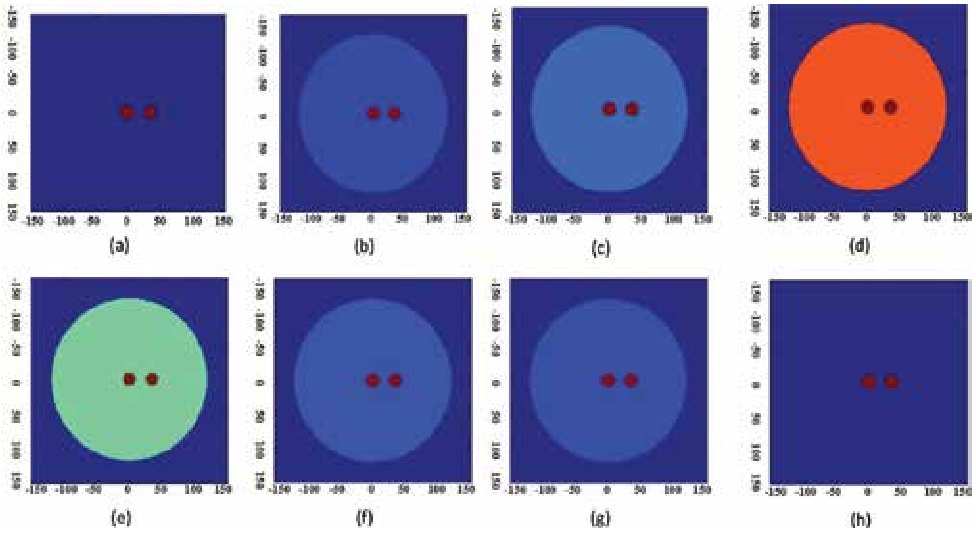

**Figure 5.** Reconstructed images of Model I with operating frequency of (a) 19 GHz, (b) 20 GHz, (c) 21 GHz, (d) 22 GHz, (e) 23 GHz, (f) 24 GHz, (g) 25 GHz, (h) 26 GHz.

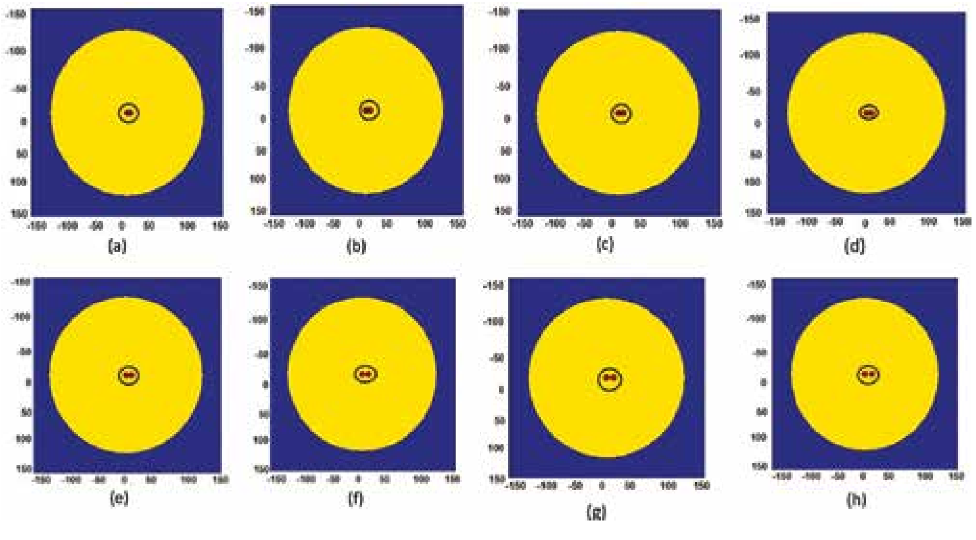

**Figure 6.** Reconstructed images of Model II when the distance between two wood spheres is: (a) 0 mm, (b) 1 mm, (c) 2 mm, (d) 3 mm, (e) 4 mm, (f) 5 mm, (g) 6 mm, (h) 7 mm.

wof human model's clothing has been successfully imaged, and structures of the tested human model are clearly identified with operation frequency of 96 GHz. Color bar plots signal energy on a linear scale, normalized to the maximum in the image space and values below 0.1 are rendered as blue.

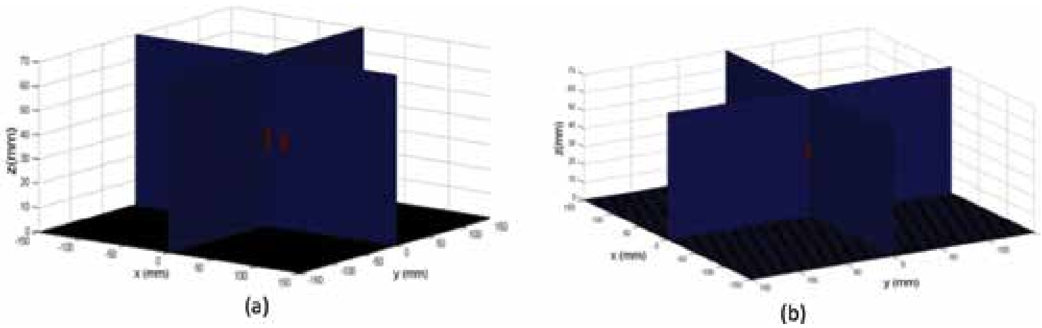

**Figure 7.** (a) 3D reconstructed image of Model III, (b) 3D reconstructed image of Model IV.

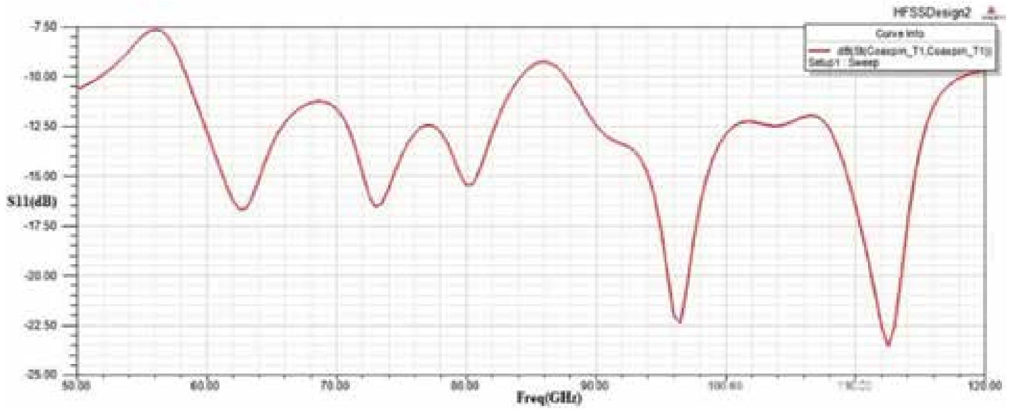

**Figure 8.** Simulated S11 value of the designed 4-band patch antenna.

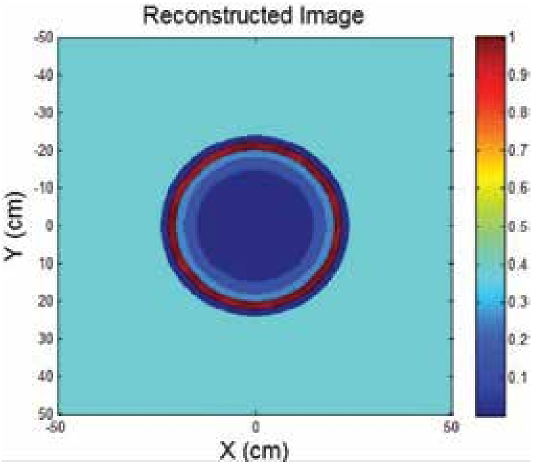

**Figure 9.** Reconstructed 2D image of Model V.

## 4. Experimental validation

An experimental study was conducted to evaluate the 3D HMMW system for concealed MFO detection (see **Figure 10**). A concealed steel ball (10 mm in diameter) embedded in a plastic box (100 × 100 × 40) mm$^3$ that filled of emulsifying wax (see **Figure 10(c)**). An array of 16 open-ended waveguide antennas with one element for transmitter and others for receivers. The plastic box was placed at $z = 0$ mm, and the sensor array plane was moved from $z = -600$ mm to $z = -560$ mm in 40 equal steps during data collection. During data collection, the VNA excited MMW signals to each transmitter located on the sensor array at frequency of 23 GHz. The scattered signals from the target object were measured by each detector. 2D and 3D images of the target object were reconstructed using the proposed imaging algorithms (as detailed above).

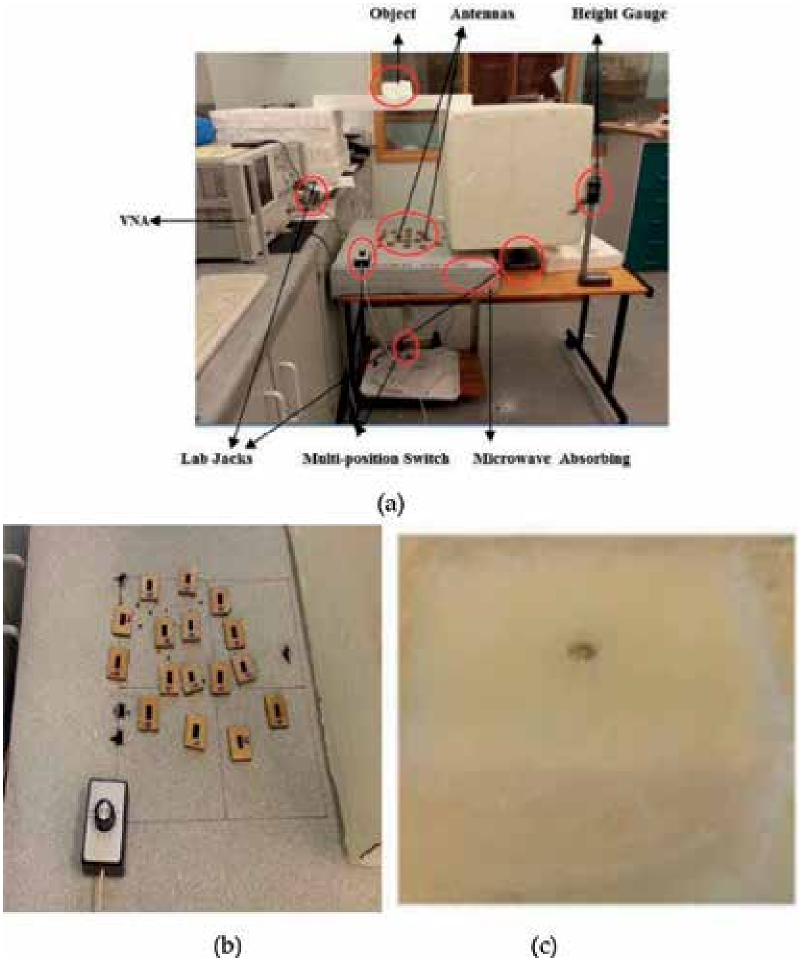

**Figure 10.** (a) HMMW measurement setup; (b) sensor array; (c) target object.

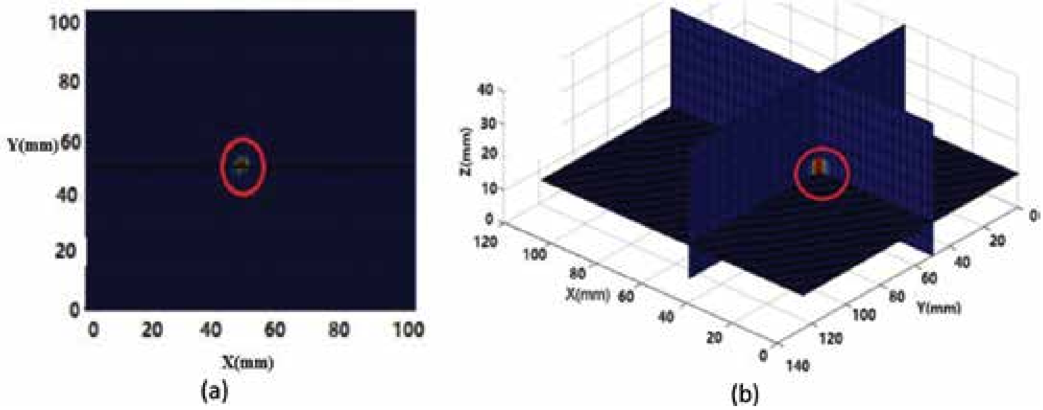

**Figure 11.** (a) 2D reconstructed image of concealed steel ball, (b) 3D reconstructed image of concealed steel ball.

**Figure 11** shows the 2D and 3D reconstructed images of the concealed metallic steel ball. The steel ball is clearly identified in the reconstructed images with correct location, shape and size.

## 5. Conclusions

This chapter investigated the 3D HMMW method for various concealed objects detection and the theory has been evaluated through numerical and experimental validations. It was found that various small concealed metallic and wood objects with different sizes and locations can be identified in the reconstructed HMMW images. Results showed that the proposed HMMW has the potential for investigating characterization and structure of concealed objects. The potential applications of the 3D HMMW include on body weapon detection and packed food quality control.

## Acknowledgements

The author gratefully acknowledges the financial supports from the National Natural Science Foundation of China (Grant No. 61701159, JZ2017GJQN1131), the Natural Science Foundation of Anhui Province (Grant No. 101413246, JZ2017AKZR0129), the Foundation for Oversea Master Project from the Ministry of Education of the People's Republic of China (Grant No. 2160311028), and the start-up funding from the Hefei University of Technology (Grant No. 407037164).

## Conflict of interest

The author declares no conflict of interest.

## Author details

Lulu Wang[1,2]*

*Address all correspondence to: luluwang2015@hfut.edu.cn

1 School of Instrument Science and Opto-electronics Engineering, Hefei University of Technology, Hefei, China

2 Institute of Biomedical Technologies, Auckland University of Technology, Auckland, New Zealand

## References

[1] Gianesin B, Zefiro D, Paparo F, Caminata A, Balocco M, Carrara P, et al. Characterization of ferromagnetic or conductive properties of metallic foreign objects embedded within the human body with magnetic iron detector (mid): Screening patients for MRI. Magnetic Resonance in Medicine. 2015;**73**(5):2030-2037

[2] Appleby R, Wallace HB. Standoff detection of weapons and contraband in the 100 GHz to 1 THz region. IEEE Transactions on Antennas & Propagation. 2007;**55**(11):2944-2956

[3] Bavirisetti DP, Dhuli R. Two-scale image fusion of visible and infrared images using saliency detection. Infrared Physics & Technology. 2016;**76**:52-64

[4] Nation J, Jiang W. The utility of a handheld metal detector in detection and localization of pediatric metallic foreign body ingestion. International Journal of Pediatric Otorhinolaryngology. 2017;**92**:1

[5] Chen HM, Lee S, Rao RM, Slamani MA, Varshney PK. Imaging for concealed weapon detection: A tutorial overview of development in imaging sensors and processing. IEEE Signal Processing Magazine. 2005;**22**(2):52-61

[6] Zhu JZ, Zhang CS, Feng FZ, Min QX, Chao X. Study on probability of detection for fatigue cracks in sonic infrared imaging. Infrared Physics & Technology. 2006;**77**:296-301

[7] Shi X, Yang MH. Development of passive millimeter wave imaging for concealed weapon detection indoors. Microwave & Optical Technology Letters. 2014;**56**(7):1701-1706

[8] Kemp MC. Millimetre wave and terahertz technology for the detection of concealed threats: A review. International Society for Optics and Photonics. 2006;**6402**:10-19

[9] Farsaei AA, Mokhtari-Koushyar F, Seyed-Talebi SM, Kavehvash Z, Shabany M. Improved two-dimensional millimeter-wave imaging for concealed weapon detection through partial Fourier sampling. Journal of Infrared, Millimeter, and Terahertz Waves. 2016;**37**(3):267-280

[10] Du K, Wang W, Nian F, Chen W, Hu FJ. Concealed objects detection in active millimeter-wave images. Systems Engineering & Electronics. 2016;**38**(6):1463-1469

[11] Grossman EN, Miller AJ. Active millimeter-wave imaging for concealed weapons detection. Proceedings of SPIE - The International Society for Optical Engineering. 2003;**5077**: 62-70

[12] Smith GJ. Detection of contraband concealed on the body using x-ray imaging. Human Detection & Positive Identification Methods & Technologies. 1997;**2932**:115-120

[13] Jannson T, Gertsenshteyn M. Hard X-ray focusing optics for concealed object detection. Proceedings of SPIE. 2006;**6213**:2-12

[14] Farhat NH, Guard WR. Millimeter wave holographic imaging of concealed weapons. Proceedings of the IEEE. 1971;**59**(9):1383-1384

[15] Collins DH, Mcmakin DL, Hall TE, Gribble PR. Real-time holographic surveillance system. 1995; US patent, US5455590

[16] Zhao Y, Wang Z, Jiang Z. Digital holographic imaging for diffuse-reflection metal surface with strong feature. In: International Symposium on Optoelectronic Technology and Application. 2016; 101553V

[17] Sheen DM, Collins DH, Hall TE, Mcmakin DL, Gribble PR, Severtsen RH. Real-time wideband holographic surveillance system. 1996; US Patent, US5557283

[18] Nagayama Y, Ito N, Kuwahara D, Tsuchiya H, Yamaguchi S. Development of 2-d horn-antenna millimeter-wave imaging device (HMID) for the plasma diagnostics. Review of Scientific Instruments. 2017;**88**(4):1647

[19] Alotaibi NN, Hamdi KA. Switched phased-array transmission architecture for secure millimeter-wave wireless communication. IEEE Transactions on Communications. 2016; **64**(3):1303-1312

[20] Hu F, Cheng Y, Gui L, Wu L, Zhang X, Peng X, et al. Polarization-based material classification technique using passive millimeter-wave polarimetric imagery. Applied Optics. 2016;**55**(31):8690

[21] Hung CY, Weng MH, Yang RY, Wu HW. Design of a compact CMOS bandpass filter for passive millimeter-wave imaging system application. Journal of Electromagnetic Waves & Applications. 2009;**23**(17-18):2323-2330

[22] Kock WE. Microwave holography. In: Engineering Applications of Lasers and Holography. US: Springer; 1975

[23] Silver S. Microwave antenna theory and design. P. Peregrinus on behalf of the Institution of Electrical Engineers. 1984. pp. 87-90

[24] Wang L, Al-Jumaily AM, Simpkin R. Imaging of 3-D dielectric objects using far-field holographic microwave imaging technique. Progress in Electromagnetics Research B. 2014;**61**:135-147

[25] Levanda R, Leshem A. Synthetic aperture radio telescopes. IEEE Signal Processing Magazine. 2010;**27**:14-29

[26] Wang L, Al-Jumaily AM, Simpkin R. Holographic microwave imaging for medical applications. Journal of Biomedical Science & Engineering. 2013;**6**(8):823-833

[27] Born M, Wolf E. Principles of Optics: Electromagnetic theory of propagation, interference and diffraction of light. Cambridge University Press. 2000

## Section 4

# Microwave Heating and Drying Technologies

# Microwave Technology in Freeze-Drying Process

Mohsen Kalantari

Additional information is available at the end of the chapter

http://dx.doi.org/10.5772/intechopen.74064

## Abstract

Dehydrating is one of the most common processes in industry. This process is implemented by various techniques, such as freeze-drying. It is an energy-consuming process. Microwave sources are a good choice to supply the energy needed for this process. In reality, it is microwave-assisted freeze-drying. The microwave sources can be delivered around a few kilowatts. Electromagnetic energy is converted into thermal energy due to the interaction of electromagnetic fields and materials. In addition to providing energy, the microwave-assisted freeze-drying is time-saving. This method is fast due to penetrating electromagnetic fields in the material. It results in volumetrically heating instead of heating from the surface of the material in conventional methods. Usually, the frequency of electromagnetic fields is 2450 MHz, which is allocated by regulatory commissions in dielectric heating methods. In the following, the mechanism of this method is described. All relations governing the transfer of mass and heat are mentioned. How to transfer and dissipate energy is described. Dielectric properties of different materials are listed. The effective parameters in determining dielectric properties are discussed.

**Keywords:** freeze-drying, dielectric heating, microwave energy

## 1. Introduction

Population growth of human societies results in increasing the demand for requirements such as food, clothing, housing, etc. Meeting them requires new industrial methods instead of traditional ones. The production of foodstuff is included in this principle. Today, different processes are being done on the mineral, vegetable, and animal products. Some of them are pasteurization, sterilization, conservation, etc. Each of them is used for a specific purpose. During these processes, physical, chemical, and biological changes occur. They affect the quality of foodstuff (color, flavor, volume) [1].

Drying is the most common way to increase the life of food products to make them easier to maintain [2]. Meanwhile, microwave technology has achieved a significant position among other methods in food industry. Not only is this method used in food industry but also in pharmaceutical industry and medical sciences, for removing water from aqueous solutions and preserving the blood, bone, and skin [3–5].

In conventional method for drying foodstuff, it is heated, usually by flowing hot air, to evaporate its moisture. Also, the heating can be done by other methods from direct solar radiation to using microwave energy [1, 6]. In freeze-drying method, removing the moisture content of material is done by sublimation of water molecules with internal heating after freezing the material and creating a vacuum [7]. Compared with conventional methods, it causes small irreversible changes in food and thus keeps the quality of product at an excellent level [1, 2, 7]. Rehydration, color (browning), and volume (volume reduction and consequently shrinkage) are key parameters in determining the quality of foodstuff and are considered in [1]. Low temperature in this method helps to stop most bivological reactions, and hence it is suitable for dehydrating heat-sensitive material like biological products [1–3]. However, this method is expensive [1, 7]. It is suitable for valuable foodstuffs like coffee [1]. Accordingly, researchers are trying to find the optimal method by a combination of different methods.

Ref. [1] is a valuable review on the studies, which are done about the quality of foodstuff from different drying methods, and collects and presents different graphs about these parameters. Author in [1] presents a chart which determines the contribution of energy consumed in different operations of freeze-drying process. Also, the cost breakdown for drying two samples (high- and low-value foods) is determined in [1].

Drying (or dehydrating) is removing moisture content from a material. This phenomenon, which required phase change in water content of material, requires a lot of energy [6].

In the traditional method, the needed energy must be transferred from dried layer (into frozen bulk), which has the low thermal conductivity. This means that it takes long time [6]. Microwave technology helps to transfer the needed energy in a form of electromagnetic wave into the frozen region, independent of thermal characteristics of dried layer. Then, the electromagnetic field is dissipated in frozen region and increases its temperature. Since the field is distributed in the frozen region, the dissipation occurs throughout frozen bulk. In fact, it creates internally volumetrically heating [2, 6, 7].

In [8], it is mentioned that the volume reductions (shrinkage) for strawberry dried by freeze-drying and air-drying methods are around 6.6 and 80%, respectively [1, 8].

Ref. [3] considered the conventional and microwave-assisted freeze-drying methods. It showed that the drying time is less than 20% for microwave-assisted freeze-drying method because of volumetrically heating in this method.

## 2. The freeze-drying process

In freeze-drying process, the material must be frozen in the first step. Then, it is followed up with creating vacuum and injecting energy by microwaves in the chamber or storage compartment which contains the frozen food material [2] (**Figure 1**).

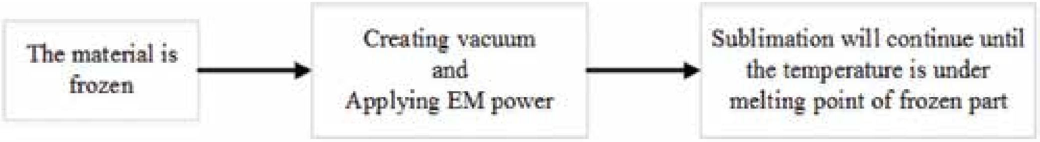

**Figure 1.** Steps must be passed in microwave-assisted freeze-drying process.

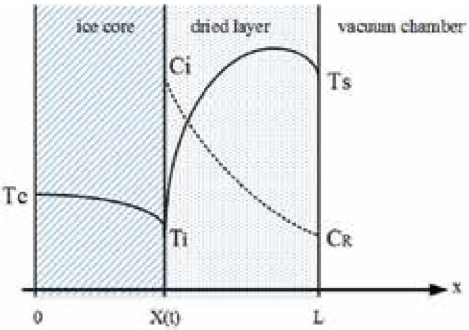

**Figure 2.** Profile of different layers with typical variations of temperature in them for an infinitely long slab of material with thickness L (reproduced from [2]).

What happens during these stages? The heating of the frozen food by microwave energy causes the frozen bulk temperature to increase. With increasing bulk temperature, frozen molecules of water receive enough energy and transit from solid phase to gas phase (sublimation of frozen molecule of water). These molecules migrate (from frozen bulk) into vacuum region of chamber. In other words, the moisture is removed from frozen region, and food material is dried. This sublimation starts from the outer layer. Now, a new region forms in frozen bulk from interface of food material and vacuum and dried region (**Figure 2**). As the time proceeds, the interface between dried and frozen regions will retreat. Therefore, the frozen bulk of material is thinned, and the volume of dried section increases [2].

According to the above discussion, we are faced with three physical phenomena: producing thermal energy by dissipation of microwave energy (in frozen bulk), heat transfer (in frozen and dried regions of food material), and mass transfer which is related to the movement (flow) of water vapor in the system (in the dried region). The heat transfer in the freeze zone is done by conduction, while the heat is transferred in the dried region in conduction and convention.

## 3. Heat and mass transfer equations

As mentioned previously, with increasing the temperature of bulk, two heat transfers are carried out in the bulk. The heat transfer in the frozen region is conductive, while the heat transfer in dried region is a combination of conductive and convective. The heat transfer in frozen region obeys the following relation:

$$\rho_F C_{PF}\frac{\partial T_F}{\partial t} + \vec{\nabla}\cdot\left(-\vec{k}_F\cdot\ \vec{\nabla}\, T_F\right) = p_d \tag{1}$$

where $T_F$, $\rho_F$, $C_{PF}$, $\vec{k}_F$, and $p_d$ are temperatures of frozen region, density of frozen material, heat capacity of the frozen material, the vector of thermal conductivity of frozen material, and density of dissipated microwave power, respectively. All of them are for frozen zone. The convective transfer in dried region is due to the flow of water vapor through this region. Hence, in dried region, the heat transfer obeys the following relation:

$$\rho_D C_{PD}\frac{\partial T_D}{\partial t} + \vec{\nabla}\cdot\left(-\vec{\mathrm{k}}_{\mathrm{D}}\cdot\ \vec{\nabla}\, T_D\right) = p_d - C\vec{W}\cdot\vec{\nabla}\, T_D \tag{2}$$

where $C$ and $\vec{W}$ are concentration and the vector of mass flux, respectively. These two parameters are related to water vapor. All other parameters are the same ones in the previous formula but for dried zone. This relation shows our need to know the concentration of water vapor. The water vapor concentration obeys the mass transfer relation. Relation (3) specifies the variation of concentration ($C$) of water vapor in dried layer:

$$\vec{\nabla}\cdot\left(\vec{D}\cdot\vec{\nabla}\, C\right) = \sigma\frac{\partial C}{\partial t} \tag{3}$$

where $\vec{D}$ and $\sigma$ are the vector of effective diffusivity and porosity of the dried material, respectively. It is possible to find the distribution of temperature by simultaneously solving these equations. Initial and boundary conditions must be considered to solve these equations. Also, the thermodynamic equilibrium, governed at the interface of frozen and dried region, determines the relationship between the concentration of water vapor and the temperature of frozen region [2, 3].

It is evident that density and porosity of food material, along with moisture and fat content, are the key factors in the determining the process.

## 4. The transient variation of temperature during freeze-drying

When an infinitely long slab of the proposed material is available, it can be assumed that all variations happen in direction orthogonal to the surface of slab (one-dimensional variation). The typical distribution of temperature in different layers (frozen, dried, and vacuum) and the concentration of water vapor in dried layer are shown in **Figure 2**. It is sufficient to show the variation only in just half of the structure because of symmetry.

where $T_c$, $T_i$, $T_S$, $C_i$, and $C_R$ are the temperatures in the middle of frozen bulk, the temperature of interface (between frozen and dried regions), the temperature of vacuum, the concentration of water vapor in interface (between frozen and dried regions), and the concentration of water vapor in interface of vacuum and dried regions [2]. The sublimation will continue until the temperature of dried zone (in the interface) is kept under the melting point of frozen region [2]. The variation of temperature in dried region is a part of the parabolic. It is valid for frozen region, too.

For beef meat, cut into a slab, the temperature distribution is demonstrated for different times by [2] (**Figure 3**). Its thickness is 1 inch and is in the middle of chamber.

From **Figure 3**, the concentration of water vapor in dried region is decreased by getting away from the interface (between frozen and dried layers). The necessary energy for this system is provided by electromagnetic waves at 2450 MHz. In [2], it is assumed that the electric field is approximately uniform throughout the material and its intensity equals to 12.5 KV/m. The total pressure and partial pressure of water vapor in the vacuum region are 0.29 and 0.075 mmHg, respectively. The drying time for this meat is measured 6 hours when applied electric field is nearly 10 KV/m [9]. Generally, the higher the electric field intensity, the smaller the drying time (**Figure 4**).

In [2], it has been shown that the optimum operation of freeze-drying process is obtained near the corona and melting point. For a slice of meat in a rectangular cross section, the variation of temperature and concentration happened in two dimensions. **Figures 5** and **6** are shown in simulation and experimental results [7].

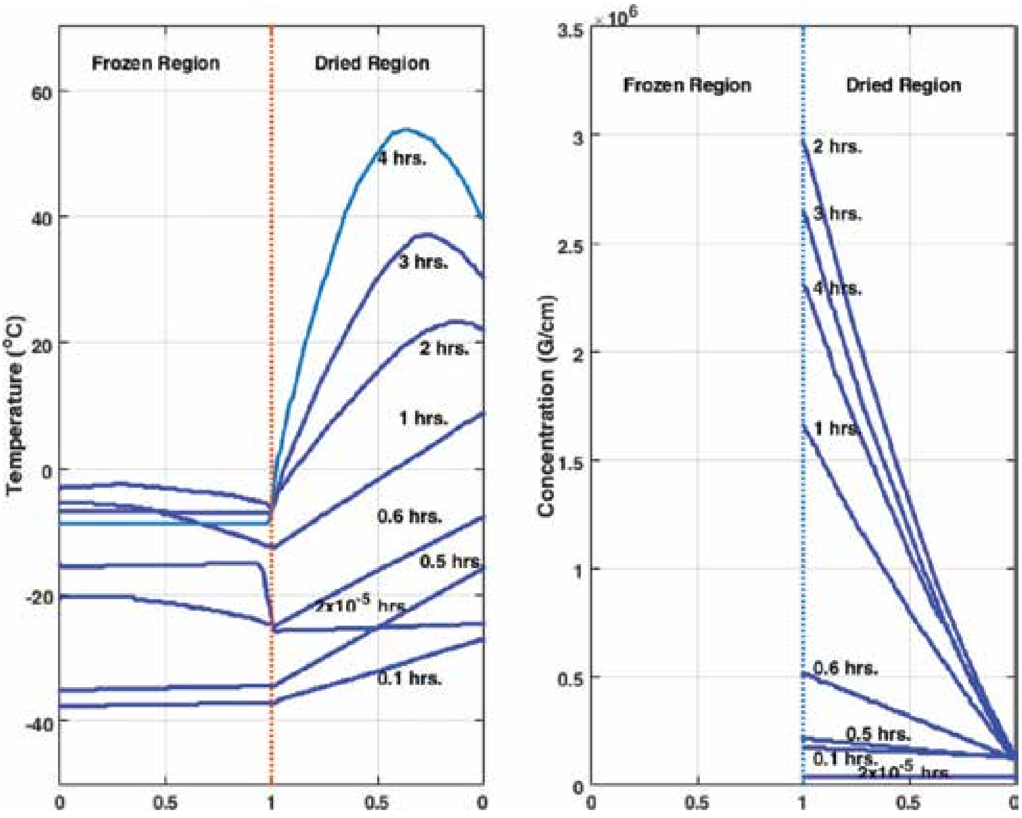

**Figure 3.** The temperature (left) and concentration (right) profiles for a slab of beef meat in different times (reproduced from [2]).

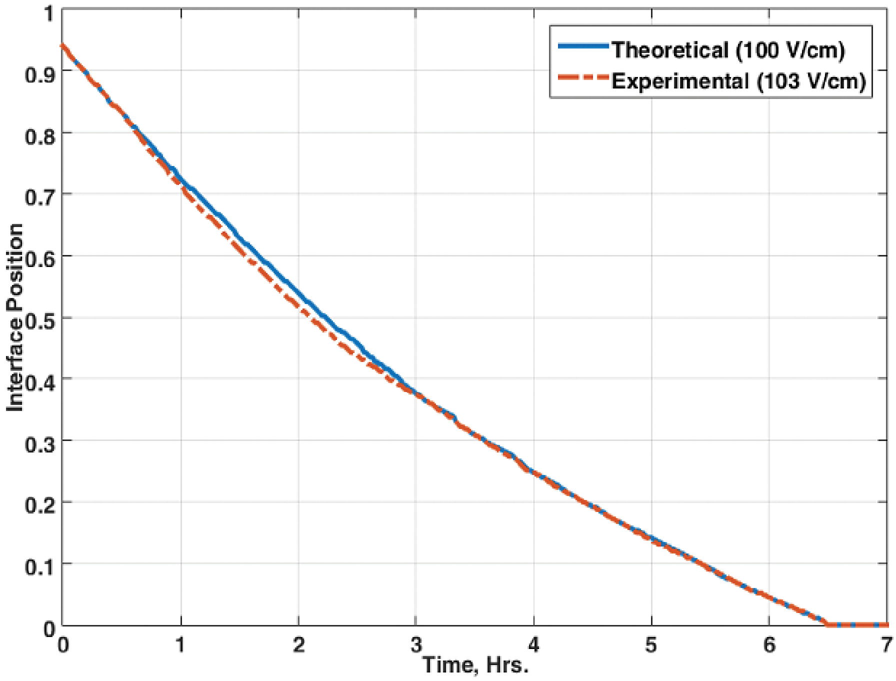

**Figure 4.** Dry time for a slab of beef meat (reproduced from [9]).

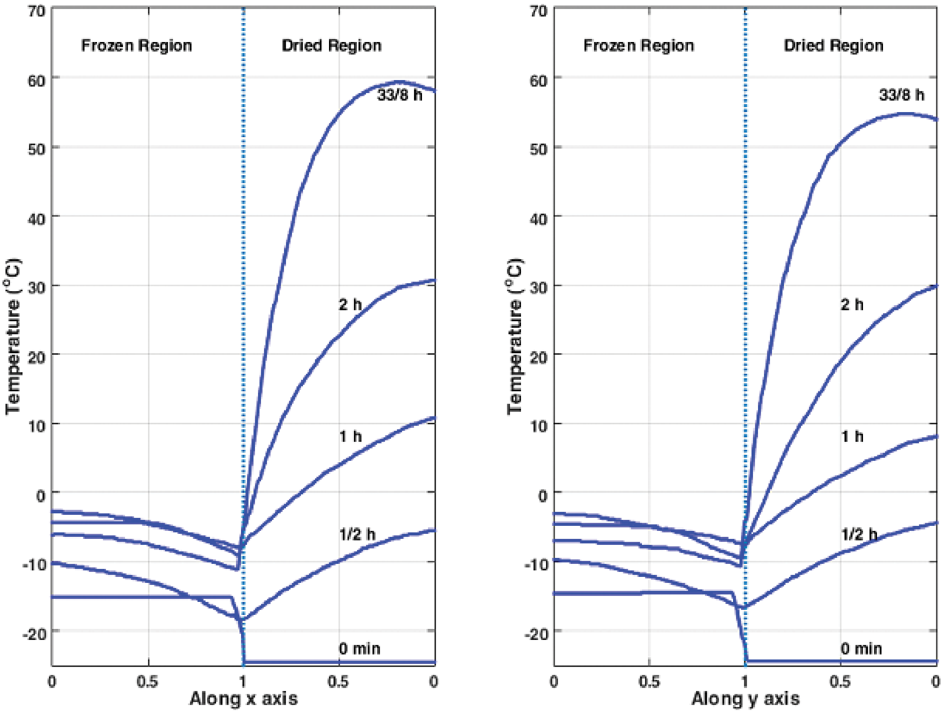

**Figure 5.** The temperature profile along X and Y axes for a bar of meat with square cross section (reproduced from [7]).

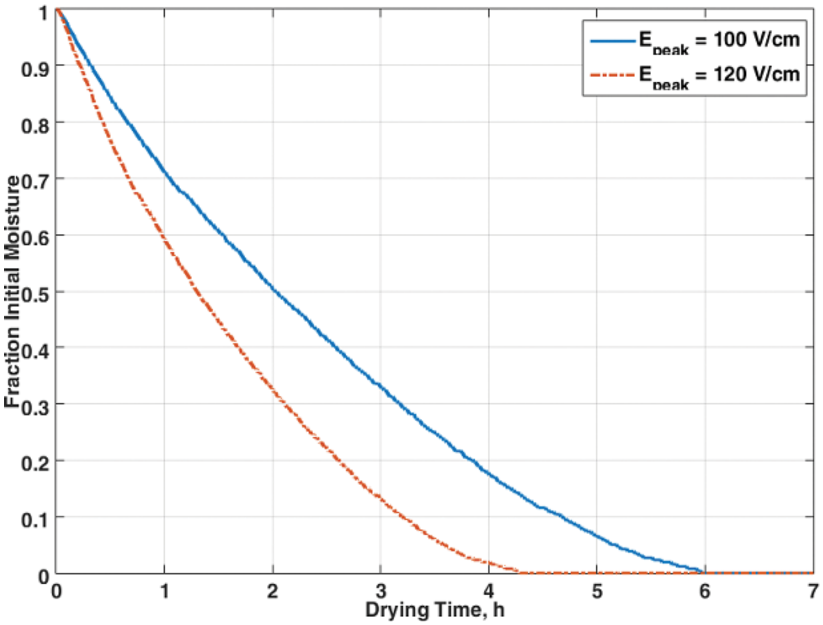

**Figure 6.** The time variation of moisture content for a bar of meat with square cross section (reproduced from [7]).

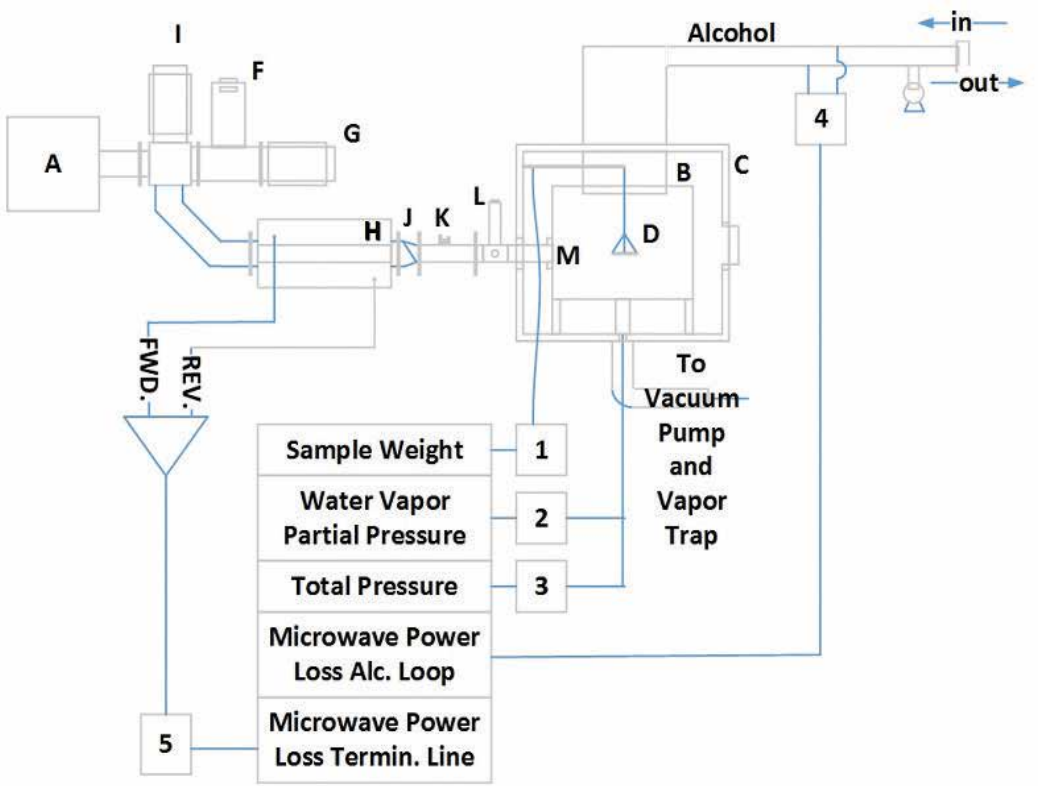

**Figure 7.** A setup used to microwave-assisted freeze-drying process (reproduced from [2]).

**Figure 7** shows a setup used in [9] for freeze-drying process by injecting microwave power. A microwave oven supplies sufficient adjustable energy. A magnetron with the capability of delivering 1.2 KW adjustable power at 2450MHz is used in the oven (A). The proposed material (D) is located in the middle of microwave cavity (B), and they are surrounded by a vacuum chamber (C). This cavity has dimensions 39 × 39 × 51 cm, all of its walls are made of perforated aluminum sheets to supply the needed electromagnetic boundary conditions and provide a path to free flow of water vapor simultaneously. To avoid harmful reflection from the cavity, a circulator is used just after the generator. To absorb the reflected power, it is necessary to match other ports of the circulator. A twist (J) is used to change the polarization of transmitted wave. The electric field, at the output of twist, is vertical to slab of beef meat. A bidirectional coupler (H) is used to measure the forward and reflected waves. These data are used to determine lost power, including all components in addition to proposed material (D) [2].

Also, [3] presents a microwave freeze-drying setup in a laboratory scale.

## 5. Microwave energy and dielectric properties of different materials

According to what had been mentioned previously, the needed enthalpy for sublimation is provided by electromagnetic radiation at microwave frequency. Microwave heating is the result of the interaction between microwave fields and dielectric properties of material. In this heating, the required power for sublimation is carried by electromagnetic fields to the frozen region, independent of thermal characteristic of dried region, and then it is dissipated in frozen region and converted to heat. This means that any frozen point is a source of heat [3]. Compared to conventional freeze-drying process, penetrating electromagnetic fields and transferring the needed energy, independent of thermal characteristics of dried region, are the main factors in accelerating dehydrating process in microwave freeze-drying process [3]. Volumetric heating of frozen material accelerates drying process as fast as 75% [7].

For dielectric heating, some specific frequencies are released by the Federal Communications Commission (FCC) in microwave region: 913, 2450, and 5800 MHz [10, 11]. The 2450MHz is more common and used in home microwave oven [10].

Microwave radiation has unique advantages that make it suitable for food industry. The following are two of them:

(a) Microwave radiation is nondestructive and non-ionization radiation; hence, it is safe and does not contaminate and deteriorate the material.

(b) The electromagnetic waves are passed from dielectric materials in microwave frequencies, while these media are not transparent to light and infrared radiation (opaque). It is a useful tool for probing the dielectric material thoroughly [12]. This property is used in freeze-drying method to transfer energy inside the dielectric.

Also, microwave radiation is widely used in agriculture: remote sensing, short-range radars, and Doppler radar. Short-range radars are helpful for recognizing and tracking the seasonal migration of birds and insects. Also, Doppler radar is used to monitor the mass flow rate of crop [12], detecting and controlling the insects in stored grains and heating seeds with impermeable coat by microwave radiation to improve their germination and determination of moisture content of agricultural products [12].

Microwave energy is used to defrosting meat. It reduces the required time from hours to a few minutes. Also, it is used in sterilizing some heat-sensitive foods and cacao bean roasting [12].

In microscopic scale, when a dielectric is subjected to the electric field, their molecules are arranged to reduce the overall electric field in the bulk of dielectric (**Figure 8**). This arrangement depends on constitutive molecules and their polarizations. In other words, the molecules reacted to the applied field.

The molecules start to oscillate by applying the electric field with sinusoidal variation. Friction between molecules in the oscillation produces heat (as a thermal source) and increases the temperature of dielectric [7, 10]. Since the needed energy for oscillating molecules is provided by the electric field, the generated heat is as a result of energy conversion (from electromagnetic to thermal). Another phenomenon, which is effective in the loss factor of a dielectric, is ionic conduction. It relates to movement of dissolved ions, and the generation of heat when these ions collide with other molecules and atoms [10]. In a macroscopic view, this phenomenon is characterized by imaginary part of permittivity. Also, real part of permittivity is known as an ability of structure to be polarized.

Generally, the electromagnetic properties of each material are specified by relative electric permittivity ($\varepsilon_r$) and magnetic permeability ($\mu_r$), both of them are complex quantities. The real and imaginary parts of $\varepsilon_r$, which are known as dielectric constant and loss factor, are related to stored and dissipated electrical energy in the material, respectively [12]:

$$\varepsilon_r = \varepsilon_r' - j\,\varepsilon_r'', \; tan(\delta) = \frac{\varepsilon_r''}{\varepsilon_r'}, \; p_d = \omega\varepsilon_0\varepsilon_r''\,|E|^2 \tag{4}$$

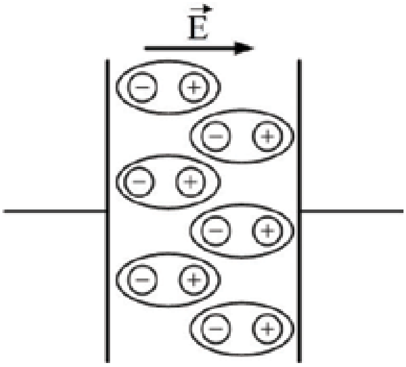

**Figure 8.** The arrangement of molecules when dielectric is subjected in external electric field.

where $p_d$ is the volume density of dissipated power (W/m$^3$) and $E$ is root-mean-square value of electric field. This is the rate of absorbed microwave energy which is converted to heat. In reality, these parameters must be replaced in the right-hand side of Eqs. (1) and (2) [10].

The dissipated power is proportional to $\varepsilon''$ and square of applied electric field. The more $\varepsilon''$, the more the dissipated power. In freeze-drying process, the dissipation factor of frozen meat is much more than a dried meat, so the dissipated power in the frozen region is much more than a dried region. The dissipated power can be maximized if the material is located in where the electric field is maximum. The more $\varepsilon'$, the more the ability in polarization for a dielectric.

To obtain the electromagnetic fields formed in foodstuff, Maxwell's equations must be solved. They depend on the cavity, dielectric property, and geometry of material [10]. As known, Maxwell's equations are a set of partial differential equations that are coupled to each other:

$$\overrightarrow{\nabla} \times \vec{E} = -\frac{\partial \vec{B}}{\partial t}, \overrightarrow{\nabla} \times \vec{H} = \vec{J} + \frac{\partial \vec{D}}{\partial t}, \overrightarrow{\nabla} . \vec{D} = \rho, \overrightarrow{\nabla} . \vec{B} = 0, \vec{D} = \varepsilon_0 \varepsilon_r \vec{E}, \vec{B} = \mu_0 \mu_r \vec{E} \tag{5}$$

The last two equations determine the interaction of electromagnetic fields with matter. By considering the boundary conditions, solving these equations determines electromagnetic fields.

As mentioned previously, microwave energy is needed to heat the frozen material in microwave freeze-drying method. Accordingly, a microwave system must be designed to generate and deliver microwave energy to an applicator in the chamber. Therefore, each microwave system consists of three parts, source, applicator, and transmission media, for transferring power from the source to the applicator [13]. The applicator plays the role of a load in this system. Usually, waveguides and their components are used to provide transmission media.

Typically, vacuum tubes are used for generating high power at microwave frequencies. They include klystron, magnetron, traveling-wave tube (TWT), and so on. The magnetron is a more common tube which is used in the industry and home applications [13]. The following figure shows the position of magnetron among other microwave sources.

The output power of magnetron is usually ranged between 500 and 1500 W for home microwave oven [14]. For industry application, this power is up to 10 KW and more [7, 13, 15] (**Figure 9**).

Generally, the mechanism of a vacuum tube is due to the interaction between electromagnetic field and electron beam inside a vacuum envelope (**Figure 10**) [14]. For magnetron, the envelope consists of multi-cavity resonators along the peripheral of a cylinder. An electron gun, coincided with the cylindrical axis of the tube, produces an electron beam in the magnetron. In practice, energy is transferred to the electromagnetic field through electron beam, after electron bunching occurs. The way for output power can be provided through a probe, loop, or window [14].

The efficiency of microwave oven is less than 50%, which is more than conventional heating [14]. For modern magnetrons, this parameter is 70% [13, 16] (**Figure 11**).

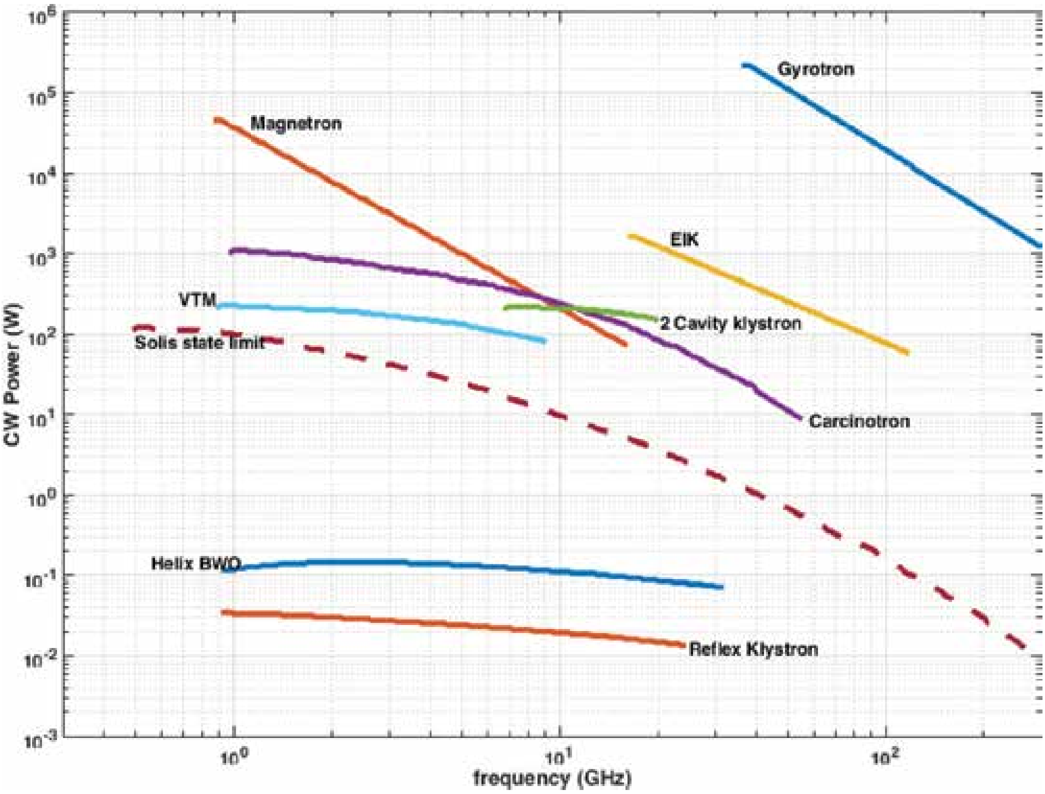

**Figure 9.** The position of magnetron among other microwave sources (reproduced from [14]).

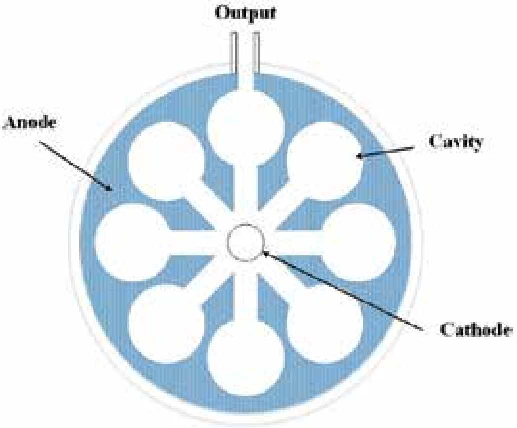

**Figure 10.** Top view of a magnetron (reproduced from [13]).

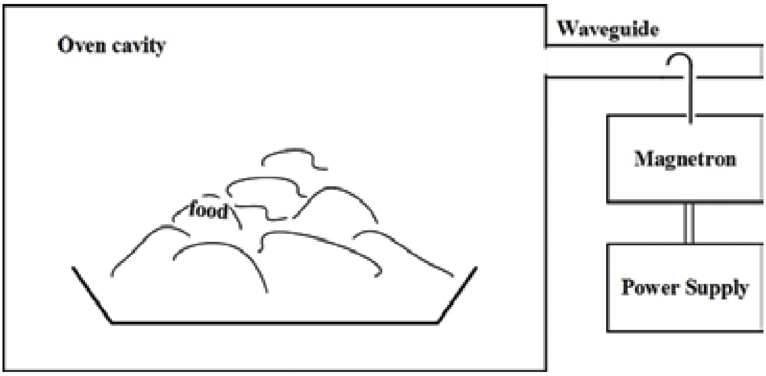

**Figure 11.** A microwave oven (reproduced from [14]).

The waveguide is a hollow conductor with uniform cross section, usually rectangular and circular, that is a mediator between source and load for transferring energy. **Figure 12** shows the rectangular and circular waveguides.

The energy transfer in waveguides is carried out in a form of propagating modes. To determine different modes in a waveguide, Maxwell's equations must be solved with respect to necessary boundary conditions (zero tangential electric fields in the sidewalls of waveguide). In reality, each mode determines the distribution of electric and magnetic fields in the transverse plane. Each mode is characterized by its cutoff frequency ($f_c$). For frequencies higher than $f_c$, the mode propagates inside the waveguide, and the mode is evanescent for frequencies lower than $f_c$ [14]. Hence, the waveguides are known as high-pass structures. The mode with the lowest $f_c$ is known as dominant mode. From the lowest to highest frequencies, this mode is the first mode that is propagated in the waveguide. With increasing frequency, other modes are excited in the waveguide. This state is called overmode [14]. Usually, each waveguide is used in a dominant mode. The dominant mode is $TE_{10}$ for rectangular waveguide and is $TE_{11}$ for circular waveguide.

Among other guiding-wave structures, waveguide has low loss property in high frequency, which enables it to carry very high power.

According to the above discussions, a wave can be propagated along the waveguide. When the open end of waveguide is shorted, the power is reflected back (to the source), and standing wave is formed in the waveguide. A cavity can be made by blocking both ends of a section of

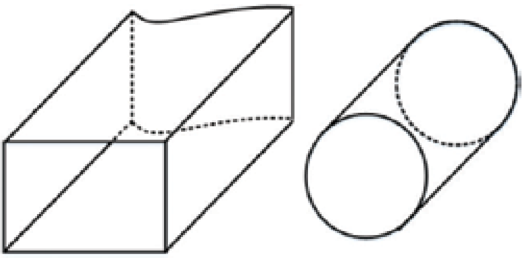

**Figure 12.** Rectangular and circular waveguides.

waveguide. This structure is capable to store energy at specific frequencies. These frequencies are determined by characteristic equation. For dissipating the stored energy, it is enough to fill the cavity with lossy material. The cavity is excited by a probe, a loop, or an aperture in its sidewall. The excited fields are achieved by solving Maxwell's equations with respect to boundary conditions. The boundary conditions are zero tangential electric fields in all sidewalls of the cavity.

Dependent on the electrical length of different dimensions of the cavity, the cavities are divided into two categories: mono-mode and multimode cavities. The mono-mode cavity has small dimensions, in the range of wavelength, so that the single mode is excited inside it [13]. Therefore, this cavity is not suitable for big-volume material [13]. The excited mode is created at certain frequency because of resonant nature of mono-mode cavity. For maximizing absorbed power, the foodstuff must be located in the position(s) of the maximum electric field. Since maximum electric field occurs in one or a few positions, then the single-mode cavity is suitable for material with high loss. Increasing the dimensions of the cavity causes the excitation of different modes simultaneously. The excitation of different modes is dependent on cavity dimensions, the location of material and its electrical characterizations, and so on. The excitation of multimodes results on nonuniform field distribution in the cavity and nonuniform heating absorption in turn [13].

In freeze-drying method, frozen material is placed inside a cavity. The cavity is excited, and microwave energy is dissipated by material to provide needed energy for sublimation. In other words, the material absorbs microwave energy (a sink for microwave energy), and it is similar to a load for microwave system. Some stubs are used to match the load and prevent the reflecting waves coming back to the source.

Different methods are developed for measuring the permittivity of material. One of them uses resonant cavity to measure the permittivity. It is used in microwave frequencies and is based on perturbation theory. In this method, a small volume of material (relative to volume of the cavity) is placed in the point where the electric field is maximum. The existence of material in the cavity is equal to change in resonant frequency of the cavity [14]:

$$\frac{\omega - \omega_0}{\omega_0} \approx -\frac{\int_{V_0}(\Delta\varepsilon\,|E_0|^2 + \Delta\mu\,|H_0|^2)dv}{\int_{V_0}(\varepsilon\,|E_0|^2 + \mu\,|H_0|^2)dv} \tag{6}$$

Subscript 0 indicates the parameters of the cavity in the absence of material. Another method uses open-ended transmission line. This structure behaves as a resonator at microwave frequency. Different parameters affect the resonant frequency of this structure such as the length of line and fringing fields in the open end of line. The existence of different materials in the open end of line changes the fringing fields. In equivalent circuit, these fields are modeled by a capacitor (**Figure 13**). Its capacitance is affected by the medium at the open end of line. Changes in resonant frequency are due to permittivity of the proposed material, provided that other key factors do not change [12].

For low frequency, it can be possible to use a capacitor for measuring dielectric permittivity of material. In this method, the proposed material is used as a dielectric for the capacitor. It is sufficient that this capacitor is connected to a sinusoidal signal generator with a resistor in a series of combination. Now, the voltage dropped through the capacitor is measured in two

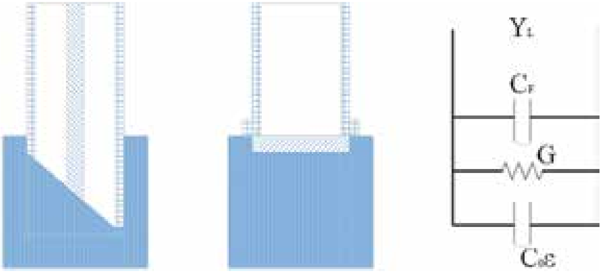

**Figure 13.** Open-ended transmission line and its equivalent circuit (reproduced from [12]).

cases: a capacitor with and without the proposed material as the insulator of capacitor. The change in dropped voltage depends on the change in capacitance. Accordingly, the change in capacitance of capacitor is related to the permittivity of material.

While for most of agricultural products, $\mu_r$ is assumed to be the unity, since most of the foodstuffs are nonmagnetic products [10], the permittivity for each material depends on its moisture content, operating frequency, temperature, etc. [12]. Different models have been proposed to follow the frequency variation of a dielectric such as Drude, Debye, Lorentz and Cole-Cole models [10].

For food products, the chemical compositions such as salt play a decisive role in dielectric properties of products [10]. Also, dielectric properties can be affected from physical properties, such as bulk density, particle size, and homogeneity [10]. For hygroscopic material, the water content is the most important factor in the dielectric constant [10].

The dielectric constant for water is 78 at room temperature. For the moist food, this parameter ranges between 50 and 70, and their loss factor is less than 25 [10]. For organic constituents in food material, the dielectric constant and loss factor are less than 3 and less than 0.1, respectively [10, 17].

Researches and studies have shown that water is the most important part which absorbs microwave energy in foodstuff [10, 17–19]. The dielectric property of water is listed in **Table 1** for different frequencies.

**Table 2** lists the dielectric properties of some fruit and vegetable in two frequencies.

| **Frequency (MHz)** | | **0.6** | **1.7** | **3** | **4.6** | **7.7** | **9.1** | **12.5** | **17.4** | **26.8** | **36.4** |
|---|---|---|---|---|---|---|---|---|---|---|---|
| $\varepsilon'$ | $T = 20°C$ | 80.3 | 79.2 | 77.4 | 74 | 67.4 | 63 | 53.6 | 42 | 26.5 | 17.6 |
| | $T = 50$ °C | 69.9 | 69.7 | 68.4 | 68.5 | 67.2 | 65.5 | 61.5 | 56.3 | 44.2 | 34.3 |
| $\varepsilon''$ | $T = 20°C$ | 2.75 | 7.9 | 13 | 18.8 | 28.2 | 31.5 | 35.5 | 37.1 | 33.9 | 28.8 |
| | $T = 50$ °C | 12.5 | 3.6 | 5.8 | 9.4 | 14.5 | 16.5 | 21.4 | 27.2 | 32 | 32.6 |

**Table 1.** The dielectric property of water [10, 20].

| **Fruit/vegetable** | | **Apple** | **Banana** | **Carrot** | **Grape** | **Mango** | **Orange** | **Potato** | **Strawberry** |
|---|---|---|---|---|---|---|---|---|---|
| Moisture content (%) (wet basis) | | 88 | 78 | 87 | 82 | 86 | 87 | 79 | 92 |
| Tissue density ($g.cm^{-3}$) | | 0.76 | 0.94 | 0.99 | 1.1 | 0.96 | 0.92 | 1.03 | 0.76 |
| $\varepsilon'$ | 915 MHz | 57 | 64 | 59 | 69 | 64 | 73 | 62 | 73 |
| | 2450 MHz | 54 | 60 | 56 | 65 | 61 | 69 | 57 | 71 |
| $\varepsilon''$ | 915 MHz | 8 | 19 | 18 | 15 | 13 | 14 | 22 | 14 |
| | 2450 MHz | 10 | 18 | 15 | 17 | 14 | 16 | 17 | 14 |

**Table 2.** The dielectric properties of some fruits and vegetables in two frequencies [10, 15].

Ref. [10] is a valuable and comprehensive paper that reviews many references and collects (and integrates) diverse information about dielectric property of different agriculture and food materials (flour, dough, milk, cheese, nuts, fish, seafood, meat). More discussions are available on how to change the dielectric property for different materials [10].

## 6. Conclusion

The freeze-drying method is described in this chapter. Different relations, related to heat and mass transfer in the system, are mentioned. Time variation of temperature in different layers of system is shown. Then, the interaction between electromagnetic field and molecules of material is expressed. Dielectric properties of different foodstuffs are presented from different references. Different parts of a microwave system are fairly explained, too.

The final stage of freeze-drying method is time-consuming when the frozen region is disappearing. This method is costly and affordable for high-value food like coffee.

## Author details

Mohsen Kalantari

Address all correspondence to: mohsen_kalantari@ymail.com

Department of Electrical Engineering, Shahid Beheshti University, Tehran, Iran

## References

[1] Ratti C. Hot air and freeze-drying of high-value foods: A review. Journal of Food Engineering. 2001;**49**(4):311-319

[2] Ma YH, Peltre PR. Freeze dehydration by microwave energy: Part I. Theoretical investigation. AICHE Journal. 1975;**21**(2):335-344

[3] Wang W, Chen G. Freeze drying with dielectric-material-assisted microwave heating. AICHE Journal. 2007;**53**(12):3077-3088

[4] Wang W, Chen G. Theoretical study on microwave freeze-drying of an aqueous pharmaceutical excipient with the aid of dielectric material. Drying Technology. 2005;**23**(9-11): 2147-2168

[5] Adams GDJ. Freeze-drying of biological materials. Drying Technology. 1991;**9**(4):891-925

[6] Sunderland JE. Microwave freeze drying. Journal of Food Process Engineering. 1980;**4**(4):195-212

[7] Ang TK, Ford JD, Pei DCT. Microwave freeze-drying of food: A theoretical investigation. International Journal of Heat and Mass Transfer. 1977;**20**(5):517-526

[8] Janković M. Physical properties of convectively dried and freeze-dried berrylike fruits. A Publication of the Faculty of Agriculture, Belgrade. 1993;**38**(2):129-135

[9] Ma YH, Peltre PR. Freeze dehydration by microwave energy: Part II. Experimental study. AICHE Journal. 1975;**21**(2):344-350

[10] Venkatesh MS, Raghavan GSV. An overview of microwave processing and dielectric properties of agri-food materials. Biosystems Engineering. 2004;**88**(1):1-18

[11] Decareau VR. Microwaves in the Food Processing Industry. London: Academic Press. Inc; 1995

[12] Kraszevvski AW, Nelson SO. Microwave techniques in agriculture. Journal of Microwave Power and Electromagnetic Energy. 2003;**38**(1):13-35

[13] Schubert H, Regier M. The Microwave Processing of Foods. Taylor & Francis; 2005

[14] Pozar DM. Microwave Engineering. John Wiley & Sons; 2012

[15] Nelson SO, Forbus WR, Lawrence KC. Microwave permittivities of fresh fruits and vegetables from 0.2 to 20 GHz. Transactions of the ASAE. 1994;**37**(1):183-189

[16] Yokoyama R, Yamada A. Development status of magnetrons for microwave ovens. In: Proceeding of 31st Microwave Power Symposium, Boston, Massachusetts. 1996. pp. 132-135

[17] Mudgett RE. Dielectric properties of food. In: Decareau RV, Editor. Microwaves in the Food Processing Industry. Orlando: Academic Press; 1985. pp. 15-37

[18] Von Hippel AR. Dielectric Materials and Applications (Vol. 2). Artech House on London: Demand; 1954

[19] Nelson SO, Kraszewski AW. Grain moisture content determination by microwave measurements. Transactions of the ASAE. 1990;**33**(4):1303-1305

[20] Hasted JB. Aqueous Dielectrics. New York: Chapman and Hall; 1973

Chapter 9

# Microwave-Assisted Green Extraction Technology for Sustainable Food Processing

Ruhan Askin Uzel

Additional information is available at the end of the chapter

http://dx.doi.org/10.5772/intechopen.76140

**Abstract**

Today, the relationship between the concepts of environment, food, society, and health are frequently examined. It is necessary for people to understand the process consciously from the time when the foodstuffs are procured to reach their hands in order to prepare healthy living conditions for them. Previously used techniques for the production of foodstuffs, although adequate in terms of yield, can hardly adapt to environmental criteria. Instead, green techniques are being used that provide savings both in time and energy and that nutrients in foods can be obtained without loss as much as in traditional techniques. Green technology is most obviously applied to extraction. Microwave-assisted extraction (MAE), which is known as a kind of green extraction technology, can be easily and innovatively compared with other extraction techniques. Within the scope of this study, the concept of sustainability in food production has been explained, and the traditional and new extraction techniques have been explained. As a new extraction technique, information about the types of green extraction method has been given, and explanations have been made to explain the definition, mechanism, application fields, advantages, and disadvantages of MAE technique.

**Keywords:** extraction, food process, green technology, microwave-assisted techniques, sustainability

## 1. Introduction

Food has a vital role in human's life. Increasing demand on food because of growing population of the world necessitates to change food production and consumption ways [1]. The idea of "sustainable development" or "sustainability" has become increasingly prominent across the globe, applied and discussed at the international and national level [2]. In this context, resources need to be used effectively for both food production and food consumption. For that reason, food industry officials have to become conscious on sustainable green food production and are researching alternative food processing techniques. There is an increasing public awareness of health, environment, and safety hazards associated with the use of organic solvents in food processing. High cost of organic solvents and increasingly stringent environmental regulations have pointed out the need for development of new and clean technologies for food product processing [3]. At this point, the importance of new and environmentally friendly techniques and their multidisciplinary combinations becomes noticeable. Those alternative techniques have been focused to acquire energy from various sources while controlling the emission rate as well as applying the limits on food safety and control. Among them, being a green technology, microwave-assisted extraction (as a side branch of extraction) has been proposed in a new promising way to produce inevitable variety of food production [4].

Microwave-assisted green extraction technology is a new promising warranty of alternative investment channels for innovative applications and scale-up processes. The possibility of using microwave-assisted technologies has received an increasing attention to develop new technologies for the production of materials or to substitute traditional technologies based on the use of organic solvents. This multidisciplinary synergy will allow scientists to develop products of standardized concentration of active ingredients and will simultaneously produce nutraceutical and pharmaceutical products of much higher concentration and quality than possible by conventional chemical engineering unit operations, such as liquid/liquid extraction, distillation, mechanical micronization, liquid- and/or gas-phase reactions, etc.

In the context of this chapter, the importance of microwave-assisted green extraction technology focusing on food examples will be introduced. Besides, while practicing production techniques about food, some technical expressions such as raw material selection, energy efficiency, resource and waste management, product valorization, fractionation, and analysis methods will also be explained in the framework of emerging microwave technologies' concept. To conclude, within the scope of this chapter, how to produce different foodstuffs or raw materials not only by classical methods but also by cooperation with different innovative techniques of microwave technology will be explained with examples of various food samples while providing theoretical background on food processes.

## 2. Sustainable food systems

It is an inevitable reality that food materials are necessary for the survival of life. In today's world, everybody is producing as much food as they can, but still 800 million people are starving. It is estimated that about 2 billion of the number are included with malnourished people. There can be many reasons for hunger. As well as environmental reasons such as soil and water deficiency and climate change, control of markets and food systems by companies, unfair income distribution, and prices can also create hunger [5]. The last half-century has been endeavoring to end the hunger and malnutrition of the world, to enable people to access healthy food and to produce food using sustainable technologies. It is obvious that the concepts of food, health, safety, and environment and the demographic and ethnic structure of the societies, as well as the lifestyle and social development levels of the societies, are mutually connotations. However, taking environmental considerations into consideration, it is essential to take important steps in order to apply green production principles, go beyond awareness in the awareness of the situation, and make food production based on sustainable bases.

According to the definition of the United Nations, sustainability is stated as "the ability of future generations to meet today's needs without jeopardizing their ability to meet their own needs" [6]. So, it can be defined and practiced in a way that today's social order will enable the living standards and business models to be used without damaging the possibilities of meeting the needs of future generations of resources that exist in nature. It is possible to classify the concept of sustainability as three-dimensional when going out from the definitions made. The factors that make up these dimensions can be grouped into three classes: social, economic, and ecological. The common goal for all factors is to solve current global problems.

Sustainability in food, which is the starting point of the food industry, is possible with adequate systems and applications to produce adequate and high-quality agricultural products at reasonable costs and to continuously improve the protection of agricultural land, farmers, and the environment and natural farming resources. Good sustainable food production practices are systems developed for this purpose. The concept of "sustainability" has gained importance because of the ever-increasing world population and increasing new resource requirements, rising energy prices, and climate changes caused by greenhouse gases. Environmental, social, and economic indicators can be taken into account as indicators of sustainability in food production.

It is generally known that sustainability has economic, social, and environmental dimensions. Sustainability in food is the system in which the social, economic, and environmental dimensions are taken into account in the process from the production to consumption of food. Processes such as the cooperation and cooperation of the civilian people or a group about food, forming their own structures, are defined as sustainable food systems [7]. These structures and processes include production, processing, distribution, wholesale and retail sales, consumption, and waste disposal. Sustainable food systems consist of producers' markets, producer-consumer cooperatives, community-supported agricultural systems, ecological markets, urban gardening, slow food systems, and food banks. The aims of sustainable food systems that have been developed in recent years in our country are defined as:

**a.** To promote adequate, nutritious, and healthy food access for all community members.

**b.** To support small family farming and ensure sustainable agricultural practices.

**c.** To provide direct connection between consumers and producers in processing and marketing processes.

**d.** To ensure the recycling of financial capital and to create business opportunities in food and agriculture-related enterprises.

**e.** To improve the working and living conditions of the workforce in the farm and food system.

**f.** To support local production, processing, and consumption.

The research shows that local products are sold in sustainable food systems and that products are produced by sustainable agricultural systems; thus, natural resources, especially local seeds, are protected. It is stated that the producers are actively involved, developing the producer and consumer interaction and increasing the solidarity. Provision of food safety and security in sustainable food systems, conservation and improvement of health, prevention of diseases, protection of nature, protection of agricultural biodiversity, strengthening of local and rural areas, and ensuring socioeconomic development are taken into consideration.

## 3. Extraction for food production

Among the methods used to obtain fast, accurate, and reliable results in food analyses, the first step is extraction process [8]. Extraction refers to the removal of another liquid phase by taking advantage of the different solubility characteristics of one or more compounds present in the solid or liquid phase [9]. The use of classical extraction methods such as Soxhlet, percolation, and steam distillation is very common in extraction stage [8]. Soxhlet extraction is the method that is frequently used in food extraction and analysis. However, the low efficiency in this method limits the use of the technique, which is low in the analysis and high in solvent consumption [10]. Taking all these conditions into account, the development of new extraction methods has been accelerated.

### 3.1. Traditional extraction techniques

Separation of a substance from two or multicomponent mixtures or the removal of undesirable impurities by solvent aid is called extraction. "Liquid-liquid extraction" is that if the mixture to be separated consists of liquid components. If a substance or group is to be separated from a solid material, this process is called "solid-liquid extraction."

#### *3.1.1. Liquid-liquid extraction*

Liquid-liquid extraction is called separation by contacting a substance dissolved in the liquid solution with another liquid, which does not mix with the solution. The first application of this process is the extraction of gold and silver from the liquid copper by the Romans using lead as solvent.

A simple extraction process consists of three basic components: solute, carrier, and solvent. The part rich in the feed liquid separated from the extractant is called raffinate (aqueous phase), and the part rich in solvent is called the extract (organic phase).

Extraction is generally preferred over distillation in the following cases. These are:

**a.** The presence of dissolved or complexed inorganic substances in the solution

**b.** The desire to separate a very low concentration component

**c.** Separation of components which are very close to boiling or melting points

**d.** Separation of azeotrope-forming mixtures

For example, water can be removed from acetic acid by distillation or liquid-liquid extraction using an organic solvent. Liquid-liquid extraction is used in the industrial separation of many mixtures. In the inorganic chemical industry, extraction is carried out at the removal of water from materials with high boiling points such as phosphoric acid, boric acid, and sodium hydroxide and organics containing hydrogen bonds such as formaldehyde.

#### *3.1.2. Solid-liquid extraction*

Solid-liquid extraction is called separation of one or more components contained in the solid with the aid of a bit solvent. The process can be considered in four stages:

**a.** The phase change of the solute phase and the solvent-phase flow.

**b.** Mechanical separation of the extract phase.

**c.** The separation of the solute from the extract phase.

**d.** The refined solvent is to be sent to the process.

Solid-liquid extraction is the process of separating sugar from sugar beet by means of hot water in a food industry; extracting oils from plants such as peanut, soybean, flaxseed, bean, and cottonseed through organic solvents such as hexane, acetone, and ether; and extracting oils of tea and fish from tea leaves to be used in different processes.

#### *3.1.3. Solvent selection in extraction process*

The most important key parameter in an effective extraction process is the choice of an appropriate solvent. “Similar solver” principle is used. In general, the following considerations are applied when choosing solvents:

**a.** Dispersion coefficient

**b.** Density and viscosity

**c.** Resolution

**d.** Selectivity

**e.** Surface tension between phases

**f.** Reusability

### 3.2. New green techniques for sustainable food production and processing

The efficient use of resources in different branches of the food industry and the maintenance of sustainability is a matter that has been on the move in recent times. At the same time as the use of renewable energy resources, the sector may be economically more advantageous in terms of product cost. Green technology can be applied in many important areas such as logistics, packaging, and waste disposal in food sector. The application of the green extraction technology, which has been particularly popular in recent years, to the food sector has been one of the important outputs of these researches. Extraction processes have also become commercially available in the fields of polymer technology, pharmaceutical industry, certain chemicals, and specialty oils. Products which cannot be obtained by conventional methods or which are difficult to obtain can be produced with high performance by this application. Such applications for environmentally friendly fluids offer significant potential for both technical and economic success. At present, there are many factors that are not paying attention to nutrition inevitably, and it is necessary to present an alternative by increasing the frequency of sharing meetings and by using new technological opportunities for consumers and using new technologies for healthy nutrition. Just as it is in green technology, it is a common view of the food industry that it is an important opportunity to emphasize that these studies have been successfully applied to agricultural products as a healthy alternative to food and that it is an opportunity to share new application fields as research models.

### *3.2.1. Supercritical extraction*

Many food items are produced using different methods and are used after a number of separations [11]. It is also possible to use alterative techniques in conditions more suitable to the particular techniques utilized in production. The primary goal of the production and decomposition processes is to have a process that contributes to the people in production, to the manufacturing enterprises, to the sector, and even to the environment. For this reason, supercritical fluids (SCFs), which have become increasingly popular in the last 40 years, have become the focus of many different food production processes [12–14]. As a result, legal regulations on solvent residue limits in food products and environmental regulations on sector wastes have become widespread, increasing the use of SCFs.

SCFs have several advantages over the conditions provided in conventional methods. The most important advantage is that it allows for less solvent consumption and shorter processing times, as well as achieving dimensions that will not harm the environment in waste regimes. Another important feature of SCFs is that the dissolution power can be controlled by changing the density because the physicochemical properties are located between the gas and liquid phases. A small change in the pressure and/or temperature parameters can make a significant difference in the fluid density used and can increase the solving power by about 80–100 times. Materials with different polarities on this count can be processed by using only one type of SCF. This is due to the fact that the molecular diffusion rate of SCFs is as high as that of gases and the solubility density is as effective as liquids [15]. In parallel with the technological developments used in recent years, new materials and methods have been started to be used in the food processes that are progressing to start with raw material supply [16]. Supercritical extraction (SFE), microwave extraction (MWE), and ultrasonic extraction applications are the most well-known examples.

#### *3.2.1.1. Definition and basic properties of supercritical fluids (SCFs)*

SCF is defined as the fluid whose temperature and pressure values are above the critical temperature (Tc) and critical pressure (Pc) values. In other words, an element or a component can be defined as a mixture of Tc and Pc. Like a gas, it is a compressible flow that can take the form of a container and fill it. It is not a liquid, but has near-liquid density and solubility values (**Figure 1**). Tc and Pc values are different for each supercritical fluid. Tc and Pc values for carbon dioxide, one of the most common supercritical fluids, are 31.1°C and 7.38 MPa and 646.8°C and 22.06 MPa for water, another fluid. Controlled increase in temperature and pressure values brings these two parameters together at a common point called the "critical point." The said Tc and Pc values are the temperature and pressure values possessed at the critical point. When this point is reached, the solvent is described as SCF. The properties in the SCF region are a combination of the good solvency of the fluids and the good diffusivity of the gases (**Table 1**).

Different thermodynamic properties that SCFs exhibit at the critical point and near these points can be predicted with the aid of phase diagrams. From these approaches, different modeling and system optimization studies can be done on the way of engineering.

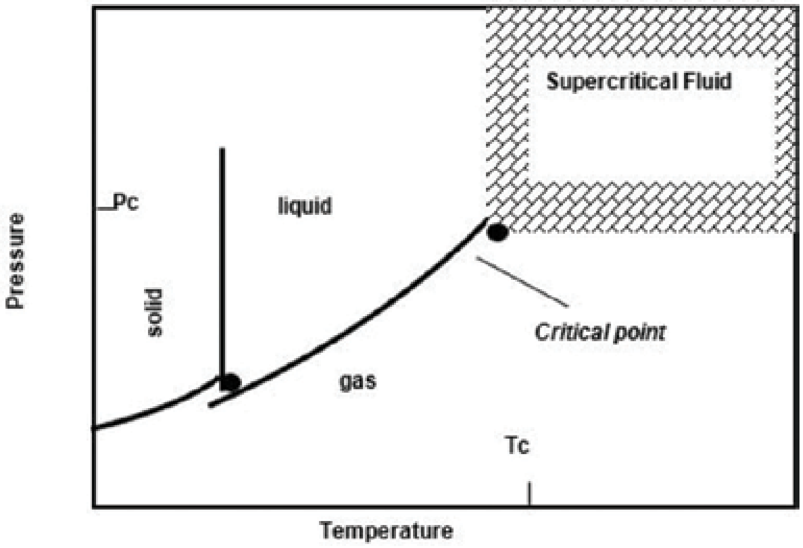

**Figure 1.** SCF temperature-pressure diagram.

| Property | Gas | SCF | Liquid |
|---|---|---|---|
| Density (g/mL) | (0.6–2) × $10^{-3}$ | 0.2–1.0 | 0.6–1.6 |
| Viscosity (g $cm^{-1}$ $s^{-1}$) | (1–3) × $10^{-3}$ | (1–9) × $10^{-3}$ | (0.2–3) × $10^{-2}$ |
| Diffusivity ($cm^2$ $s^{-1}$) | 0.1–0.4 | (2–7) × $10^{-4}$ | (0.2–2) × $10^{-5}$ |
| Surface tension (dynes $cm^{-1}$) | 0 | 0 | 30–60 |

**Table 1.** Properties of some fluids at critical conditions.

### *3.2.1.2. Application areas of supercritical fluid extraction (SFE) in food industry*

SFE is an important alternative to traditional extraction methods. The SFE process can be carried out as a continuous and continuous process depending on the production capacity. In the extraction process, the food substance to be extracted is placed in the extraction cell located in the heating chamber. SCF fed to the system with the aid of a pump is brought to the desired pressure value according to the polarity and solubility characteristics of the target food material and reaches the appropriate temperature level corresponding to the pressure value with the help of the heating reservoir. At this time, the solvent is transported to subcritical or supercritical conditions, and the sample migrates to the extracellular medium contained in the food. Throughout the extraction period, the pressure value of the solvent leaving the extraction cell begins to decrease by interfering with the food and extracting the target material with the polarity appropriate to it. This liquid which is loaded with the target substance and which is in the properties of SCF passes through the liquid fascia by lowering the pressure and, preferably, depending on the desired temperature value. It is separated from the target substance extracted from the difference of boiling point and density due to the physicochemical property. It is then fed back to the system for reuse with the pump again (**Figure 2**).

The viscosity of the SCF is lower than the liquids, and the flow properties are good. Due to its low surface tension, it penetrates into food raw materials and increases extraction yield. The resolution values can be changed by adjusting the temperature-pressure values. Costs are low, solvents are used, and extraction does not leave waste as a result. Due to all these positive features, SFE operated using SCF has a wide use as a good example of green technology.

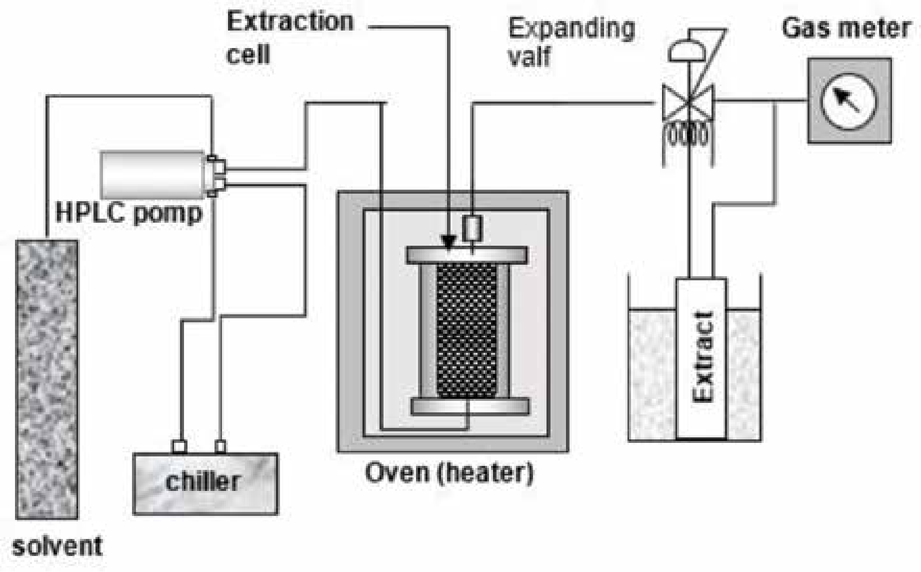

**Figure 2.** SFE system.

SFE has been used commercially in the food industry for the first time to remove caffeine from coffee. In addition, spices are used to obtain important components from many foodstuffs such as aromatics, essential oils, medicinal plants, fruits and vegetables, and animal oils.

### 3.2.2. *Ultrasound-assisted extraction*

Ultrasonic sound waves are the sound waves on the level that the human ear can handle. Ultrasonic wave application is divided into two groups as low-energy and high-energy application in food industry. The amount of energy produced in this classification is the most important criterion and is defined by sound power (W), sound density ($W/m^2$), or sound energy density ($W/m^3$). Low-energy ultrasonic application is most commonly used to determine the physicochemical properties (rigidity, maturity, composition, particle size, acidity, etc.) of foods. High-energy ultrasonic application is used for microbial and enzymatic inactivation in food. High-energy ultrasonic application affects food physically, chemically, and mechanically, while low-energy ultrasonic application does not.

Ultrasound technique has been successfully used in food industry to determine chocolate content and eggshell thickness; to determine fat content; to determine lean tissue in meat; to determine contaminants such as metal, glass, or wood in food; and to determine food composition and particle size. In addition to these, it has been reported that it can be used as an alternative to traditional extraction methods in many studies such as extraction of phenolic compounds from the consortia, extraction of red and yellow pigments, extraction of fat and proteins from soybean, and oil extraction from oil seeds. Ultrasonic application increases the surface area between solid and liquid parts by decreasing particle diameter. The mechanical activity of the ultrasound accelerates the distribution of solvent toward the tissues. Because mechanically the cell wall is destroyed, the passage of the component to solvent, which is the solvent, will be facilitated. Ultrasonication also increases the extraction kinetics and the quality of the extract.

In recent years it has been reported that the combination of ultrasound and supercritical carbon dioxide application significantly increases the extraction efficiency. There are many more studies in which ultrasound techniques are used for extraction purposes.

### 3.2.3. *Ohmic heating-assisted extraction*

Ohmic heating is a process applied by the passage of electric current through the food. It is also known as joule heating, electric-heating and electrical resistance heating. Ohmic heating is achieved by the conversion of electrical energy into heat energy, depending on the electrical resistance of the glass. In other words, when food shows resistance against flow, heat formation is seen. The higher the electrical resistance of a food, the more homogeneous heating is achieved. Therefore, since the conductivity of solid materials is higher, if the process conditions are applied correctly, it will heat up faster than liquid materials. One of the advantages of ohmic heating is that it homogenizes food very quickly. It is very suitable for materials sensitive to heat since the hot zone does not occur on the surface during heating. Other important advantages of the system are its high product quality, silent operation, and its ability to be used in particulate matter. The success of ohmic heating depends primarily on the rate of heat production, the electrical conductivity of the food, the composition of the food, the intensity of the electric field, and the duration of the waiting period.

Preliminary treatment of rice brass raw materials and extraction of oils by solvent extraction are examples of studies in which ohmic heating systems are used as pretreatment in extraction processes. For food samples pretreated using ohmic heating method, the yield varied between 49 and 92%, while for non-pretreated samples, the yield was 53%.

### *3.2.4. Pulsed electric field extraction*

Pulsed electric field (PEF) technology is a food preservation process that is based on the use of the electric field to eliminate food-borne pathogenic microorganisms and to control microorganisms that destroy food, is nonthermal, and does not adversely affect food quality. A typical PEF unit consists of a high-voltage boost generator, application chamber, flow control system, control, and monitor device. The most important one of these is the application chamber, and it must be treated with care during design.

The successful results of PEF technology in liquid foods (especially fruit juice, milk, etc.) are noteworthy and lead to the production of high-capacity systems. In the near future, it is known that in developed countries, high-quality products will be obtained by processing liquid and semiliquid foods with PEF technology. In this context, it will be inevitable that many countries will follow these developments as the result of the conjunctural changes that will take place in the competition of international food trade. For this purpose, attention should be paid to other disciplines (such as machinery, industry, electrical-electronics, materials, and food engineering) to produce PEF technology in our country. Initiation of studies on PEF technology, transmission, and dissemination of this technology in the industry will enable the technology to be produced by the domestic industry.

### *3.2.5. Microwave-assisted extraction*

The use of microwave technology, which has been in use since the Second World War, in the analytical laboratory was at the end of the 1970s. Microwaves are electromagnetic radiation that varies in the range of 0.3–300 GHz and are usually extracted at 2.5–75 GHz in natural products. The efficiency of microwave energy depends largely on the content of the solvent, the plant material, and the applied microwave power. The advantage of microwave heating is the decomposition of oxidized weak hydrogen bonds at the poles of the molecules. Extraction with microwave is realized with two different systems. The most common system is the closed system extrusion made in a closed container that can control temperature and pressure. The other method is carried out in an open container under atmospheric pressure. The advantage of this method is that the amount of extraction and the amount of solvent used are largely small.

## 4. Process and procedure of microwave-assisted extraction

There are two mechanisms in microwave heating: dielectric conduction and ionic conduction. The principle in dielectric heating is to rearrange the molecules in the dipolar structure by rotation in the presence of electrical changes. The dipoles are arranged at 2450 MHz and distributed randomly at $4.9 \times 10^9$ times in the second. As a result of this motion, heat is generated by the vibration. In the ionic conduction mechanism, the magnetic field is generated by the movement of ions at the end of the application. The solvent heats up by friction resulting from the resistance of the solvent to the ion flux. In most applications, two mechanisms occur simultaneously.

The frequency, microwave power and heating speed, temperature, mass of food, water content, density, physical geometry, thermal properties, electrical conductivity, and dielectric properties of food are affected by microwave heating. Microwave, which has been used for various applications in food for many years, is also a preferred method for increasing extraction efficiency (**Table 2**). Contrary to classical heating, in the case of microwave heating, for example, all are heated uniformly and quickly at the same time. The cells are heated by microwave radiation by the moisture in them and apply pressure to the cell wall as a result of evaporation. The cell wall is disrupted by this high pressure, and the passage of the components to the solvent is ensured. One of the most important parameters in extraction process is solvent choice. Solvents with a larger dipole moment will heat up faster. According to the solvent dipole moments, acetonitrile, methanol, acetone, ethyl acetate, water, ethyl alcohol and hexane are the most commonly used solvents for phenolic substance extraction from plant source. The nonpolar solvent hexane (dipole moment <0.1) will not heat up in the microwave.

Microwave extraction is performed with two different systems (**Figure 3**). The most common system is the closed system extrusion made in a closed container that can control temperature and pressure. The other method is carried out in an open container under atmospheric pressure. The advantage of this method is that the amount of extraction and the amount of solvent used are small at large. The principle of heating using microwave energy is based on the direct effect of the microwave on the molecule through ion conduction and dipole rotation (rotation). In most applications, these two mechanisms come into play simultaneously. Ionic conduction is the electrophoretic migration of ions when a magnetic field is applied. The solution results in

| Application | Purpose | Product |
|---|---|---|
| Tempering | Temperature rise below freezing point | Meat, fish, butter |
| Vacuum drying | Moisture content reduction | Seeds, cereals, citrus juices |
| Freeze drying | Moisture content reduction | Meat, vegetables, fruits |
| Drying | Moisture content reduction | Pasta, rice, snacks |
| Cooking | Aroma and texturing | Ham, meatballs, potatoes |
| Bleaching | Inactivation of impaired enzymes | Fruit, corn, potato |
| Baking | Heating and activation of bleaching agents | Bread, pasta, donut |
| Roasting | To develop heating and heating reactions | Coffee, cocoa, berries |
| Pasteurization | Inactivation of vegetative microorganism | Dairy products, ready-to-eat foods |
| Sterilization | Inactivation of microbial spores | Pastries, cheeses, milk, fruit juices |

**Table 2.** Microwave applications in the food industry.

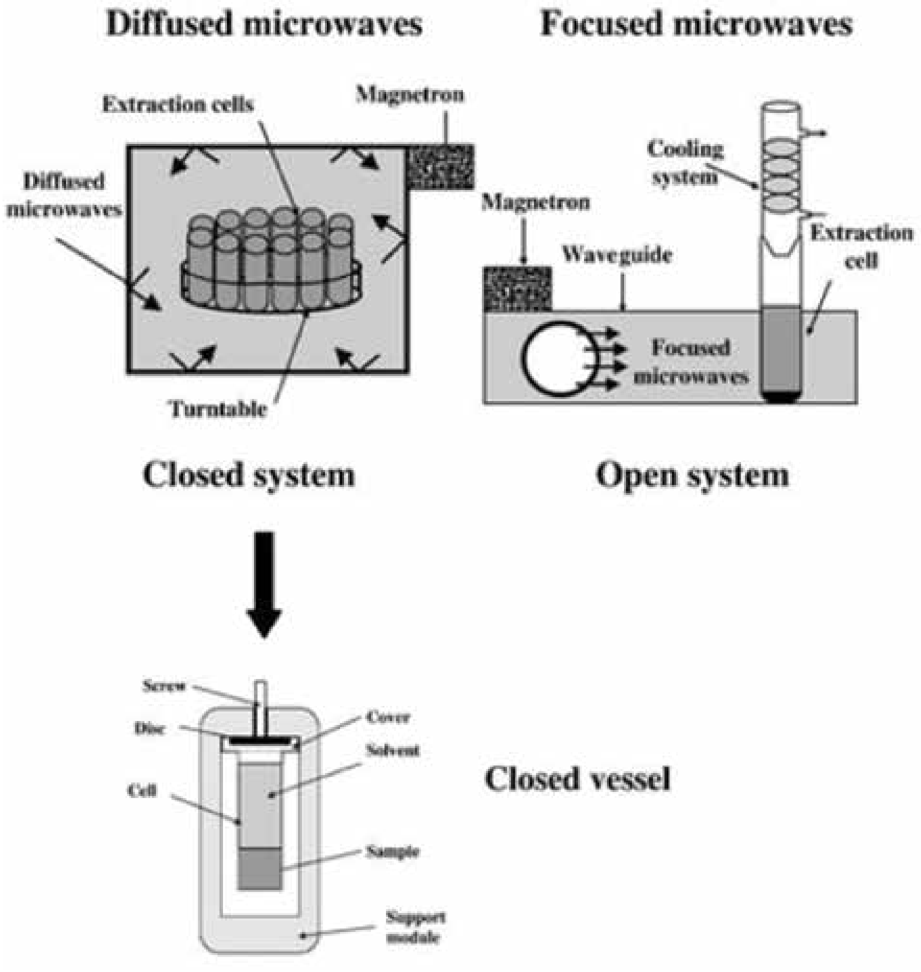

**Figure 3.** Schematic view of the microwave-assisted extraction system (closed system and open system).

a resistive friction (friction) to this ion flow, and thus the solution heats up. Extraction is usually carried out in a closed container. In this case the pressure increases, and the solvent can be heated to higher temperatures than the boiling point. For most solvents (such as acetone, acetone hexane, acetone), the temperature in the container is two to three times the boiling point of the solvent. Two main types of MAE systems can be used: closed-vessel system (under controlled temperature and pressure) and open-vessel system (atmospheric temperature). Both systems and MAE apparatus (DKSH Australia Pty. Ltd.) are shown in **Figures 3** and **4**, respectively.

While the cells are being irradiated simultaneously in the closed-vessel system, the vessels are successively irradiated in the open system. In open vessels the temperature is limited by the atmospheric pressure boiling point of the solvent, while in closed vessels, the temperature can be increased by the applied pressure. The closed container system seems to be most

**Figure 4.** MAE apparatus.

appropriate if it is a fugitive compound. However, in closed containers it is necessary to wait for the temperature to fall before opening the container after extraction. The main difference is the heat. The extraction process begins with the extraction cell being loaded, for example. Microwave radiation is applied, and the pre-extraction step is started to heat the solvent to the set values. Normally, heating takes less than 2 min. The specimen is then irradiated and generally extracted at intervals of 10–30 min [17–19].

The advantages of microwave-assisted extraction are reduction in solvent consumption, increase in extraction efficiency, high recovery, ease of use and low cost, wide solvent, and solvent blends. The disadvantages are that if the target component or solvent is polar or volatile, the efficiency of the microwave is too weak, and it is applied at high temperatures such as 110–150°C, which requires additional filtration or centrifugation to separate the solids as compared to supercritical fluid extraction.

## 5. Applications of MAE as a green extraction technique in food industry

MAE is usually used in environmental analyses. Extraction of polyaromatic hydrocarbons, polychlorobiphenyls, and organochlorine pesticides from matrices such as sediment and soil has been studied. MAE has also been applied to food analyses. Extraction of 16 organochlorine insecticides in sesame seeds, use of microwave confinement in drug extraction from seed, and extraction and testing of lidocaine, methadone, diazepam, nordiazepam, proxifene, and norproxifen materials as model medicines are the main applications in which the MAE technique is used. At the same time, extraction of natural products such as drugs (pentobarbital, ketamine, diazepam); extraction from skeletal tissues; extraction of natural products such as terpenes, alkaloids, volatile oils, and carotenoids; extraction of color pigments in the paprika; identification of pesticide residues in sunflower seeds; discovery of a rapid method using dichloromethane solvent; and applications such as rapid extraction of aromatic hydrocarbons are examples of other applications that can be given for MAE technique. The irradiation power, time, number of revolutions, and solvent volume among the MAE method parameters can be optimized using experimental design methodology [20]. Examples of food industry that can be given to microwave-assisted extractions are very diverse and are summarized in general as the following, diversified by explaining the study title and scope:

**a.** Supercritical carbon dioxide and microwave-assisted extraction of functional lipophilic compounds from *Arthrospira platensis*: The study investigated the effect of extraction parameters on lipophilic material content in the extracts obtained by using SFE and MAE methods. Pressure and temperature in the study were 45 MPa and 60°C, respectively. When the cosolvent is used at 53.33% of $CO_2$ ratio, the highest amount of extracts was obtained. In case of MAE extraction, the most efficient experimental condition was obtained at 400 W and 50°C [21].

**b.** Green extraction from pomegranate marcs for the production of functional foods and cosmetics: The aim of the study was to investigate the potential of retrieving polyphenolic antioxidants by green extractions directly from wet pomegranate juice marcs, the fresh edible by-products obtained after pomegranate juice processing. Green extraction was performed below 50°C, microwave-assisted extraction (MAE) was done below 300 W, and ultrasound-assisted extraction (UAE) was operated with the output of 200 W. Each technique has been efficient in obtaining different foodstuffs [22].

**c.** Applications of green extraction of phytochemicals from fruit and vegetables: This study compared the conventional methods for extraction with the new methods that are called green extraction techniques and for recovery of phytochemicals and natural compounds (phenolic compounds, ascorbic acid, carotenoids, aroma compounds, etc.) obtained from plant materials [23].

**d.** Novel eco-friendly techniques for extraction of food-based lipophilic compounds from biological materials: This study investigated the various possible novel eco-friendly extraction methods, their scientific concepts, principles, challenges, limitations, and technological effort needed for successful implementation at the production scale [24].

**e.** Phenolic compound recovery from grape fruit and by-products: Several convectional and emerging technologies (including MAE) have been evaluated in order to recover phenolic compounds from grape fruits and wastes such as chemical, physical, and biotechnological techniques, which offer different advantages related to economic, environmental, time-saving, and yield aspects [25].

**f.** Microwave-assisted extraction of free amino acids from foods: In this study the use of microwave energy to assist extraction of amino acids from foods is presented. This method is compared with shaking extraction, and the effects of various experimental conditions on the extraction yield are tested (irradiation time, temperature, extractant volume, mixing, etc.) in order to determine the optimum extraction conditions. The efficiency of extraction gave better results for MAE by 10%, and the extraction time was reduced by 66% [26].

**g.** Microwave-assisted extraction of flavonoids: This study investigated the MAE mechanism and exerts the key points that bring advantage in extraction [27].

**h.** Microwave-assisted extraction of anthocyanin from Chinese bayberry and its effects on anthocyanin stability: The study used MAE to extract antioxidant compounds from Chinese bayberry at 80°C for 15 min. The results for anthocyanin content and antioxidant activity were obtained as 2.95 ± 0.08 $\text{mg}\cdot\text{g}^{-1}$ and as 279.96 ± 0.1 $\mu\text{mol g}^{-1}$, respectively. So, MAE showed an important potential to recover bioactive compounds [28].

**i.** Microwave-assisted extraction of pectin from jackfruit rinds using different power levels: Since conventional extraction of pectin is time-consuming (1 h), this study focused on the use of MAE to recover pectin from fruit material (10 min). The experiments were done at 90°C for conventional method, and three different power levels of 450, 600, and 800 W were used for MAE. The highest efficiency was obtained at 450 W power [29].

**j.** Optimization of microwave-assisted extraction of ergosterol from *Agaricus bisporus* L. by-products using response surface methodology: The study compared MAE with conventional methods for time and solvent consumption. MAE was efficient where conventional methods were inappropriate. Ergosterol component was best extracted at around 19.4±2.9 min and at around 132.8±12.4 C yielding 556.1±26.2 mg of extract [30].

**k.** Microwave-assisted extraction of phenolic compounds from olive leaves—a comparison wıth maceration: The purpose of the study was to extract phenolic compounds from olive leaves of with MAE methods using different solvents. Among the solvents used, ethanol was the most efficient where acetone was the least. The highest extraction yield was obtained at 24 h with conventional method, while it was obtained at 15 min with MAE method [31].

**l.** Extraction of phenolic compounds from melissa using microwave and ultrasound: The comparison of microwave and ultrasound has been studied for the extraction of essential oils from melissa. Extraction time and solid-to-solvent ratio were investigated for recovery of total phenolic compounds (TPC). Recovery rate for TPC was 145.8 mg extract/dry matter using MAE in 80% power rate where the yield was 105.5 mg extract/dry matter in 50% power rate [32].

## 6. Advantages and disadvantages of MAE

MAE process efficiency is dependent on various extraction parameters. These parameters can be counted as the nature of raw material, strength and level of microwave irradiation, extraction time, extraction pressure, and solvent flow rate. In the extraction process where the heat-labile compounds have to be recovered, lower levels of irradiation may bring lower efficiency because sensitive component recovery effectiveness may be decreased due to high microwave power levels. Extraction time is also important that is acts together with the microwave power. Even if the same amount of microwave power is used, if a raw material is extruded for a longer period, the yield will definitely be lower. Because the liminal structure of the material will

| Open-vessel system | | Closed-vessel system | |
|---|---|---|---|
| **Advantages** | **Disadvantages** | **Advantages** | **Disadvantages** |
| Enhanced and safer possibility of reagent addition | Comparatively exhibit less precision than in close-vessel system | Higher temperature and constraints of closed vessel system render reduced extraction time | Application of high pressure poses safety risks |
| Utilization of vessel manufactured from various materials, that is, quartz or glass | Inability to process multiple samples simultaneously due to low throughput of equipment | Avoidance of loss of volatile substances | High-solution temperature is not permissible by constituent material of vessel |
| Easy removal of excessive quantities of employed solvents | Longer time spans are required than closed-vessel system | Less solvent requirement due to the absence of evaporation phenomenon | Impossibility of regent addition since it is single-step process |
| Easy processing of larger samples volumes | — | No production of hazardous fumes during pressurized extraction under closed-vessel system | Constraint of cooling down vessel before opening rendering prevention of volatile constituents |
| No need of operational cooling down or depressurization | — | High yield by using ionic liquids at ambient temperature | Handling and processing of limited sample volumes |
| Cost-effective availability of sophisticated equipment for polyphenol extraction | — | Simple procedural setup without any inherent complexity as compared to SFE and other techniques | Requirement of cooling step after each treatment for further processing |

**Table 3.** Advantages and disadvantages of MAE depending on the operating systems.

deteriorate over time and gradually lose its originality. In this case, especially the structure of the food material or the preparation before extraction will enter the circuit. Of course, the preparation of the foodstuff or the preparation before extraction is particularly important here. Because the structure of a solid material is tighter, the solvent that extracts may not penetrate into every cell. Rather, it is possible to obtain a higher extraction yield than the granular or powdery sample forms in order to increase the food-solvent interaction. All this facts are considered together with the correct solvent selection and effect of external forces.

Although the process parameters are well combined, even if the sample material is carefully chosen, it will have disadvantages as well as the advantages provided by the MAE technique. **Table 3** summarizes the advantages and disadvantages of the MAE technique for using open-vessel and closed-vessel systems [33].

## 7. Conclusion

For many years, various extraction techniques have been used to recover organic and/or inorganic compounds from food materials. But referring to their positive and negative effects and when they are compared to modern techniques, traditional extraction methods have been assigned to be inadequate in terms of green technology applications and waste of time/money, etc. However, there may be strict regulations about the use and recycling of solvents that are used in conventional techniques. In addition, thermal degradation of organic materials may occur due to the long extractions at elevated temperature. Many extraction studies could not be carried to further innovative applications because of using the area of expertise to only extract and to only characterize the extracted compounds from food materials. In later periods, researchers have started to investigate the possible ways to make optimization studies being related to extraction and to collaborate by exerting multidisciplinary studies to test the synergy between the extraction modules. So, being one of the green extraction methods, microwave-assisted extraction has many advantages of being cheap and safe and is applicable to a wide range of food materials [2, 3, 11]. This emerging technique uses the advantages of diffusivity of solvents being close to gases and being at least two orders of magnitude larger than liquids. By exploiting the advantage of the microwave-assisted extraction system and observing the basic principles of the extraction system, the current study has conveyed the information on the operation and industrial usage of extraction. The current status of the method gives a promising sign for the use of green extraction in the food industry, and it can be evaluated as convenient to be scaled up and to be transferred to other disciplines such as pharmacy, chemistry, medicine, materials science, etc.

## Author details

Ruhan Askin Uzel

Address all correspondence to: ruhan.uzel@yasar.edu.tr

Department of Food Processing, Yasar University, Izmir, Turkey

## References

[1] Müller A, Schmidhuber J, Hoogeveen J, Steduto P. Some insights in the effect of growing bio-energy demand on global food security and natural resources. Water Policy. 2008; **10**(1):83-94. DOI: 10.2166/wp.2008.053

[2] Holden E, Linnerud, Banister D. The imperatives of sustainable development. Sustainable Development. 2017;**25**(3):213-226. DOI: 10.1002/sd.1647

[3] Tiwari BK. Ultrasound: A clean, green extraction technology. Trends in Analytical Chemistry. 2015;**71**:100-109. DOI: 10.1016/j.trac.2015.04.013

[4] Anne YL, Tixier SF, Vian MA, Chemat F. Solvent-free microwave extraction of bioactive compounds provides a tool for green analytical chemistry. Trends in Analytical Chemistry. 2013;**47**:1-11. DOI: 10.1016/j.trac.2013.02.007

[5] Prosekov AY, Ivanova SA. Providing food security in the existing tendencies of population growth and political and economic instability in the world. Foods and Raw Materials. 2016;**4**(2):201-211. DOI: 10.21179/2308-4057-2016-2-201-211

[6] Griggs D, Smith MS, Gaffney O, Rockström J, Öhman MC, Shyamsundar P, Steffen W, Glaser G, Kanie N, Policy NI. Sustainable development goals for people and planet. Nature. 2013;**495**:305-307. DOI: 10.1038/495305a

[7] Kahl J, Strassner C, Hertwig J, Gould D, Bügel S, Paoletti F, Lairon D. Learning from the organic food system as a model for sustainable food systems–The Organic Food System Program. In: Proceedings of the workshop of the FAO/UNEP Programme on Sustainable Food Systems; 8–9 June 2016; Rome. Italy: IEEE; 2016. pp. 295-302

[8] Benthin B, Danz H, Hamburger M. Pressurized liquid extraction of medicinal plants. Journal of Chromatography A. 1999;**837**:211-219. DOI: 10.1016/S0021-9673(99)00071-0

[9] Anonymous. Extraction (chemistry) [Internet]. 2013. Available from: http://en.wikipedia.org/wiki/Extraction_(chemistry) [Accessed: 2017-09-11]

[10] Carabias-Martinez R, Rodriguez-Gonzalo E, Revilla-Ruiz P, Hernandez-Mendez J. Pressurized liquid extraction in the analysis of food and biological samples. Journal of Chromatography A. 2005;**1089**:1-17. DOI: 10.1016/j.chroma.2005.06.072

[11] Stephanie C, Stephanie J, Buddhi L. Food Processing: Principles and Applications. 2nd ed. John Wiley and Sons; 2014. 578 p. DOI: 10.1002/9781118846315

[12] Fages J, Lochard H, Letourneau JJ, Sauceau M, Rodier E. Particle generation for pharmaceutical applications using supercritical fluid technology. Powder Technology. 2004; **141**(3):219-226. DOI: 10.1016/j.powtec.2004.02.007

[13] Schacht C, Zetzl C, Brunner G. From plant materials to ethanol by means of supercritical fluid technology. The Journal of Supercritical Fluids. 2008;**46**(3):299-321. DOI: 10.1016/j.supflu.2008.01.018

[14] Herrero M, Cifuentes A, Ibañez E. Sub-and supercritical fluid extraction of functional ingredients from different natural sources: Plants, food-by-products, algae and microalgae: A review. Food Chemistry. 2006;**98**(1):136-148. DOI: 10.1016/j.foodchem.2005.05.058

[15] Ji M, Chen X, Wai CM, Fulton JL. Synthesizing and dispersing silver nanoparticles in a water-in-supercritical carbon dioxide microemulsion. Journal of the American Chemical Society. 1999;**121**(11):2631-2632. DOI: 10.1021/ja9840403

[16] Perrut M. Supercritical fluid applications: industrial developments and economic issues. Industrial and Engineering Chemistry Research. 2000;**39**(12):4531-4535. DOI: 10.1021/ie000211c

[17] Brunner G. Applications of supercritical fluids. Annual Review of Chemical and Biomolecular Engineering. 2010;**1**:321-342. DOI: 10.1146/annurev-chembioeng-073009-101311

[18] Jung J, Perrut M. Particle design using supercritical fluids: Literature and patent survey. The Journal of Supercritical Fluids. 2001;**20**(3):179-219. DOI: 10.1016/S0896-8446(01)00064-X

[19] Letellier M, Budzinski H. Microwave assisted extraction of organic compounds. Analusis. 1999;**27**(3):259-270. DOI: 10.1051/analusis:1999116

[20] Priego-Capote F, Luque-Garcia U, Castro MDL. Automated fast extraction of nitrated polycyclic aromatic hydrocarbons from soil by focused microwave-assisted Soxhlet extraction prior to gas chromatography-electron capture detection. Journal of Chromatography A. 2003;**994**(1–2):159. DOI: 10.1016/S0021-9673(03)00441-2

[21] Esquivel-Hernández DA, López VH, Rodríguez-Rodríguez J, Alemán-Nava GS, Cuéllar-Bermúdez SP, Rostro-Alanis M, Parra-Saldívar R. Supercritical carbon dioxide and microwave-assisted extraction of functional lipophilic compounds from *Arthrospira platensis*. International Journal of Molecular Sciences. 2016;**17**:658. DOI: 10.3390/ijms17050658

[22] Raffaella B, Federica T, Carla V, Chiara L, Paola Z, Brunella P. Green extraction from pomegranate marcs for the production of functional foods and cosmetics. Pharmaceuticals. 2016;**9**:63. DOI: 10.3390/ph9040063

[23] Chan WC, Ismail M. Supercritical carbon dioxide fluid extraction of *Hibiscus cannabinus* L. seed oil: A potential solvent-free and high antioxidative edible oil. Food Chemistry. 2009; **114**(3):970-975. DOI: 10.1016/j.foodchem.2008.10.055

[24] Kate AE, Anupama S, Shahi NC, Pandey JP, Om P, Singh TP. Novel eco-friendly techniques for extraction of food based lipophilic compounds from biological materials. Natural Products Chemistry and Research. 2016;**4**(5):1-7. DOI: 10.4172/2329-6836.1000231

[25] Cecilia CL, Romeo R, Ernesto JS, Guillermo N, Guillermo CG. Phenolic compounds recovery from grape fruit and by-products: An overview of extraction methods. In: Grape and Wine Biotechnology. InTech; 2016. pp. 103-123. DOI: 10.5772/64821.ch5

[26] Ágnes K, Katalin G, Livia SS. Microwave-assisted extraction of free amino acids from foods. Zeitschrift für Lebensmittel-Untersuchung und -Forschung A. 1998;**207**:26-30. DOI: 10.1007/s002170050290

[27] Winny R, Valérie O. Microwave-assisted extraction of flavonoids: A review. Food and Bioprocess Technology. 2012;**5**:409-424. DOI: 10.1007/s11947-011-0573-z

[28] Wenkai D, Shiping J, Guofu Z, Peilong S. Microwave-assisted extraction of anthocyanin from Chinese bayberry and its effects on anthocyanin stability. Food Science and Technology Campinas. 2015;**35**(3):524-530. DOI: /10.1590/1678-457X.6731

[29] Koh PC, Leong CM, Noranizan MA. Microwave-assisted extraction of pectin from jackfruit rinds using different power levels. International Food Research Journal. 2014;**21**(5): 2091-2097. DOI: 10.1016/j.carbpol.2013.05.052

[30] Sandrine A, Heleno MA, Prieto LB, Alírio R, Maria FB, Isabel CFR. Optimization of microwave-assisted extraction of ergosterol from *Agaricus bisporus* L. by-products using

response surface methodology. Food and Bioproducts Processing. 2016;**100**(A):25-35. DOI: 10.1016/j.fbp.2016.06.006

[31] Rafiee Z, Jafari SM, Alami M, Khomeiri M. Microwave-assisted extraction of phenolic compounds from olive leaves—A comparison wıth maceration. The Journal of Animal and Plant Sciences. 2011;**21**(4):738-745. DOI: 1018-7081

[32] İnce AE, Şahin S, Şümnü SG. Extraction of phenolic compounds from melissa using microwave and ultrasound. Turkish Journal of Agriculture and Forestry. 2013;**37**:69-75. DOI: 10.3906/tar-1201-1

[33] Kashif A, Hafiz MS, Joong-Ho K. Green extraction methods for polyphenols from plant matrices and their byproducts: A review. Comprehensive Reviews in Food Science and Food Safety. 2017;**16**:295-315. DOI: 10.1111/1541-4337.12253

Chapter 10

# From Field to Shelf: How Microwave-Assisted Extraction Techniques Foster an Integrated Green Approach

Roberto Rosa, Erika Ferrari and Paolo Veronesi

Additional information is available at the end of the chapter

http://dx.doi.org/10.5772/intechopen.73651

## Abstract

Microwave-assisted extraction of organic compounds from vegetal matrixes is a relatively young field of research. The exceptional results achievable at the laboratory scale by microwave-assisted extraction, like shorter extraction times, lower average temperatures, reduction of organic solvents use, higher yields and selectivity, as well as energy and cost saving, are not always accompanied by a successful scale up. Nevertheless, microwave-assisted techniques of extraction have been multiplying during last decades. In this framework, a deeper knowledge of microwave applicator design criteria is mandatory. This chapter starts from the basis of microwave heating and the relevant material properties involved in a successful microwave-assisted extraction application, to continue with a short overview on how such properties can be measured and used to optimize the experimental setup or a possible scale up of the process under investigation. A comprehensive review of recent applications of microwave-assisted extraction, applied to vegetal matrixes, is presented next. The chapter ends reviewing duplex treatments of vegetal matrixes for extraction purposes, where microwave heating is coupled to other techniques, like ultrasounds, and indicating new paths, where the recent advent of new microwave solid-state generators has led to better process control and higher yields and energy efficiency.

**Keywords:** extraction, LCA, modeling, green chemistry, process intensification, energy efficiency

## 1. Introduction

The concept and principles of green chemistry as formulated by Anastas and Warner [1], were used as a guide in order to promote the concept of sustainable development also in the analytical procedures, particularly in the sample preparation techniques, leading to what is nowadays recognized as green analytical chemistry [2], that is characterized by the following 12 principles [3]:

- **i.** Direct analytical techniques should be applied to avoid sample treatment.
- **ii.** Minimal sample size and minimal number of samples are goals.
- **iii.** In situ measurements should be performed.
- **iv.** Integration of analytical processes and operations saves energy and reduces the use of reagents.
- **v.** Automated and miniaturized methods should be selected.
- **vi.** Derivatization should be avoided.
- **vii.** Generation of a large volume of analytical waste should be avoided and proper management of analytical waste should be provided.
- **viii.** Multi-analyte or multi-parameter methods are preferred versus methods using one analyte at a time.
- **ix.** The use of energy should be minimized.
- **x.** Reagents obtained from renewable source should be preferred.
- **xi.** Toxic reagents should be eliminated or replaced.
- **xii.** The safety of the operator should be increased.

The first and fundamental step at the basis of most of the analytical procedures is represented by the extraction of the target analyte, therefore green extraction procedures need to be implemented as well in any analytical procedure. This led to the so-called green extraction, and particularly by focusing on the extraction of natural compounds from matrices of vegetal origin, to the concept of green extraction of natural products which was for the first time defined by Chemat et al. [4] as "based on the discovery and design of extraction processes which will reduce energy consumption, allowing the use of alternative solvents and renewable natural products, as well as ensuring a safe and high quality extract/product". In order to pursue this highly desired goal, six principles were defined by the same researchers group as follows:

- **i.** Innovation by selection of varieties and use of renewable plant resources.
- **ii.** Use of alternative solvents and principally water and agro-solvents.
- **iii.** Reduce energy consumption by energy recovery and using innovative technologies.
- **iv.** Production of co-products instead of waste to include the bio- and agro-refining industry.
- **v.** Reduce unit operations and favor safe, robust and controlled processes.
- **vi.** Aim for a non-denatured and biodegradable extract without contaminants.

It immediately appeared clear, as the use of microwave heating rather than more conventional heating strategies, represented in all likelihood the most suitable solution in order to pursue, at least, the above-mentioned principles (ii) and (iii) of green extraction of natural products. Water and most of the preferred agro-solvents (e.g. ethanol) are known to be excellent chemical environments to interact with the electromagnetic energy at the microwave frequencies [5, 6]. Moreover, at a more microscopic level, direct interaction of the cell structure with microwave energy, was reported to lead a completely different extraction mechanism, based on the synergistic action of heat and mass transfer, working in the same direction (i.e. at the opposite of what happens with conventional extraction techniques), as depicted in **Figure 1** [7].

All of these unique characteristics instantly gave rise to a wide variety of different extraction processes employing microwave energy, that started being developed and investigated, giving rise to what is nowadays known as microwave-assisted extraction (MAE) [8].

The persistent increase in the interest toward chemical compounds of natural origin is due to the great number of epidemiological investigations that continuously highlight the human health benefits deriving from a regular consumption of fruits and vegetables [9, 10]. Moreover further driving forces are the toxicity of some synthetic analogs, the cost of raw materials and manufacture, as well as the possibility to obtain significant amounts of such chemicals also from by-products deriving from food industries [11–13].

The most representative MAE techniques (both performed in the presence of an extracting solvent and in solvent-free conditions) will be accurately reviewed in Section 2. Despite the exceptional results achievable at the laboratory scale, like shorter extraction times, lower average temperatures, reduction of organic solvents use, higher yields and selectivity, as well as energy and cost saving, they are not always accompanied by a successful scale up. Therefore, a deeper understanding of how microwave extraction works and of the related microwave equipment design is required in order to better exploit the benefits deriving from dielectric

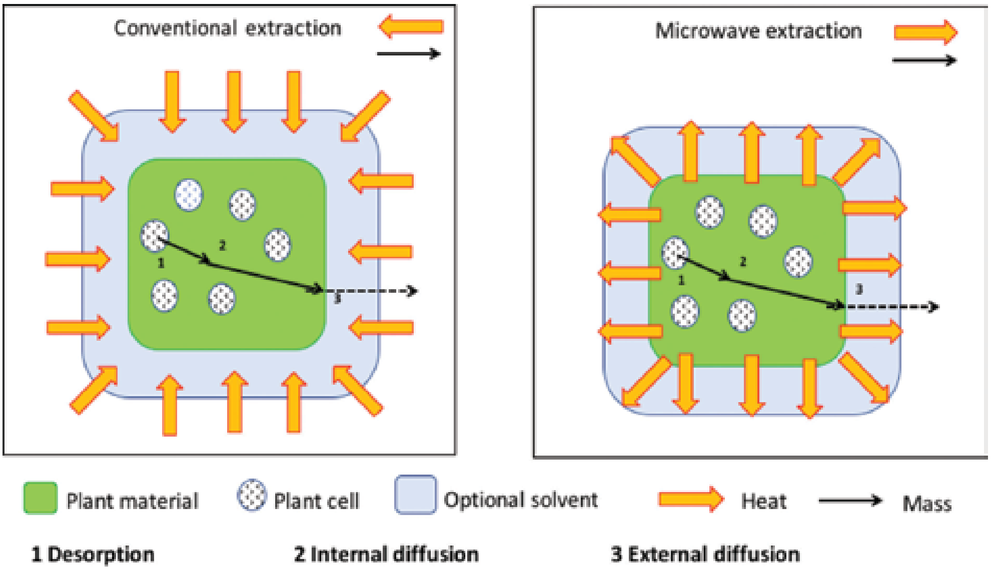

**Figure 1.** Heat and mass transfer mechanisms involved during conventional and microwave-assisted extraction. Adapted from [7].

heating of vegetal matrixes, with the ideal result of being able to achieve greener extraction processes, with almost no preparatory or separation steps, literally "from the field to the shelf". This is indeed the main focus of Section 3.

Section 4 is devoted to the environmental assessment evaluation of MAE with respect to traditional Soxhlet-based extraction, presenting a cradle to the grave life cycle assessment (LCA) study for the case of curcumin molecule extraction at a laboratory scale.

In Section 5, advantages deriving from the coupling of microwaves with further innovative techniques/extraction systems will be reviewed, highlighting their consequences in a process intensification perspective.

## 2. Microwave-assisted extraction (MAE): state of the art

Extraction of natural occurring chemical compounds is only one of the plenty food-processing technologies in which the use of microwave energy demonstrated significant advantages and unique possibilities [14]. The existing microwave-based techniques have been extensively reviewed [15–18], thus the present section is dedicated only at presenting the principles at the basis of the mostly employed ones, essentially presenting a major classification among those based on the use of a solvent and those operating in solvent-free conditions.

### 2.1. Microwave-assisted solvent extraction (MASE)

The first use of microwave energy for extraction purposes [19] was practically reported simultaneously with the first experiments performed in organic synthesis field which led to tremendous increase in yields and reduction in reaction times [20, 21]. Similarly, the use of water, methanol or a mixture of both solvents resulted in higher extraction yields, as a consequence of the polarity of the employed solvents, thus of their ability to efficiently be heated under a microwave field. Indeed, most of the solvents recommended by both green chemistry and green extraction principles can be efficiently heated when exposed to electromagnetic fields at the microwave frequencies. Therefore, necessarily the first use of microwave energy in the extraction of naturally occurring chemical compounds involved the use of solvent, leading to the group of experimental techniques called microwave-assisted solvent extraction (MASE) [22].

The extraction mechanism when using microwaves absorbing solvents is fundamentally similar with those of conventional extraction procedures. Nevertheless, the possibility of microwave to instantly and precisely furnish energy to the extraction mixture led first of all to advantages in terms of extraction times.

A further possibility is represented by the use of non-polar microwave-transparent solvents, like hexane and toluene, for example, even if not properly recommended in a green chemistry perspective [23]. In this latter case, the plant matrix needs to be wet in order to well couple with microwave energy. In doing so, the analytes of interest are then released in the solvent. The reported advantages of this latter approach in the green chemistry perspective are the typical less amount of solvent needed when compared to extraction technique based on a conventional mechanism.

Independently by the solvent employed, MASE techniques can be performed by employing both closed and open vessels, each of which possesses the proper advantages. When closed vessels are employed, temperature higher with respect to the boiling point of the used solvent can easily be reached, therefore typically reaching higher extraction yields. This could potentially be performed also by exploiting conventional heating strategies (e.g. by using an autoclave), but it would, however, need longer times to reach the selected extraction temperature.

In case of open vessels, the peculiar heating mechanism of microwaves together with its volumetric character is considered responsible for significant reduction in the processing time.

### 2.2. Solvent-free microwave extraction (SFME)

The unique possibility offered by microwave energy to directly interact with the plant cells containing the target chemicals together with the possibility to realize a heat transport occurring in the same direction as the mass transport (see **Figure 1**), led to the development of extraction technique characterized by the absence of any extraction solvent.

Indeed, solvent-free microwave extraction (SFME) techniques, invented in 2004 [24, 25] needs to be performed on fresh plant matrices, since the water contained in it is directly heated by interaction with microwaves, breaking the plant gland and releasing, for example, the essential oil. The water steam generating from the plant drives the essential oil recovered outside the microwave furnace, where a condenser is employed in order to cool down the distillate. The plants that have been efficiently exposed to SFME of essential oils have been reviewed in [26].

A further extraction technique employing microwave energy and solvent-free conditions is the so-called microwave hydrodiffusion and gravity (MHG) patented by Chemat et al. in 2008 [27]. In this configuration, the effect of the gravity is exploited synergically to the warming of the water (and other polar molecules) contained in the plant matrix, the latter leading to the disruption of the cell walls and the releasing of these substances (hydrodiffusion) outside the plant matrix. The extract is recovered at the bottom, outside the microwave furnace, where a refrigerator is placed.

## 3. Microwave reactor

Electromagnetic energy at the microwave frequencies can interact with matter according to its electric, dielectric and magnetic properties. In case of extractions from vegetal matrixes, usually the electric field component of the electromagnetic field is predominant in determining the heat generation inside the load, according to the simplified equation of the power density:

$$Pd = 2\pi f \varepsilon_0 \varepsilon'' |E|^2 \tag{1}$$

where Pd is the power density in W/m$^3$, f is the frequency of the oscillating electromagnetic field in Hz, $\varepsilon''$ the imaginary part of the complex permittivity (loss factor) and $|E|$ is the electric field strength, in V/m at a given position in space (i.e. for instance, inside the load). Power density, at its turn, determines how heat is generated and hence the temperature distribution inside a given load.

Limitedly to microwave-assisted extraction we can easily assert that it is possible to limit the heating preferably to the plant material, especially to the water therein contained, provided the proper choice of the optional solvent is made so that it has lower values of the loss factor. Otherwise, concurrent absorption of the microwaves occurs both from the plant material and the solvent. This can be used to achieve peculiar temperature distributions inside the reactor, as shown in **Figure 2**, where the early stages of heating in a single mode applicator (see next) of a load composed of a cylindrical shaped container (40 mm diameter), filled with solvent, containing dispersed spheres (2 mm radius) of plant material, 100 W power, 2450 MHz frequency, has been simulated. In this extremely simplified model, involving only the applicator, up to the movable short circuit (right end of color plots in **Figure 2**) the ambient temperature in the applicator has been set to 20°C and convection has been neglected, to better evidence the different heat generation pattern and relative temperature difference between solvent (permittivity of 2.41 – i × 0.096 for toluene and of 81 – i × 12 for water) and plant material (permittivity of 8 – i × 3).

The thermal plot sows, also another important phenomenon which can occur during microwave heating, depend on the load thermal properties, that is, the presence of overheated regions inside the load, with an external lower temperature (the so-called "inversion of temperature profiles", as it is opposite to what happens during conventional heating, where the maximum temperature, in absence of exothermal reactions, occurs at the load borders).

Another important aspect, shown by the thermal plots, is that microwave heating is not necessarily homogenous, and this can be ascribed once again to the electric field distribution, which, at its turn, depends also on the applicator geometry.

According to previous equation, another possibility would be changing the operating frequency, but this can be done provided the chosen frequency falls within the Industrial, Scientific and Medical (ISM) allowed ones, or proper shielding of possible emitted fields is provided. **Figure 3** shows an example of operating at higher frequency (5800 MHz) on the same load of **Figure 2**. At that frequency, the applicator used is no longer classifiable as a single mode one, as there is more than one mode inside the applicator (see next), and this is reflected into the electric field and temperature distribution.

Another possible option could be to change the dielectric properties of the load, but they are usually given by the nature of the plant material. However, additives like conducting or semiconducting particles could be added to modify the loss factor, but then subsequent separation would be needed.

Hence, it is evident that with a limited choice of available ISM frequencies and permittivity values given by the load nature, the proper control of the electric field strength inside the load becomes relevant. This can be accomplished by the proper design of the microwave applicator, that is, of the space where microwave-matter interaction occurs.

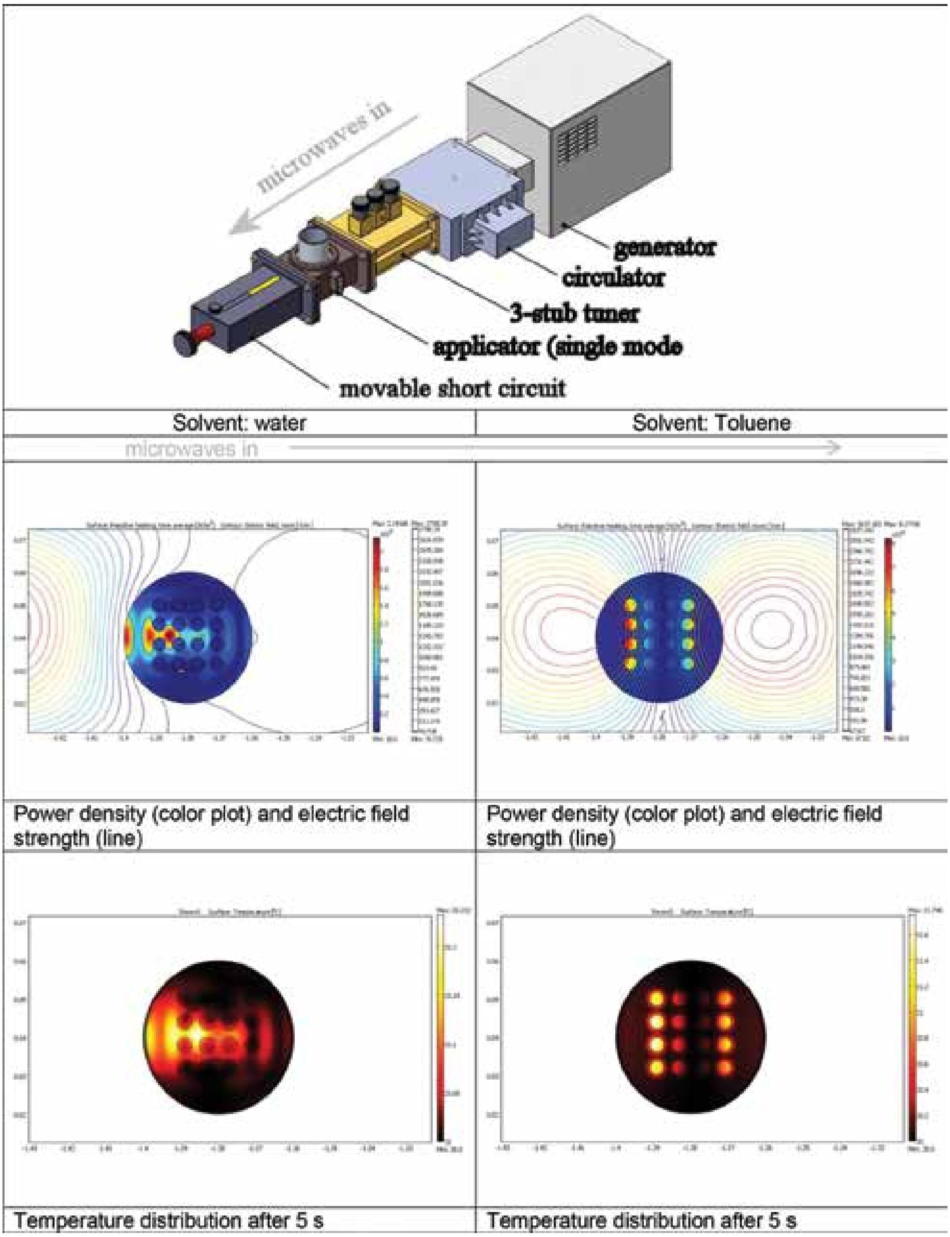

**Figure 2.** Power density, electric field strength and temperature distributions inside a microwave single mode applicator with a load constituted by plant material (depicted as the 16 spherical particles) and the extraction solvent (water or toluene).

### 3.1. Permittivity measurement techniques

In order to properly design (or select) a microwave applicator, the load permittivity should be known, as it affects both how heat is generated inside the load itself and the energy efficiency

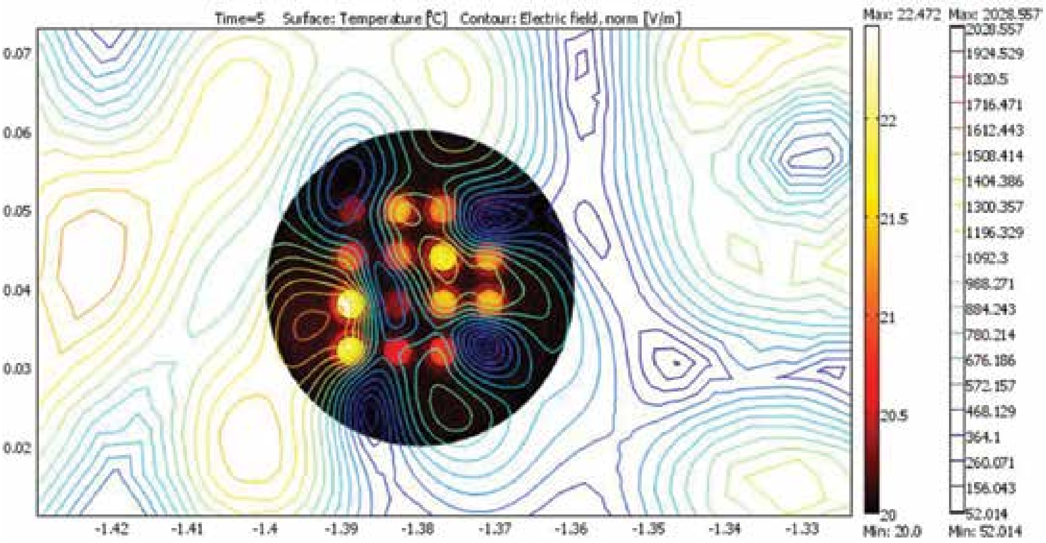

**Figure 3.** Temperature distribution and electric field strength inside the same microwave single mode applicator of **Figure 2**, in which the irradiating frequency was set to 5800 MHz. Again the 16 spherical particles represent the plant material and the surrounding environment is the solvent (toluene).

of the microwave applicator (i.e. the ratio between the power emitted from the microwave generator and the power transmitted to the load). As a matter of fact, every time an incident electromagnetic field passes through a different medium (for instance, from air, to solvent, to plant material), it is partly transmitted, partly absorbed and partly reflected. Hence, it can happen that only a small portion of the incident power is effectively absorbed and converted into heat, while the remaining could be reflected back to the generator, lowering the efficiency and requiring means to protect the generator from such reflections.

There is not a universal measuring technique to determine the permittivity of materials: it strictly depends on the frequency range of the measurement, on the state of the materials (liquid, solid, etc.) and on the expected values of permittivity.

Permittivity at the microwave frequencies is a complicated function which relates the electric flux density to the electric field in the medium [28]. It describes the interaction of a material in the presence of an electric field. It is a complex number and it accounts for different dispersion phenomena, like dipolar polarization, ionic polarization, interfacial polarization, etc. Its real part accounts for energy stored in the material, while the imaginary part, known also as loss factor, accounts for losses. The real part is sometimes indicated as dielectric constant, but this term is deprecated as it would suggest a "constant" behavior that does not correspond to the reality, given the strong dependence of permittivity on frequency. The ratio between the imaginary and real part of the complex permittivity is indicated as tanδ.

Depending on the expected values of permittivity and frequency, different techniques can be used to measure such parameter:

- Parallel plate: (sometimes called capacitance method) uses a parallel plate capacitor, with the material sandwiched in between (**Figure 4**). This method uses an impedance analyzer. It is typically used at the lower frequencies, below 1 GHz. Accuracy is typically ±1% for $\varepsilon_r'$ and ±0.005 for $\tan\delta$.

- Coaxial probe: this method uses an open-ended coaxial probe, usually with a network analyzer (**Figure 5**). Cheaper measurement systems are nowadays available on the market [30]. It is the easiest method to use for liquids, or soft semi-solids, although very flat hard solids can be measured as well, provided an excellent contact (i.e. with no air gaps) is achieved. As a matter of fact, the assumption is that the material under testing is of "semi-infinite" thickness, homogenous, non-magnetic and isotropic. Typical ranges of frequency are from 200 MHz to 50GHz, with the possibility of continuous sweeping of frequency during the measurement (wide band). The method is usually not suitable for materials having a low (<0.1) $\tan\delta$ or high $\varepsilon_r'$ (>100). Accuracy is typically ±5% for $\varepsilon_r'$ and ±0.05 for $\tan\delta$.

- Resonant cavity: this method uses a resonant cavity for the sample holder, and a network analyzer. Instead of using expensive network analyzers, a lower cost version uses a source (PLL Microwave Synthesizer), which generates the microwave stimulus, a set of directional couplers to separate reflected and transmitted signals, a microwave receiver based on the AD-8302 integrated circuit for magnitude and phase detection and a measurement probe, where the material to be measured is placed. A control unit (Microprocessor System) is connected through a USB link to a personal computer which includes all the required processing to determine dielectric properties from the measurements and to transform the outputs into the desired representation. The dielectric probe is designed as a microwave resonator where the interaction of the signals with the material takes place. In the embodiment shown in **Figure 6**, vials containing the material under test are introduced in the microwave resonator through a hole at the top of the probe. After sample insertion, the probe response (resonant frequency and quality factor) is shifted depending on the sample dielectric properties. From the measurement of the new response, the complex permittivity of the sample

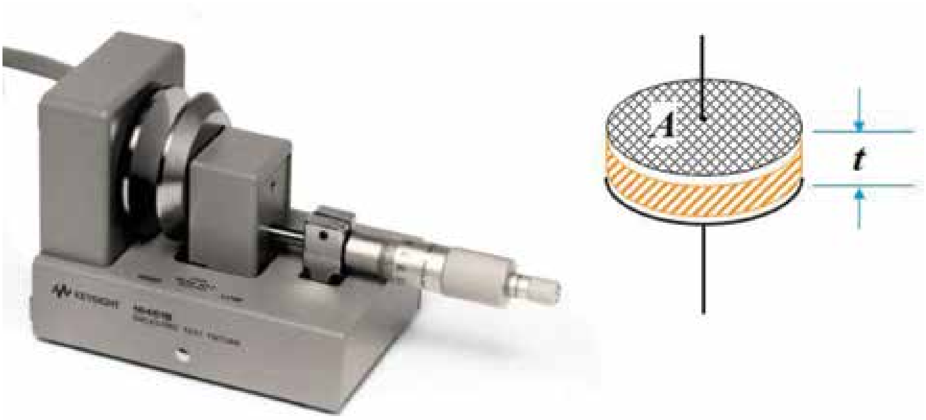

**Figure 4.** Parallel plate fixture and schematic functioning—Keysight technologies [29].

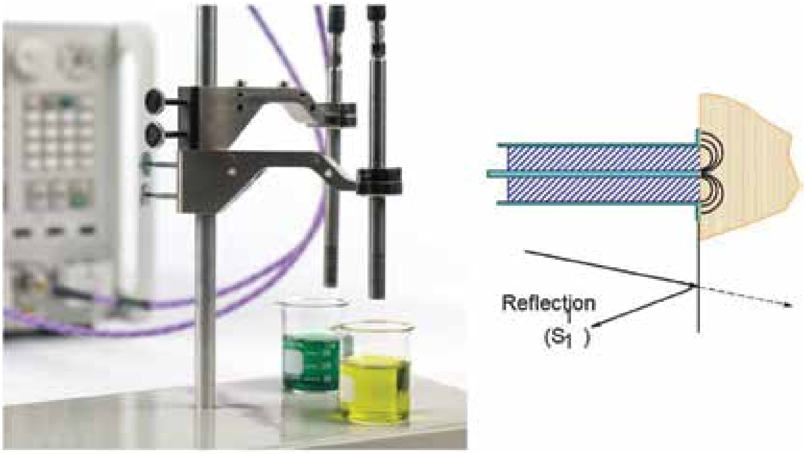

**Figure 5.** Coaxial probes and schematic functioning—Keysight technologies [29].

is calculated by using the electromagnetic model of the structure by a numerical procedure. This method has the best loss factor resolution. However, it is a narrow band method, giving information only at some specified frequencies, and requiring different cavities for different frequencies. However, as it is a differential measurement technique, no special calibration of the network analyzer is needed. It can be used also on thin films. In order to achieve precise measurements, the sample volume must be precisely known, and its dimensions should be chosen so that they do not shift excessively the resonant frequency of the cavity (out of cavity frequency range). This can occur also with small but highly lossy samples. Accuracy is typically ±1% for $\varepsilon_r'$ and ±0.00001 for tanδ.

- Transmission Line: this method (**Figure 7**) can use a variety transmission lines for sample holders with a network analyzer (or equivalent). Lines can be coaxial, waveguide and even free space is considered a transmission line technique, in the "transmitter-receiver" configuration. It is useful for a broad frequency range, from the low microwave region to the mm-wave one. Sample preparation can result difficult, as samples must be precisely machined, and thus it is best indicated for hard machineable solids (liquids and powders must be contained), but it can be applied also to magnetic materials. This technique, based on the propagation trough the dielectric, needs large samples for low frequencies and small samples for high frequencies. Accuracy is typically ±2% for $\varepsilon_r'$ and ±0.01 for tanδ.

### 3.2. Applicator design and selection

The choice or the proper design of an applicator is mandatory to determine the success of a microwave-assisted heat treatment. A typical sequence of actions leading to the development and industrialization of the chosen solution starts from very simple experimental tests, then moving to more complex questions (and answers) aimed at determining the effective yield and efficiency of the process and its correlated costs. An estimation of the costs of the whole sequence is difficult to be made in advance, except for the preliminary tests, which usually

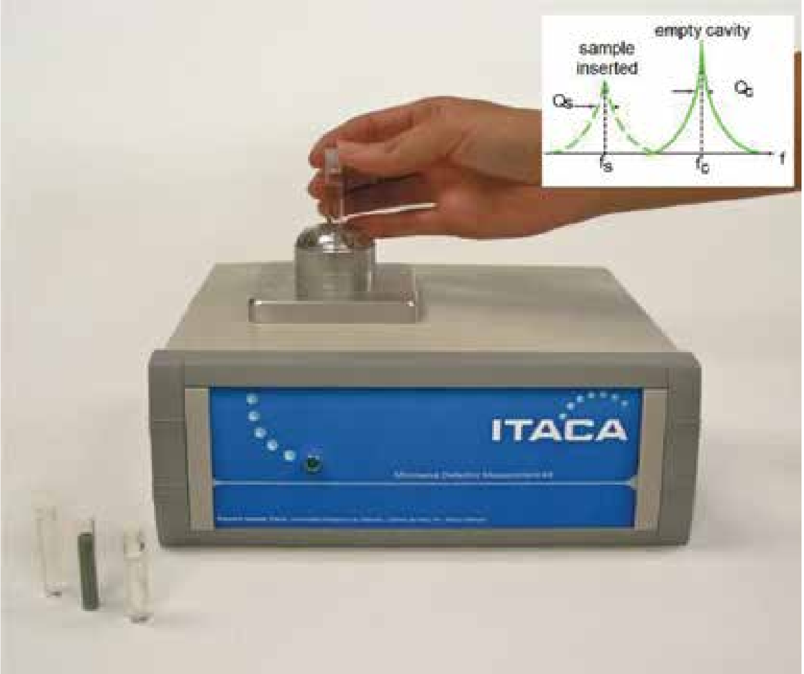

**Figure 6.** Resonant cavity and schematic functioning—ITACA [30].

require some thousands of euros. Sometimes, the preliminary tests costs can be quite high, depending on the amount and kind of material to be treated. The costs due to the subsequent steps (i.e. prototype and industrialization), as a rule of thumbs, increase dramatically as the sequence tends to the full industrialization of the investigated process.

The path leading to the full scale up, however, is not as straight as it could seem from the preliminary microwave heating tests results, and the proper applicator choice must take into account the characteristics of the process to be implemented.

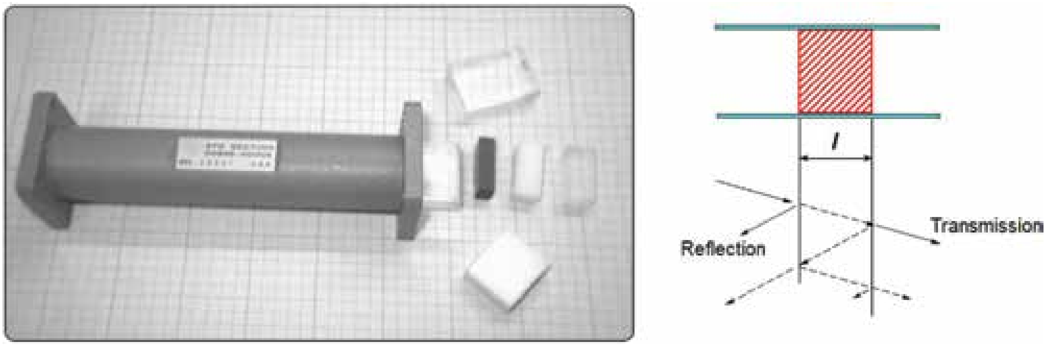

**Figure 7.** Transmission line and schematic functioning—Keysight technologies.

The process analysis is a typical tool to determine the mandatory process requirements, and the range of variability of some of the parameters involved. First of all, the process must be identified (drying, tempering, heating, melting, etc.), taking into account that sometimes more than a single operation could be performed in the same applicator (e.g. defrosting + heating; heating + solvent removal + melting; etc.). It is important to know if the material will flow continuously or if the process is suitable for batch loading of the applicator. The properties of materials play a fundamental role, and usually they are difficult to determine with good approximation, since they can change, also abruptly, as the microwave treatment proceeds. The knowledge of temperature-dependent thermal, dielectric and electrical properties is mandatory to properly design a new applicator, especially if modeling software will be used.

A good process analysis makes the subsequent steps easier, and, due to the peculiarities of the microwave heating, some aspects usually neglected in conventional heating must be taken into account, like the dielectric and electric properties of the supports (vials, stirrers, belts, trays, etc.) or of the materials used to build the applicators wall, and the compliance to national or worldwide regulations on emission and safety. A comprehensive list of questions, whose answer should be known before even starting the design, is reported in [31].

The objectives of the microwave heating application should be also stated clearly, trying to understand whether homogenous heating or efficient heating is the key issue, or a tradeoff between the two. As a matter of facts, having a good energy efficiency does not necessarily means that homogenous heating can be achieved, as all the incident power could be dissipated in only small portions of the load.

The process analysis should then lead to the selection of the preferred applicator geometry, which could be summarized as follows:

- Single mode applicators: applicators where there is only one mode (i.e. the electromagnetic field pattern inside the applicator, generally quantified for rectangular applicators as the number of half wavelengths which can exist in each one of the three applicator dimensions). Such applicators are generally small and can reach extremely high electric field strengths (used also for plasma generation). Numerical solutions for the electromagnetic field distribution inside single mode applicators exist, but the presence of the perturbing load must be taken into account. Many single mode applicators are based on cylindrical or prismatic shapes, where one of the dimensions is of the order of magnitude of the microwave wavelength.
- Multimode applicators: applicators where multiple modes exist, each one with its own pattern and the resulting electromagnetic field is given by the superimposition of such modes, at the operating frequency of the microwave generator. They can have even large dimension and have room to install rotating dishes or mode stirrers, that is, reflecting movable surfaces used to perturb the electromagnetic field distribution, randomly, thus improving the homogeneity of heat generation. Domestic microwave ovens belong to this class of applicators.
- Radiant applicators: applicators which are antenna-like, that can be used to irradiate the load both in free space or used as feeds in closed applicators. In the second case, shielding is easier, while in the former case, care must be taken in order to avoid unwanted microwave leakage. If properly designed, they can guarantee a good heat generation homogeneity,

also on large dimensions. Usually they are less dependent on load position and nature compared to the resonant applicators, like the single mode ones.

Single mode applicators are the preferred choice in laboratory scale equipment, as they usually allow the repeatable positioning of the load, providing extremely high repeatability of results, which is not guaranteed in case of multi mode applicators, where load positioning is severely affecting the performances of the applicator itself.

Another problem rises when selecting the type (and number) of microwave sources required for a given application. Multimode applicators allow to install more than one source on the applicator walls, while single mode applicators are more difficult to be adapted for multi-feeds, given their generally smaller dimensions. Moreover, the source itself can affect the selection of the applicator, as the recent advent of solid-state microwave generators, as opposed to the more conventional magnetrons, is changing the way microwaves can be delivered to the load. This has been recently addressed in the AMPERE (Association for Microwave Power in Europe for Research and Education [32]) freely accessible newsletter: Trends in RF and Microwave Heating: SPECIAL ISSUE ON SOLID-STATE MICROWAVE HEATING [33].

Transitions from vacuum tubes to solid-state electronics had already occurred decades ago in the areas of communication, computers and control, and microwave heating is next, thanks to the availability of generators of higher and higher power (but still much lower than a high power magnetron, for the time being). The solid-state microwave heating technology offers several advantages over magnetrons, like frequency and phase variability and control, low input-voltage requirements, compactness, longer life span and reliability. On the other hand, solid-state generators are more sensitive to reflected power and they should be protected using expensive ferrite isolators. Their efficiency is currently similar to the magnetron's one, but their cost for unit power is much higher than magnetrons. However, the cost predictions are subjected to uncertainties, such as the market response to the new technology and the level of mass demand for such products.

Solid-state generators emit at one precise frequency, and not with a relatively large band, like magnetrons. They are more stable in frequency over time, hence they behave quite much as an ideal source which is used in modeling microwave heating. The possibility to control the relative phase and amplitude of multiple generators has opened new possibilities, like the localized overheating of certain load parts and the advent of "autotuning" algorithms which allow to achieve the maximum efficiency by controlling the emitted frequency, in real time.

After the type of applicator has been chosen (a choice which probably will have to be revised or modified as the investigation proceeds), the design phase can begin. The simplest way to obtain a suitable applicator, is to adapt something already existing, preferably if available on the market and not too expensive. This way, unfortunately, is not generally the one leading to the best results. Theoretically, there should be an applicator for each load (and loading conditions). Luckily, there are many different ways to obtain a "different" applicator starting from the same structure: movable parts, impedance matching devices, mode stirrers, they all help conferring a higher flexibility to a given applicator, allowing its use for a certain range of loads, with satisfactory performances.

For a new process or a new product, however, a completely new design is usually required. The design step can be conducted using modeling tools (computer simulations), or by subsequent trials and errors (this approach requires a high expertise and suits best the modification of existing applicators). Each one of the approaches is not definitive and presents some advantages and drawbacks. Considering, for instance, the design of a multi-feed applicator, the use of modeling software can lead to the best solution (and not only to the satisfactory one) regarding the feed positions for a certain loading condition, without having to rely solely on experience. On the other hand, if many ports are present, with no symmetry, the modeling can become quite time-demanding; moreover, models are always a simplification of the real device, and the difference between the modeled material and the real one can sometime lead to big differences between the modeling results and the real testing. For instance, permittivity measurements can be affected by large errors, especially when referring to high temperatures or in presence of phase changes.

Usually the information required for the model to be representative of reality are difficult to be obtained, and they should be expressed as a function of temperature. Coupling the electromagnetic field modeling and the thermal/fluid-dynamical one can be sometimes very difficult. Taking into account the variation of the dielectric properties with temperature is relatively easy, since there is a 1:1 spatial correspondence among model referring to different temperatures or times. Instead, if the material undergoes a pronounced dimensional change (shrinkage, foaming, etc.), a complete description of its deformation and its effects on the electromagnetic field distribution can be very difficult to obtain.

Thus, the two approaches seem separate, but combining the two is probably the best choice to design the applicator. Starting from the model, there is always something in the real world (a deformed welded zone, some deformation in handling, a slightly different material than the one modeled) which needs to be compensated. But, also, there is always some model which should be examined to understand how a variation of a certain component or geometry of one part of the applicator influences the overall applicator performance.

In the field of microwave-assisted extractions, there are some aspects of the applicator design which require a more detailed discussion.

One of these is the evaluation of the required installed power to achieve a certain productivity. The determination, or rather, the estimation of the required installed power, can be performed by two different means. The theoretical approach uses relatively simple equations (if some simplifying assumptions are made) to determine the power required to achieve the desired result (heating, drying, etc.), using the heat equation. Taking into account, at this preliminary design stage, which will be the applicator efficiency and the power losses due, for instance, to heat losses, which is almost impossible. The theoretical approach uses thermodynamics equations to calculate the power consumption, assuming that there is no difference of the energy balance between a conventional and a microwave-assisted process. This assumption applies to almost all cases, but some chemical reactions paths seem to be quite different under microwave irradiation, requiring low activation energies or occurring with faster kinetics, probably due to the localized overheating not detectable by conventional temperature measurement systems. However, since in these cases the theoretical approach would overestimate the installed power, it can still be considered satisfactory.

The experimental approach, instead, allows to determine an upper constraint to the power to be installed to achieve the desired result. However, it suffers from the fact that the data used for the installed power calculation are dependent on the type of applicator used and on the load itself, as shown in **Figures 8** and **9**, where the same applicator has been loaded with different amounts of load (**Figure 8**) and where different applicators have been used to process the same load (**Figure 9**).

In the case shown in **Figure 8**, it is evident a nonlinear dependence of the specific power consumption on the load mass, due to excessive power reflections in case of small loads, which then tends to become constant when the reflections are low enough not to become predominant. In the other case (**Figure 9**), the different electric field strength on the load, due to different applicators geometries and efficiency (affected by the reflection coefficient), is responsible for such differences in the specific energy consumption.

The experimental approach is definitely rough, but at least it allows to determine the maximum power which will be required by the process (it is the maximum since there is always an applicator able to perform the desired treatment using an amount of energy equal or less than the energy consumption recorded in the preliminary tests).

Moreover, when deciding the installed power, it is mandatory to consider that there could be some physical limits to the power density. The main limits concern the product's integrity, the completion of reactions and the prevention of arcs or plasma formation.

A particular care must be taken in case of thermal runaway. This phenomenon often occurs when the loss factor of the material increases as temperature increases: in this case, if a region of the material exposed, for instance, to higher electric field, reaches a temperature higher than the surrounding material, it tends to increase its temperature much more than the surroundings. As a matter of fact, the higher loss factor, if the electric field is constant, leads to a higher power density, and thus to an increased heat generation and temperature increase, which, at its turn, causes a further increase of the loss factor.

Another important aspect in designing or selecting a microwave applicator for microwave-assisted extraction is the tradeoff between heating homogeneity and energy efficiency. If the load can be moved, mixed, stirred, then it is easier to achieve more uniform heating [36] due to mass transfer, but if heating homogeneity has to rely solely on heat generation and transfer,

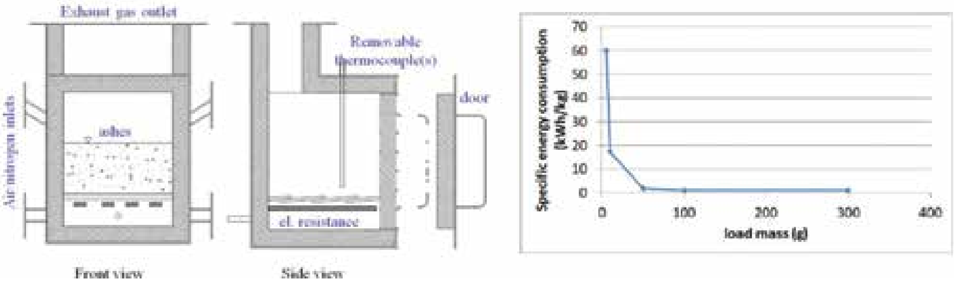

**Figure 8.** Specific energy consumption as a function of load mass during the 2.45 GHz microwave heating of ashes from lignite combustion power plants [34].

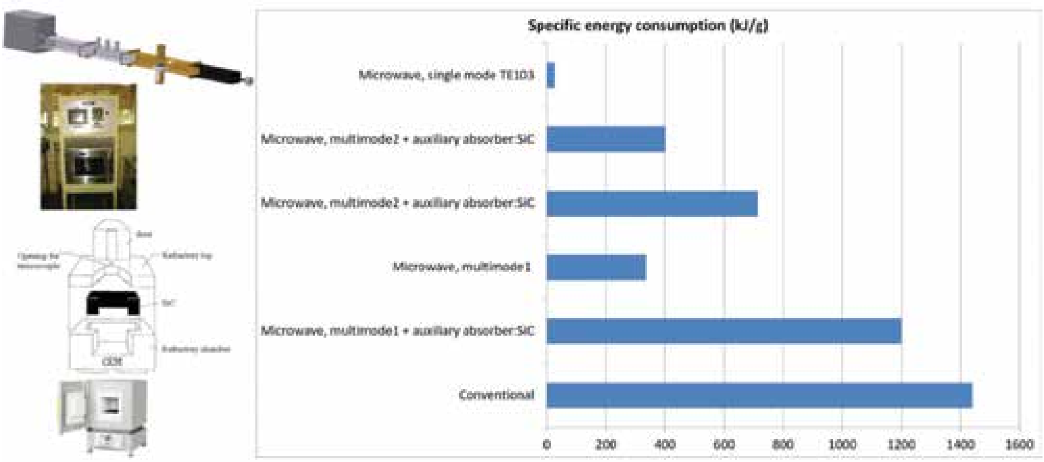

**Figure 9.** Specific energy consumption measured during the synthesis of the cobalt aluminate pigment in four different furnaces: conventional—Nannetti, Italy; Multimode1—CEM MAS (USA); Multimode2—Radatherm (Australia); single mode—self-assembled. Data from [35].

then the design becomes more critical and the use of multiple microwave sources is generally preferable. Control systems should be faster and robust, preferably adaptive, since the load usually is of natural origins, and thus it has a higher variability compared to pre-processed or synthetic starting materials.

Last but not least, since during pure (i.e. not hybrid) microwave processing heat is generated in the load and the surrounding environment remains colder, it is important also to provide sufficient thermal insulation to avoid heat losses. This is generally accomplished using insulating materials, but care must be taken when inserting them in the microwave applicator, as they could be (or become) good microwave absorbers, with the result of competing with the load in microwave power absorption and to fail as insulating materials. In this framework, another important component which is usually subjected to high electric field strength is the pressure window: in some installations, where it is required to separate the microwave generation zone from the microwave application one, like in vacuum processing, or even in case of pressurized environments, there is the need for a material able to transmit microwaves and to isolate the two environments. The requirement of materials for pressure windows are very demanding: they should withstand the load (pressure difference), with large safety coefficient, they must hold the pressure and being cleanable to avoid possible overheating of deposited particles of the load, they should present high transmission and low absorption or reflection of microwaves; they should be thermo-mechanically stable and chemical inert; they should withstand the process temperature without carbonizing, they should resist also to thermal shock and the thermal fatigue. Optionally, they should be optically transparent (common devices for arc detection are light sensors that are installed along the microwave transmission line), hence an opaque window would mask the occurrence of an arc. Moreover, for safety reasons, generally it is preferable to install two pressure windows (the second for safety in case of failure of the first one, but also for impedance matching purposes, that is, to minimize reflected power).

## 4. Is MAE really green?

Even if microwave-assisted extraction techniques are typically considered greener with respect to more conventional extraction processes mainly as a consequence of the enhanced heating rates which are obtainable with the use of microwaves and the resulting reduction in processing time, together with the reduction and sometimes elimination of any solvent, the accurate comparison between the environmental assessments of the different extraction procedures is surprisingly scarce in the scientific literature, making any trustworthy conclusions a sort of act of belief.

Recently, cradle to the grave environmental evaluations of laboratory scale conventional Soxhlet-based extraction as well as of microwave-assisted extraction were performed by applying the life cycle analysis (LCA) methodology [37]. This approach allows considering practically all the fundamentals damage categories that could have an impact on this particular process, thus including, for example, energy consumptions, abiotic resources depletion, transport, laboratory facilities, emissions as well as the disposal of waste [38].

Particularly, that study focused on the natural compound Curcumin that is actually under exponentially increasing investigation for its antioxidant, anti-inflammatory and anticancer properties [39]. In order to realize the most suitable comparison between conventional and MAE procedures, the evaluation of the total potential damage of both approaches was referred to the same mass unit or curcumin molecule (i.e. 1 kg). Both experiments were performed exploiting a similar configuration and the same extractive solvent (i.e. acetone), with the same solid to liquid ratio. In detail, conventional extraction was performed using a conventional Soxhlet apparatus reported on the left of **Figure 10**, while MAE was performed in a $TE_{103}$ single mode applicator operating at the frequency of 2.45 GHz that is reported on the right of **Figure 10**.

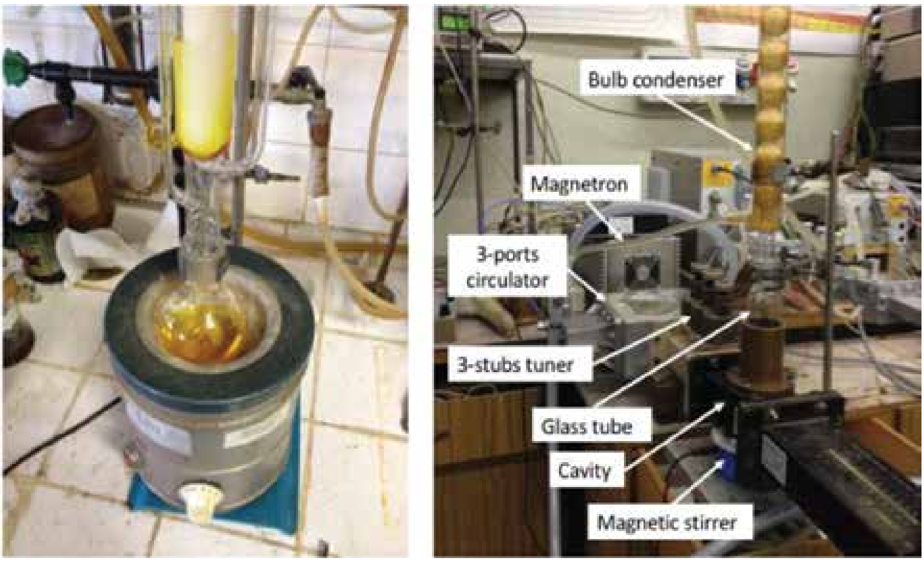

**Figure 10.** Conventional Soxhlet-based apparatus (left) and microwave-assisted extraction applicator (right).

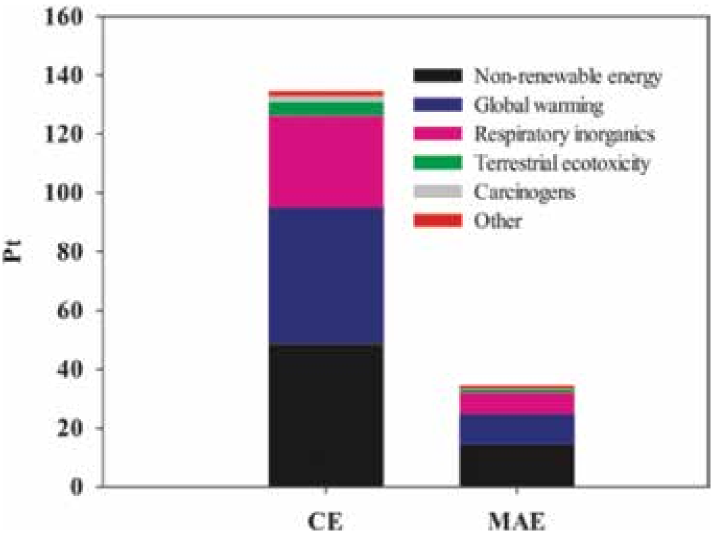

**Figure 11.** Comparative analysis of curcumin life cycle produced by conventional extraction (CE) and by MAE technique, at a laboratory scale. Adapted from [37].

Conventional Soxhlet extraction was prolonged for 24 h, while the use of microwave energy allowed obtaining comparable extraction yields in only 5 min of heating at reflux conditions. Single score evaluation results are reported in **Figure 11**, where Pt represents the eco-indicator points: the lower its value is the better that particular process will impact on the environment. Particularly, the conventional Soxhlet-based extraction resulted in 135 Pt, while the environmental damage associated with the proposed MAE resulted ca. 75% lower (i.e. 34.4 Pt), thus suggesting a greener character of microwaves with respect to conventional extraction procedures, at least in the considered lab-scale scenario. In both cases the three most impacting categories resulted "non-renewable energy", "global warming" and "respiratory inorganics", primarily as a consequence of consumptions of abiotic resources and emission of inorganic species, which are associated to the processes used to describe the electrical energy demand of the extraction techniques compared.

These results are worth to note also because they were obtained taking into account the poor efficiency a 2.45 GHz microwaves magnetron generators.

## 5. Coupling with further techniques

In an effort to continuously improve extraction efficiency and contemporary increase the green characteristics of microwave-assisted extraction in a process intensification (PI) perspective [40], several integrating technologies have recently been coupled with microwave heating [15]. The most widely employed ones are summarized in the next sub-sections.

### 5.1. Ultrasonic microwave-assisted extraction (UMAE)

Similar to MAE techniques, the use of ultrasounds (US) was also reported to tremendously increase extraction yields and reduce extraction time as well as the amounts of solvents needed, as a results of a combination of different extraction mechanisms like fragmentation, erosion, capillarity, detexturation and sonoporation [41].

Independently by the mechanism (or combination of different ones) which are responsible for a given extraction procedure, acoustic cavitation is at the basis of ultrasound-assisted extraction (UAE), since it lead to high shear forces, generation of microjets, shock waves and pressure variations.

Simultaneous irradiation of microwaves and ultrasounds for extraction purposes was firstly reported by Cravotto et al. [42] for the extraction of vegetable oils, resulting in higher yields in comparison with the sole use of microwave energy (employing both open and closed vessels). A dedicated PEEK horn was used in order to avoid arcing and further unwanted phenomena, into the multimode microwave cavity, as a consequence of the use of metallic horns. In all likelihood, the higher extraction yields typically reported when microwave energy is combined with ultrasounds is related to the further contribution offered by ultrasounds to the disruption of plant cell walls (manifested at lower frequencies), thus further enhancing the mass transfer from the plant to the extracting solvent.

A further peculiarity of US is the acceleration in the rehydratation and swelling of the plant, therefore, this can be exploited in the use of a combination of both microwaves and ultrasounds for the extraction from previously dried matrices.

### 5.2. MAE in ionic liquids (ILs)

The nature of ionic liquids (ILs) makes them suitable candidate solvents to efficiently couple with the electromagnetic energy at the microwave frequencies, mainly due to the ionic losses contribution to the loss factor value. Indeed, ILs are organic salts existing in the liquid state, constituted by an organic cation and an organic or inorganic anion [43].

Further properties (different from their chemical structure) of ILs that led to intensification of extraction processes from plant materials are their excellent solvating properties, a high thermal stability together with an easy to tailor viscosity. These properties significantly contributed to spread their utilization in extraction of both polar and non-polar natural compounds.

Despite the reported advantages, several concerns related to the use of ILs still exist. Indeed, even if considered green solvents as a consequence of their extremely low volatility, issues related to their toxicity and the high cost associated to their preparation remain.

### 5.3. Deep eutectic solvents (DESs)

In a continuous research for new green solvents for extraction purposes, deep eutectic solvents (DESs) were recently investigated for the extraction of bioactive compounds [44]. Even if they can be seen as ILs analogs (since they possess similar physicochemical properties), they have been reported to be biodegradable and to possess lower toxicity and production costs.

DESs are systems composed by an eutectic mixture of Lewis or Brønsted acids and bases characterized by melting points much lower with respect to the individual constituents [45].

More recently natural deep eutectic solvents (NADESs) were developed by combining primary metabolites and bio-renewable starting materials, like sugars, amino acids and organic acids [46].

Similar to ILs, their chemical structure (or better in this case the chemical structure of the constituents the eutectic mixture) assure an excellent microwaves absorbing ability, thus making them suitable candidate solvents to be used in MAE as recently proposed, for the extraction of genistin, genistein and apigenin from pigeon pea roots [47]. Efficiency of DESs in coupling with microwave energy, was recently proved to lead to a greater (with respect to more conventional MW-coupling solvents like water and methanol) degree of disruption of cell walls [48].

### 5.4. Design of experiments (DoE)

A further tool that can significantly intensify every kind of extraction process (and not only), thus including also microwave-assisted procedures, is represented by design of experiments (DoE). DoE is a well-recognized collection of statistical and mathematical tools that has been widely exploited to improve and optimized extraction processes [49], as well as many other application fields in chemistry and materials science [50–53]. It relies in a statistical-based methodology used to systematically plan all the experiments to perform in order to obtain trustworthy and robust data without loosing extremely useful information on individual variables as well as interaction effects among different variables on the final goal of the study that could be, for example, the optimization of a certain MAE protocol. Indeed, traditionally the optimization of the extraction conditions for a certain technique and a certain matrix, are performed by the one-factor-at-time (OFAT) approach, that is extremely time and energy demanding and moreover, it could lead to the loss of the effects caused by several extraction parameters acting in combination. Therefore, in this perspective DoE approach can be easily considered an important tool to pursue a more rapid green process intensification development.

In a recent work [49], these statistical techniques were applied to the microwave-assisted extraction of phenolic compounds from *Juglans regia* L. fresh male flowers and unripe walnuts seeds, with the aim to investigate the role on the extraction efficiency of temperature, extraction time and number of microwaves heating cycles.

## 6. Conclusions

Microwave-assisted extraction (MAE) of naturally occurring chemical compounds is an extremely efficient extraction technique mainly as a consequence of the unique heating mechanism that is able to generate peculiar and otherwise impossible to reach extraction mechanisms. Different variants of MAE can be though according to the system matrix-solvent to be employed. Indeed, the choice of the kind of MAE technique to be applied, cannot discern from a fundamental aspect to be considered, that is represented by the detailed knowledge of the dielectric properties of the matrix as well as the solvent, to be used. They represent important parameters to be used as input information for numerical simulation studies aimed at predict the microwave power distribution and the temperature evolution into the load during the extraction process.

Numerical simulation is fundamental also since it allows to rapidly select the optimal dimensions of the microwave cavity for a particular load (with particular dielectric properties).

In this view, it can be seen in a process intensification perspective.

In the same perspective, MAE has been shown to significantly benefit from the coupling of a different number of integrating technologies and tools.

However, it has been shown that although MAE can effectively and quantitatively considered greener with respect to conventional soxhlet-based extraction, for example, in the case of lab-scale extraction of curcumin molecule, general conclusions cannot be drawn, since case to case evaluations are mandatory. The use of cradle to the grave LCA evaluation is highly recommended to reach such assessments.

## Author details

Roberto Rosa[1], Erika Ferrari[2] and Paolo Veronesi[1]*

*Address all correspondence to: paolo.veronesi@unimore.it

1 Department of Engineering "Enzo Ferrari", University of Modena and Reggio Emilia, Modena, Italy

2 Department of Chemical and Geological Sciences, University of Modena and Reggio Emilia, Modena, Italy

## References

[1] Anastas PT, Warner R. Green Chemistry, Theory and Practice. New York: Oxford University Press; 1998. p. 30

[2] Tobiszewski M, Mechlinska A, Namiesnik J. Green analytical chemistry-theory and practice. Chemical Society Reviews. 2010;**39**:2869-2878

[3] Galuszka A, Migaszewski Z, Namiesnik J. The 12 principles of green analytical chemistry and the SIGNIFICANCE mnemonic of green analytical practices. Trends in Analytical Chemistry. 2013;**20**:78-84

[4] Chemat F, Vian MA, Cravotto G. Green extraction of natural products: Concept and principles. International Journal of Molecular Sciences. 2012;**13**:8615-8627

[5] Hayes BL. Microwave Synthesis: Chemistry at the Speed of Light. CEM Publishing; 2002

[6] von Hippel AR. Dielectric Materials and Applications. The MIT Press; 1954

[7] Perino-Issartier S, Zill-e-Huma YJ, Vian MA, Chemat F. Solvent-free microwave-assisted extraction of antioxidant from sea buckthorn (*Hippophae rhamnoides*) food by-products. Food and Bioprocess Technology. 2011;**4**:1020-1028

[8] Veggi PC, Martinez J, Meireles MAA. Fundamentals of microwave extraction. In: Chemat F, Cravotto G, editors. Microwave-Assisted Extraction for Bioactive Compounds Theory and Practice. New York: Springer; 2013

[9] Bao Y, Han J, Hu FB, Giovannucci EL, Stampfer MJ, Willet WC, Fuchs CS. Association of nut consumption with total and cause-specific mortality. New England Journal of Medicine. 2013;**369**:2001-2011

[10] Le V, Esposito D, Grace MH, Ha D, Pham A, Bortolazzo A, Bevens Z, Kim J, Okuda R, Kormarnytsky S, Lila MA, White JB. Cytotoxic effects of ellagitannins isolated from walnuts in human cancer cells. Nutrition and Cancer. 2014;**66**:1304-1314

[11] Contini M, Baccelloni S, Massantini R, Anelli G. Extraction of natural antioxidant from hazelnut (*Corylus avellana* L.) shell and skin wastes by long maceration at room temperature. Food Chemistry. 2008;**110**:659-669

[12] Oliveira I, Sousa A, Ferreira ICFR, Bento A, Estevinho L, Pereira JA. Total phenols, antioxidant potential and antimicrobial activity of walnut (*Juglans regia* L.) green husks. Food and Chemical Toxicology. 2008;**46**:2326-2331

[13] Wijngaard H, Hossain MB, Rai DK, Brunton N. Techniques to extract bioactive compounds from food by-products of plant origin. Food Research International. 2012;**26**:505-513

[14] Ekezie FGC, Sun DW, Han Z, Cheng JH. Microwave-assisted food processing technologies for enhancing product quality and process efficiency: A review of recent developments. Trends in Food Science and Technology. 2017;**67**:58-69

[15] Ekezie FGC, Sun DW, Cheng JH. Acceleration of microwave-assisted extraction processes of food components by integrating technologies and applying emerging solvents: A review of latest developments. Trends in Food Science and Technology. 2017;**67**:160-172

[16] Vinatoru M, Mason TJ, Calinescu I. Ultrasonically assisted extraction (UAE) and microwave assisted extraction (MAE) of functional compounds from plant materials. Trends in Analytical Chemistry. 2017;**97**:159-178

[17] Chan CH, Yusoff R, Ngoh GC, Kung FWL. Microwave-assisted extractions of active ingredients from plants. Journal of Chromatography A. 2011;**1218**:6213-6225

[18] Kala HK, Mehta R, Sen KK, Tandey R, Mandal V. Critical analysis of research trends and issues in microwave assisted extraction of phenolics: Have we really done enough. Trends in Analytical Chemistry. 2016;**85**:140-152

[19] Ganzler K, Salgò A, Valkò K. Microwave extraction a novel sample preparation method for chromatography. Journal of Chromatography A. 1986;**371**:299-306

[20] Gedye RN, Smith FE, Westaway KC, Ali H, Baldisera L, Laberge L, Roussel J. The use of microwave ovens for rapid organic synthesis. Tetrahedron Letters. 1986;**27**:279-282

[21] Giguerre RJ, Bray TL, Duncan SM, Majetich G. Application of commercial microwave ovens to organic synthesis. Tetrahedron Letters. 1986;**27**:4945-4948

[22] Li Y, Tixier ASF, Vian MA, Chemat F. Microwave-assisted extraction of antioxidants and food colors. In: Chemat F, Cravotto G, editors. Microwave-Assisted Extraction for Bioactive Compounds Theory and Practice. New York: Springer; 2013

[23] Prat D, Hayler J, Wells A. A survey of solvent selection guides. Green Chemistry. 2014;**16**:4546-4551

[24] Chemat F, Smadja J, Lucchesie ME. Solvent free microwave extraction of volatile natural compounds. European Patent EP 1 439218 $B_1$; 2004

[25] Chemat F, Lucchesie ME, Snadja J. Solvent free microwave extraction of volatile natural substances. American Patent US 0187340 $A_1$; 2004

[26] Chemat F, Vian MA, Fernandez X. Microwave-assisted extraction of essential oils and aromas. In: Chemat F, Cravotto G, editors. Microwave-Assisted Extraction for Bioactive Compounds Theory and Practice. New York: Springer; 2013

[27] Chemat F, Vian MA, Visinoni F. Microwave hydrodiffusion for isolation of natural products, European Patent EP 1,955,749 $A_1$

[28] IEEE standard definitions of terms for radio wave propagation

[29] http://www.keysight.com

[30] http://www.itaca.upv.es/

[31] Metaxas AC, Meredith RJ. Industrial Microwave Heating. Peter Peregrinus: London; 1983

[32] www.ampereeurope.org

[33] Ampere newsletter 89. July 2016. pp. 1-38. ISSN: 1361-8598

[34] Leonelli C, Veronesi P, Siligardi C, Carrea F, Pellacani GC. Fly and bottom ash treatment in 2.45 GHz multimode cavity at variable powers. In: Proceedings of the 7th International Conference on Microwave and High Frequency Heating, 343-344, Servicio de Publicaciones; Valencia, Valencia (ES); 13-17 Sept 1999

[35] Veronesi P, Leonelli C, Bondioli F. Energy efficiency in the microwave-assisted solid-state synthesis of cobalt aluminate pigment. Technologies. 2017;**5**:42

[36] Kappe CO. Controlled microwave heating in modern organic synthesis. Angewandte Chemie, International Edition. 2004;**43**:6250-6284

[37] Zerazion E, Rosa R, Ferrari E, Veronesi P, Leonelli C, Saladini M, Ferrari AM. Phytochemical compounds or their synthetic counterparts? A detailed comparison of the quantitative environmental assessment for the synthesis and extraction of curcumin. Green Chemistry. 2016;**18**:1807-1818

[38] Tufvesson LM, Tufvesson P, Woodley JM, Borjesson P. Life cycle assessment in green chemistry: Overview of key parameters and methodological concerns. International Journal of Life Cycle Assessment. 2013;**18**:431-444

[39] Goel A, Kunnumakkara AB, Aggarwal BB. Curcumin as "Curecumin": From kitchen to clinic. Biochemical Pharmacology. 2008;**75**:787-809

[40] Stankiewicz A, Moulijn JA. Process intensification: Transforming chemical engineering. Chemical Engineering Progress. 2000;**96**:22-34

[41] Chemat F, Rombaut N, Sicaire AG, Meullemiestre A, Tixier ASF, Vian MA. Ultrasound assisted extraction of food and natural products. Mechanisms, techniques, combinations, protocols and applications. A review. Ultrasonics Sonochemistry. 2017;**34**:540-560

[42] Cravotto G, Boffa L, Mantegna S, Perego P, Avogadro M, Cintas P. Improved extraction of vegetable oils under high-intensity ultrasound and/or microwaves. Ultrasonics Sonochemistry. 2008;**15**:898-902

[43] Tang B, Bi W, Tian M, Row KH. Application of ionic liquid for extraction and separation of bioactive compounds from plants. Journal of Chromatography B. 2012;**904**:1-21

[44] Abidin MHZ, Hayyan M, Hayyan A, Jayakumar NS. New horizons in the extraction of bioactive compounds using deep eutectic solvents: A review. Analytica Chimica Acta. 2017;**979**:1-23

[45] Abbott AP, Boothby D, Capper G, Davies DL, Rasheed RK. Deep eutectic solvents formed between choline chloride and carboxylic acids: Versatile alternatives to ionic liquids. Journal of the American Chemical Society. 2004;**126**:9142-9147

[46] Dai Y, Rozema E, Verpoorte R, Choi YH. Application of natural deep eutectic solvents to the extraction of anthocyanins from *Catharanthus roseus* with high extractability and stability replacing conventional organic solvents. Journal of Chromatography A. 2016;**1434**:50-56

[47] Cui Q, Peng X, Yao XH, Wei ZF, Luo M, Wang W, Zhao CJ, Fu YJ, Zu YG. Deep eutectic solvent-based microwave-assisted extraction of genistin, genistein and apigenin from pigeon pea roots. Separation and Purification Technology. 2015;**150**:63-72

[48] Chen J, Liu M, Wang Q, Du H, Zhang L. Deep eutectic solvent-based microwave-assisted method for extraction of hydrophilic and hydrophobic components from radix salvia miltiorrhizae. Molecules. 2016;**21**(10):1383

[49] Rosa R, Tassi L, Orteca G, Saladini M, Villa C, Veronesi P, Leonelli C, Ferrari E. Process intensification by experimental design application to microwave-assisted extraction of phenolic compounds from *Juglans regia* L. Food Analytical Methods. 2017;**10**:575-586

[50] Poli G, Sola R, Veronesi P. Microwave-assisted combustion synthesis of NiAl intermetallics in a single mode applicator: Modeling and optimisation. Materials Science and Engineering A. 2006;**441**:149-156

[51] Gonzalez EIC, Mugoni C, Montorsi M, Siligardi C. Evaluation of the correlations between temperature, humidity, incident UV light and the photocatalytic activity of TiO2 films using a rationale approach. Applied Surface Science. 2016;**378**:73-79

[52] Mugoni C, Licciulli A, Diso D, Siligardi C. Lanthanum glass infiltrated alumina/alumina composites for dental prosthetic applications. Ceramics International. 2015;**41**:13090-13099

[53] Gonzalez EIC, Montorsi M, Mugoni C, Montorsi M, Siligardi C. Improvement of the adhesion between $TiO_2$ nanofilm and glass substrate by roughness modifications. Physics Procedia. 2013;**40**:19-29

*Edited by Kok Yeow You*

Recently, the rapid development of microwave technologies has had a significant impact on current industrial, agricultural, medical, and food processing fields. This book is a self-contained collection of valuable scholarly papers related to the microwave applications. This book contains 10 chapters that cover several subtopics of the microwave engineering, namely, microwave system design models, emerging microwave devices, and microwave heating/drying technologies. Hence, this book should be useful to the academics, scientists, practicing researchers, and postgraduate students whose works are related to microwave technologies.

Published in London, UK

IntechOpen

ISBN 978-1-83881-397-0
9 781838 813970